



**Politecnico
di Torino**

ScuDo

Scuola di Dottorato ~ Doctoral School

WHAT YOU ARE, TAKES YOU FAR

Doctoral Dissertation
Doctoral Program in Materials Science and Technology (36th Cycle)

Laser Directed Energy Deposition for Processing and Repairing Steels

Josip Vinčić

Supervisors

Prof. Diego Giovanni Manfredi

Prof. Federica Bondioli

Doctoral Examination Committee:

Prof. Michael Benoit, University of Waterloo

Prof. Alessandro Morri, Università degli Studi di Bologna

Politecnico di Torino
2023

This thesis is licensed under a Creative Commons License, Attribution - Noncommercial - NoDerivative Works 4.0 International: see www.creativecommons.org. The text may be reproduced for non-commercial purposes, provided that credit is given to the original author.

I hereby declare that, the contents and organisation of this dissertation constitute my own original work and does not compromise in any way the rights of third parties, including those relating to the security of personal data.

.....

Josip Vinčić
2023

Summary

This doctoral thesis presents a comprehensive investigation into the microstructural and mechanical properties of steels processed using the additive manufacturing (AM) technique known as Laser Directed Energy Deposition (L-DED), using as raw materials powders or wires. The primary objectives were to develop the main process parameters to fabricate effective objects with different types of steels and to repair industrial tools. The present thesis begins by providing a thorough technological background, explaining the processes involving different feedstocks, and trying to establish a metallurgical foundation for the steel alloys studied.

The subsequent chapters are organized based on the specific steel studied, each chapter delving into the material properties and characterization, into the main process parameters optimization, and then into the post heat treatment effects.

Beginning with stainless steel 316L (Chapter 2), the study progressed from characterizing the powder employed in the L-DED process to optimizing the main process parameters of the system employed to obtain bulk dense samples. Detailed analyses of the microstructure and mechanical properties of the bulk 316L samples fabricated by L-DED were conducted. Investigations into different deposition strategies were also undertaken, focusing on understanding the impact of heat accumulation. A factor screening approach was employed, measuring multiple responses concerning various factors and covariates. The chapter dedicated to stainless steel 316L concluded in determining also the optimal process window for another L-DED system with the starting material in wires.

It was found that the optimized process parameters using a Laserdyne 430 by Prima Additive with 2 mm laser spot diameter utilize a specific volumetric energy density of 133.3 J/mm^3 , ensuring the production of fully dense, crack-free specimens. The microstructural analysis exhibited a typical AM microstructure

with micro-segregation and some Mn/Si oxide inclusions. The microhardness exhibited a decrease towards the top of the samples due to reduced cooling rates, with a mean value of 203 HV.

Processing 316L stainless steel wire with the LAWS 250 system by Liburdi, which utilizes a 0.3 mm laser spot diameter and has a fixed wire feeding position, revealed the main process parameters for all feeding directions. However, challenges emerged with the wire feeding system, resulting in issues such as porosity and misalignment during subsequent track depositions. The following experimental chapter (Chapter 3) delved into hot work tool steels, in particular the W360 steel (from Böhler), to be processed through Laserdyne 430 system. This segment commenced with characterizing the starting powder, followed by the optimization of the main process parameters. Heat treatments were then applied to the as-built L-DED samples of W360, leading to discussions on microstructural evolution of the as-built, as-quenched, and hardened W360 samples. Optimized parameters yielded a specific volumetric energy density of 82.1 J/mm³ for samples with 99.85% relative density. The as-built W360 sample exhibited a typical AM microstructure, characterized by a cellular-dendritic pattern with small carbides observed in the intercellular regions. The effect of post processing heat treatment was also investigated. Post-quenching, the samples displayed the typical microstructure of hot work tool steels, consisting of small martensite laths and carbides. After three consecutive tempering cycles on the quenched samples microstructure exhibited a tempered martensite matrix with grown Mo-rich carbides. The as-built sample demonstrated a mean microhardness of 642 HV, while as-quenched sample had 744 HV and tempered samples showed 634 HV microhardness.

Chapter 4 was then focused on the 18Ni-300 maraging steel, again in powder form. The exploration commenced with characterizing the initial powder, proceeded to optimize the main process parameters, and culminated in a detailed analysis of the microstructural and mechanical properties of the samples fabricated by L-DED using a LAWS 250 system with 0.3 mm laser spot diameter. Optimized parameters yielded a specific volumetric energy density of 121.9 J/mm³ for building samples with 99.62% relative density. The as-built 18Ni-300 samples revealed a typical AM microstructure with a cellular-dendritic pattern comprising both equiaxed and columnar dendrites together with the Ti-rich black nanoparticles. The mean microhardness value of as-built 18Ni-300 sample was 331 HV.

The final chapter, Chapter 5, focused on studies involving the application of L-DED in repair processes, starting from powders and using Laserdyne 430 system. A thorough investigation of D2 tool steel was conducted to comprehend its

behaviour in the L-DED process used as a substrate. Once understood, the deposition of W360 on the D2 steel substrate was executed to investigate the feasibility of the repairing process by L-DED. The initial worn industrial blade, made of D2 cold work tool steel in a hardened state, featured large carbides dispersed within the martensitic matrix, presenting challenges for repair attempts. Through an annealing process, the microhardness of the D2 substrates decreased, facilitating successful welding on annealed D2 substrates. Subsequently, crack-free, nearly fully dense W360 samples were deposited onto annealed D2 steel substrates, indicating promising results for repair applications. Optical micrographs revealed a typical AM microstructure, and EDS analysis indicated Cr and V-rich carbides. However, microhardness measurements highlighted the need for adjustments in the heat treatment process for W360 steel to achieve the desired microhardness, emphasizing the importance of careful consideration and optimization of repair process parameters.

In summary, these findings underscore the significance of careful consideration and optimization of the repair process parameters to ensure successful and durable repairs of industrial components made in tool steels.

Acknowledgment

I am extremely grateful for the unwavering support and guidance I have received throughout my research journey, and I wish to express my deepest gratitude to those who have played a crucial role in shaping this experience.

First and foremost, I extend my heartfelt appreciation to Professor Diego Manfredi, my supervisor, for his exceptional mentorship, unwavering expertise, and continuous support. Professor Manfredi's guidance has been invaluable, and I am profoundly grateful for his encouragement during challenging times. His kind words, friendship, and leadership have made a significant impact, not only on my academic endeavours but also on my personal growth.

I am also indebted to Alberta Aversa, my unofficial advisor, whose contributions to both my research and personal life have been immeasurable. Collaborating with Alberta has been a truly enriching experience, and her support has been a constant source of inspiration. Beyond academia, being her friend has been inspiring, especially during our coffee and gelato times. I am very grateful for her steady support.

I extend my gratitude to Professor Michael Benoit, my supervisor during the visiting period at the University of British Columbia, for his hospitality and mentorship. I am thankful for the opportunity to work on various projects under his guidance and for the valuable knowledge imparted during my time in his research group.

Special thanks go to my dear friends and collaborators: Adriano Pilagatti from Politecnico di Torino, Christopher Paul from the University of British Columbia in Kelowna, and the dynamic duo from Prima Additive, Ioannis Stavridis, and Guido Barale. Your friendship and collaboration have enriched my experience, both professionally and personally.

I am grateful to all the members of the Gamma Team research group for providing a stimulating environment and to Professor Federica Bondioli for involving me in challenging project. I also appreciate the immediate inclusion by Professor Benoit's research group at UBCO.

I extend my gratitude to the Italian Institute of Technology and Politecnico di Torino for funding my PhD research, which made this journey possible.

To my family, thank you for your support, guidance, and love throughout this journey. Your advice and encouragement have been instrumental in reaching this

milestone. To my Call of Duty squad “Kršni momci” for helping me survive the least pleasant times of COVID restrictions. To my friends from all around the world, your support and companionship have been invaluable, and I am grateful for your presence in my life.

Thank you all for being an integral part of this significant chapter in my academic and professional life.

Contents

1. Introduction.....	1
1.1 Additive manufacturing	1
1.1.1 Directed Energy Deposition.....	4
1.1.2 Laser Directed Energy Deposition.....	7
1.1.3 Laser Directed Energy Deposition with Powder Feedstock.....	9
1.1.4 Laser Directed Energy Deposition with Wire Feedstock	11
1.2 Steels.....	13
1.2.1 Stainless steels	17
1.2.2. Tool steels.....	19
1.2.3. Maraging steels	22
1.3 Additive manufacturing of steels.....	24
1.3.1. Stainless steel 316l by L-DED.....	25
1.3.2. Hot work tool steel by L-DED.....	26
1.3.3. Maraging steel by L-DED	27
1.4 Research objectives	28
2. AISI 316L by DED.....	30
2.1 Powders for L-DED-P	30
2.2 Process parameters optimization for L-DED-P.....	34
2.3 Microstructural analysis of samples by L-DED-P.....	38
2.4 L-DED-P deposition strategy – influence of heat accumulation.....	42
2.5 Factor screening for multiple responses in L-DED-P	48
2.5.1 Height assessment	53
2.5.2 Density assessment.....	56
2.5.3 Porosity assessment.....	58
2.5.4 Hardness assessment	61
2.5.5 Conclusions on factor screening	64
2.6 Effects of wire feeding direction and main process parameters in L-DED-W.....	65
2.6.1 Single track deposition	67

2.6.2	Single layer deposition	71
2.6.3	Control and configuration challenges on L-DED-W	71
3.	W360 by L-DED	76
3.1	W360 powder for L-DED-P process	76
3.2	Process parameters optimization for W360 by L-DED	78
3.3	Heat treatment of the W360 as-built samples	81
3.4	Microstructural evolution during heat treatment of W360	82
4.	18Ni-300 by L-DED	91
4.1	18Ni-300 powder for L-DED-P process	91
4.2	Process parameters optimization for 18Ni-300 by L-DED.....	93
4.3	Microstructural analysis of 18Ni-300 samples built with optimized parameters	99
5.	L-DED in repair of D2 steel components	104
5.1	Characterization and preparation of an industrial tool for repair process	104
5.2	Repair process of D2 steel using the W360 steel by L-DED.....	110
6.	Conclusions	116
316L	by L-DED	117
W360	by L-DED	117
18Ni-300	by L-DED.....	118
L-DED	in repair of D2 steel components.....	118
7.	Appendix – A – Experimental procedure	120
A.1	Step 1: Single tracks	120
A.2	Step 2: Single layers	122
A.3	Step 3: Bulk samples.....	123
8.	Appendix – B – Experimental equipment and characterization methods.....	124
B.1	Powder characterization	124
B.1.1	Laser granulometry.....	124
B.1.2	Electron microscopy	124
B.1.3	Apparent density measurement	124
B.1.4	Tapped density measurement.....	125
B.1.5	Flowability measurement.....	126
B.1.6	True density measurement	127

B.1.7 Porosity evaluation	127
B.1.8 LECO analysis.....	127
B.1.9 Oxide evaluation.....	128
B.2 L-DED machines and heat treatment instrument.....	128
B.2.1 Laserdyne 430	128
B.2.2 Laws 250.....	129
B.2.3 Nabertherm RHTC 80-710/15.....	130
B.3 Microstructural and mechanical analysis – equipment and procedure	131
B.3.1 Microstructural analysis.....	131
B.3.2 Thermal analysis.....	132
B.3.3. Mechanical properties.....	132
9. References	133

List of Tables

Table 1.1 Comparison of different heat sources in DED [50,51]. Build volume refers to the relative size of components that can be processed by the subject process. Detail resolution refers to the ability of the process to create small features. Deposition rate refers to the rate at which a given mass of product can be produced. Coupling efficiency refers to the efficiency of energy transfer from the energy source to the substrate, and Potential for contamination refers to the potential to entrain dirt, gas, and other possible contaminants within the part.....	7
Table 1.2 Stability of carbides arranged in the order of decreasing carbide stability [93].....	20
Table 2.1. Standard and nominal chemical composition of AISI 316L stainless steel powder.....	31
Table 2.2. Flow properties of 316L powder.....	32
Table 2.3. Results of LECO analysis for 316L powder before and after use...34	
Table 2.4. Process parameter ranges and steps used for deposition of STs for DoE #1, DoE #2 and DoE #3.....	35
Table 2.5. Optimized process parameters used for building 316L cubes.....	37
Table 2.6. EDS point analysis results of cell boundary and cell with reported % wt. of main alloying elements.....	39
Table 2.7. EDS point analysis results with reported % wt. of elements.....	41
Table 2.8. L-DED-P process parameters subdivision.....	49
Table 2.9. Investigated factors and their levels.....	50
Table 2.10. Experimental data used for ANCOVA method.....	51
Table 2.11. ANCOVA results for Height assessment.....	53
Table 2.12. ANCOVA results for density assessment.....	56
Table 2.13. ANCOVA results for Porosity assessment.....	59
Table 2.14. ANCOVA results for Hardness assessment.....	61

Table 2.15. Nominal chemical composition of 316L wires employed.....	66
Table 2.16. Process parameter ranges and steps used for deposition of STs for DoE #1 and DoE #2.....	67
Table 3.1. Nominal chemical composition of the W360 steel powder used in this study.....	76
Table 3.2. Bulk properties of W360 powder.....	78
Table 3.3. Process parameter ranges and steps used for deposition of STs for DoE.....	79
Table 3.4. Main process parameters optimized to manufacture bulk samples made of W360 steel by L-DED.....	80
Table 3.5. EDS spot analysis with main alloying elements in % wt. of W360 by L-DED samples in AB, Q, and HT conditions. The spot number is related to Fig. 3.8.....	85
Table 4.1. Standard and nominal chemical composition of the 18Ni-300 powder.....	91
Table 4.2. Process parameters used for deposition of STs for DoE #1 and DoE #2.....	93
Table 4.3. Labelled sets of parameters used for creation of SLs.....	96
Table 4.4. Measured microhardness, porosity and utilized energy density for each cube deposited.....	98
Table 4.5. Summarized process parameters and calculated specific volumetric energy density for the selected set of parameters (cube 1).....	98
Table 5.1. Nominal chemical composition of D2 cold work tool steel.....	105
Table 5.2. Combinations for 316L STs deposition on D2 substrate.....	106
Table B.1 Scale of Flowability for Compressibility Index and Hausner Ratio [214].....	126
Table B.2. Specifications of Laserdyne 430 by Prima Additive.....	129
Table B.3. Specifications of LAWS 250 by Liburdi Automation.....	130

List of Figures

Figure 1.1 AM vs. subtractive manufacturing. a) In subtractive manufacturing, a block of material is processed by material-removing machines according to digital design before obtaining the final 3D object together with a large amount of residual material. b) In AM, a starting material (powder, liquid, filament, etc.) is processed by a 3D-printing machine, which deposits just the required amount of material in layer-by-layer fashion before the final 3D object is obtained. The amount of residual material left over after the process is significantly lower than that resulting from subtractive manufacturing [5].....	2
Figure 1.2 AM techniques.....	3
Figure 1.3 Schematical representation of four zones with different thermal history.....	5
Figure 1.4 Schematic of DED systems employing a) laser with powder feedstock; b) laser/electron beam/plasma or electric arc with wire feedstock.....	5
Figure 1.5 Effects of relationship between Z-axis increment and layer thickness in L-DED process: a) optimized working distance; b) too great distance; c) too short distance [55].....	8
Figure 1.6 Theoretical absorption as a function of wavelength for a range of common metals [60].	9
Figure 1.7 Schematic of L-DED-P deposition head.	10
Figure 1.8 Schematic of L-DED-W.	12
Figure 1.9 Schematic representation of different wire feeding directions relative to the motion of the deposition head (shown by red arrow): (a) front feed in which the deposition head travel direction is opposite to the direction of the wire feed, (b) back feed in which the deposition head travel direction is in the same direction as the wire feed, and (c) side feed in which the deposition head travel direction is orthogonal to the direction of the wire feed.....	12
Figure 1.10 The phase diagram for pure iron [84].....	14
Figure 1.11 Crystal lattices of: a) body-centered cubic and b) face-centered cubic [85].	15
Figure 1.12 Effect of temperature on mean volume per atom in crystal structures of iron at ambient pressure [86].	16
Figure 1.13 Stainless steel alloys composition and properties [90].....	17

Figure 1.14 Calculated effect of carbon on the phase diagram for 18Cr-8Ni steel. θ_1 and θ_2 , stand for $M_{23}C_6$ and M_7C_3 respectively [89].....	18
Figure 1.15 Phase diagram related to Fe – Ni system [96].....	22
Figure 1.16 Effect of ageing temperature on the strength and ductility [95]..	23
Figure 1.17 Schaeffler constitution diagram showing the location of the composition of the AISI 316L stainless steel (red circle) [120],[130].....	25
Figure 2.1 AISI 316L powder particle size distributions in the as received condition: the dotted blue curve corresponds to the distribution in volume, while the red curve to the cumulative volume distribution.	31
Figure 2.2 SEM micrographs of a) AISI 316L powder in the as received condition, and magnifications showing b) a particle with smaller satellites, c) an agglomerate particle, and d) an elongated powder particle.....	32
Figure 2.3 a) OM micrograph of powder cross section, b) OM micrograph with higher magnification of powder particle with trapped gas porosity, c) schematic of hollow powder particle with swirl spin indicated, d) SEM micrograph of hollow powder particle with open porosity.	33
Figure 2.4 SEM micrograph used for EDS point analysis with table of results reported in % in wt.	34
Figure 2.5 Diagram summarizing the dilution over AR with selection criteria lines with selected OM micrographs of STs representing different extremes and acceptable melt pool geometry.....	35
Figure 2.6 Diagrams showing: a) the linear energy density over linear mass deposition density for DoE #1 with marked in green STs in acceptable melt pool geometry from Fig. 2.5 and a process window for the DoE #2; b) results of cross-section analysis of STs from DoE #2 with green criteria lines at dilution values of 0.95 and 1.05; c) the linear energy density over linear mass deposition density for DoE #2 with accepted STs from Fig. 2.6 (b) marked with filled marker 2.5 and a process window for the DoE #3.	36
Figure 2.7 OM micrographs of cross-sections of the STs from DoE #3 with corresponding dilution and AR values reported under each micrograph.....	37
Figure 2.8 OM micrographs of 316L sample showing: a) melt pool boundary and grains with different types of dendritic structures, b) highlighted grains, c) equiaxed cellular structure, and d) cellular structure.	38
Figure 2.9 a) SEM micrograph of as-built 316L used for EDS line and point analysis, b) results of EDS line analysis.	39
Figure 2.10 XRD pattern of an as-build L-DED 316L sample.....	40
Figure 2.11 a) SEM micrograph used for EDX point analysis and b) EDS line analysis results... ..	41
Figure 2.12 a) schematic representation of microhardness measurements with reported zones of sampling along building direction and b) microhardness mean results for each zone.	42
Figure 2.13 Schematic representation of deposition strategies investigated: a) strategy “123”, b) strategy “X3”.	43
Figure 2.14 OM micrographs: a) of sample “123”-3 showing the grains with both equiaxed and columnar dendrites, b) of sample “X3” showing the grains with	

both equiaxed and columnar dendrites, c) at higher magnification showing the rounded shape cells for “123”-3 sample, and d) at higher magnification showing the rounded shape cells for “X3”-3 sample.	44
Figure 2.15 a) OM micrograph with an example of triangle method measurement, b) PCAS results plotted for each sample.	45
Figure 2.16 XRD patterns of: a) samples built with “123” deposition strategy, b) samples built with “X3” strategy.	46
Figure 2.17 Microhardness: a) schematic representation of microhardness measurements, b) plotted results of mean values for each sample and for each deposition strategy average of all three samples (blue notes – “123”; red notes – “X3”), c) results of bottom zone for each sample, d) results of central zone for each sample, and e) results of top zone for each sample.	47
Figure 2.18 Effects of factors on the height response.	54
Figure 2.19 Two-way interaction plots for height response.....	55
Figure 2.20 Powder and built samples density comparison.....	57
Figure 2.21 Normal probability plot for the porosity.....	58
Figure 2.22 Matrix plot of the porosity against density.....	60
Figure 2.23 Effects of factors on the hardness response.	62
Figure 2.24 Two-way interaction plots for hardness response.....	63
Figure 2.25 Contour plots of hardness: a) qualitative level $O_v = 0\%$, and b) qualitative level $O_v = 50\%$	64
Figure 2.26 Optical micrograph of 316L wire cross-section.....	67
Figure 2.27 Diagram summarizing the dilution over AR with selection criteria lines for F feeding direction with selected OM micrographs of STs representing different extremes and acceptable melt pool geometry.	68
Figure 2.28 Diagram summarizing the dilution over AR with selection criteria lines for B feeding direction with selected OM micrographs of STs representing different extremes and acceptable melt pool geometry.	68
Figure 2.29 Diagram summarizing the dilution over AR with selection criteria lines for S feeding direction with selected OM micrographs of STs representing different extremes and acceptable melt pool geometry.	69
Figure 2.30 Diagram summarizing the dilution over AR with selection criteria lines for all three feeding directions for selected sets of parameters.....	70
Figure 2.31 OM micrographs of STs cross-sections for sets of parameters plotted in Fig. 2.30.	71
Figure 2.32 OM micrographs of STs cross section with indication of keyhole geometry and indicated relation in sizes of bead width, wire diameter and laser spot diameter.	72
Figure 2.33 Frame captures of: a) cut off wire tip, b) regular shape wire tip, c) small droplet shape wire tip, d) large droplet shape wire tip, e) melted metal dropping during the deposition.	73
Figure 3.1 W360 powder particle size distributions in the as received condition: the dotted blue curve corresponds to the distribution in volume, while the red curve to the cumulative volume distribution [119].....	77

Figure 3.2 SEM micrographs of a) W360 powder in the as received condition, and magnifications showing b) a particle with smaller satellites, c) an agglomerated powder particle [119].	77
Figure 3.3 Optical micrographs of cross-sections of the W360 STs produced with coloured marks corresponding to criteria defined in legenda of the diagram of Fig. 3.4 [119].	79
Figure 3.4 Diagram summarizing dilution over AR with selection criteria lines [119].	79
Figure 3.5 The complete heat treatment performed on W360 samples: diagram with indication of sample condition in each step considered for characterization [119].	81
Figure 3.6 Optical micrographs of W360 AB (a, b), Q (c, d) and HT (e, f) samples at different magnifications [119].	83
Figure 3.7 FESEM micrographs of revealed microstructure of AB (a, b), Q (c, d) and HT (e, f) samples at different magnifications [119].	84
Figure 3.8 SEM micrographs used for EDS spot analysis a) of AB sample, b) of Q sample, c) of HT sample [119].	85
Figure 3.9 XRD patterns of a) AB, Q and HT samples with reported α values; b) a magnification of the first peak for the α (110) value in AB, Q and HT samples in comparison to the theoretical one (dotted line) [119].	87
Figure 3.10 Heating DSC curves of the AB, Q and HT samples [119].	88
Figure 3.11 a) Schematic representation of microhardness measurements with reported zones of sampling along building direction; b) Microhardness mean values for AB, Q and HT W360 samples reported for different positions along building direction [119].	89
Figure 4.1 SEM micrographs of a) 18Ni-300 powder in as-received condition, b) spherical particle with some satellite powder, and c) elongated powder particle.	92
Figure 4.2 OM micrograph of 18Ni-300 powder cross-section.	92
Figure 4.3 Diagram summarizing the dilution over AR with selection criteria lines with selected OM micrographs of STs representing different extremes and acceptable melt pool geometries for DoE #1 of 18Ni-300.	94
Figure 4.4 Diagram summarizing dilution over AR with selection criteria lines for DoE #2.	95
Figure 4.5 Optical micrographs of cross-sections of the 18Ni-300 STs from DoE #2 with coloured marks. Based on results in Fig. 4.4, if outside of the criteria line marked with red, if inside marked with yellow or green.	95
Figure 4.6 Pictures of cubes built with different sets of parameters, labelled as indicated in Table 4.3.	96
Figure 4.7 a) Average porosity per sample, b) example of void porosity, and c) example of different sizes of gas pores.	97
Figure 4.8 OM micrographs of etched as-built 18Ni-300 showing: a) interconnected melt pools, b) dendritic microstructure with both rounded and elongated cells.	100

Figure 4.9 SEM micrograph of as-built 18Ni-300, red arrows highlighting grain boundaries and yellow arrows highlighting black precipitates.....	101
Figure 4.10 EDS element maps corresponding to the SEM micrograph from Fig. 4.9 of: a) Fe, b) Ti, c) Ni, and d) Mo.....	102
Figure 4.11 Results of microhardness measurements along building direction for 18Ni-300.....	103
Figure 5.1 Received worn industrial blade: a) picture of received blade, b) sliced blade for material investigation, and c) technical drawing of as produced blade.....	105
Figure 5.2 OM micrographs revealed microstructure of as-received D2 steel.....	106
Figure 5.3 OM micrographs of 316L STs deposited on as-received D2 steel with different combinations of laser passes.....	107
Figure 5.4 OM micrographs showing the microstructure of: a) as-received D2 steel, b) annealed D2 steel.....	108
Figure 5.5 XRD patterns of as-received and annealed D2 steel.....	108
Figure 5.6 OM micrographs of 316L STs deposited on annealed D2 steel with different combinations of laser passes.....	109
Figure 5.7 OM micrographs of the ST cross section with insert of micrographs showing the microstructure of not HAZ on the left and the microstructure of HAZ on the right, also microhardness measurements are reported for not HAZ and HAZ.....	110
Figure 5.8 OM micrographs of transition zone between D2 substrate and deposited W360 of: a) as-built sample, b) heat treated sample.....	111
Figure 5.9 OM micrograph of a crack in the transition zone between deposited W360 and D2 substrate.....	111
Figure 5.10 SEM micrograph of the transition zone between deposited W360 and D2 substrate in as-built sample with corresponding EDS maps for the most relevant elements.....	112
Figure 5.11 SEM micrograph of the transition zone between deposited W360 and D2 substrate in heat treated sample with corresponding EDS maps for the most relevant elements [210].....	113
Figure 5.12 a) schematic representation of microhardness measurements performed and b) plotted microhardness results [210].....	114
Figure A.1 Schematic explanation of the deposition procedure [210].....	120
Figure A.2 Schematic explanation of: a) cut performed to analyse the single tracks deposited [119]; b) geometrical features of a ST cross-section considered as reference [119].....	121
Figure A.3 Characteristic melt pool geometries with associated dilution values.....	121
Figure A.4 Schematical representation of overlapping effect.....	122
Figure A.5 Bulk sample deposition strategy: a) scanning pattern; b) rotation per layer.....	123
Figure B.1 Apparatus for measuring apparent density and flowability with density cup and Hall flowmeter funnel [212].....	125

Figure B.2 Laserdyne 430 by Prima Additive: a) picture of building chamber, control panel and powder feeder; b) picture of deposition head and working table.....128

Figure B.3 LAWS 250 by Liburdi: a) picture of building chamber; b) picture of deposition head.....130

List of Acronyms

% at. – atomic percentage
%por – internal porosity percentage
% wt. – weight percentage
AB – as built
AC₁ – austenite onset temperature
AC₃ – austenite finish temperature
adj MS – adjusted mean squares
ADT – Anderson-Darling test
AM – Additive Manufacturing
AR – aspect ratio
bcc – body-centered cubic
BJ – Binder Jetting
CAD – Computer-Aided Design
CI – compressibility index
CNC – Computer Numerical Control
CT – computed tomography
D – bead depth
DED – Directed Energy Deposition
df - degrees of freedom
d_l – laser beam diameter
DoE – design of the experiment
DSC – Differential Scanning Calorimetry
d_w – wire diameter
EBM – Electron Beam Melting
EBSD – Electron Backscatter Diffraction

EDS – energy-dispersive X-ray spectroscopy
 E_{pass} – specific energy density of laser pass
 E_s – specific surface energy density
 E_v – volumetric energy density
fcc – face-centered cubic
FESEM – Field Emission Scanning Electron Microscope
FIB-SEM Focused Ion Beam- Scanning Electron Microscope
G – bead growth
 h_d – hatch distance
hpc – hexagonal close-packed
HAZ – heat-affected zone
HR - Hausner ratio
HT – Heat Treatments
IHT – Intrinsic Heat Treatment
L-DED – Laser Directed Energy Deposition
L-DED-P – Laser Directed Energy Deposition with powder feedstock
L-DED-W – Laser Directed Energy Deposition with wire feedstock
LAWS – Liburdi Automated Welding System
LENS – Laser Engineered Net Shaping
LMD – Laser Metal Deposition
LOF – lack-of-fit
M300 - 18Ni300
ME – Material Extrusion
 M_f – martensite finish temperature
MJ – Material Jetting
 m_p – mass of powder
 M_s – martensite start temperature
OM – optical microscopy
Ov – Overlap
P – laser power
PBF – Powder Bed Fusion
PBF-EB – Powder Bed Fusion with Electron Beam Energy Source
PBF-LE – Powder Bed Fusion with Laser Energy Source
PCAS – primary cellular arm spacing
Q – quenched
 Q_p – powder feed rate
SEM – Scanning Electron Microscope
SL – Single Layer
SLA – Stereolithography
SLM – Selective Laser Melting
SLS – Selective Laser Sintering
ST – Single Track
 T_c – Curie temperature
 v - scan speed
 V_{cg} – carrier gas flow rate

V_{dc} – density cup volume
VPP – Vat Photopolymerization
 V_{tap} – volume after tapping
W – bead width
W-EDM – wire-electrical discharge machine
XRD – X-ray Diffraction
 Δz – layer thickness
 α_w – feeding angle
 ϵ_f – elongation to fracture
 ρ_{app} – apparent density
 $\rho_{full\ dense, t^\circ C}$ – density of fully dense material
 $\rho_{p, t^\circ C}$ – true density of a powder
 ρ_{tap} – tapped density
 σ_{UTS} – ultimate tensile strength
 σ_y – yield strength
 τ_{layer} – interlayer cooling time

Chapter 1

Introduction

1.1 Additive manufacturing

Additive Manufacturing (AM), also known as 3D printing, is a groundbreaking manufacturing process that enables the creation of complex three-dimensional objects by adding material layer by layer. Unlike traditional subtractive manufacturing methods, which involve cutting or shaping materials, AM builds objects from the ground up, offering unparalleled design freedom and customization. The development of AM technologies can be traced back to the 1980s when the first AM processes were introduced. Initially, the focus was primarily on prototyping applications, but over time, the capabilities expanded to include functional part production [1], [2], [3]. Major milestones in the development of AM technologies include the invention of Stereolithography (SLA) by Charles W. Hull in 1983 and the introduction of Selective Laser Sintering (SLS) by Carl Deckard and Joseph Beaman in the late 1980s. As the technology advanced, it gradually encompassed a wide range of materials, applications, and processes, enabling the creation of complex geometries and intricate structures [1], [4].

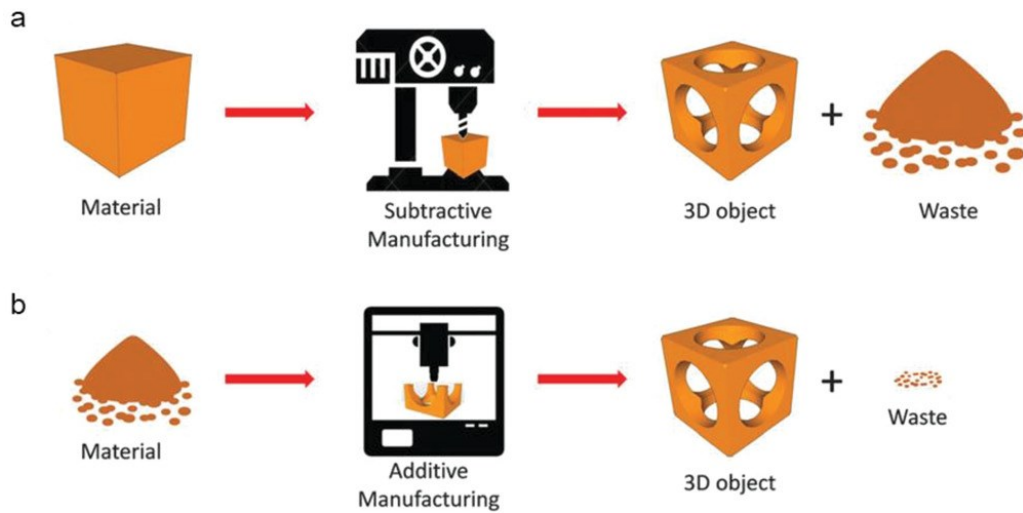


Figure 1.1 AM vs. subtractive manufacturing. a) In subtractive manufacturing, a block of material is processed by material-removing machines according to digital design before obtaining the final 3D object together with a large amount of residual material. b) In AM, a starting material (powder, liquid, filament, etc.) is processed by a 3D-printing machine, which deposits just the required amount of material in layer-by-layer fashion before the final 3D object is obtained. The amount of residual material left over after the process is significantly lower than that resulting from subtractive manufacturing [5].

AM offers several unique benefits that contribute to its growing popularity across industries. It provides unprecedented design freedom, allowing for the creation of highly complex geometries and intricate internal structures that are challenging or impossible to produce with traditional manufacturing methods. This freedom enables designers to optimize parts for performance, lightweighting, and customization, leading to improved functionality and efficiency [6], [7]. In contrast to traditional manufacturing, which often involves significant material wastage due to its subtractive nature, AM is an additive process that utilizes only the required amount of material. This reduction in waste not only minimizes environmental impact but also improves material efficiency (Fig. 1.1). Furthermore, unused or excess material from one build can be reused for subsequent builds, maximizing resource utilization [8], [9], [10], [11]. Moreover, AM streamlines the manufacturing process by eliminating the need for complex tooling, reducing setup time, and enabling rapid iteration and prototyping. This agility translates into shorter lead times and reduced costs for product development. Additionally, AM facilitates on-demand production, eliminating the need for large inventories and enabling just-in-time manufacturing [3], [7]. Another captivating benefit of AM is its ability to customize and personalize on a mass scale. It empowers the production of unique, one-of-a-kind products tailored to specific customer requirements, preferences, or medical needs. This capability has significant implications for industries such as healthcare, automotive, and consumer goods, where personalized products are in high demand [2], [8], [12], [13]. Furthermore, AM has the potential to revolutionize supply chains by enabling localized production. Instead of relying solely on centralized manufacturing facilities and long-distance shipping, AM

allows for distributed manufacturing closer to the point of demand. This localization can reduce logistics costs, shorten delivery times, and enhance sustainability by minimizing transportation-related emissions [1], [14], [15].

The ISO/ASTM 52900 standard provides a comprehensive classification system for AM processes and specifies the terms and definitions used in the field. The standard, titled "Additive manufacturing - General principles - Terminology" aims to establish a consistent and unified framework for describing and categorizing AM technologies. AM processes are classified into seven techniques based on their fundamental characteristics and principles as illustrated in Fig 1.2 [16]: Material Extrusion (ME), Vat Photopolymerization (VPP), Powder Bed Fusion (PBF), Material Jetting (MJ), Binder Jetting (BJ), Sheet Lamination (SL), and Directed Energy Deposition (DED). Within the AM domain, a wide range of materials can be processed, including polymers, ceramics, composites, and metals. With a focus on metal AM, the ISO/ASTM 52900 standard recognizes two metal fusion-based technologies: DED and PBF [1], [12], [16], [17].



Figure 1.2 AM techniques.

PBF processes involve the selective fusion of a material powder bed using a focused heat source, typically a laser or an electron beam, through proper lenses and mirrors in a scanning systems. The ISO/ASTM 52900 standard further classifies PBF into two subcategories: PBF with Laser Energy Sources (PBF-LE) and PBF with Electron Beam Energy Sources (PBF-EB). PBF-LE techniques, such as Selective Laser Melting (SLM) and Selective Laser Sintering (SLS), utilize a laser to selectively melt or sinter the powdered material. On the other hand, PBF-EB techniques, such as Electron Beam Melting (EBM), employ an electron beam as the energy source to selectively melt the powdered material [1], [12], [16], [17], [18], [19].

DED is a metal fusion-based AM technology that involves the layer-by-layer deposition of material using a focused energy source, such as a laser or an electron

beam. The process entails melting metal powder or wire and precisely depositing it onto a substrate or previously deposited layers. DED enables the fabrication of large-scale, near-net-shape parts and the addition of features to existing components [1], [12], [16], [20], [21], [22].

1.1.1 Directed Energy Deposition

DED is a metal fusion-based AM technology that has gained significant attention in recent years. It offers unique capabilities for fabricating complex metal parts with a high degree of design freedom and customization. DED is a versatile process that can be used with various feedstock materials and heat sources, providing flexibility in material selection and process parameters [1], [20].

The development of DED technology can be traced back to the early days of AM. It emerged as an extension of traditional welding processes and has since evolved into a sophisticated AM technique. The initial applications of DED were focused on repair and cladding operations in industries such as aerospace, automotive, and oil and gas [23], [24]. However, advancements in hardware, software, and material science have expanded the scope of DED to include the fabrication of fully functional parts, making it an attractive option for various industries, including aerospace, defence, and tooling [6], [15], [25], without the limitations of the building chamber dimensions, like in PBF.

In the DED systems, material in either powder or wire form is fed into a focused thermal energy source (e.g., laser or electron beam, electric arc), where it is melted using a protective atmosphere and subsequently deposited onto the substrate or previously deposited material. The deposition head, consisting of the heat source and material feeding system, can be moved in a 2D pattern according to a CAD model; as the deposition head is scanned along this pattern, the molten deposited material rapidly solidifies and bonds with the substrate or previously deposited material. After scanning one layer, the deposition head is moved up (or the substrate is moved down) and deposition of the subsequent layer begins. Due to the layer-by-layer deposition process used in DED, the resulting parts frequently exhibit non-uniform microstructures and properties [26], [27]. This non-uniformity arises due to the complex thermal history experienced by the manufactured samples. A cross-section of a DED sample along the building direction can be divided into four schematic zones (Fig. 1.3). Beginning from the substrate material, the initial zone is referred to as the "not affected zone." Close to the first deposited layer, there is the "heat-affected zone." The third zone comprises "tempered metal," corresponding to the primary deposited part. The top layer of the sample, corresponding to the last deposited layer, forms the "non-tempered metal" zone [28], [29]. During the process, the first layer is generally deposited on a cold substrate at ambient temperature, leading to rapid cooling due to heat dissipation. With each subsequent layer deposition, the heat from the energy source to the solidifying material traverses through the previously deposited layers into the substrate, creating an intrinsic heat treatment (IHT) effect. However, the final layer

deposited does not undergo this reheating process, and consequently, it exhibits a microstructure characteristic of the as-built material [30], [31], [32]. Therefore, to achieve a uniform microstructure and, consequently, uniform mechanical properties in bulk samples produced by L-DED, post-processing heat treatments (HT) are commonly employed [33], [34].

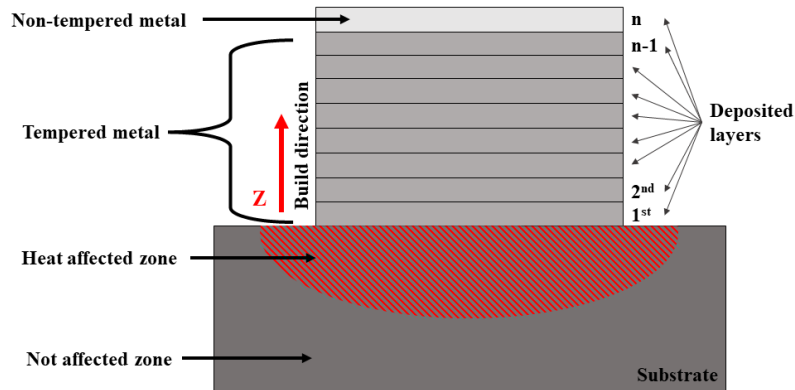


Figure 1.3 Schematical representation of four zones with different thermal history.

DED configurations with powder material feedstock utilize a laser as the thermal energy source, while DED systems using wire feedstock utilize an electric or plasma arc, a laser, or an electron beam as the thermal energy source like indicated in Fig. 1.4 [1], [20].

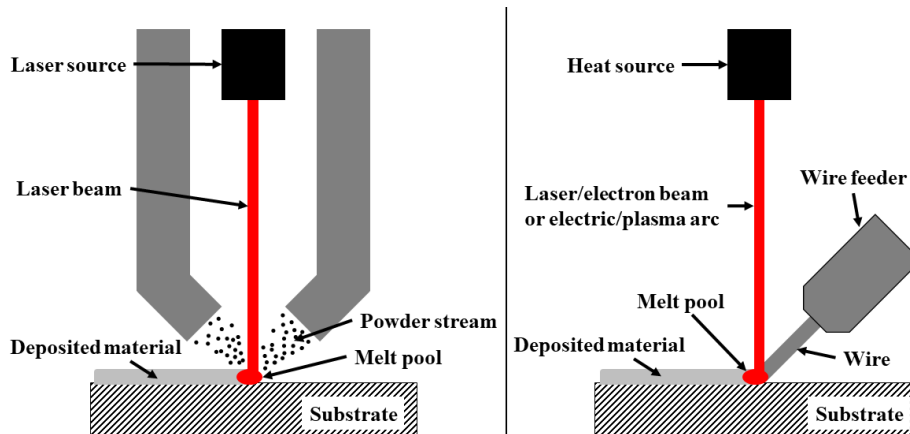


Figure 1.4 Schematic of DED systems employing a) laser with powder feedstock; b) laser/electron beam/plasma or electric arc with wire feedstock.

DED offers several advantages compared to other metal AM technologies. Firstly, it is well-suited for large-scale fabrication and repair of metal components. Its ability to deposit material layer by layer allows for the creation of large and complex parts without the need for extensive post-processing or assembly. Additionally, it is widely used for the repair and restoration of high-value metal components, such as turbine blades and aerospace structures, enabling cost-

effective repairs without the need to replace entire components. [20], [21]. Also, it typically offers high deposition rates, making it efficient for producing parts with reduced build times. This is especially beneficial for industries that require rapid production and short lead times [20], [35]. DED is compatible with a wide range of metal feedstock materials, including various alloys and even dissimilar materials. Multiple material deposition simultaneously or sequentially enables the fabrication of functionally graded structures, metal matrix composites, and the integration of dissimilar materials in a single part. This flexibility allows for the fabrication of parts with tailored material properties for specific applications [20], [36], [37], [38]. Compared to PBF, it allows incorporation of real-time monitoring and control systems, allowing for adjustments to be made during fabrication to ensure quality and accuracy. This capability helps in achieving consistent and reliable results [20], [39]. Also, DED systems can be configured with multi-axis capabilities, allowing for more complex geometries to be fabricated without the need for additional support structures [40]. And, since DED is an additive process, it minimizes material waste, utilizing only the required amount of feedstock material. This efficiency contributes to reduced material costs and lower environmental impact, especially using a wire feedstock [20], [35], [41], [42].

DED utilizes various heat sources each heat source offers unique advantages and finds applications in different industries [20], [27]. Laser-based DED employs high-power lasers, such as CO₂ lasers or fiber lasers, to generate intense heat that melts the feedstock material [36], [43], [44]. In electron beam-based DED, a focused beam of high-energy electrons is used as the heat source. The electron beam is generated in a vacuum chamber and directed onto the workpiece's surface [20], [45], [46]. Plasma arc-based DED utilizes a high-temperature plasma arc for material melting and deposition. The plasma arc is formed by ionizing a gas using a high-frequency electric field [20], [42], [47]. Electric arc-based DED involves the formation of an electric arc between an electrode and the workpiece, creating a high-temperature plasma [42], [47]. Comparison of different heat sources in some specifications is given in Table 1.1. The cold spray-based DED utilizes a supersonic jet of solid-state particles accelerated by compressed gas to deposit material onto the workpiece. Unlike other heat-based DED processes, cold spray DED does not involve melting the feedstock material. Instead, it relies on the kinetic energy of particles to form a strong bond with the substrate. Cold spray DED is valued for its ability to process temperature-sensitive materials and for reducing the heat-affected zone [48], [49].

Table 1.1 Comparison of different heat sources in DED [50], [51]. Build volume refers to the relative size of components that can be processed by the subject process. Detail resolution refers to the ability of the process to create small features. Deposition rate refers to the rate at which a given mass of product can be produced. Coupling efficiency refers to the efficiency of energy transfer from the energy source to the substrate, and Potential for contamination refers to the potential to entrain dirt, gas, and other possible contaminants within the part.

Heat source	Build volume	Detail resolution	Deposition rate	Coupling efficiency	Potential for contamination
Laser	3	2	2	1	3
Electron beam	4	1	3	4	4
Plasma/electric arc	3	1	3	4	2

* Comment: 1 is the lowest, and 4 is the highest.

Among these heat source options, laser is the most studied one, and the only one with opportunity of being used for both, powder and wire feedstock.

1.1.2 Laser Directed Energy Deposition

Laser Directed Energy Deposition (L-DED), also known as Laser Metal Deposition (LMD) or Laser Engineered Net Shaping (LENS), is a metal AM process that utilizes a high-power laser as the heat source to melt and fuse metal powders or wires onto a substrate [1], [20], [36]. L-DED operates based on the principle of focused laser energy melting metal powders or wires as they are deposited onto a substrate or previously laid layers. All L-DED systems consist of axis control system, laser system, and material feeding system [1], [20].

Axis control system plays a crucial role in achieving precise and accurate fabrication of complex three-dimensional parts [51], [52]. The axis control system is responsible for controlling the movement of the deposition head, an integrated laser head with material feeding system, and/or the workpiece during the DED process. It ensures that the material is deposited at the correct location with the desired dimensions and geometries [51]. Machines typically have a multi-axis control system, which includes at least three linear axes (X, Y, and Z) and often additional rotary axes (A, B, and C). The linear axes control the movement of the deposition nozzle or the workpiece along the X, Y, and Z directions, while the rotary axes allow for rotational movement around X, Y, and Z axis, enabling fabrication on complex curved surfaces without need for supporting structures. The axis control system is governed by a Computer Numerical Control (CNC) system. The CNC system interprets the digital design data from the computer-aided design (CAD) software and generates precise toolpaths for the deposition process [53]. Modern DED systems often incorporate real-time monitoring and feedback mechanisms. Sensors are used to monitor the position of the deposition nozzle or the workpiece during the process. The feedback data is continuously fed back to the CNC system, allowing it to make adjustments in real-time if any deviations from the desired path are detected [39], [54]. The real-time monitoring and feedback mechanisms utilized for controlling the layer height during the deposition process help in overcoming typical deposition problems like overgrowing and undergrowing of the build part (Fig. 1.5). Layer height refers to the thickness of each individual layer of material deposited on the workpiece. Precise control of the

layer height is essential to achieve the desired dimensional accuracy and mechanical properties of the final part [24], [55].

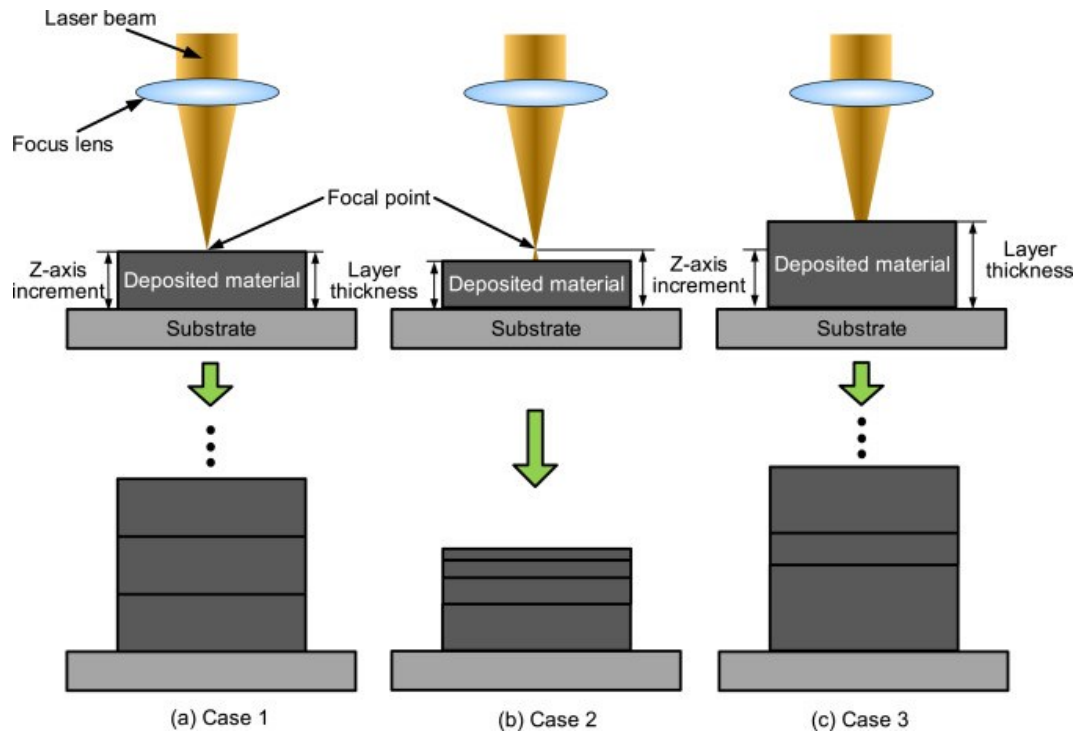


Figure 1.5 Effects of relationship between Z-axis increment and layer thickness in L-DED process: a) optimized working distance; b) too great distance; c) too short distance [55].

The laser system is a critical component that provides the high-energy source necessary for melting and fusing metal powders or wires during the AM process. It plays a key role in determining the quality, efficiency, and capabilities of the L-DED process [56], [57]. There are several types of lasers utilized, the choice of laser type depends on factors such as the material being processed, and the specific application. The choice of laser type will have different laser wavelength, therefore different energy absorption for different materials (Fig. 1.6). Some common types of lasers used in L-DED are fiber, CO₂, Nd:YAG, and diode lasers [56], [58]. They usually employ a high-power laser source, which generates a concentrated and intense beam of light. The laser power can range from few hundred watts to several kilowatts, depending on the specific application and the material being processed. Higher laser power allows for faster melting rates and higher deposition rates, contributing to increased productivity in L-DED [56], [59].

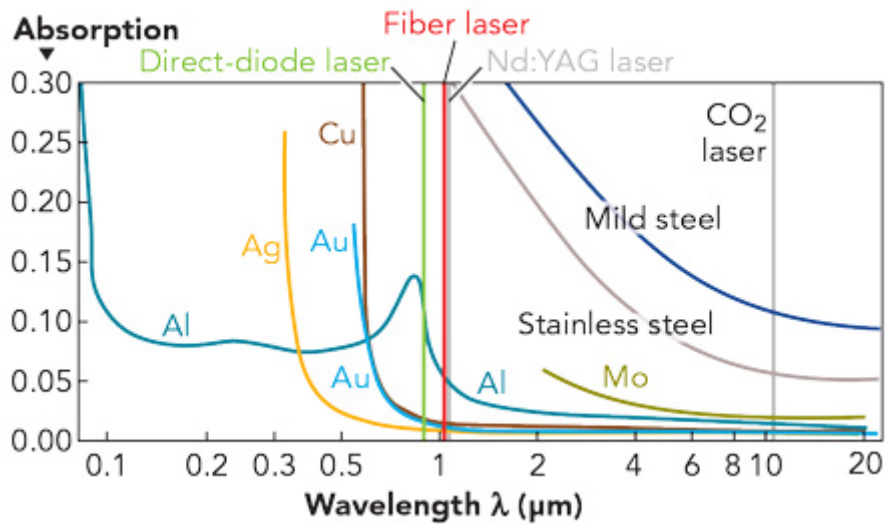


Figure 1.6 Theoretical absorption as a function of wavelength for a range of common metals [60].

The material feeding process is also a crucial aspect of AM technologies [61]. The system involves supplying the material feedstock to the deposition zone where the laser melts and fuses the material to build up the desired part [12], [20], [23], [62]. Material feeding in L-DED is carefully controlled to ensure the precise deposition of layers and to achieve the final product without defects with the desired properties[24]. For L-DED, the material feedstock can be in the form of metal powder or wire [20], [62]. Depending on the feedstock type, two configurations of L-DED are recognized: L-DED with powder feedstock (L-DED-P) and L-DED with wire feedstock (L-DED-W) [1], [20].

1.1.3 Laser Directed Energy Deposition with Powder Feedstock

As the name suggests, L-DED-P is an AM technique that utilizes a laser beam to melt and fuse metal powder particles, enabling the construction of three-dimensional components [1], [20]. In this process, a powder delivery system supplies the metal powder to the deposition zone [23]. The metal powder is fed into the laser beam through one or more powder nozzles through powder/gas feeding lines with the carrier gas stream, typically consisting of an inert gas such as nitrogen or, even more preferably, argon (Fig. 1.7) [23], [63]. External powder feeders contain one or more powder hoppers connected to a continuous delivery system, which includes a rotating disk that determines the amount of powder delivered to the carrier gas [64]. The stream of pressurized inert gas fluidizes and carries the metallic powder to the laser spot [61].

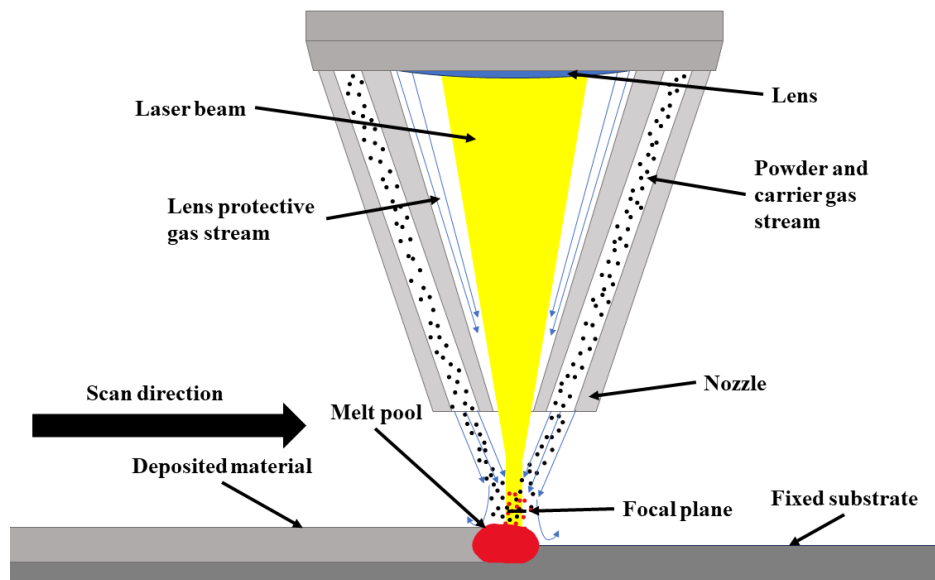


Figure 1.7 Schematic of L-DED-P deposition head.

The interaction between the laser and the powder typically takes place within a time range of 0.2 to 8 milliseconds [65]. As the particles are exposed to the laser beam, they undergo rapid heating [66]. The degree of temperature elevation depends on their specific position within the powder stream and in relation to the laser beam. This dependence arises from both the distribution of powder concentration and the power distribution of the laser beam, following a Gaussian function [67]. Additionally, factors such as particle size, particle velocity, and the flow of the carrier/shielding gas contribute to the elevation of powder temperature [23]. For example, Peyre et al. conducted calculations that yielded a maximum temperature of 1350 K for particles with a diameter of 25 μm and 900 K for particles with a diameter of 45 μm in the case of Ti-6Al-4V, under identical conditions at the centre of the powder stream [68]. Moreover, the design of the powder stream flow is intended to intersect with the laser at the focal plane of the laser through the special design and positioning of the nozzles (Fig 1.7) [23]. The shape of the powder stream, the distribution of laser intensity, the speed of the powder, and the distribution of maximum powder temperature are all significantly influenced by the feeding angle, which is determined by the design of the nozzle(s) [23], [69]. As a result, certain particles experience melting while still in flight, while others undergo heating close to the melting temperature just before entering the melt pool [66], [70].

In the laser-powder systems, the absorption of the laser energy, or in other words energy efficiency is mostly depending on the powder material and the type of laser utilized (e.g. wavelength), like already explained and illustrated in Fig. 1.6 [23], [56], [58]. Apart from the type of laser and material, the energy efficiency also depends on surface preparation and temperature. The energy efficiency usually ranges from 0.15 and 0.50 [71]. Unocic and DuPont [72] experimentally measured using a Seebeck envelope calorimeter energy efficiency for a continuous wave Nd:YAG laser of H13 tool steel and was shown to range between 0.30 and 0.50.

Another efficiency in laser-powder systems is powder catchment efficiency that is defined as the ratio of the deposition rate to the powder feeding rate [35]. This parameter refers to the ability of the DED system to effectively capture and utilize the powder particles that are carried toward the substrate during the deposition process [73]. Proper powder catching ensures that a high percentage of the fed powder particles are successfully deposited onto the intended substrate, minimizing wastage, and optimizing material usage [23]. Several factors like process parameters, gas flow, powder properties, and machine configuration influence powder catching efficiency [35], [74]. The choice of process parameters, such as laser power, scan speed, and powder feed rate, impact powder catching efficiency, higher power produces larger melt pool size, hence increases the efficiency [14], [23]. While with higher scan speeds the efficiency decreases, as well as for higher powder feed rates [35], [75]. The direction and velocity of the carrier and shielding gas flow, play a role in guiding the powder particles toward the melt pool. Proper gas flow control is essential to direct the particles effectively and prevent them from escaping the deposition area by ensuring certain particle velocity which determines the interaction time between particles and the laser beam [66], [70], [73], [76]. The size, shape, and flowability of the powder particles can influence how they interact with the laser or energy source and how effectively they adhere to the substrate [23], [74], [77], [78]. The machine configuration in terms of nozzle design, laser type and laser spot also significantly influence the powder catching efficiency. The design of the nozzle through which the powder is delivered into the melt pool affects the trajectory and distribution of powder particles [23], [69]. The laser type coupled with the material used have better energy efficiency, resulting in better powder catching efficiency and larger laser spots result in larger melt pool sizes [56], [58], [79].

1.1.4 Laser Directed Energy Deposition with Wire Feedstock

In L-DED with wire feedstock (L-DED-W), a continuous metal wire is fed into the deposition zone through a nozzle. The focused laser beam is then applied to the point where the wire intersects with the substrate or previously deposited material (Fig 1.8). The heat generated by the laser melts the wire, which fuses with the underlying material to form a solidified layer. Wire feedstock offers higher deposition rates compared to powder-based systems and in the case of wire feeding, the volume of the deposited material is always the volume of the fed wire, so there is 100% feedstock capture efficiency (except a little “splatter” from the melt pool) [1].

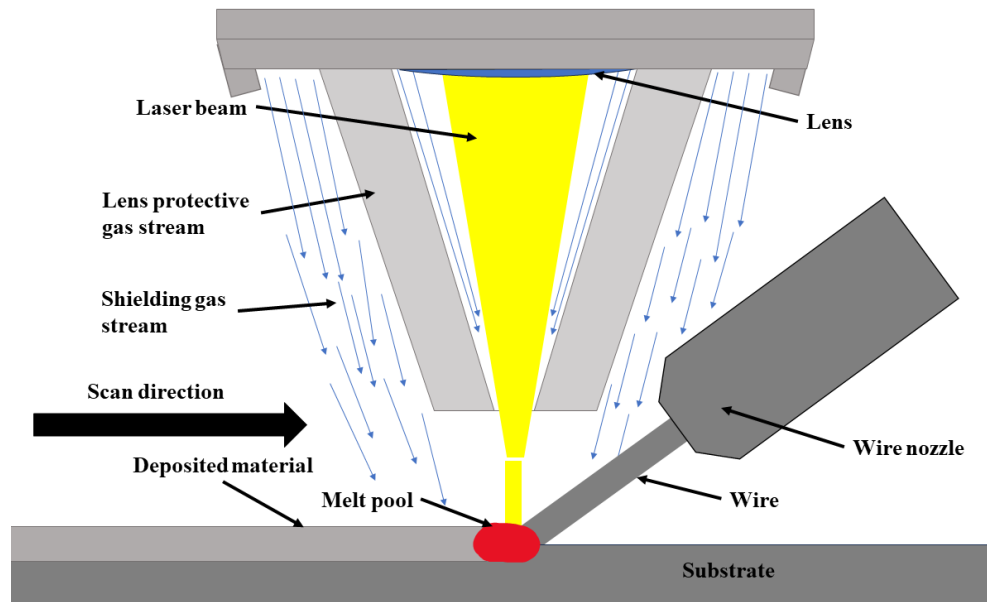


Figure 1.8 Schematic of L-DED-W.

In L-DED-W process is also sensitive to the interactions between laser beam and wire. Findings from laser-powder interactions are not necessarily applicable to laser-wire interactions. Apart from laser power, scan speed and wire feed rate, there are some other parameters that influence the interactions between laser beam and wire, such as angle between laser beam and wire, wire tip position relative to the melt pool, and feed direction [51].

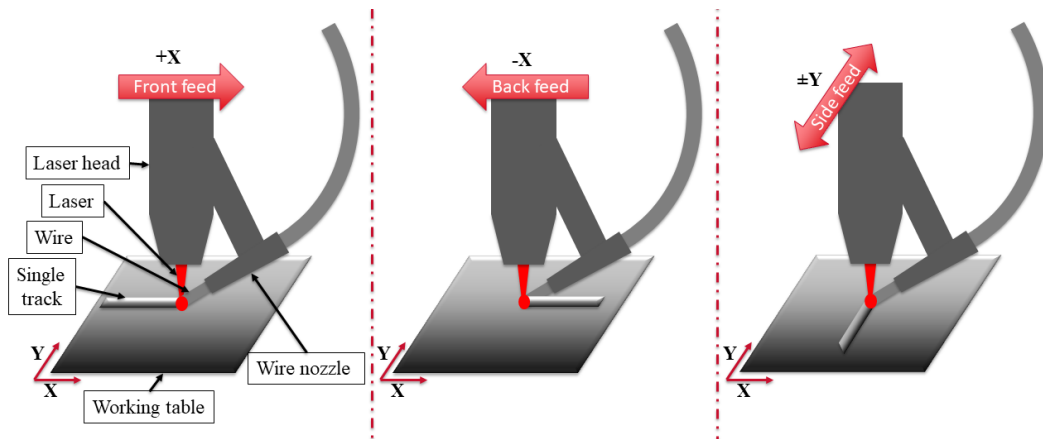


Figure 1.9 Schematic representation of different wire feeding directions relative to the motion of the deposition head (shown by red arrow): (a) front feed in which the deposition head travel direction is opposite to the direction of the wire feed, (b) back feed in which the deposition head travel direction is in the same direction as the wire feed, and (c) side feed in which the deposition head travel direction is orthogonal to the direction of the wire feed.

The direction in which the wire is fed into the melt pool can affect the molten metal transfer and deposition characteristics. Front feeding (Fig. 1.9 (a)), where the wire is fed into the melt pool in the opposite direction to the deposition head travel direction, is the preferable feeding configuration. It provides stable wire melting

and smooth depositions, allowing better wire-melt pool interactions, improved metallurgical bonding, and a reduced probability of defects [41], [80], [81]. Back feeding (Fig. 1.9 (b)), where the deposition head travel direction aligns with the wire feed direction, poses challenges due to wire obstruction and interference with the laser beam. It can cause issues such as wire stubbing, lack of fusion, or poor bead formation, leading to increased porosity and reduced part quality [41], [80]. Side feeding (Fig. 1.9 (c)), where the deposition head travel direction is orthogonal to the wire feed direction, presents challenges related to wire stability, positioning, and control. The wire may experience lateral deflection or misalignment, affecting the accuracy and consistency of deposition, especially if wire feeding is high. Side feeding can result in irregular bead profiles, increased spatter, and potential lack of fusion. To overcome the challenges associated with different wire feed directions in L-DED-W, adjusting laser power, scan speed, and wire feed rate for each feed direction can optimize process stability and deposition characteristics [41], [80]. Fine-tuning these parameters can help overcome specific challenges associated with each feed direction, ensuring proper wire melting and adequate material deposition [51], [82].

1.2 Steels

Iron (Fe) is a chemical element with the atomic number 26 and is one of the most abundant metals, making about 5% of the Earth's crust. It is a transition metal belonging to the d-block of the periodic table. Iron has been used by humans for thousands of years and plays a vital role in various aspects of everyday life, industry, and technology. Pure iron is a ferromagnetic, silvery-grey metal with a density of 7.87 g/cm³. It has a melting point of 1538 °C and a boiling point of 2862 °C. It is prone to oxidation, leading to the formation of iron oxide, commonly known as rust, when exposed to moisture and oxygen. Iron can exist in various oxidation states, the most common being +2 and +3. In nature it is primarily found in the form of iron ores, such as hematite (Fe₂O₃) and magnetite (Fe₃O₄), as well as in various iron-bearing minerals. These ores are mined and processed the most commonly through the blast furnace to extract iron in its metallic form [83].

The pure iron can exist in three allotropes naturally in bulk form, body-centered cubic (bcc, α -iron, ferrite), face-centered cubic (fcc, γ -iron, austenite), and hexagonal close-packed (hcp, ϵ -iron) which is existing only in high pressure conditions, like illustrated in the phase diagram of pure iron in Fig 1.10 [83]. The δ -iron that can be observed in the Fig. 1.10 is only a high temperature α -iron, therefore not an actual allotrope.

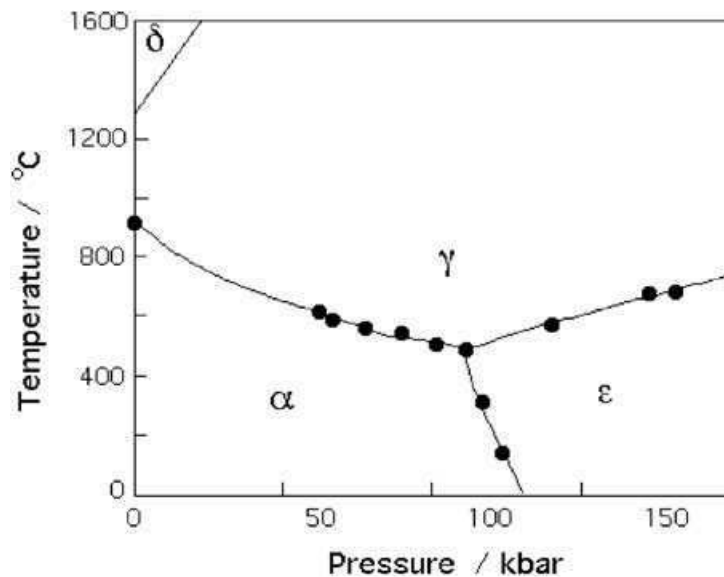


Figure 1.10 The phase diagram for pure iron [84].

The α -iron phase is the stable form of iron at temperatures below 910 °C and has a bcc crystal structure, which means that the iron atoms are arranged in a three-dimensional cubic lattice with iron atoms at each corner of the cube and one atom in the centre, like indicated in the Fig 1.11 (a). The bcc structure of alpha iron results in a relatively open and less densely packed arrangement of atoms compared to other iron phases. The α -iron exists at temperatures below the Curie temperature of 770 °C and remains stable until it undergoes a phase transformation to the gamma iron phase (austenite) at temperatures above the A_3 transformation temperature of 910 °C. It is relatively soft, ductile, and easily deformed, exhibiting good formability, and can be easily worked into various shapes through processes like forging, rolling, or stamping. At temperatures below the Curie temperature, alpha iron is ferromagnetic, meaning it can be magnetized. It exhibits a spontaneous magnetic field and can retain magnetization even after the external magnetic field is removed. It is not commonly used in its pure form due to its relatively low strength and hardness. However, it serves as a foundational phase in the production of various iron-based alloys, including carbon steels. The addition of carbon and other alloying elements to alpha iron can enhance its mechanical properties and make it suitable for specific applications in industries such as construction, automotive, and manufacturing [83].

The γ -iron phase is the iron stable form of iron at elevated temperatures and has a face-centered cubic (fcc) crystal structure, which means that the iron atoms are arranged in a three-dimensional cubic lattice with iron atoms at each corner of the cube and one atom in the centre of each face, like illustrated in Fig 1.11 (b). The fcc structure of gamma iron results in a more closely packed arrangement of atoms compared to the alpha iron phase. It exists at temperatures above the A_{c3} transformation temperature of 910 °C and remains stable until it undergoes a phase transformation to the α -iron phase at temperatures below the A_{c1} transformation temperature of 770 °C. The phase transformation between γ -iron (austenite) and α -iron (ferrite) is an important phenomenon in iron and steel metallurgy. Heat

treatment processes such as quenching and tempering can control the transformation and result in desired microstructures and properties in iron and steel alloys. The γ -iron phase has higher strength and hardness compared to the α -iron phase, and it exhibits improved mechanical properties such as increased tensile strength and hardness. The fcc crystal structure of γ -iron allows for greater resistance to deformation compared to the bcc structure of alpha iron. The γ -iron phase, particularly in the form of austenite, finds extensive use in various applications. Austenitic stainless steels, which contain high amounts of γ -iron, exhibit excellent corrosion resistance, high ductility, and good formability. They are widely used in industries such as food processing, chemical processing, automotive, and construction [83].

In the context of practical metallurgy and iron alloys, the focus is mainly on the stable forms of iron, namely ferrite (α -iron and δ -iron) and austenite (γ -iron) [83].

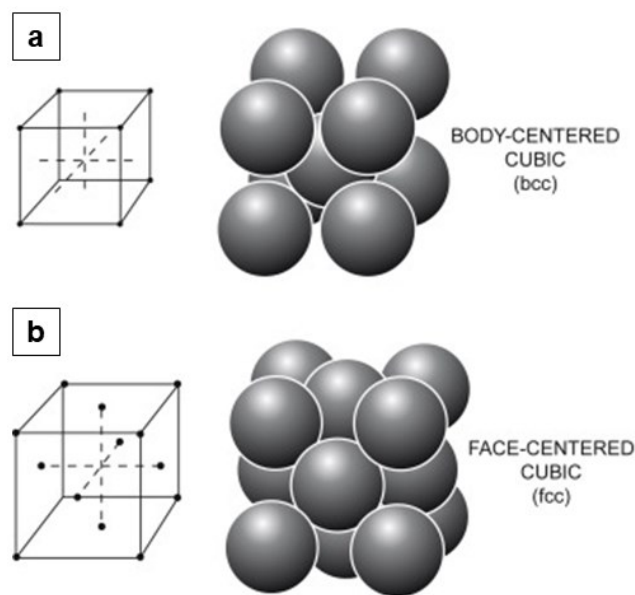


Figure 1.11 Crystal lattices of: a) body-centered cubic and b) face-centered cubic [85].

The majority of steels rely on just two allotropes, α and γ . Like already stated, bcc ferrite, at ambient pressure, is stable up to 910 °C (A_{c3}), when it transforms into the fcc austenite. With further heating it transforms back to ferrite at 1390 °C (A_{c4}). The high-temperature ferrite is traditionally labelled δ , although it is no different in crystal structure from α . The δ -ferrite remains stable until reaching the melting temperature of 1536 °C [83].

In Fig 1.12, the phase changes in the mean volume per atom of iron as a function of temperature are illustrated. It is important to observe that during the γ - to α -transformation, there is an approximate 1 to 3% change in atomic volume. This volume change can result in the generation of internal stresses during the transformation process. Also, it can be observed that α and δ ferrite are the part of the same function confirming the bcc crystal structure [83].

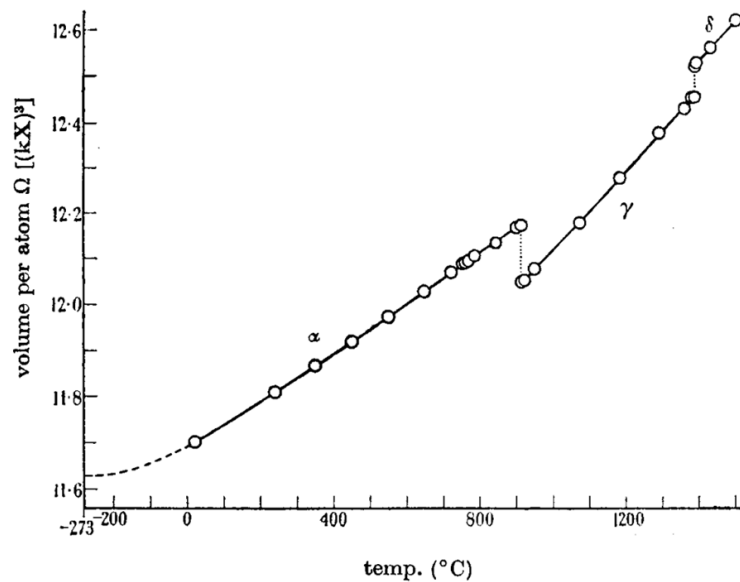


Figure 1.12 Effect of temperature on mean volume per atom in crystal structures of iron at ambient pressure [86].

The introduction of carbon into iron is sufficient to create what we commonly refer to as steel. However, steel is a broad term encompassing a vast array of complex compositions. Even a minor concentration of carbon, for instance, 0.1–0.2 in weight percentage (% wt.) or roughly 0.5–1.0 in atomic percentage (% at.), has a profound strengthening effect on ferritic iron. This phenomenon has been recognized for over 2500 years, as blacksmiths of old understood that iron heated in a charcoal fire readily absorbed carbon through solid-state diffusion. Nevertheless, the intricate processes through which carbon assimilation transforms a relatively soft metal into an exceptionally robust and often tough alloy have only been comprehensively explored in recent times [87].

Steels represent a class of alloys primarily centered around iron (Fe) as the base metal, with carbon (C) serving as the principal alloying element. They find widespread use across various industries due to their exceptional mechanical properties, adaptability, and cost-effectiveness. Steels deliver an impressive blend of strength, resilience, malleability, and weldability, making them indispensable in applications spanning from structural components to automotive parts, machinery, tools, and consumer goods [87].

In addition to carbon, steel may incorporate variable quantities of other alloying elements like manganese (Mn), silicon (Si), chromium (Cr), nickel (Ni), molybdenum (Mo), vanadium (V), and numerous others. These alloying elements are introduced to confer specific properties upon the steel. This categorization can be further delineated based on the steel's chemical composition, microstructure, and attributes, resulting in classifications such as carbon steel, alloy steel, stainless steel, and tool steel [87], [88].

Among the given classifications in the following sections focus will be given to austenitic stainless steels, tool steels, and maraging steels which are classified as ultra-low carbon steels.

1.2.1 Stainless steels

Stainless steels are a family of iron-based alloys celebrated for their corrosion resistance, achieved through the strategic addition of chromium, constituting a minimum of 10.5% of the alloy's weight. This critical chromium threshold forms a protective oxide layer on the steel's surface, rendering it impervious to rust formation even in humid, unpolluted environments, thus earning the illustrious moniker "stainless." The core of stainless steel's corrosion resistance lies in its ability to self-heal via a thin resilient surface passive film. Remarkably, this passive film can mend itself when subjected to various environmental challenges, making stainless steels immensely versatile [89], [90], [91].

Within the stainless steel family, we find a variety of alloying combinations tailored to specific needs. The austenitic grades, such as Fe–Cr–Ni and Fe–Cr–Ni–Mn–N, are affectionately remembered by their former AISI type numbers, encompassing the 300 and 200 series, respectively. Meanwhile, the Fe–Cr grades display martensitic properties at lower chromium levels and ferritic characteristics at higher levels, earning their place in the 400 series. Stainless steels exhibit further diversity through duplex grades, offering a balanced composition comprising roughly 50% austenite and 50% ferrite, and precipitation hardening grades, predominantly martensitic in nature, tailored for applications demanding higher strength. The stainless steel family encompasses around 180 distinct alloys, each meticulously crafted to bolster resistance against a plethora of corrosion types (Fig 1.13) [90], [91].

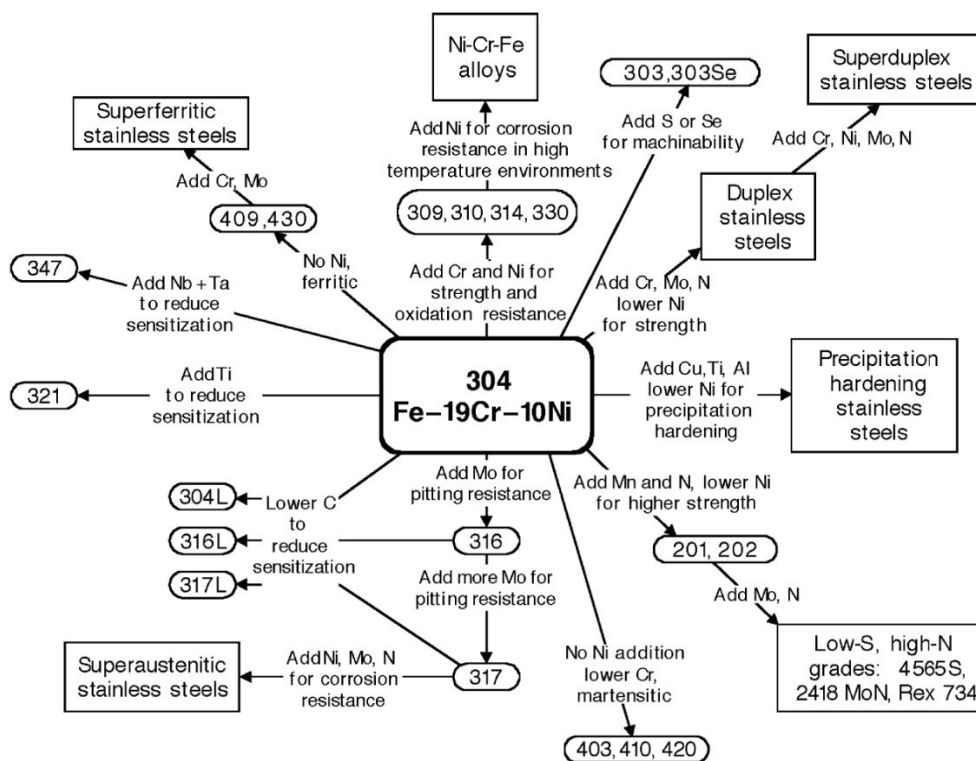


Figure 1.13 Stainless steel alloys composition and properties [90].

Among the most renowned stainless steel grades type 304 (UNS Number S30400) is often encountered, an austenitic variety containing 18-20 % wt. chromium and 8-12 % wt. nickel. Furthermore, grade type 316 (UNS S31603), also often encountered, is austenitic stainless steel with 16-18 % wt. chromium, 10-14 % wt. nickel, and 2-4 % wt. of molybdenum [90], [91].

Austenitic stainless steels, characterized by their excellent corrosion resistance and high-temperature stability, typically comprise 18 to 30 % wt. chromium, 8 to 20 % wt. nickel, and 0.03 to 0.1 % wt. carbon. At 800 °C, carbon's solubility limit is around 0.05 % wt., which increases to 0.5 % wt. at 1100 °C. Therefore, subjecting austenitic steels to solution treatment within the range of 1050 °C to 1150 °C dissolves all carbon into the matrix. Rapid cooling from this temperature range results in a supersaturated austenite solid solution at room temperature (Fig 1.14) [89], [91].

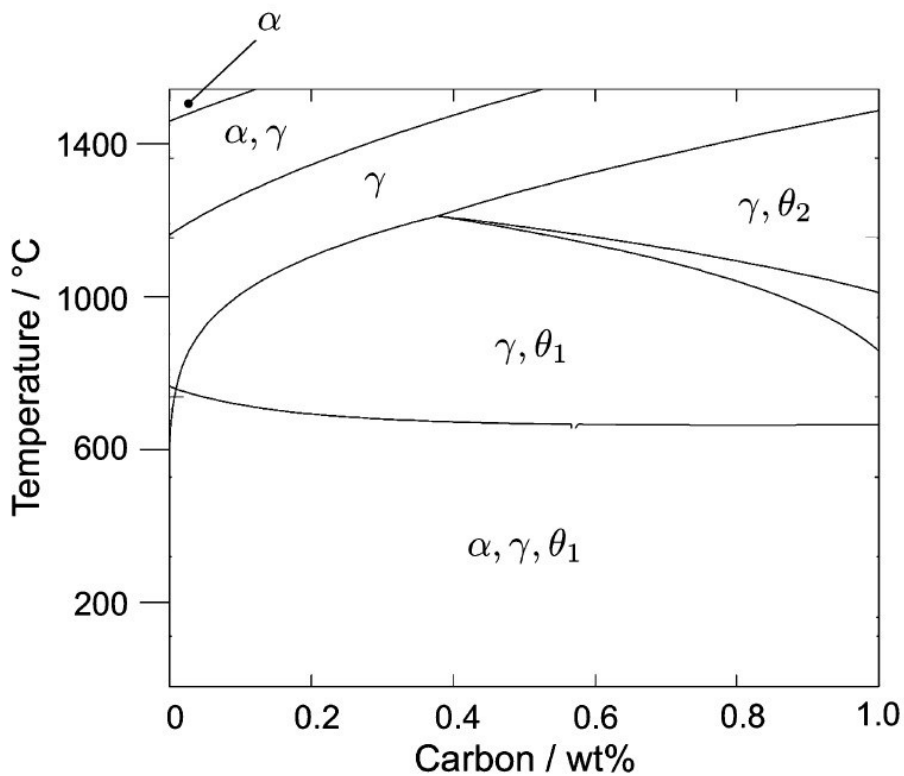


Figure 1.14 Calculated effect of carbon on the phase diagram for 18Cr-8Ni steel. θ_1 and θ_2 , stand for $M_{23}C_6$ and M_7C_3 respectively [89].

However, slow cooling or reheating within the range of 550 °C to 800 °C triggers the precipitation of carbon from the solution, typically in the form of chromium-rich carbides like $M_{23}C_6$, even when the steel's carbon content is very low (< 0.05 % wt.). These carbides tend to nucleate at the grain boundaries of the austenitic structure, affecting mechanical properties and corrosion resistance. The onset of intergranular corrosion is notable in these regions, where the surface oxide-film becomes chromium-depleted and anodic compared to its surroundings. This

can lead to severe intergranular corrosion and even steel disintegration. The lattice parameter of $M_{23}C_6$ is approximately three times that of austenite, making it easily identifiable via electron diffraction patterns. The critical temperature range for chromium carbide nucleation and growth is 500 °C to 850 °C. Consequently, any process that allows slow passage through this range renders the steel susceptible to intergranular corrosion. Welding, in particular, creates these conditions in the heat-affected zone, leading to localized corrosion in specific chemical environments. Various strategies exist to reduce or eliminate $M_{23}C_6$ formation and its associated intergranular corrosion risk, termed stabilization: solution treatment, carbon content reduction, control of $M_{23}C_6$ kinetics, strong carbide-forming elements, and grain boundary engineering. To counter grain boundary corrosion, certain austenitic steel grades, such as 304 and 316, are manufactured with low carbon content (<0.03 % wt.) and designated 304L and 316L [89], [91].

The austenitic steels do not exhibit remarkable strength or ductility. Typically, they possess a 0.2 % proof strength of around 250 MPa and a tensile strength ranging between 500 and 600 MPa. These properties highlight the significant work-hardening capacity of these steels, rendering their processing more challenging than that of mild steel. However, it's crucial to note that stainless steels find their exceptional utility in their other properties, particularly their corrosion resistance [89], [91].

1.2.2. Tool steels

Tool steels, widely employed in tooling components, must withstand high loads repeatedly without wear or deformation. Their choice becomes paramount when tools operate at high temperatures, balancing toughness, wear resistance, and resistance against temperature-induced softening. Tool steel properties emanate from alloying additions to plain carbon steel. These alloying elements enhance steel properties across four principal categories [92], [93]:

- i. wear resistance
- ii. toughness or strength
- iii. hardenability, hardness accuracy, and hardening safety
- iv. high-temperature hardness or “red hardness”

Carbon content in tool steels typically ranges from 0.4 % to 1.5 % wt., and they're meticulously formulated under stringent conditions to yield desired quality. The carbides in their structure play a pivotal role in defining tool steel attributes. Prominent alloying elements that induce carbide formation in tool steel include tungsten, chromium, vanadium, and molybdenum. Adjusting the carbide phase composition and characteristics can alter the hardening properties, such as critical temperature, carbide solution during heating, grain enlargement when heated, hardenability, and resultant products upon cooling. These changes also affect the formation of martensite and the retention of austenite the martensite start

temperature (M_s) and the martensite finish temperature (M_f) during cooling, along with tempering property adaptations during reheating [92], [93].

The stability of carbides can be ranked in decreasing order, as depicted in Table 1.2. More stable carbides avidly combine with carbon and can pre-empt elements lower in the table when present in multi-alloy steel. These stable carbides also display superior hardness and wear resistance. However, dissolving these stable carbides into the matrix requires prolonged heating at higher temperatures. This increases the steel's resistance to grain growth and promotes the presence of harder, wear-resistant carbides in the hardened steel matrix [92], [93].

Table 1.2 Stability of carbides arranged in the order of decreasing carbide stability [93].

Increasing stability of carbides ↑ ↑ ↑ ↑ ↑	Titanium	MC
	Tungsten	M₆C
		M₂C
		M₂₃C₆
	Molybdenum	M₆C
		M₂C
		M₂₃C₆
	Vanadium	MC
	Chromium	M₇C₃
		M₂₃C₆
M₃C		
Manganese	M₃C	
Iron	M₃C	

Alloying elements can be divided into two primary groups based on their influence on the critical austenite formation temperature. Ferrite formers, the first group, elevate this temperature, encompassing elements like titanium, vanadium, molybdenum, silicon, tungsten, and chromium. The second group, austenite formers, expand the austenite range by decreasing its formation temperature. This group includes carbon, nitrogen, nickel, manganese, copper, and cobalt [92], [93], [94].

Concerning the influence of alloying elements on the M_s and M_f temperatures for martensite transformation: except for cobalt and aluminum, all elements reduce the martensite start temperature, resulting in increased retained austenite. Carbon is notably potent in reducing the M_s temperature and elevating retained austenite. Barring cobalt, every alloying element in tool steels, including carbon, typically expands the isothermal transformation curve. This increases hardenability, reducing the need for aggressive quenching. However, the undissolved carbides' presence is a consideration, as strong carbide-forming elements can sequester carbon, impeding its dissolution in the austenite matrix. This might lead to lower carbon concentration in the austenite, potentially reducing isothermal transformation times [92], [93].

Tempering, an essential final stage in tool steel's heat treatment, precipitates dissolved carbides in a refined dispersion, enhancing toughness and achieving the

targeted hardness level. Two primary reactions typify secondary hardening in tool steel [92], [93]:

1. Transformation of the retained austenite present in all un-tempered steels. In low and medium-alloy steels, this austenite either becomes bainite or partially stabilizes at minor tempering temperatures. In high-alloy steels, this austenite persists up to 427–538 °C (800–1000 °F), when a conditioning reaction begins, turning the austenite to martensite upon cooling.
2. Precipitation of sub-microscopic carbides, mainly between 482–538 °C (900–1000 °F).

It's vital to understand that carbide-forming elements' effect during tempering depends on the preceding hardening heat. For instance, tungsten, molybdenum, and vanadium play critical roles in precipitating carbides during tempering. To witness this rehardening effect, these elements should be in substantial concentrations. Conversely, chromium reduces the softening rate during tempering without triggering genuine secondary hardening. Cobalt enhances the effects of tungsten and molybdenum, elevating secondary hardening and heat resistance. The tempering curve of carbide-rich steels can be significantly modulated by the hardening phase, influencing the dissolved carbon and alloy quantities available for precipitation during tempering [92], [93].

Historically, various tool and die steels have been developed to tailor properties for specific applications. They broadly fall into six categories: high-speed steels, carbon tool steels, low-alloy tool steels, special purpose tool steels, cold work tool steels, and hot work tool steels. Each category has further subdivisions based on various factors like alloying elements, heat treatment methods, and inherent properties. [92], [93], [94].

High-speed steels, distinguished for their ability to preserve hardness at elevated temperatures, are predominantly employed in the manufacture of cutting tools, including drills, end mills, and taps. These steels are predominantly composed of W, Mo, Co, and V. Their capacity to maintain hardness under high-temperature conditions facilitates increased cutting speeds. Carbon tool steels, with their primary hardening attribute being their C content, are relatively cost-effective and are suitable for crafting tools like knives, razors, and woodworking implements. However, improper tempering can render them brittle. Low-alloy tool steels, containing minimal alloying elements, are engineered to strike a balance between toughness, wear resistance, and hardness. These steels offer superior hardenability compared to carbon tool steels and are ideal for applications demanding wear resistance where the use of high-alloy steels would be cost-prohibitive. Special purpose tool steels cater to specific applications or display distinct characteristics. For instance, while some are formulated to offer abrasion resistance, others are designed to thwart softening at high temperatures. These steels might incorporate elements such as Si, S, or Se to bestow unique properties. Cold work tool steels, aptly named, are tailored for tools operating at ambient temperatures, typical

examples being tools used for stamping, cutting, or forming. These steels are renowned for their wear resistance, dimensional stability post heat treatment, and robustness. Tool steels from the D, A, and O groups are categorized under this type. Lastly, hot work tool steels are designed to endure high temperatures and are integral for processes like forging, die casting, and extrusion. Their salient features include resistance to thermal fatigue and abrasion, in addition to sustaining hardness under elevated temperature conditions [92], [93], [94].

1.2.3. Maraging steels

Maraging steels belong to a unique category of ultra-high-strength steels. Unlike conventional steels, they undergo a distinctive hardening process that doesn't rely on carbon. Instead, their strength arises from the precipitation of intermetallic compounds at a temperature of approximately 480 °C (900 °F). The term "maraging" is a fusion of "martensite" and "age hardening", which highlights the aging of a low-carbon, Fe-Ni martensite matrix. Commercial maraging steels are designed to achieve specific yield strengths between 1030 to 2420 MPa. Some experimental variants have even reported yield strengths as high as 3450 MPa [94]. Characterized by an extremely low C content, no more than 0.03 % wt., maraging steels also contain significant amounts of Ni, between 17–19 % wt. Other constituents include Co (8–12 % wt.), Mo (3–5 % wt.), Ti (0.2–1.8 % wt.), and Al (0.1–0.15 %wt.). This specific composition aims to prevent the formation of titanium carbide (TiC) precipitates, which can significantly diminish impact strength, ductility, and toughness. Nevertheless, the high alloy content, particularly Co, means that maraging steel carries a higher cost [94], [95].

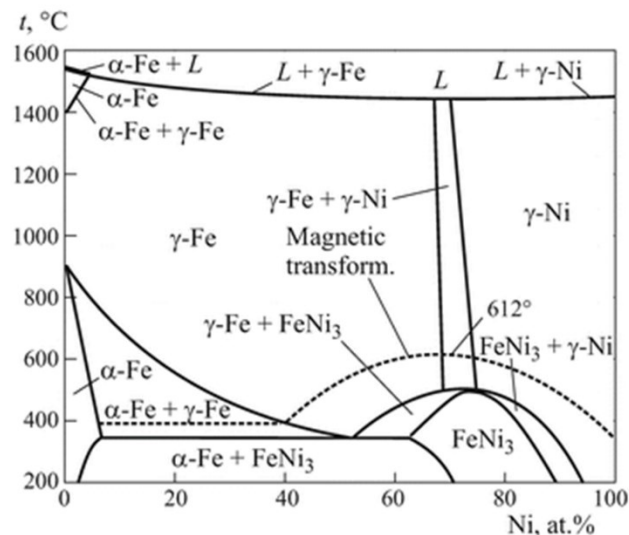


Figure 1.15 Phase diagram related to Fe – Ni system [96].

The production of maraging steel involves a process termed austenitizing, where the steel is heated to around 850 °C, falling within the austenite phase region

(Fig 1.15). Following this, it undergoes a gradual air cooling to foster a martensitic microstructure. Generally, slow cooling of hypoeutectic steel from the austenite phase results in the formation of ferrite and pearlite. In contrast, rapid cooling methods, like quenching in water or oil, are employed to form martensite. However, due to maraging steel's elevated Ni content, martensite formation occurs even during slow cooling, thereby inhibiting ferrite and pearlite formation. This resulting martensitic structure is softer than its counterpart in conventional carbon steels, which is beneficial as it offers greater ductility and toughness without requiring tempering [95].

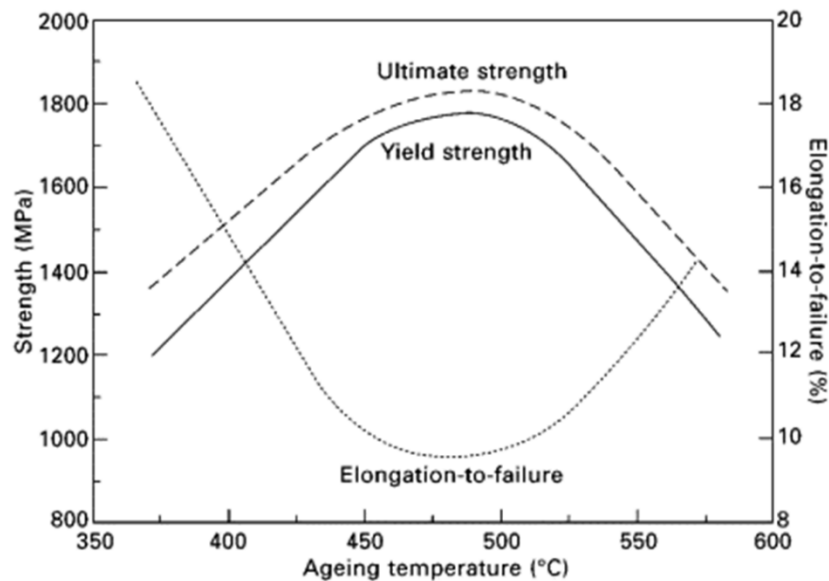


Figure 1.16 Effect of ageing temperature on the strength and ductility [95].

Post-quenching, maraging steel experiences a strengthening stage through thermal ageing, a prerequisite for its use in aircraft components. The steel undergoes heat treatment at 480–500 °C for several hours, facilitating the formation of hard precipitates dispersed within the softer martensitic matrix. The primary types of these precipitates are Ni_3Mo , Ni_3Ti , Ni_3Al , and Fe_2Mo , appearing in high volumes due to the alloy-rich composition of the steel. Its negligible C content ensures an almost complete absence of carbide precipitation. Co, a key element in maraging steel, plays diverse roles. It not only limits the solubility of Mo, thereby increasing the volume of Mo-rich precipitates, but also ensures even dispersion of these precipitates throughout the martensitic matrix, consequently reducing the ageing time required for optimal hardness. Precipitates in maraging steel serve to limit dislocation movement, thereby strengthening the material through precipitation hardening. Fig 1.16 illustrates how the ageing temperature impacts the tensile strength and ductility of maraging steel. Age-hardening at the optimal temperature range of 480–500 °C over a span of several hours allows the steel to approach a yield strength of around 2000 MPa while still maintaining commendable ductility and toughness. Nonetheless, over-ageing may lead to reduced strength due

to precipitate enlargement and the martensite's decomposition, causing its reversion to austenite [95].

1.3 Additive manufacturing of steels

AM has evolved to incorporate a variety of metallic systems, encompassing Ti alloys, Ni-based superalloys, Al alloys, and notably, steels. While steels now constitute roughly a third of all metal AM-related publications, it could be stated that they remain underrepresented given that they form nearly 80 % of all metallic components used in engineering. The environmental footprint of AM is a topic of ongoing debate. However, there's potential for it to reduce greenhouse gas emissions, particularly when producing intricately shaped steel parts. This approach could bypass the emissions associated with less efficient conventional production techniques. Beyond its ecological promise, AM brings an unmatched level of design versatility, enabling the creation of intricate geometries or lightweight, hollow structures that would challenge traditional manufacturing methods. With steel's inherent recyclability, AM's significance extends to the circular economy. It presents an opportunity to manufacture high-value items from recycled powders and reintegrate AM by-products into new creations [97].

AM offers a unique capability by constructing materials layer by layer, each with a thickness of a few tens to thousand of microns. This approach facilitates the creation of location-specific microstructures, possessing tailored mechanical [98], [99] and corrosion properties [100] that remain challenging, if not unfeasible, via conventional manufacturing techniques. Therefore, it is essential to understand the microstructural evolution during AM. The thermal history experienced by metals in AM is different from traditional manufacturing processes. Microstructures in AM are the result of rapid solidification rates ($dT/dt: 10^3\text{--}10^8\text{ K/s}$) [101], with values in the range 10^3 to 10^4 K/s for L-DED processes, high thermal gradients ($dT/dx: 10^3\text{--}10^7\text{ K/m}$), and thermal fluctuations due to the sequential melting and deposition of consecutive multiple layers [18], [27], [97], [102], [103]. The evolution of key microstructural features, including solidification morphology, segregation, cells, grain structure (size and shape), crystallographic texture, microstructure stability, secondary phases, defects, and inclusions, is influenced by the above mentioned thermal aspects. In AM microstructures, subgrains are solidification cells with orientations very similar to one another, defined by the segregation of alloying elements and the accumulation of dislocations at their boundaries [104].

To date, a range of steels have been successfully processed using L-DED technology. Commonly studied AM materials include alloy steels, carbon steels, stainless steels, and tool steels [36]. Among carbon and alloy steels, recent studies have reported processing grades such as 18Ni300 (M300), AerMet100, AISI 4140, 4340, 34CrNiMo6, 24CrNiMo, 12CrNi2, 12CrNi2Y, 50Cr6Ni2Y, and Fe-9Cr using L-DED technology [105], [106], [107], [108], [109], [110], [111], [112], [113], [114], [115]. For tool steels, research on grades like H13, D2, M4, M2, and

W360 is available in scientific literature [31], [116], [117], [118], [119]. In the group of stainless steels, AISI 316L, 304L, and 420 are frequently cited [120], [121], [122]. Additionally, studies on duplex and precipitation-hardening stainless steel grades such as DSS 2205, SAF2507, 15–5 PH, 17-4 PH, among others, have also been published [123], [124], [125], [126].

1.3.1. Stainless steel 316l by L-DED

In recent years, the application of AM technologies to stainless steels has surged, primarily due to their robust mechanical properties. These steels are well-suited for diverse applications spanning industries such as automotive, aerospace, and petrochemicals [127], [128], [129]. Among these, AISI 316L steel stands out as the most extensively processed and researched. Its popularity can be attributed to its excellent weldability and corrosion resistance [120].

The 316L stainless steels is in a composition range where solidification can occur either with a primary (δ -) ferritic phase or with a primary austenitic (γ) phase [104]. The primary solidification phase in case of 316L is austenite, as expected from the Schaeffler diagram, Fig 1.17 [120], [130]. In L-DED processing of 316L stainless steel, it is indeed observed that in the regions along the borders of the solidification cells (i.e. in the intercellular regions), the micro segregation during solidification leads to an enrichment in the ferrite stabilising elements Cr and Mo [130], [131]. Additionally, grains are elongated in the direction of thermocapillary convection within the melt pool and areas of heat sink [29]. Regions with elongated grains, ranging between 200–400 μm , consist of fine equiaxed and elongated cells, each approximately 5 μm in size [130].

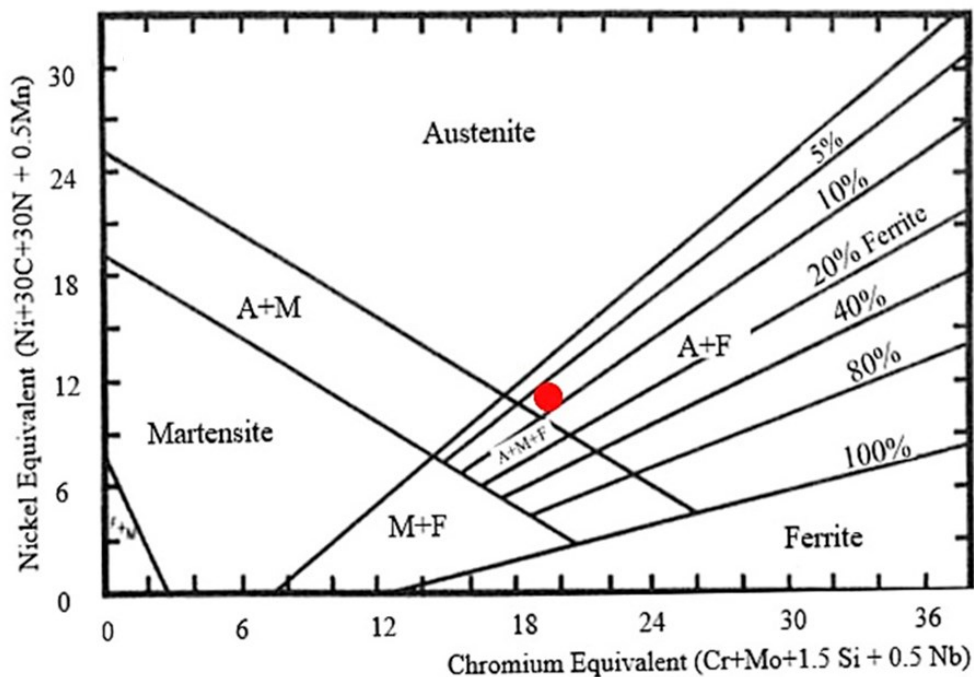


Figure 1.17 Schaeffler constitution diagram showing the location of the composition of the AISI 316L stainless steel (red circle) [120], [130].

Mechanical properties serve as critical measures of the quality of an AM process, with hardness and tensile properties typically utilized as principal performance indicators for AM components. Industrially, tensile samples are commonly constructed alongside AM components to confirm the integrity of the building process. Consequently, there has been extensive research into the mechanical properties of AM materials. Numerous studies and analyses focused on the tensile strength and hardness of as-built DED AISI 316L samples, fabricated under varying building or post-processing conditions [120]. The quality of components in DED building is largely contingent on key parameters like laser power, scan speed, and powder feeding rate. Establishing the optimal amalgamation of these process parameters is crucial not only for attaining dense samples but also for fostering the development of the desired microstructure and mechanical properties [120], [132], [133]. The relationship between building direction and tensile properties is also important in assessing the mechanical attributes of AM samples. The stress–strain curve is influenced by the anisotropy of the microstructure and the existence of certain defects [103]. Therefore, a broad range of mechanical property results is observed. However, in general, the hardness of parts produced by L-DED is higher than that of parts produced by traditional conventional technologies [120]. Reported values start from 190 HV, as indicated by Ma et al. [103], which is 20 HV higher than a cast 316L sample [134], extending up to 370 HV as reported by Zhang et al. [135]. In the literature, the yield strength (σ_y) of L-DED produced samples ranges from 300 to 610 MPa [103], [135], ultimate tensile strength (σ_{UTS}) from 536 to 900 MPa [135], [136], and elongation to fracture (ϵ_f) from 4 to 46 % [135], [136].

In AM, as-built components commonly exhibit high residual stresses, attributed to the complex thermal history experienced during fabrication. Therefore, specialized post-heat treatments are essential, serving to mitigate internal stresses and harmonize microstructures. Nevertheless, there has been a limited exploration into the impact of stress-relieving or annealing heat treatments on the properties of L-DED AISI 316L [120].

1.3.2. Hot work tool steel by L-DED

Only some grades of tool steels have successfully processed by L-DED [104]. Typically, tool steels are high-alloyed carbon steels, with the majority having an equivalent carbon content exceeding 0.50 %, as per European standard EN 1011–2 Method A, Eq. 1 [137]. According to welding literature, steels possessing an equivalent carbon content above 0.7 % are considered challenging to weld or non-weldable, owing to their tendency to form martensite during cooling, subsequently increasing the risk of cold cracking. Such cracking is associated with alterations in the specific volume throughout the solid-phase transformation [138], [139], [140], [141].

$$(1) CE = \%C + \frac{\%Mn}{6} + \frac{\%Cr+\%Mo+\%V}{5} + \frac{\%Cu+\%Ni}{15}$$

When it comes to hot work tool steels, those most extensively studied within the AM domain are chromium-molybdenum steels, with the AISI H13 (1.2344, X40CrMoV5-1) grade standing out notably [104]. Although H13 steel exhibits a relatively high processability indicator equivalent carbon content of 2.14 % wt., as per Eq. 1. The exceptional combination of hardness, toughness, thermal shock resistance, and wear resistance is what makes H13 so interesting [93].

In the as-built condition of H13 produced by L-DED, the microstructure is characterized by solidification cells and dendrites, accompanied by a martensitic phase, and retains austenite within the interdendritic regions. This cellular microstructure arises due to micro-segregation throughout the solidification process and is rich in alloying elements such as Cr, Mo, V, and C [142]. Specifically, the enrichment of carbon stabilizes the austenite to room temperature [32], [143]. The sizes of these cells vary from 2 to 30 μm , primarily depending on the sample position and the energy applied [32], [104]. Additionally, carbide precipitates, predominantly located in the interdendritic region, may form during the ITH. The majority of identified carbides are of the MC-type, supplemented by a minor presence of M_7C_3 carbides [104], [119], [144].

Numerous studies have documented the mechanical behaviour of hot work tool steel H13 fabricated by DED. In the case of material produced by L-DED in an as-built condition, the hardness is found to be between 550 and 660 HV [104], [142], [145], with the σ_{UTS} approximating 2000 MPa and the ϵ_f varying from 5 to 6 %. These values parallel those of quenched and tempered wrought material, indicative of its in-situ tempered state [104].

When it comes to the tool steels the heat treatments are extremely important for tuning of their mechanical properties. Usual post-heat treatments are performed in order to decompose the retained austenite at the temperatures above 500 $^{\circ}\text{C}$, to erase the cellular solidification microstructure by heating above 700 $^{\circ}\text{C}$ [31], [32], [139]. Another post-heat treatment often performed is to obtain microstructure and mechanical properties similar to conventionally produced material by austenitizing followed by quenching and tempering cycles [31], [32], [104], [139], [146]. Also, some innovative post-heat treatments like high pressure heat treatments are investigated and utilized [147] Apart from the post-heat treatments it is important to mention the ITH that has significant influence on properties of as-build samples [104]. H13 produced via DED exhibits a martensitic microstructure, with some presence of retained austenite. The martensite found is tempered due to the ITH from the heat input during the process [31]. This tempering effect becomes evident when comparing the hardness of the top layer, which did not experience ITH, to the lower layers that undergo IHT [104], [148].

1.3.3. Maraging steel by L-DED

In the group of maraging steels, the most widely used alloy in AM is 18Ni-300 (1.2709, X3NiCoMoTi 18-9-5) [88], [106], [149], [150], [151], [152].

When compared with conventionally manufactured (wrought) maraging steels, typically almost entirely martensitic, those produced by DED exhibit a significantly different microstructure [88], [104]. In samples produced by DED cellular/dendritic solidification microstructure appears with cell sizes around 5 μm [88], [151], [152]. It is also reported that the prior austenite grains in DED-produced samples are relatively large, reaching up to 1 mm in diameter. Within these solidification microstructures, blocks of martensite laths predominantly inhabit individual solidification cells, often, but not invariably, bounded by retained austenite along cell peripheries [88], [104]. This retained austenite results from the enrichment of alloying elements in the interdendritic (intercellular) regions due to microsegregation during solidification. The accumulation of Ni stabilizes the austenite to room temperature [88], [152]. As a result, maraging steels fabricated through DED contain a significant amount of austenite, ranging between 6 and 11%, depending on the specific processing conditions utilized [88], [104].

In literature, the microhardness of as-built 18Ni-300 maraging steel by L-DED has been reported to be around 350 HV, while the tensile properties. While no literature that has reported tensile properties of as-built samples by L-DED [88], [149]. In order to give some idea about tensile properties of as-built AM 18Ni-300 samples values for L-PBF produced samples are reported. The σ_{UTS} approximating 1150 MPa and the ϵ_f varying from 5 to 13 % [104].

The steel undergoes heat treatment at 480–500 °C for several hours, facilitating the formation of hard precipitates dispersed within the softer martensitic matrix. However, the cellular as-built microstructure is maintained at typical aging temperatures. When exposed to higher aging temperatures, such as 600 °C, considerable austenite reversion occurs [104], [153]. After a solution treatment, generally conducted between 815 and 840 °C, where the steel reaches a fully austenitic phase, the cellular microstructure is completely dissolved. It is then succeeded by a completely martensitic, but coarser microstructure upon quenching, resulting in a reduction in hardness and strength relative to the as-built state [104], [154]. Furthermore, there is evidence of the initial stages of precipitation in L-DED-produced material, leading to elevated hardness. This phenomenon is linked to the repetitive reheating of the material with the addition of new tracks and layers, a condition known as IHT [88], [104].

1.4 Research objectives

Trying to summarize, in this thesis the primary aim was to demonstrate the capability of the L-DED technology both for creating 3D objects in steels and for repairing industrial tools in steels, using two different systems with powder feeding, and one system with wire feeding. To achieve these goals, multiple research sub-objectives were established. The first sub-objective was to comprehend the L-DED process of steels using powders or wires as feedstock. This involved investigating the use of the well known stainless steel 316L as the primary material, first analysing the characteristics of the starting 316L powder and optimizing the L-DED main process parameters using predicting models to produce defect-free samples.

The machine employed is a Laserdyne 430 by Prima Additive with 2 mm laser spot diameter. Subsequently, a microstructural and mechanical characterization was conducted to gain insights into material properties and behaviour. Furthermore, the influence of heat accumulation during the L-DED process on microstructural and mechanical properties was explored through various deposition strategies. For the second sub-objective, the utilization of L-DED with 316L wires feedstock was explored, beginning with the optimization of process parameters for L-DED. The machine used is a LAWS 250 by Liburdi with 0.3 mm laser spot diameter and fixed wire feeding position. This led to further aims, such as investigating the effects of different feeding directions on melt pool shape, microstructure, and mechanical properties.

A third sub-objective was to process, for the first time to the authors' knowledge by L-DED using Laserdyne 430 system, the W360 hot work tool steel provided by Böhler. Bulk samples were successfully deposited, and then their microstructural and mechanical properties were analysed in different conditions: as built, and after a heat treatment involving austenitizing, quenching, and tempering to assess the evolution of microstructure in each step.

The fourth sub-objective was to optimize the main process parameters of the L-DED system LAWS 250 for the 18Ni-300 maraging steel in powder. The exploration commenced with characterizing the initial powder, proceeded to optimize the main process parameters, and culminated in a detailed analysis of the microstructural and mechanical properties of the samples.

The last sub-objective was related to the use of L-DED technology to repair tool steels. The L-DED from Prima Additive, Laserdyne 430, with the laser spot diameter of 2.0 mm was used for the repair of D2 tool steel blades with the W360 hot work tool steel. Initial objectives included investigating the starting D2 material and optimizing main process parameters for W360 steel.

Chapter 2

AISI 316L by DED

In this chapter, the data obtained from experimental investigations conducted regarding stainless steel 316L processed by L-DED from powders (L-DED-P) and L-DED from wires (L-DED-W) are presented in six main sub-chapters, defined as follows:

- Powders for L-DED-P
- Process parameters optimization for L-DED-P
- Microstructural analysis of samples by L-DED-P
- L-DED-P deposition strategy – influence of heat accumulation
- Factor screening for multiple responses in L-DED-P
- Effects of wire feeding direction and main process parameters in L-DED-W

2.1 Powders for L-DED-P

In this study, a commercially available gas-atomized pre-alloyed AISI 316L stainless steel powder, provided by Oerlikon (Freienbach, Switzerland), was utilized for AM sample production through L-DED. The powder chemical composition, detailed in Table 2.1, remained consistent throughout the experiments. All the measurements and analyses performed on powder samples are detailed in Appendix B.1. The particle size distribution of the powder exhibited a unimodal and Gaussian pattern, with D10 at 49.2 μm , D50 at 60.9 μm , and D90 at 74.6 μm , as depicted in Fig 2.1. Notably, this distribution fall within the lower spectrum, deviating from the conventional range of 50-150 μm typically used in L-DED processes. Fig. 2.2 (a) presents a SEM micrograph of the as-received powder, revealing predominantly spherical particles. However, the micrograph also unveils the presence of various defects: satellites (Fig. 2.2 (b)), agglomerates (Fig. 2.2 (c)), and elongated particles (Fig. 2.2 (d)). The occurrence of satellite particles is common in gas atomized powders, affecting powder flow behaviour. These particles are formed due to differences in droplet velocities, sizes, and cooling times during the atomization process. Larger droplets often split into smaller ones with varying speeds, with smaller droplets cooling more rapidly. These smaller droplets may collide with larger ones and adhere on their surface, forming satellites[155]. Additionally, irregular powder particles, including agglomerates and elongated shapes, significantly influence powder flowability [155], [156], [157]. During atomization, if a droplet is in a low-velocity gas field or experiences minimal

relative velocity between the gas and the droplet, it doesn't fragment but can deform. Upon reaching the solidification point, the droplet retains this irregular shape [155].

Table 2.1 Standard and nominal chemical composition of AISI 316L stainless steel powder.

wt. %	C	Fe	Cr	Ni	Mo	Mn	P	S	Si	N
<i>Standard</i>	0.03	Bal.	16.0- 18.0	10.0- 14.0	2.00- 3.00	2.00	0.045	0.03	0.75	0.1
<i>Nominal</i>	<0.01	65.72	17.34	12.55	2.34	1.40	0.012	<0.01	0.49	0.08

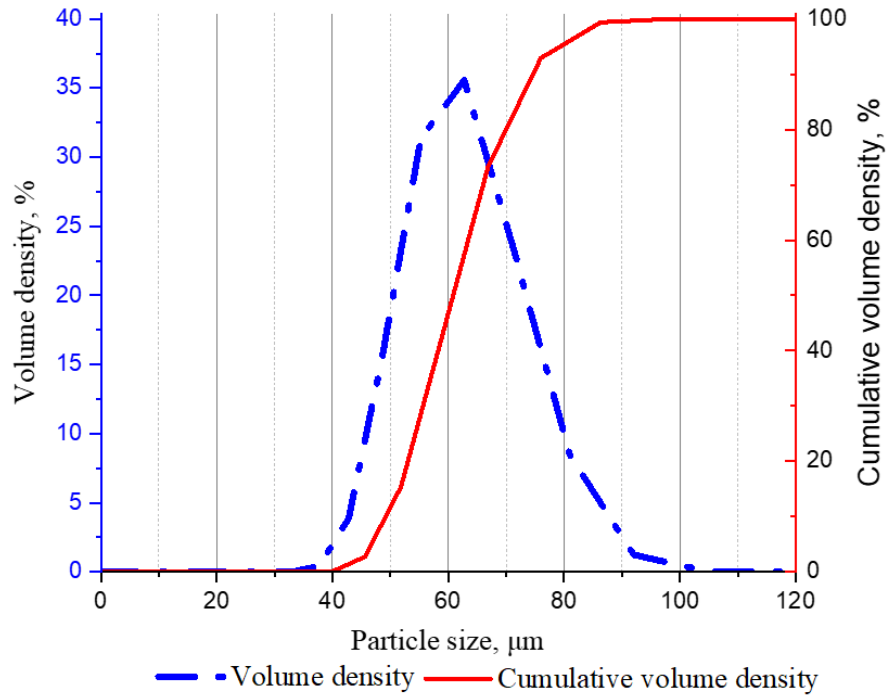


Figure 2.1 AISI 316L powder particle size distributions in the as received condition: the dotted blue curve corresponds to the distribution in volume, while the red curve to the cumulative volume distribution.

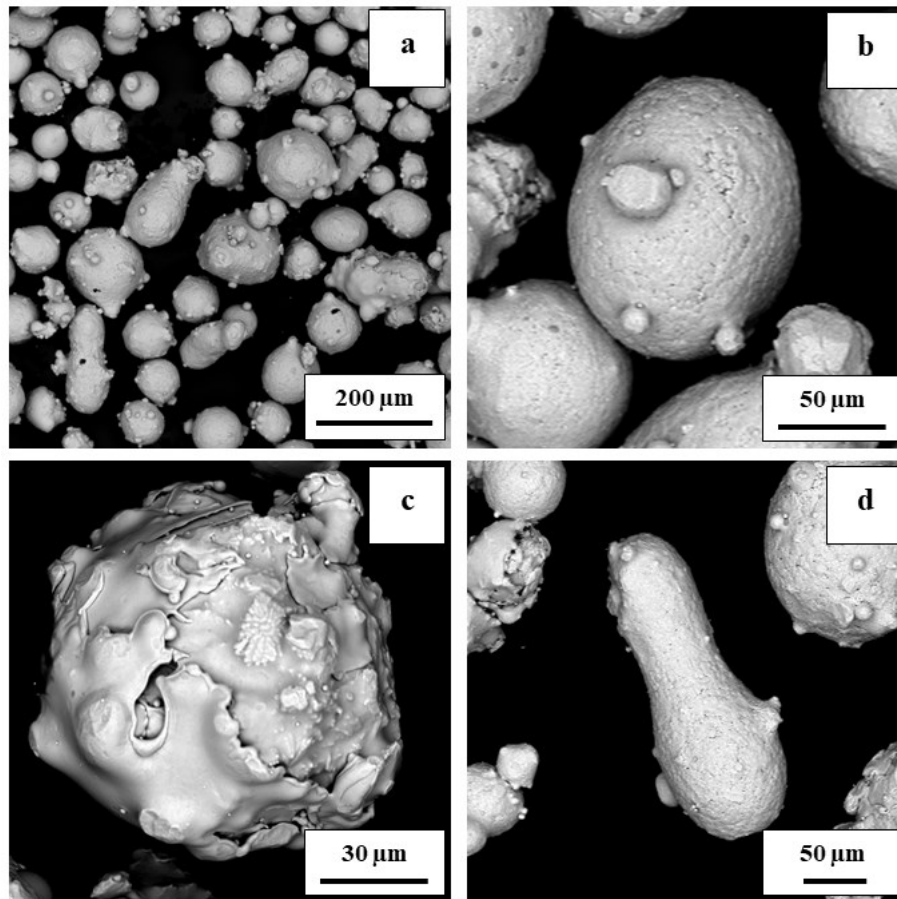


Figure 2.2 SEM micrographs of a) AISI 316L powder in the as received condition, and magnifications showing b) a particle with smaller satellites, c) an agglomerate particle, and d) an elongated powder particle.

Given the identified particle types in the powder batch, evaluating the powder's bulk properties became imperative. The powder exhibited excellent flow properties: in Table 2.2 the values of a Hall flow meter measurement, a compressibility index (CI), a Hausner ratio (HR) together with the apparent density (δ_{app}) and the tapped density (δ_{tap}) are reported.

Table 2.2 Flow properties of 316L powder.

<i>Property</i>	<i>Value</i>
<i>Hall flow meter measurement</i>	14 s/50g
<i>CI</i>	8.3%
<i>HR</i>	1.09
δ_{app}	4.52 g/cm ³
δ_{tap}	4.93 g/cm ³

The powder true density was assessed, revealing a measurement of 7.896 g/cm³ at 20.0 °C. This prompted further evaluation for potential internal porosity because in the literature the density of stainless steel 316L is taken to be 7.98 g/cm³ [158], [159]. Image analyses of OM micrographs of the powder cross-section confirmed the presence of internal porosity (Fig 2.3 (a)). During gas atomization, most of the bubbles within the molten metal droplets escape. In case a bubble does not escape

it becomes a pore (Fig 2.3 (b)). This phenomenon can be attributed to the spinning of the molten droplets exhibiting a high swirl velocity that generates centrifugal force, maintaining low-density gas at the droplet centre, leading to the formation of hollow powder. This phenomenon is schematically illustrated in Fig 2.3 (c). Hollow powder particles can either retain closed porosity (Fig 2.3 (b)) or develop openings if the metal crust breaks, as shown in Fig. 2.3 (d), which might not be apparent from true density measurements. The internal porosity of 316L powder was quantified and found to be 1.3 %.

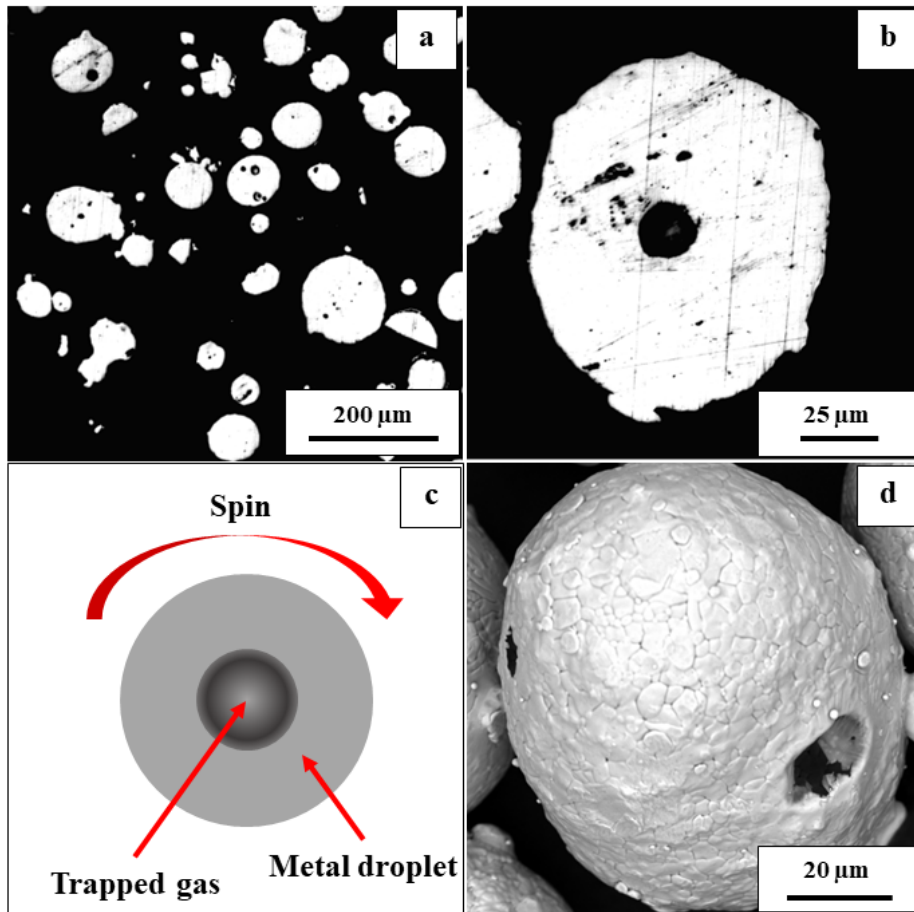


Figure 2.3 a) OM micrograph of powder cross section, b) OM micrograph with higher magnification of powder particle with trapped gas porosity, c) schematic of hollow powder particle with swirl spin indicated, d) SEM micrograph of hollow powder particle with open porosity.

An in-depth examination of SEM micrographs of the as-received 316L powder revealed the presence of distinctive darker areas, suspected to be oxides (Fig. 2.4). A large amount of similar dark spots on the powder particles was found by Saboori et al. on recycled powder [160]. Their study on the effect of powder recycling on L-DED-fabricated AISI 316L parts indicated differences in mechanical properties between components constructed with fresh and recycled powders. Parts produced with recycled powder exhibited significantly reduced elongation values, primarily due to inclusions of large non-metallic phases in DED samples. The powder analysed in this thesis displayed few oxide inclusions on its surface (Fig 2.4), as

confirmed by EDS spot analysis performed on darker and surrounding areas, as shown in Fig 2.4. The results are summarized in the Table of Fig 2.4. Furthermore, LECO analysis was employed on the powder sample to quantify the levels of oxygen and nitrogen present. To discern variations in oxygen levels between the as-received fresh powder and the used powder, a parallel analysis was conducted post-use. The findings of the LECO analysis are tabulated in Table 2.3, illustrating a fivefold increase in oxygen levels in the used powder, while nitrogen levels remained consistent pre- and post-use, aligning with the data in Table 2.1 for chemical composition. This increase in oxygen levels in the used powder results from particles undergoing partial heating during the L-DED process. Once they exit the zone of reduced oxygen content, created by the implementation of inert shielding gas, oxidation rapidly occurs.

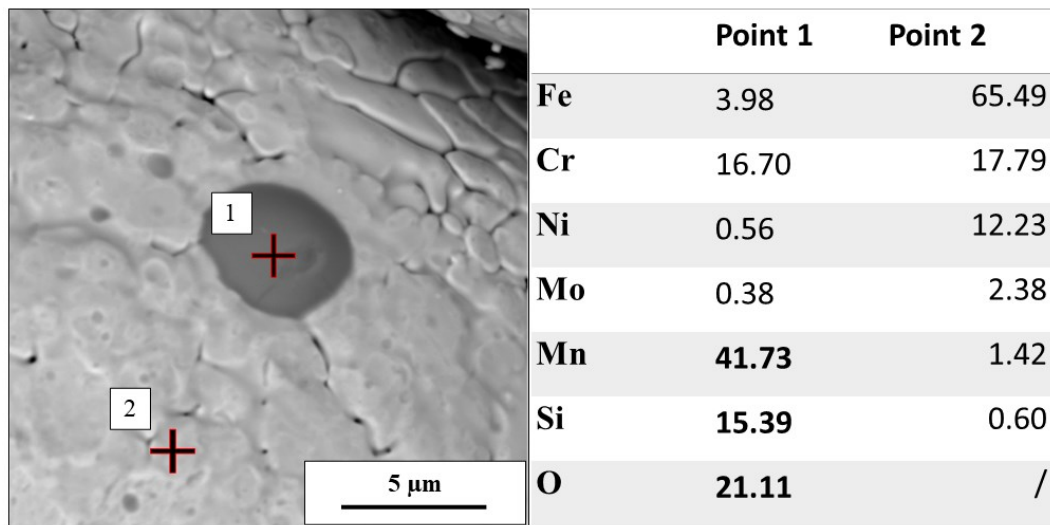


Figure 2.4 SEM micrograph used for EDS point analysis with table of results reported in % in wt.

Table 2.3 Results of LECO analysis for 316L powder before and after use.

wt. %	Before use	After use
Oxygen	0.0344 ± 0.0025	0.163 ± 0.006
Nitrogen	0.0733 ± 0.0003	0.0826 ± 0.0002

This comprehensive powder characterization provides essential insights for understanding subsequent L-DED-P investigations.

2.2 Process parameters optimization for L-DED-P

The L-DED system employed in this study was the Laserdyne 430 by Prima Additive, detailed in Appendix B.2.1. To ensure the production of dense and crack-free L-DED samples, a meticulous multi-step approach, outlined in Appendix A – Experimental Procedure, was followed. Single tracks (STs) measuring 40 mm in length were deposited on a 316L substrate using the methodology described in Appendix A.1. The design of the experiment (DoE) encompassed a range of

parameters including laser power (P) and scan speed (v) for the fixed powder feed rate (Q_p) for the initial process window, as summarized in Table 2.4. The Q_p was fixed at 8 g/min based on the previous experiences on using Laserdyne 430 with 2.0 mm laser spot diameter, providing an optimal layer growth of around 0.5 mm.

Table 2.4 Process parameter ranges and steps used for deposition of STs for

DoE #1, DoE #2 and DoE #3.	DoE #1		DoE #2		DoE #3	
	Range	Step	Range	Step	Range	Step
Power [W]	500 – 1000	100	700 – 900	40	780 – 820	20
Scan speed [mm/min]	600 – 800	50	600 – 700	25	600 – 650	25
Powder feed [g/min]	8	/	8	/	8	/

The STs were then examined following the procedure described in Appendix A.1. The results are summarised in Fig 2.5 in which dilution is plotted over aspect ratio (AR) with some selected examples of OM micrographs showing extremes and acceptable cross-section geometries.

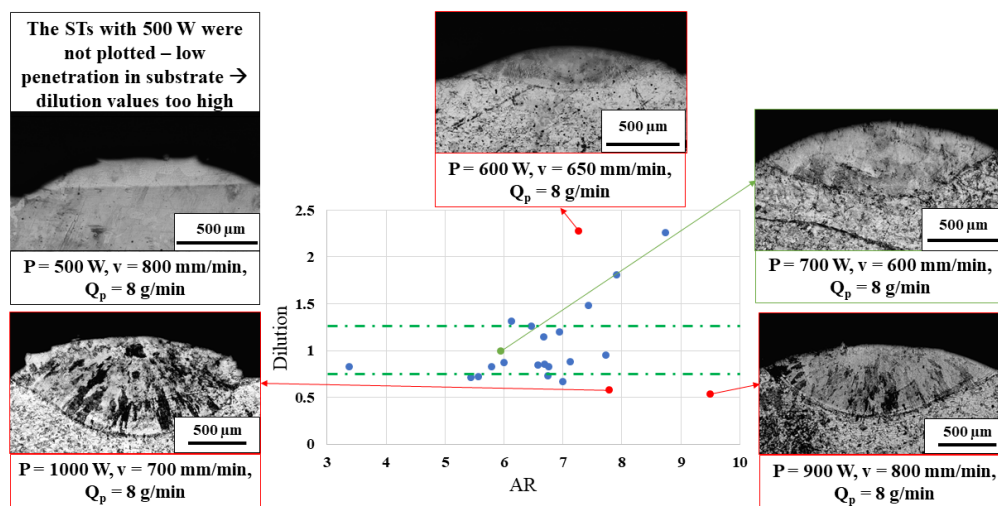


Figure 2.5 Diagram summarizing the dilution over AR with selection criteria lines with selected OM micrographs of STs representing different extremes and acceptable melt pool geometry.

The results of this initial DoE, depicted in Fig 2.5, showcased a distinct pattern. STs built with a laser power of 500 W exhibited minimal substrate penetration, leading to extremely high dilution values. An example of these tracks having an insufficient penetration is illustrated in top-left OM micrograph in Fig. 2.5. Using these building parameters could lead to weak metallurgical bonding. STs deposited at 600 W demonstrated improved but still inadequate substrate penetration, failing to achieve the desired dilution values around 1.0. Conversely, STs created with higher power settings exhibited excessive penetration, evident from dilution values below 0.75. Ultimately, an acceptable process window was identified, with STs generated at laser power levels between 700 and 900 W, scan speeds between 600

and 700 mm/min, and Q_p set at 8.0 g/min, resulting in dilution values of 1.0 ± 0.25 . These parameters formed the basis for the second DoE, outlined in Table 6 under the "DoE #2" column.

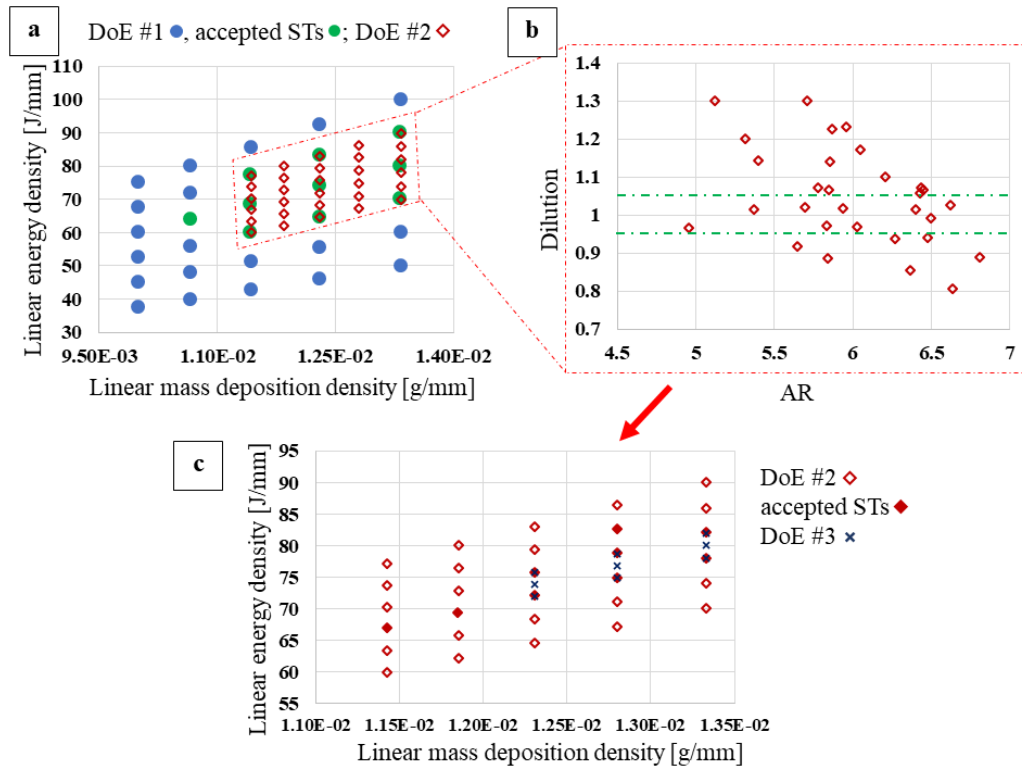


Figure 2.6 Diagrams showing: a) the linear energy density over linear mass deposition density for DoE #1 with marked in green STs in acceptable melt pool geometry from Fig. 2.5 and a process window for the DoE #2; b) results of cross-section analysis of STs from DoE #2 with green criteria lines at dilution values of 0.95 and 1.05 ; c) the linear energy density over linear mass deposition density for DoE #2 with accepted STs from Fig. 2.6 (b) marked with filled marker 2.5 and a process window for the DoE #3.

In Fig. 2.6 (a), the linear energy density and linear mass deposition density for each set of parameters from DoE #1 and DoE #2 are plotted. Additionally, the sets of parameters that had dilution values in the accepted range (Fig. 2.5) are marked in green, highlighting the decision to create a second process window within the values reported in Table 2.4. The results of DoE #2 are presented in Fig. 2.6 (b), showing the dilution over AR. The criteria for DoE #2 were selected to be a dilution of 1.0 ± 0.05 . Fig. 2.6 (c) illustrates where the accepted STs geometries fall, explaining the selection of the process parameters for DoE #3, which are reported in Table 2.4 under the "DoE #3" column. Additionally, OM micrographs of DoE #3 STs' cross-sections are shown in Fig. 2.7.

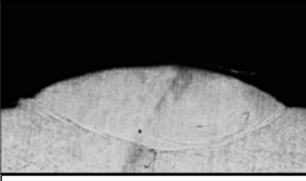
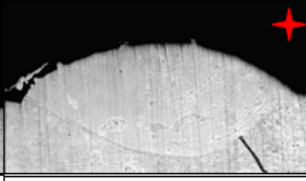
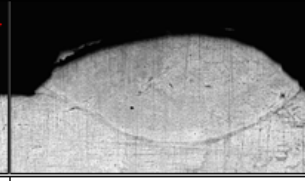
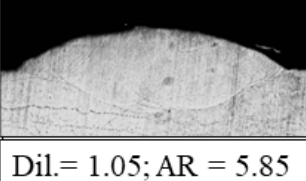
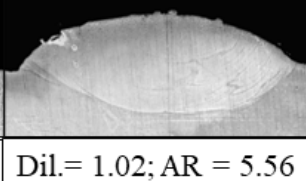
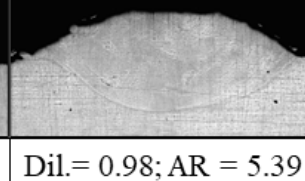
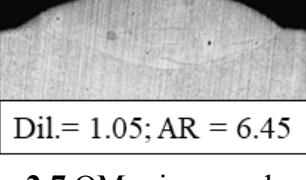
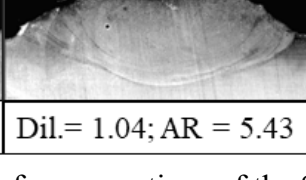
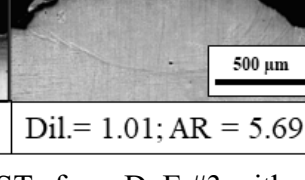
$Q_p = 8$ g/min		Power [W]			★ - selected set
		780	800	820	
Scan speed [mm/min]	600				
		Dil.= 1.02; AR = 5.94	Dil.= 1.00; AR= 5.32	Dil.= 0.96; AR = 5.85	
	625				
		Dil.= 1.05; AR = 5.85	Dil.= 1.02; AR = 5.56	Dil.= 0.98; AR = 5.39	
	650				
		Dil.= 1.05; AR = 6.45	Dil.= 1.04; AR = 5.43	Dil.= 1.01; AR = 5.69	

Figure 2.7 OM micrographs of cross-sections of the STs from DoE #3 with corresponding dilution and AR values reported under each micrograph.

All deposited STs from DoE #3 met the previously selected criteria, with dilution values ranging from 0.95 to 1.05. Given that all the samples exhibited favourable dilution values, a sample with the lowest AR value was chosen for the creation of single layers (SLs). This selection was made because it indicated the highest growth among the examined STs. The chosen set is marked with a red star in Fig. 2.7 and had a dilution of 1.00 and an AR of 5.32.

The parameters, including a P of 800 W, a v of 600 mm/min, and a Q_p of 8.0 g/min, were employed to fabricate single layers. These layers were deposited with a 40% overlap (Ov), resulting in a hatch distance (h_d) of 1.20 mm. This h_d was determined based on the measured single track (ST) width of the selected set, which was found to be 1.989 mm, rounded up to 2.00 mm, corresponding to the laser beam diameter (d_l) used. The layer thickness (Δz) resulting from these parameters was measured to be 0.503 ± 0.009 mm, rounded to 0.50 mm. All relevant process parameters utilized for creating the cubic samples are detailed in Table 2.5.

Table 2.5 Optimized process parameters used for building 316L cubes.

<i>Parameters</i>	<i>Values</i>
Power	800 W
Scan speed	600 mm/min
Powder feed	8 g/min
Laser spot diameter	2.00 mm
Overlap percentage	40%
Hatch distance	1.20 mm

Layer thickness	0.50 mm
Carrier gas flow rate (Ar)	5.0 L/min

A thorough evaluation of the obtained samples was performed, focusing on densification and defect presence through OM micrographs, as described in Appendix A.3 Step 3: Bulk Samples. The analysis revealed a porosity of 0.02%, indicating a remarkable relative density. Additionally, besides a few circular pores identified as gas porosity, no other defects such as voids or cracks were detected within the samples. Utilizing equation 2 (found in Appendix A.3), the specific volumetric energy density (E_v) utilized for producing these fully dense bulk samples with 316L powder was calculated at 133.3 J/mm^3 . These outcomes highlight the successful fabrication of high-quality, dense 316L stainless steel samples using the optimized L-DED parameters outlined in this study.

2.3 Microstructural analysis of samples by L-DED-P

After optimizing the parameters to achieve fully dense samples, cubic structures measuring $20 \times 20 \times 20 \text{ mm}^3$ were constructed on a 316L substrate measuring $120 \times 120 \times 8 \text{ mm}^3$. The cubes were separated from the substrate using a wire-electrical discharge machine (W-EDM). Subsequently, the samples underwent meticulous preparation for in-depth analysis, following the outlined procedure detailed in Appendix B.3.

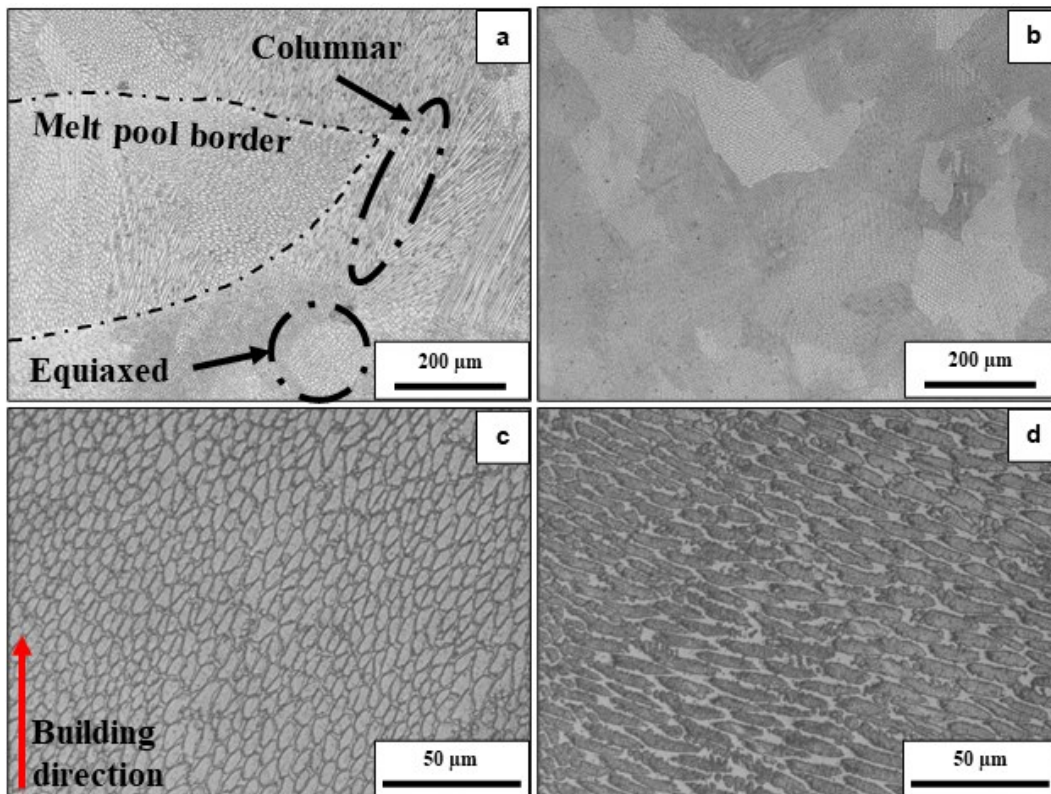


Figure 2.8 OM micrographs of 316L sample showing: a) melt pool boundary and grains with different types of dendritic structures, b) highlighted grains, c) equiaxed cellular structure, and d) cellular structure.

The OM micrograph depicted in Fig 2.8 (a) showcases the typical AM microstructure of 316L, characterized by interconnected melt pools and grains displaying a dendritic-cellular pattern, featuring both equiaxed and cellular dendrites. The melt pool borders are also clearly delineated in the micrograph. In Fig 2.8 (b), grains ranging in size from 200 to 400 μm are highlighted, consisting of a mix of equiaxed and columnar dendrites. Additionally, Fig. 2.8 (c) displays rounded cells, while Fig. 2.8 (d) exhibits slightly elongated cells. The cell sizes were measured in the middle of the samples by analysing 5 micrographs at a magnification of $\times 50$ using the ImageJ software, yielding measurements of $7.98 \pm 1.02 \mu\text{m}$. For further microstructural analysis, samples were examined using a SEM microscope (refer to Appendix B.3.1.2 for Electron Microscopy).

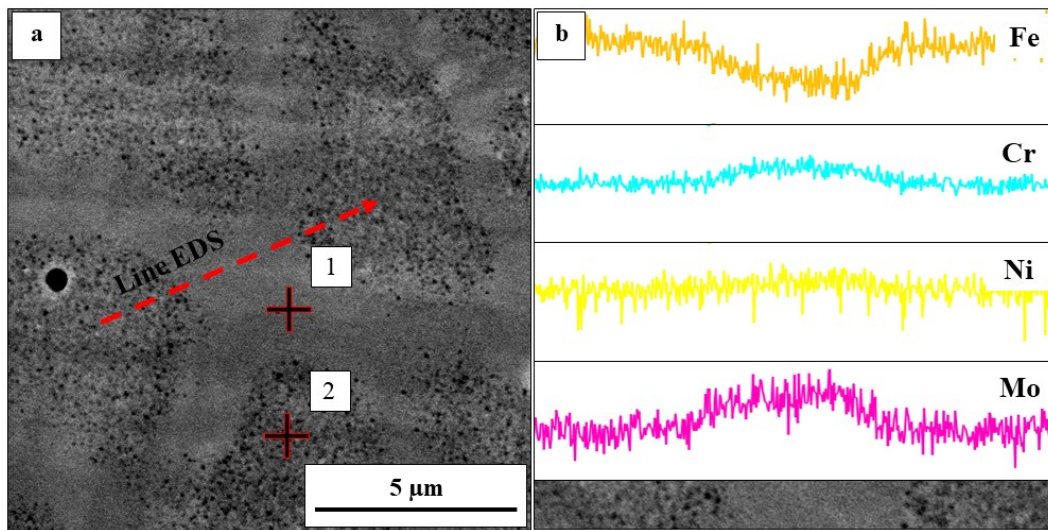


Figure 2.9 a) SEM micrograph of as-built 316L used for EDS line and point analysis, b) results of EDS line analysis.

Table 2.6 EDS point analysis results of cell boundary and cell with reported % wt. of main alloying elements.

Elements	1 – cell boundary	2 – cell
Fe	61.2	66.5
Cr	19.1	17.3
Ni	11.9	11.7
Mo	4.4	2.5
Mn	1.5	1.0
Si	1.0	0.6

The SEM micrograph (Fig. 2.9 (a)) taken in the central part of the sample of the equiaxed cellular structure reveals cells, cell boundaries (or intercellular regions), and a black spherical particle-shaped inclusion. A line EDS analysis was conducted to observe the micro-segregation of alloying elements, and the results presented in Fig. 2.9 (b) confirm this phenomenon. Notably, in the intercellular region, the concentration of Fe slightly decreases, while the concentrations of Cr

and Mo increase. Referring to the Schaeffler constitution diagram (Fig. 1.17) as a reference for the phases in 316L steel, the presence of austenite and ferrite phases is expected under moderate or fast cooling conditions [161]. Moreover, the formation of δ -ferrite is more likely due to the rapid cooling in AM processes [101], [104], [162]. Elements such as Cr, Mo, and Si stabilize δ -ferrite [162], [163], making the intercellular regions and cell boundaries highly susceptible to having a δ -ferrite microstructure. EDS point analysis was performed to quantify the elements in cells and cell boundaries, and the results are reported in Table 2.6. It is evident that Cr and Mo exhibit an increase of about 2% wt. in the cell boundary compared to the cell. Indeed, all alloying elements, except for Ni, exhibited an increase in concentration in the cell boundaries. This is consistent with the role of Ni as a promoter of the austenite phase; hence, it is not found in elevated amounts in ferritic cell boundaries.

Given the micro-segregation of alloying elements identified through EDS analysis, the formation of δ -ferrite in the intercellular areas was expected. To confirm this, XRD analysis was performed in the central part of the sample, and the results are presented in Fig. 2.10.

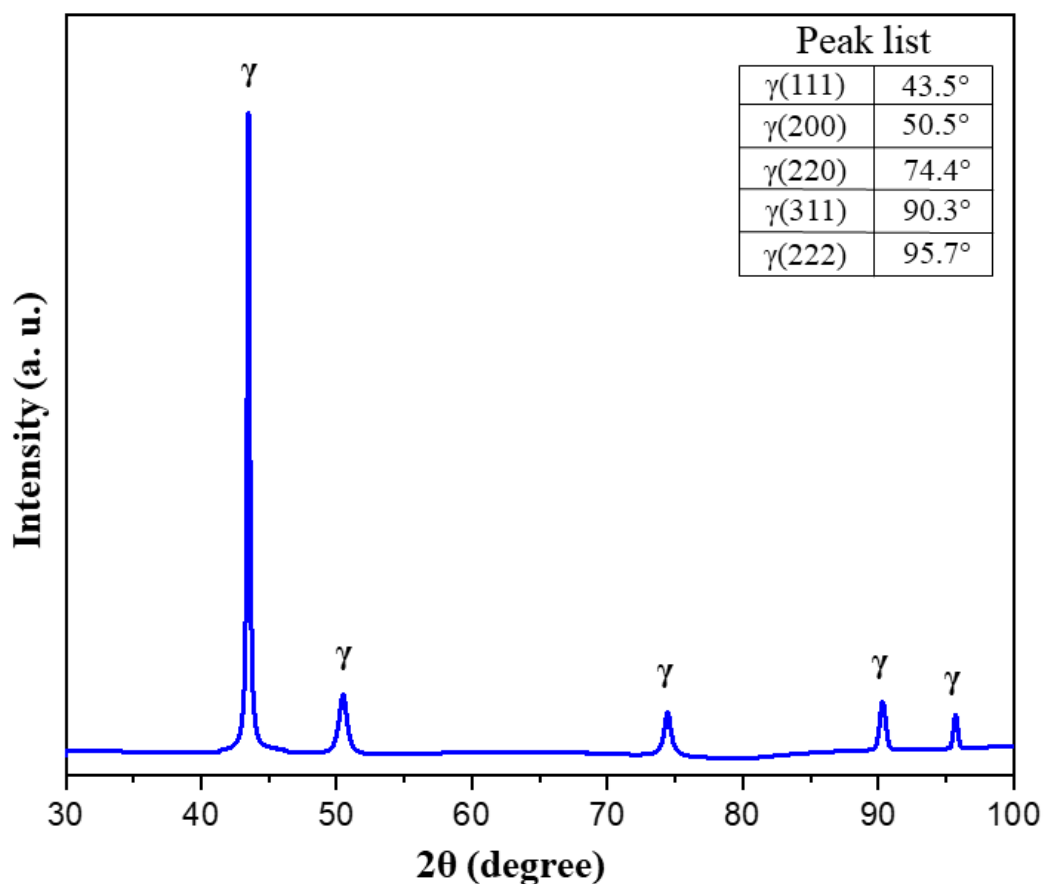


Figure 2.10 XRD pattern of an as-build L-DED 316L sample.

The peak values indicated in the upper-right corner of Fig. 2.10 correspond to the austenite- γ -ferrite system. δ -ferrite peaks were not detected probably due to its content lower than the XRD detection limit (4 % vol.). [4]

Additionally, spherical inclusions were discovered in the samples. Their chemical composition was examined using EDS point and line analysis (Fig. 2.11). The results of the EDS point analysis values for Fe, Cr, Ni, Mo, Mn, Si, and O, are outlined in Table 2.7. EDS line analysis results are plotted in Fig. 2.11 (b) for the most pertinent elements concerning inclusion analysis: Fe, Mn, Si, and O.

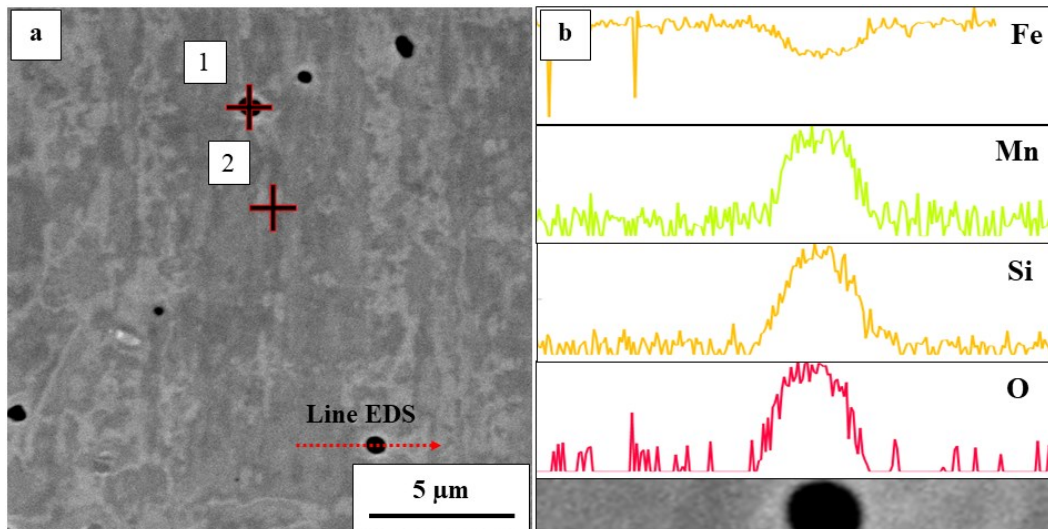


Figure 2.11 a) SEM micrograph used for EDX point analysis and b) EDS line analysis results.

Table 2.7 EDS point analysis results with reported % wt. of elements.

Elements	Point	Point
	1	2
Fe	37.8	64.6
Cr	12.7	17.3
Ni	5.5	11.6
Mo	1.7	2.7
Mn	11.8	1.3
Si	6.4	0.6
O	21.3	/

The EDS results reported in Table 2.7 clearly indicate that these inclusions are oxides, evidenced by the high O content. Moreover, the analysis revealed increased concentrations of Si and Mn at point 1. Thus, it can be concluded that these inclusions are Mn/Si oxides. Such oxides are common in steels with elevated Mn and Si content and were also previously reported in 316L samples produced via L-DED [160], [164]. This finding was further supported by EDS line analysis performed on another inclusion, clearly showing elevated concentrations of Mn, Si, and O in the inclusion zone (Fig 2.11 (b)). These observed inclusions were measured to be up to 1 µm in diameter. The presence of these inclusions is due to the nature of the L-DED process itself and due to the starting 316L powder that already had these oxide inclusions (Fig. 2.4). It should be underlined that the machine used for sample production, Laserdyne 430, did not allow to utilize shielding gas, thereby failing to create an atmosphere with reduced oxygen levels.

While the carrier gas reduces oxygen levels to some extent, it cannot completely shield the steel from oxidation.

Finally, the impact of these microstructural features on the material properties was evaluated through microhardness testing. Measurements were taken in three distinct zones from the substrate to the top of the samples, as indicated in Fig. 2.12 (a).

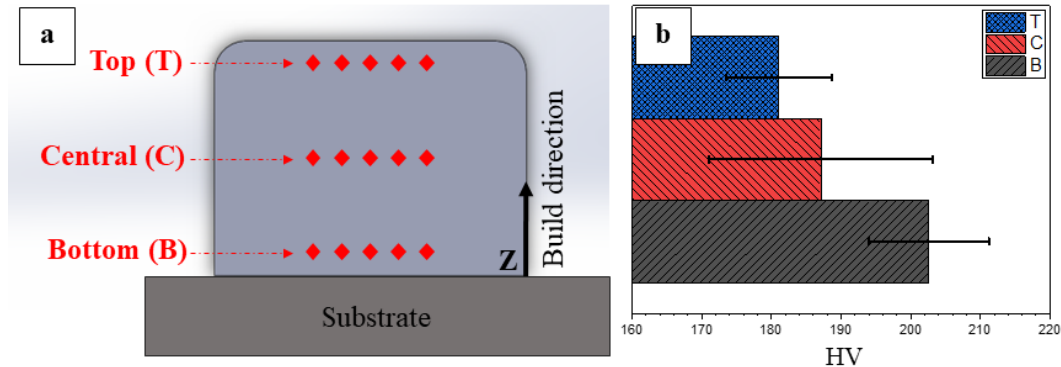


Figure 2.12 a) schematic representation of microhardness measurements with reported zones of sampling along building direction and b) microhardness mean results for each zone.

The microhardness results depicted in Fig. 2.12 (b) reveal a consistent decline in microhardness values with the height of the sample. This trend underscores the non-uniformity resulting from heat accumulation during the deposition process. Lower layers, experiencing higher cooling rates and therefore exhibit higher hardness values compared to the upper layers. Specifically, the bottom of the sample displayed a microhardness value of 203 HV, the central zone measured 187 HV, and the top layers registered 181 HV. The overall mean microhardness for the entire sample was 191 HV, which is 21 HV higher than cast 316L samples [120], [134]. While this demonstrates increased hardness compared to conventional technology, it falls within the lower range of reported hardness values for L-DED-built samples, ranging from 190 HV [103] to 265 HV [165].

2.4 L-DED-P deposition strategy – influence of heat accumulation

In this subsection, an exploration of various deposition strategies was undertaken to comprehend their impact on microstructural and mechanical properties. Samples measuring 20 x 20 x 20 mm³ were constructed on the 316L substrate with dimensions of 120 x 120 x 8 mm³ using the optimized parameters detailed in subsection 2.2 and reported in Table 2.5 and the build strategy schematically represented in Fig. 2.13. Subsequently, the samples were halved and prepared for microstructural disparities, and microhardness tests were conducted.

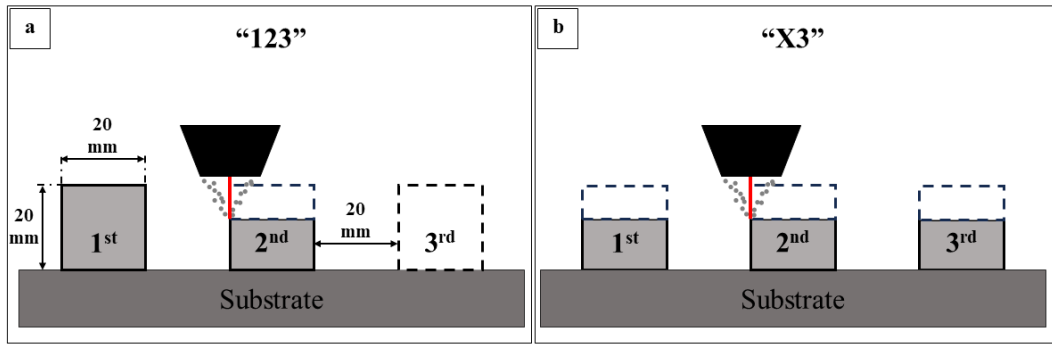


Figure 2.13 Schematic representation of deposition strategies investigated: a) strategy “123”, b) strategy “X3”.

In the "123" deposition strategy (Fig. 2.13 (a)), each sample is deposited one after the other. When the first sample is completed, the deposition of the second sample begins, followed by the third sample. In contrast, the "X3" strategy (Fig. 2.13 (b)) involves depositing all three samples simultaneously. In this approach, the first layer of the first sample is deposited, followed by the first layer of the second sample, and then the first layer of the third sample. This process continues layer by layer until all samples are completed.

Due to the sequential nature of the "123" strategy, differences in microstructure from the first to the last sample are expected to be more pronounced. The substrate starts at room temperature for the first sample and accumulates heat as the process continues. Consequently, the starting temperatures of the substrate for the second and third samples are higher, resulting in slower cooling rates. In contrast, the "X3" strategy minimizes differences between samples since they are deposited simultaneously. In this strategy, there is a larger interlayer cooling time (τ_{layer}) between the deposition of each layer. This time allows for heat to transfer to the substrate and atmosphere, leading to a lower temperature of the previously deposited layer compared to a scenario strategy “123”. Although the total time and input energy are the same for both strategies, the final substrate temperature should be similar for both cases.

After deposition, the samples were removed from the substrate using the W-EDM machine, leaving a 1 mm gap from the surface. Subsequently, the samples were halved along the X-Z plane, embedded in resin, and subjected to grinding and polishing using standard metallurgical procedures to obtain a mirror-like surface (refer to Appendix B.3.1). The polished samples were examined for porosity through OM micrographs, revealing a porosity measurement of over 99.95% for all samples. To unveil the microstructure, samples were etched by immersion using an acid mixture (refer to Appendix B.3.1.1).

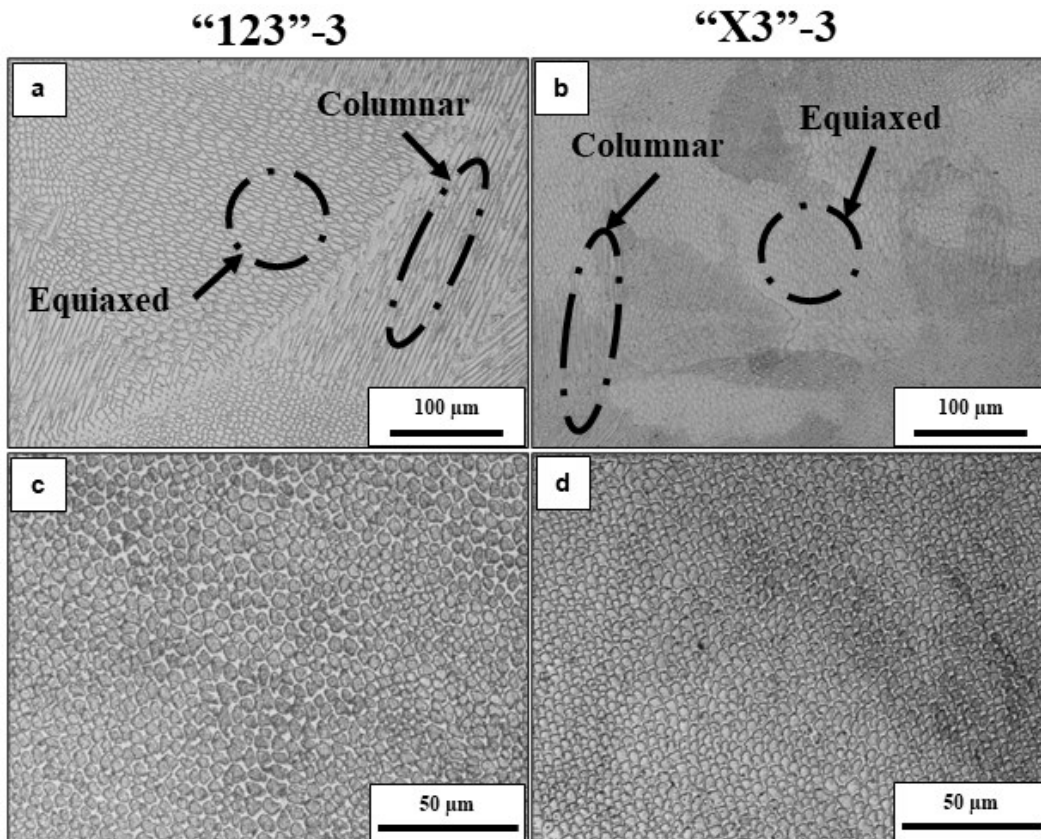


Figure 2.14 OM micrographs: a) of sample “123”-3 showing the grains with both equiaxed and columnar dendrites, b) of sample “X3” showing the grains with both equiaxed and columnar dendrites, c) at higher magnification showing the rounded shape cells for “123”-3 sample, and d) at higher magnification showing the rounded shape cells for “X3”-3 sample.

The OM micrographs presented in Fig. 2.14 reveal the microstructures of the third samples from each deposition strategy (“123” and “X3”) at different magnifications. In Fig. 2.14 (a) and (b), grains with dendritic-cellular microstructures are evident, comprising both equiaxed and columnar dendrites. Moving to Fig. 2.14 (c) and (d), it is apparent, even without precise measurements, that the “X3”-3 sample has smaller cell sizes. These observations align with the expected relationship between cooling rates and grain and cell sizes, as indicated in previous studies [103], [120], [160], [166]. The higher cooling rates anticipated in “X3” samples due to the interlayer cooling time result in smaller grain and cell sizes.

To quantify the primary cellular arm spacing (PCAS), the triangle method procedure was employed [103], [160]. In this method, distances between the centre points of any three neighbouring cells are measured and averaged, as illustrated in Fig. 2.15 (a). Five micrographs of the middle part of the samples (10 mm from the substrate) were taken at x50 magnification in a horizontal line. Thirty measurements per micrograph were conducted using the ImageJ software. The results are presented in Fig. 2.15 (b).

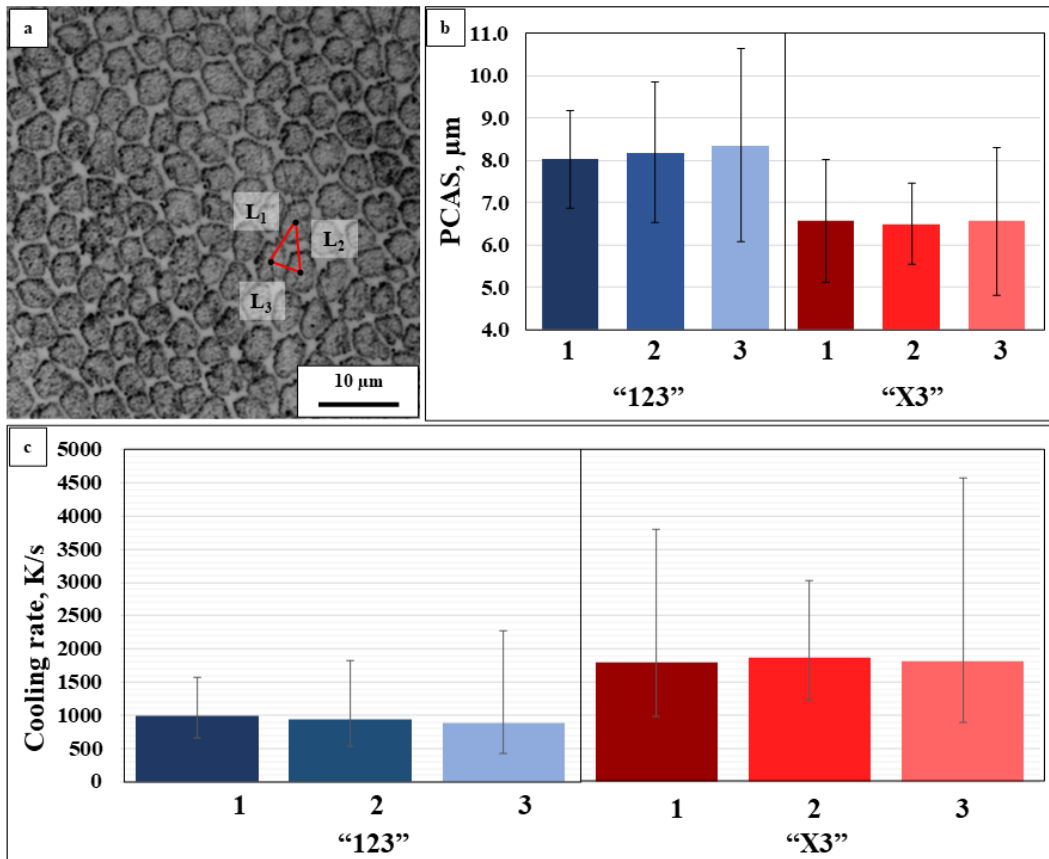


Figure 2.15 a) OM micrograph with an example of triangle method measurement, b) PCAS results plotted for each sample.

The results clearly demonstrate significant differences in the PCAS values between the two deposition strategies. The smaller PCAS values observed in the "X3" strategy can be attributed to the interlayer cooling time. Upon closer examination of the "123" strategy, it becomes evident that the mean PCAS values show a slight increase from the 1st to the 2nd and 3rd samples, measuring 8.03 μm, 8.19 μm, and 8.36 μm, respectively. Additionally, alongside the increase in mean values, the dispersion of the measured data also rises as the deposition progresses toward the last samples. In contrast, the mean PCAS values for the "X3" strategy remain within 0.1 μm, ranging from 6.50 μm for sample "X3"-2 to 6.58 μm for sample "X3"-1.

The primary factor influencing PCAS is widely acknowledged to be the cooling rate experienced during the solidification process of the alloy. Extensive experimental and theoretical investigations have explored the intricate relationship between cooling rate and PCAS [103], [160], [167], [168]. The significant relationship between these parameters is expressed in the equation:

$$(2) \quad dT/dt = (80/PCAS)^3$$

Here, dT/dt represents the cooling rate in K/s, and PCAS is in μm. Utilizing this equation, the average cooling rates were calculated and illustrated for each sample in Fig. 2.15 (c). Samples constructed using the "123" strategy were found

to have solidification cooling rates of approximately 1000 K/s. Conversely, samples built with the "X3" strategy were calculated to have experienced cooling rates of 1800 K/s. These results align with the theoretical expectations of cooling rates, indicating that "X3" samples undergo cooling rates approximately two times faster than those observed in the "123" samples.

Subsequently, XRD measurements were conducted on the samples to investigate whether different cooling rates lead to the formation of distinct phases.

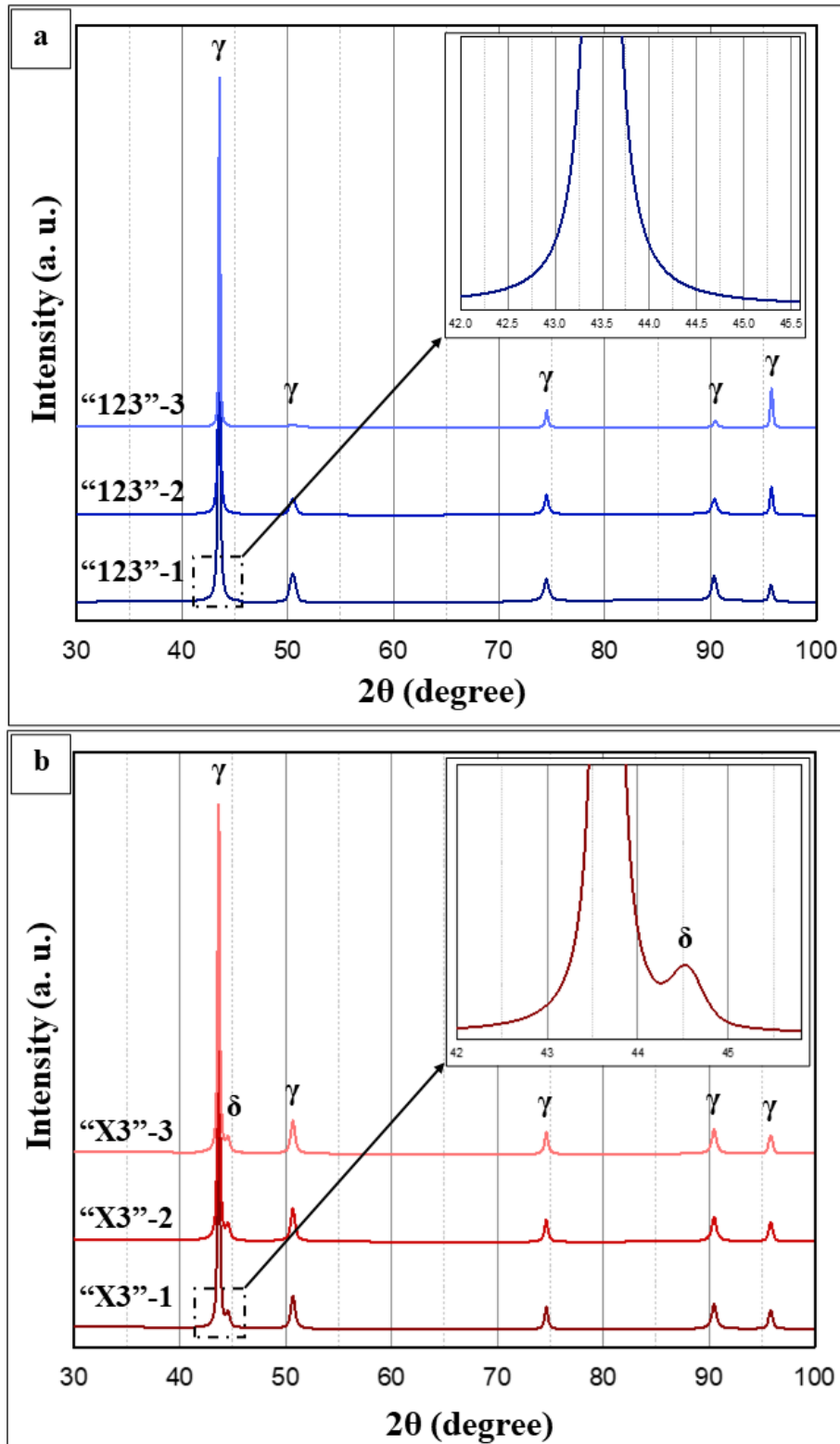


Figure 2.16 XRD patterns of: a) samples built with “123” deposition strategy, b) samples built with “X3” strategy.

The results of the XRD measurements on samples constructed using the "123" deposition strategy, presented in Fig. 2.16 (a), exclusively reveal the presence of the austenite phase with peaks observed at 43.5° , 50.5° , 70.4° , 90.3° , and 95.7° . While all three samples exhibit peaks at the same positions, the intensity of the peaks at 50.5° and 90.3° decreases progressively from the first to the last sample deposited. In contrast, the intensity of the peak at 95.7° increases as the deposition progresses. This phenomenon can be explained by the preferential orientation of the crystal structure. Higher thermal gradients tend to result in more evident crystallographic textures [169].

Fig. 2.16 (b) displays the XRD patterns of samples deposited with the "X3" strategy. In addition to austenite peaks, a δ -ferrite peak is visible, particularly in the magnified insert at the upper-right corner. Notably, all three samples from the "X3" strategy exhibit very similar patterns, indicating a higher degree of homogeneity in microstructure compared to the "123" strategy. The presence of δ -ferrite could be due to the higher cooling rate [101], [104], [162].

A direct comparison of the magnified inserts of "123"-1 and "X3"-1 clearly shows the absence of a δ -ferrite peak in "123"-1. However, this does not necessarily mean that δ -ferrite is absent; rather, it is likely present in less than 4% vol. rendering it undetectable with the utilized instrument.

Following the completion of the microstructural analysis, the mechanical response, in terms of microhardness, was assessed by making indentations at the bottom, central, and top parts of the sample, as indicated in Fig. 2.17 (a).

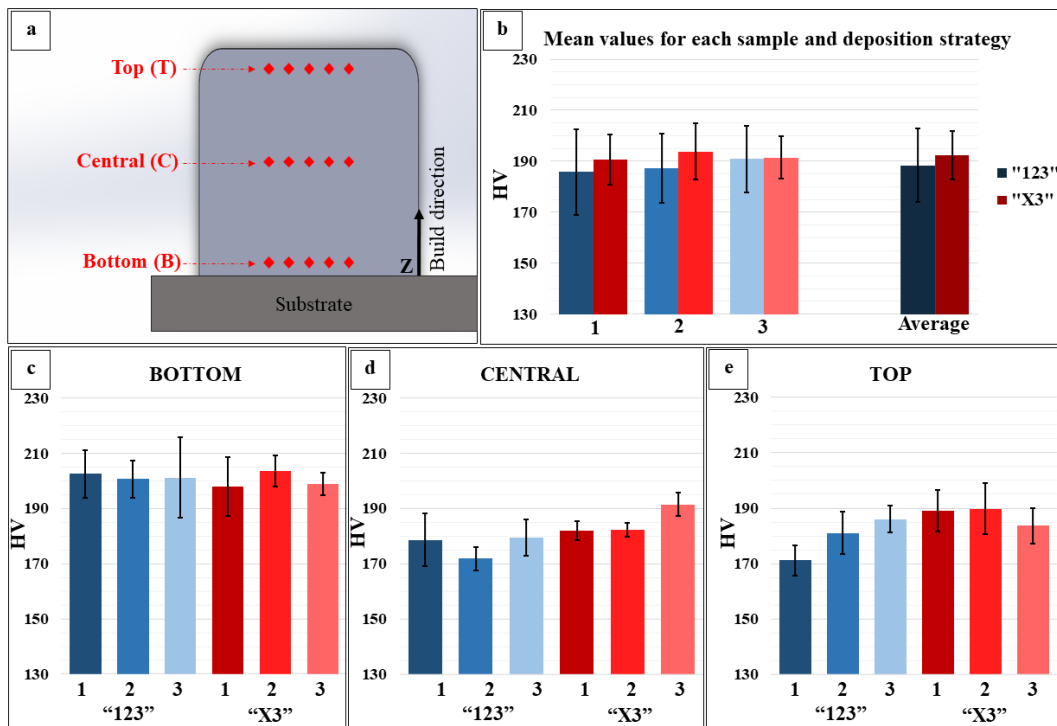


Figure 2.17 Microhardness: a) schematic representation of microhardness measurements, b) plotted results of mean values for each sample and for each deposition strategy average of all three samples (blue notes – “123”; red notes – “X3”), c) results of bottom zone for each sample, d) results of central zone for each sample, and e) results of top zone for each sample.

In Fig. 2.17 (b), the mean values of all indentations made on each sample are plotted, along with the mean values of all samples in each deposition strategy. As anticipated, the deposition strategy "X3" exhibited higher hardness values, averaging 192 HV, whereas the mean value for the "123" strategy was 188 HV. While the "X3" strategy has a higher mean value, the difference is not significant due to the standard deviation of 10 HV, compared to 14 HV for the "123" strategy. Analysing each zone individually (Fig. 2.17 (c), (d), and (e)), a certain trend observed in other studies becomes apparent. The bottom part displayed the highest microhardness values, followed by a drop in values in the central zone. Interestingly, at the top zone, the values slightly increased (except for samples "123"-1 and "X3"-3). This trend is attributed the higher cooling rates experienced by the first layers and by the IHT the material undergoes because of the subsequent layers. This IHT causes has an effect of stress relieving and a consequent reduction in hardness. However, the final layer deposited does not undergo this reheating process, resulting in higher hardness values [170], [171]. It is worth noting that microhardness measurements for samples "123"-1 and "X3"-3 were likely not performed in the last layers, explaining the absence of this effect in these samples. While certain trends and differences between deposition strategies are observable, the variations are not significant. For a more comprehensive assessment of the differences in mechanical properties, more detailed measurements should be conducted.

In summary, when analysing the different deposition orders for multiple samples on the same substrate to achieve uniform properties across all samples, two effective approaches can be employed. One method involves introducing cooling time between samples to ensure that the starting temperature of the substrate aligns with that of the first sample. Alternatively, the application of the "X3" deposition strategy proves to be an effective solution, as it results in uniform properties for all samples since they are deposited simultaneously. The deposition strategy must be designed considering these aspects, especially when building more complex components.

2.5 Factor screening for multiple responses in L-DED-P

In this subsection, a comprehensive investigation on 316L samples properties responses depending on different process parameters and starting conditions summarized in four factors and three covariates was conducted in collaboration with PhD student Adriano Nicola Pilagatti, Professor Eleonora Atzeni, and Professor Alessandro Salmi from the Department of Management and Production Engineering (DIGEP) at Politecnico di Torino.

In the present work a multi-responses factorial approach was used to optimise the L-DED-P process of AISI 316L using Fisher's factorial experiment method [172]. The initial step needed to optimize a new system involves factor screening i. e., the identification of process parameters and conditions that influence the system response, outputs [173]. This phase holds particular importance when exploring novel or inadequately studied systems or processes.

Up to now, numerous authors have studied the impact of various process parameters on the properties of DED-produced components, there has been a prevailing trend to concentrate on specific parameters, leading to a lack of comprehensive parameter screening and identification of boundary condition effects [174], [175], [176], [177], [178], [179], [180]. L-DED-P involves intricate interplays of various physical processes, like powder stream, melt pool, and track [181]. Within these macro processes two distinct sub-categories, demarcated by factors that can be controlled and those not controllable. Table 2.8 offers an overview of the parameters integral to the L-DED-P process.

Table 2.8 L-DED-P process parameters subdivision.

Manageable	Unmanageable
Laser power	Laser beam diameter & power distribution
Gas flow	Powder morphology and distribution
Powder mass flow rate	Powder & substrate material properties
Standoff	Substrate temperature & geometry
Travel speed	Boundary conditions
Toolpath	

In this study, the L-DED-P critical factors explored were specific energy density of laser pass (E_{pass}), the Z-increment of the deposition head (ΔZ), overlapping (Ov), and coefficient k . These factors are discussed in detail below.

The effects of the main process parameters P , v , and Q_p were explored. Given their interconnections, the first crucial parameter, E_{pass} , was investigated (eq. 3). E_{pass} , indicating the energy supplied in the laser spot (d_l) area, is system-independent and influences key aspects like porosity and microstructure. To ensure safe operation, the operating power was set at 80 % which was 800 W of the maximum 1000 W, and v was varied to achieve specific E levels. This strategic focus on E_{pass} provides a nuanced understanding of process outcomes, allowing for a detailed exploration of defects in the L-DED process.

$$(3) E_{pass} = P / (v \times d_l)$$

The second factor, ΔZ , represents the Z-increment of the deposition head for each new layer. To ensure the layer height approximates ΔZ , the powder feed rate (Q_p) must be optimized, particularly in the absence of a feedback control system. This precision is vital for accurate melt pool positioning [182].

The third process parameter under consideration is Ov , as shown in Fig. A.4. Ov is defined with the eq. 12 from Appendix A.2, where h_d represents the hatch distance, a distance between the centres of two consecutive tracks and W represents

the width of the track that is estimated to be d_l [183]. Unlike the hatching distance, the authors favour O_v due to its independence from specific machine characteristics. Instead, it is determined by the nominal diameter of the laser and width of the track deposited, making it an intuitive and universally applicable parameter. O_v , often overlooked, has significant implications for E_{pass} , layer geometry, and the influence of Q_p on the resulting layer height.

The fourth and final process parameter under consideration in this study is the coefficient k , a dimensionless parameter introduced to account for surplus powder that does not contribute to the generation of the track. This parameter captures deviations from the ideal scenario of no powder loss.

In Table 2.9 are summarized the investigated factors and their respective levels.

Table 2.9 Investigated factors and their levels.

	Low level	High level
E [J/mm²]	46	60
ΔZ [mm]	0.4	0.6
O_v	0	50
K	1.25	1.4

Uncontrollable parameters primarily pertain to the inherent attributes of the existing L-DED-P system, including the head configuration, as well as the properties of the commercial powder employed. Even though these conditions might be beyond direct control, they are still measurable. To capture these vital conditions, a specially designed system equipped with sensors and data acquisition tools was employed in this study. During the deposition process, this system collects data on the substrate and air temperatures and its absolute humidity inside the construction chamber.

In our experimental setup, detailed in Table 2.9, we adopted a 2^4 full factorial design, resulting in 16 samples and three replications, totalling 48 samples. Our choice of response variables was guided by their significant impact on the performance and quality of components produced through L-DED-P. Quality, in this context, refers to meeting specific criteria, such as high density and mechanical properties comparable to those of the same material processed by conventional processes [184]. The focus was on four key response variables: height, porosity, density, and hardness,

The selection of the specimen height among various geometric features holds several justifications. Firstly, it serves as a direct indicator of the accuracy of the deposition process, a pivotal factor in the L-DED-P system utilized in this study, especially due to the absence of a feedback positioning system. Therefore, if the precise height is not achieved, extra material is needed. The effects of under and overgrowing related to the Δz are shown in Fig. 1.5. The height was measured directly on the platform using the EquatorTM 300 precision gauging system by Renishaw (Wotton-under-Edge, UK).

In addition to ensuring geometric accuracy, we carefully considered other response variables related to the bulk properties of the component. These properties

play a crucial role in determining the integrity and performance of the part. Any defects or irregularities in these properties would significantly impact the final product quality. Tan and Pang [177] proposed the selected response variables related to bulk properties, including porosity, density, and microhardness.

Porosity serves as a pivotal parameter, offering insights into process issues such as lack of fusion, delamination, and other defects. For example, lack of fusion and delamination result in voids within the material, leading to high porosity values. For porosity evaluation, 25 random optical micrographs were captured each specimen utilizing the DMI 5000 M optical microscope by Leica (Wetzlar, GER) with a 100x magnification factor at the cross-section of the sample. Subsequent analysis was conducted using ImageJ software.

Density is another vital parameter that holds both qualitative and quantitative significance. Together with porosity, it provides valuable information about the effectiveness of the process parameters and the phase formed in the solidified sample. Pycnometer Ultrapyc 5000 by Anton Paar was utilized to measure density.

Finally, microhardness was chosen as a response variable due to its connection with the thermal history of the process, the morphology of the microstructure, and mechanical properties. Changes in microhardness can indicate alterations in these underlying factors, making it a reliable indicator of the overall quality and performance of the part. Consequently, microhardness analysis provides valuable insights into the effectiveness and consistency of the process. For measuring microhardness the DHV-1000 digital micro-Vickers instrument by JVS (Licheng District, Jinan, China). For each sample, five measurements were made at the bottom (2 mm from the substrate) and the top (12 mm from the substrate), using a load of 0.5 kgf and a dwell time of 15 s.

Table 2.10 displays the experimental data organized into columns including Run Order (#) and factors used E_{pass} , ΔZ , Ov , and k . Additionally, the table includes data for height, density, porosity, hardness. This structured presentation of data enables a comprehensive analysis of the experimental results. The obtained results are categorized into four sections: height, density, porosity, and hardness assessments. This comprehensive experimental design allowed for a systematic exploration of the chosen factors and their impact on the various response variables.

Table 2.10 Experimental data used for ANCOVA method.

#	E	ΔZ	Ov	k	Height	Density	Porosity	Hardness
	J/mm ²	mm	%		[%]	g/cm ³	%	HV
1	46	0.4	0	1.4	101.16	7.928	1.032	166
2	60	0.6	0	1.4	99.16	7.926	0.051	165
3	60	0.6	0	1.4	101.25	7.933	0.084	167
4	46	0.6	50	1.25	98.63	7.936	0.033	169
5	60	0.4	50	1.25	103.92	7.939	0.017	166
6	46	0.6	50	1.25	97.79	7.916	0.021	167
7	46	0.4	0	1.4	99.78	7.909	1.305	170
8	46	0.4	0	1.4	101.68	7.924	0.05	172
9	60	0.6	0	1.4	98.28	7.926	0.009	166

10	60	0.4	50	1.25	105.28	7.934	0.069	161
11	46	0.6	50	1.25	99.35	7.928	0.329	170
12	60	0.4	50	1.25	106.03	7.936	0.024	160
13	46	0.4	50	1.4	104.08	7.949	0.016	165
14	60	0.4	0	1.25	100.13	7.922	1.116	167
15	46	0.4	50	1.4	103.81	7.941	0.025	164
16	46	0.4	50	1.4	105.56	7.939	0.016	167
17	60	0.6	50	1.4	102.21	7.929	0.021	168
18	60	0.4	0	1.25	101.78	7.919	0.767	164
19	60	0.6	50	1.4	102.58	7.930	0.045	171
20	46	0.6	0	1.25	99.14	7.914	0.195	172
21	46	0.6	0	1.25	98.28	7.925	0.036	169
22	46	0.6	0	1.25	97.92	7.930	0.028	168
23	60	0.6	50	1.4	102.57	7.923	0.01	162
24	60	0.4	0	1.25	103.03	7.912	0.015	166
25	60	0.6	50	1.25	100.2	7.916	0.032	164
26	60	0.6	50	1.25	100.19	7.915	0.012	159
27	60	0.4	0	1.4	103.79	7.924	0.053	168
28	46	0.6	0	1.4	98.88	7.917	0.064	170
29	46	0.4	50	1.25	105.89	7.895	0.016	167
30	46	0.4	50	1.25	106.4	7.882	0.011	161
31	46	0.6	0	1.4	97.88	7.895	0.062	167
32	46	0.6	0	1.4	98.34	7.913	0.018	168
33	46	0.4	50	1.25	105.61	7.897	0.034	164
34	60	0.4	0	1.4	105.65	7.883	1.67	170
35	60	0.4	0	1.4	102.01	7.907	0.037	163
36	60	0.6	50	1.25	101.39	7.902	0.045	163
37	46	0.6	50	1.4	98.59	7.890	0.014	161
38	60	0.6	0	1.25	95.44	7.960	0.012	163
39	60	0.4	50	1.4	105.74	7.957	0.681	169
40	60	0.6	0	1.25	96.5	7.946	0.024	162
41	46	0.6	50	1.4	100.52	7.961	0.02	165
42	46	0.6	50	1.4	100.6	7.965	0.147	170
43	46	0.4	0	1.25	99.6	7.958	0.021	169
44	60	0.4	50	1.4	106.33	7.963	0.18	169
45	46	0.4	0	1.25	101.94	7.950	0.018	168
46	15.69	0.6	0	1.25	96.8	7.951	0.066	168
47	7.15	0.4	0	1.25	101.58	7.958	0.051	168
48	5.45	0.4	50	1.4	103.9	7.947	0.463	166

ANCOVA is a powerful statistical tool employed in this study that enables the identification of factors and noise sources influencing each response variable and suggested strategies to mitigate their effects. This method involves comparing data sets comprising two variables and subsequently generating an ANCOVA model or general linear model. This model incorporates nominal and/or ordinal variables as

independent factors, leading to the creation of prediction equations for different levels of a categorical variable. Within ANCOVA, continuous independent variables are referred to as covariates, while categorical independent variables are termed factors. By employing ANCOVA, the study could discern the impact of various parameters and effectively counteract their effects on the responses under investigation.

2.5.1 Height assessment

The height ANCOVA results are presented in Table 2.11, which displays statistical data such as degrees of freedom (df), contributions to the height trend, adjusted mean squares (adj MS), F-values, and p-values. In the creation of the model for predicting the height response, factors, linear or 2-way interactions, and covariates are considered if the p-value is less than 5%. These height assessment results are summarized, and the relationships between the height response and factors are illustrated in Fig. 2.18.

Table 2.11 ANCOVA results for Height assessment.

<i>Source</i>	<i>df</i>	<i>Contribution/%</i>	<i>Adj MS</i>	<i>F-value</i>	<i>p-value/%</i>
<i>Model</i>	14	91.24	26.815	24.56	<0.1
<i>Covariates</i>	2	4.32	2.204	2.02	14.9
<i>T_A</i>	1	2.05	4.044	3.70	6.3
<i>H_A</i>	1	2.27	0.990	0.91	34.8
<i>Linear</i>	4	74.43	76.196	69.79	<0.1
<i>E_{pass}</i>	1	1.61	8.211	7.52	1.0
<i>K</i>	1	2.47	12.820	11.74	0.2
<i>O_v</i>	1	25.85	95.684	87.64	<0.1
<i>ΔZ</i>	1	44.49	185.106	169.54	<0.1
<i>2-Way Interaction</i>	5	3.96	3.259	2.99	2.5
<i>E_{pass} · k</i>	1	1.64	6.859	6.28	1.7
<i>E_{pass} · O_v</i>	1	0.05	0.196	0.18	67.4
<i>E_{pass} · ΔZ</i>	1	0.12	0.416	0.38	54.1
<i>k · ΔZ</i>	1	1.15	4.660	4.27	4.7

<i>Ov · ΔZ</i>	1	1.01	4.162	3.81	5.9
<i>Error</i>	33	8.76	1.092		
<i>Total</i>	47	100			

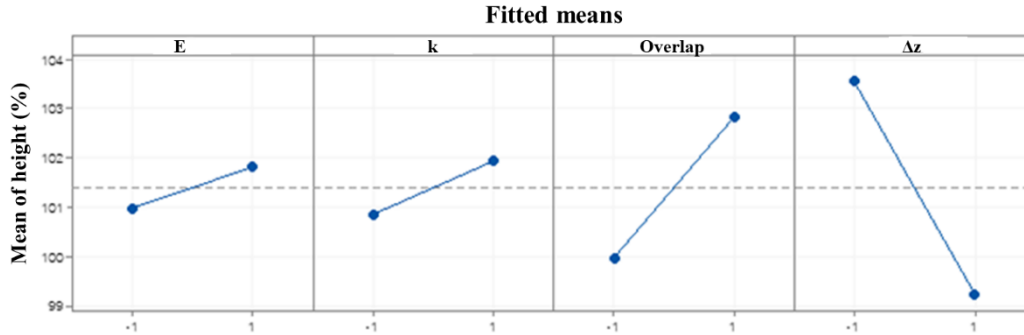


Figure 2.18 Effects of factors on the height response.

Upon careful examination, it was determined that no covariate significantly influenced the response within the studied ranges, with T_A and H_A having p-values of 6.3 and 34.8%, respectively. Additionally, Blocks were found to be statistically insignificant, showing a p-value of 19.3%. Roughly 74% of the data variability could be attributed to the main effects. ΔZ emerged as the most significant factor, explaining about 44.5% of the variability. This indicates a direct influence of the Z-axis increment on Height and layer thickness, where higher ΔZ values result in a noticeable decrease in Height. This deduction aligns with previous hypotheses and interpretations, as demonstrated in the factorial plots (Fig. 2.18 (d)). It underscores the importance of accurate layer thickness information, inputted as ΔZ in the toolpath, as elaborated in detail in section 1.1.2 (Laser Directed Energy Deposition) and schematically depicted in Fig 1.5.

The second most influential main effect is Ov , accounting for approximately 25.8% of the data variance. A significant impact of Ov on the response is evident; an increase in response is noticeable when specimens are fabricated with an Ov of 50%, indicating construction over double the laser scanning passes, as depicted in Fig. 2.18 (c). This observation is in line with the expected relationship between height response and Ov , confirmed by the model.

k is another significant contributor, indicating that supplying more powder to the melt pool at elevated levels leads to an increase in height (Fig. 2.18 (b)). This relationship between powder supply and height can be explained by the increased deposited layer thickness resulting from more powder being captured in the melt pool.

The least significant factor is E_{pass} , indicating that as the specific energy supplied to the melt pool intensifies, there is a proportional increase in the average Height of specimens. This could be due to an enhanced capacity to melt and incorporate more powder (Fig. 2.18 (a)). In this context, higher E_{pass} values imply reduced v , resulting in increased time required for layer deposition. Consequently,

with the same powder feed rate, a higher quantity of powder will be captured, leading to increased layer thickness and Height overall.

Noteworthy two-way interactions, highlighted in Fig. 2.19, include $E_{pass} \cdot k$ and $E_{pass} \cdot \Delta Z$. Regarding the E_{pass} and k interaction, it is observed that elevated values of both parameters lead to an increased response, affirming the notion that higher E_{pass} can effectively melt a larger quantity of powder. In the case of the $E_{pass} \cdot \Delta Z$ interaction, an increase in ΔZ (indicative of fewer layers) results in a decrease in height, but this response is amplified for higher values of E_{pass} .

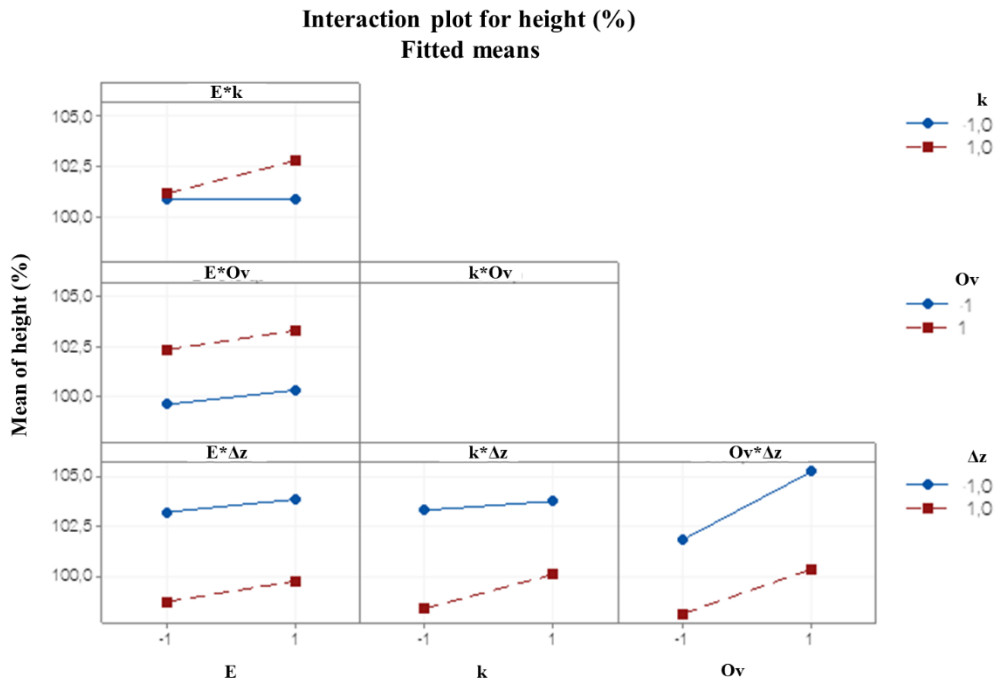


Figure 2.19 Two-way interaction plots for height response.

After identifying the active factors through ANCOVA, they were utilized to develop a simplified model using standard stepwise regression. This process led to the following equations for the two levels of Ov in coded units:

$$(4) \text{ Height/\%} = 100.000 + 0.440 \times E_{pass} + 0.448 \times k - 1.844 \times \Delta Z + 0.501 \times E_{pass} \times k + 0.352 \times k \times \Delta Z \quad (Ov = 0\%)$$

$$(5) \text{ Height/\%} = 102.799 + 0.440 \times E_{pass} + 0.448 \times k - 2.414 \times \Delta Z + 0.501 \times E_{pass} \times k + 0.352 \times k \times \Delta Z \quad (Ov = 50\%)$$

The comprehensive model assessment, featuring an S value of 1.1, an $R^2(\text{adj})$ of 87.3%, and an $R^2(\text{pred})$ of 83.2%, underlines the robustness and precision of the developed model. The scrutiny of residuals corroborates these findings, revealing no notable anomalies or indications of lack-of-fit (LOF), further affirming the model's reliability. Examining the coded equations averaged across blocks, a clear pattern emerges: the samples constructed with 50% of Ov consistently exhibit higher values than those without overlapping ($Ov = 0\%$). However, the response trend remains consistent for both construction strategies.

2.5.2 Density assessment

The ANCOVA analysis focusing on specimen density is detailed in Table 2.12, providing essential statistical insights such as df, contributions to the density trend, adj MS, F-values, and p-values. The developed model for predicting density exhibited an S value of 0.01, an $R^2(\text{adj})$ of 55.04%, and an $R^2(\text{pred})$ of 23.37%.

Table 2.12 ANCOVA results for density assessment.

<i>Source</i>	<i>df</i>	<i>Contribution/%</i>	<i>Adj MS</i>	<i>F-value</i>	<i>p-value/%</i>
<i>Model</i>	14	68.43	0.001066	5.11	<0.1
<i>Covariates</i>	2	53.20	0.000382	1.83	17.6
<i>T_A</i>	1	3.89	0.000012	0.06	81.0
<i>H_A</i>	1	49.32	0.000759	3.64	6.5
<i>Blocks</i>	3	11.22	0.000756	3.62	2.3
<i>Linear</i>	4	1.29	0.000067	0.32	86.2
<i>E_{pass}</i>	1	0.55	0.000114	0.55	46.4
<i>K</i>	1	0.00	0.000001	0.00	95.0
<i>O_v</i>	1	0.43	0.000096	0.46	50.2
<i>ΔZ</i>	1	0.31	0.000053	0.25	61.7
<i>2-Way Interaction</i>	5	2.71	0.000118	0.57	72.4
<i>E_{pass} · k</i>	1	0.10	0.000018	0.08	77.3
<i>E_{pass} · O_v</i>	1	1.11	0.000232	1.11	29.9
<i>E_{pass} · ΔZ</i>	1	0.00	0.000002	0.01	92.3
<i>k · ΔZ</i>	1	0.67	0.000149	0.71	40.4
<i>O_v · ΔZ</i>	1	0.83	0.000181	0.87	35.8
<i>Error</i>	33	31.57	0.000209		
<i>Total</i>	47	100			

In analysing the ANCOVA results related to density, a notable finding emerged: the significant influence of blocks on systematic effects, marked by a p-

value of 2.3 %. Despite being at an early screening phase, this observation has prompted several hypotheses about its origins. This influence could arise from complex high-order interactions within the blocks or inherent disparities among substrates. Additionally, variations might be attributed to the fabrication of each block on different platforms and days. Despite the data normal distribution, confirmed by the Anderson-Darling test (ADT), a plausible explanation surfaces: the observed density variability might be a manifestation of inherent process variability. This notion suggests that within the defined process parameter window and under the specified evaluation system, all specimens exhibit uniform density, enhancing the credibility of the developed equation system linking construction parameters and the powder transport mechanism.

Upon scrutinizing the density values, the recorded value stands at 7.927 ± 0.006 g/cm^3 . A comparison with the density of the virgin powder through a one-sample t-test, where the null hypothesis posits that the powder density is lower than that of the specimen, results in the rejection of the hypothesis with a p-value lower than 0.01 %. This implies that the porosity inherent in the powder could be mitigated during the fabrication process (Fig 2.20).

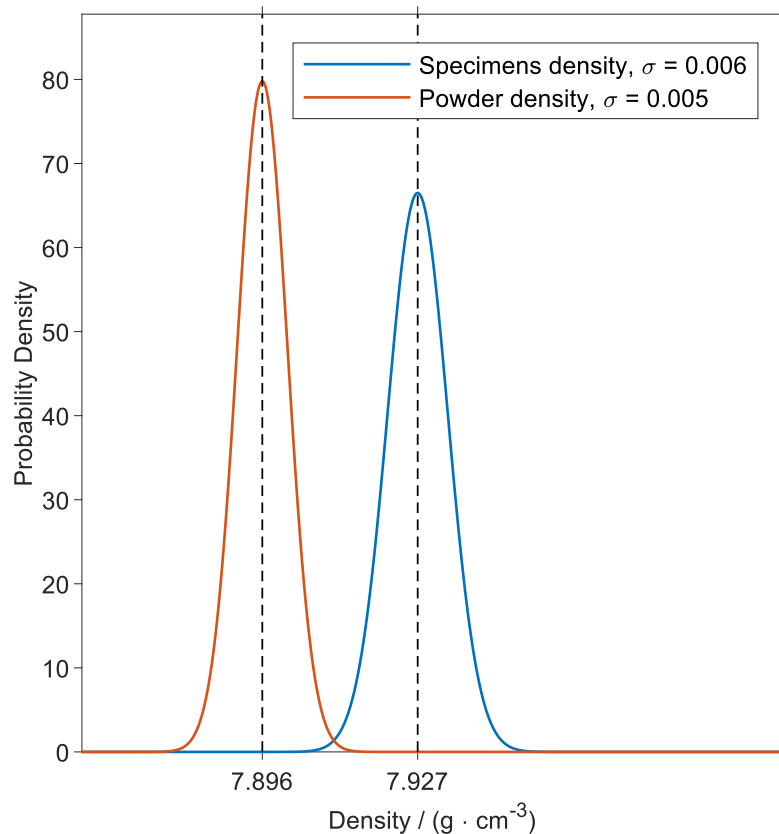


Figure 2.20 Powder and built samples density comparison.

Further reinforcing this conclusion, several crucial observations were made regarding the set of 48 specimens. Notably, there are no data outliers that could potentially skew the findings. Moreover, the null hypothesis addressing the non-normality of specimen density is not rejected, emphasizing the consistency in the sample's density. Given the ample sample size, the data aptly captures deviations

from the mean density of the powder. Such converging evidence solidifies the earlier conclusions.

2.5.3 Porosity assessment

The porosity data exhibits a distribution that deviates from the expected normality, as evident in Fig. 2.21.

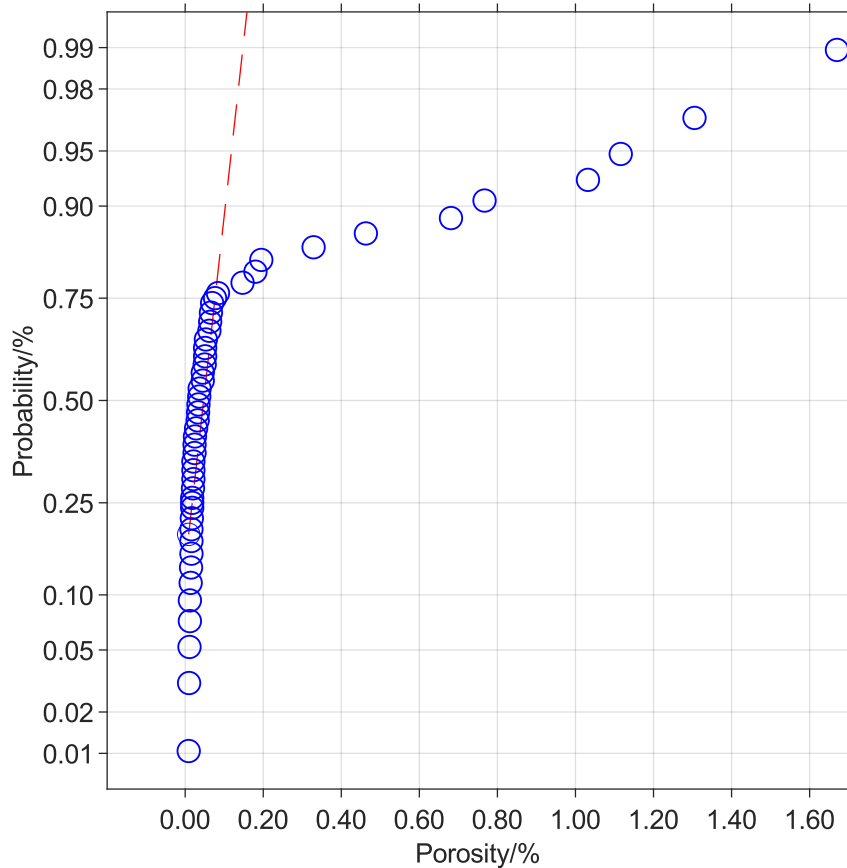


Figure 2.21 Normal probability plot for the porosity.

While there are two distinct clusters within the Normal Probability Plot (NPP), they haven't been classified as outliers. The absence of this classification is primarily due to a secondary cluster encompassing nine to eleven values, representing approximately 19% to 23% of the total observations. This grouping lacks association with any specific factor or level, demanding a unique analytical approach. To address this, the Box-Cox transformation method was applied to achieve a normal distribution, crucial for effective utilization of ANCOVA [66]. This technique rectifies non-normal datasets with positive values, making it well-suited for the current scenario where Porosity inherently assumes values greater than 0.

The ANCOVA conducted on the transformed data (Table 2.12) resulted in a non-significant p-value for the model (10.6 %). In the realms of ANCOVA, such a p-value challenges the postulated hypotheses. Essentially, the null hypothesis posits an absence of notable disparities between the groups under comparison. This result

could arise from an effect size that is too subtle for our sample size to discern or from limitations in the current measurement system. Considering these implications, a more sophisticated measurement approach, such as computed tomography (CT) scans, might provide detailed insights into porosity. One inherent limitation of the current method is its examination of a single cross-section, while the material potentially has infinite sections. The porosity of a given section could be influenced by its unique positioning within the whole, further emphasizing the need for a more nuanced measurement approach.

Table 2.13 ANCOVA results for Porosity assessment.

<i>Source</i>	<i>df</i>	<i>Contribution/%</i>	<i>Adj MS</i>	<i>F-value</i>	<i>p-value/%</i>
<i>Model</i>	14	41.77	10.2730	1.69	10.6
<i>Covariates</i>	2	1.61	9.9687	1.64	20.9
<i>T_A</i>	1	1.03	0.0318	0.01	94.3
<i>H_A</i>	1	0.58	18.7867	3.09	8.8
<i>Blocks</i>	3	9.23	8.1899	1.35	27.6
<i>Linear</i>	4	7.46	5.5396	0.91	46.9
<i>E_{pass}</i>	1	0.22	1.0419	0.17	68.1
<i>K</i>	1	2.07	4.2648	0.70	40.8
<i>Ov</i>	1	3.92	14.5590	2.40	13.1
<i>ΔZ</i>	1	1.25	2.7808	0.46	50.3
<i>2-Way Interaction</i>	5	23.47	16.1660	2.66	4.0
<i>E_{pass} · k</i>	1	0.00	0.3733	0.06	80.6
<i>E_{pass} · Ov</i>	1	1.41	5.9657	0.98	32.9
<i>E_{pass} · ΔZ</i>	1	14.19	46.9858	7.73	0.9
<i>k · ΔZ</i>	1	5.84	19.9594	3.28	7.9
<i>Ov · ΔZ</i>	1	2.03	6.9987	1.15	29.1
<i>Error</i>	33	58.23	6.0763		
<i>Total</i>	47	100			

To substantiate these claims, a correlation analysis was conducted. The underlying hypothesis suggested that an increase in porosity would lead to a decrease in density, implying a negative correlation coefficient ($r = -1$). However, the overall scatterplot in Fig. 2.22 does not reveal a trend indicative of this negative correlation. Instead, there is a conspicuous clustering of data points at lower porosity levels, challenging the expected relationship between porosity and density.

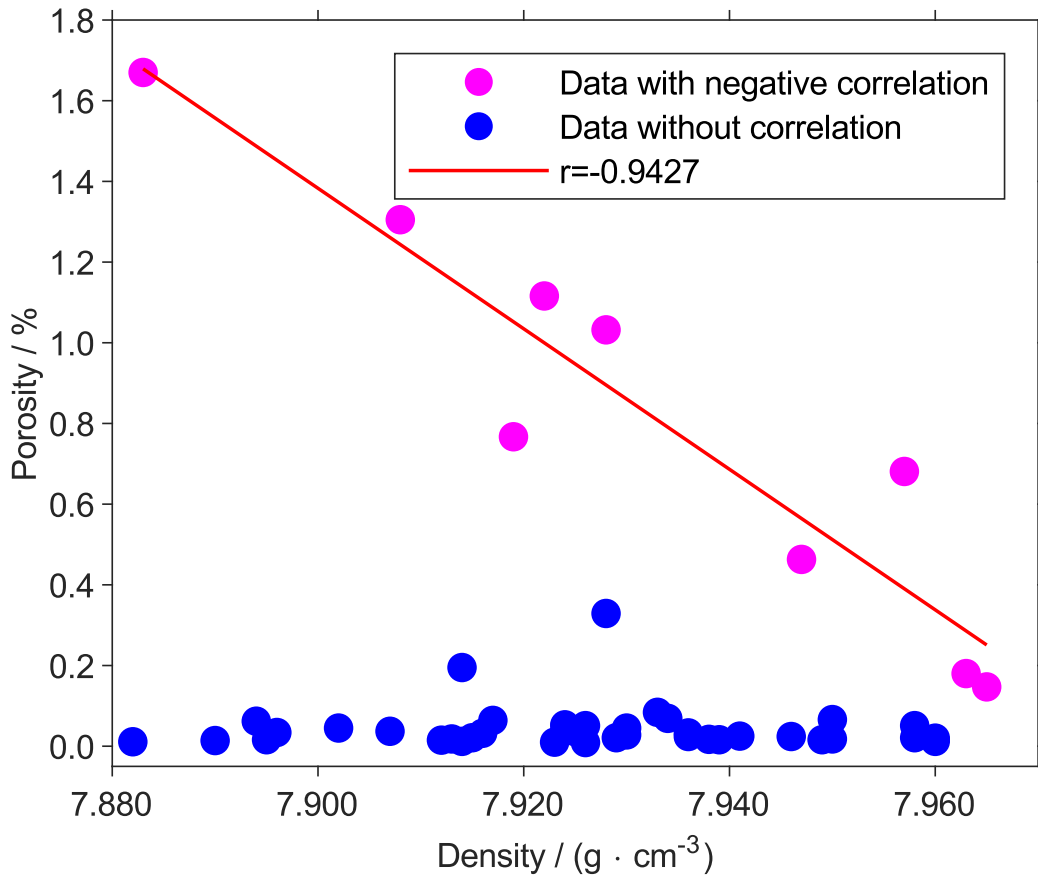


Figure 2.22 Matrix plot of the porosity against density

Upon performing the Pearson pairwise correlation test between density and porosity, a p-value of 19.2 % was obtained. Consequently, the hypothesis proposing a negative correlation between these two variables cannot be accepted. This outcome contradicts fundamental principles of physics and challenges prior assumptions. Notably, only 9 out of 48 specimens exhibited the anticipated negative trend. Hence, there is a pressing need for further investigations to delve deeper into these observations.

Expanding on this observation, when isolating and re-executing the correlation test on the subset of these 9 data points (coloured in pink in Fig. 2.22), an r-value of -0.94 is derived. This crucial result underscores that analysing porosity in a single section using an optical microscope may not adequately represent the comprehensive porosity of the entire specimen, especially for with near to full dense samples. Further research is necessary to comprehensively understand these complexities.

2.5.4 Hardness assessment

The data analysis presented in Table 2.14 confirms the significance of the model. Both covariates and blocks show no notable impact on the response. Examination of the residuals reveals a normal distribution without discernible patterns. The regression analysis delivers an S value of 2.7 and an $R^2(\text{adj})$ value of 30 %, indicating that the proposed model accounts for 30 % of the observed variance in the dependent variable. Nevertheless, a substantial 70 % of the variance remains unexplained, possibly due to methodological inaccuracies, the inherent variability of the investigated phenomena, or factors yet to be considered. Recognizing these aspects is imperative for framing the larger implications of the study.

Table 2.14 ANCOVA results for Hardness assessment.

<i>Source</i>	<i>df</i>	<i>Contribution/%</i>	<i>Adj MS</i>	<i>F-value</i>	<i>p-value/%</i>
<i>Model</i>	14	51.37	17.7502	2.49	1.6
<i>Covariates</i>	2	0.40	7.9829	1.12	33.8
<i>T_A</i>	1	0.32	13.9051	1.95	17.2
<i>H_A</i>	1	0.08	0.4297	0.06	80.8
<i>Blocks</i>	3	9.26	10.8307	1.52	22.8
<i>Linear</i>	4	29.26	33.0228	4.63	0.4
<i>E_{pass}</i>	1	12.15	56.4056	7.91	0.8
<i>K</i>	1	8.50	30.4963	4.28	4.7
<i>Ov</i>	1	8.26	41.8356	5.87	2.1
<i>AZ</i>	1	0.35	1.8386	0.26	61.5
<i>2-Way Interaction</i>	5	12.46	12.0526	1.69	16.4
<i>E_{pass} · k</i>	1	5.50	29.4848	4.14	5.0
<i>E_{pass} · Ov</i>	1	1.75	8.8860	1.25	27.2
<i>E_{pass} · AZ</i>	1	1.78	8.0750	1.13	29.5

$k \cdot \Delta Z$	1	2.36	11.3314	1.59	21.6
$Ov \cdot \Delta Z$	1	1.06	5.1119	0.72	40.3
Error	33	48.63	7.1296		
Total	47	100			

A significant observation is the near-zero value of $R^2(\text{pred})$, indicating the model's limited predictive capability for new data points. Therefore, the primary utility of this model lies in discerning factors that influence micro-hardness, a parameter intrinsically linked to Young's modulus, a crucial measure in engineering materials studies.

Upon thorough assessment, all four main effects demonstrate considerable significance, representing 29 % of the model's total variance. Factor E_{pass} is the most influential, closely followed by k and Ov . Among these main effects, ΔZ emerges as the least impactful. Regarding the two-way interactions, only $E_{\text{pass}} \cdot k$ appears to have a bearing on the response.

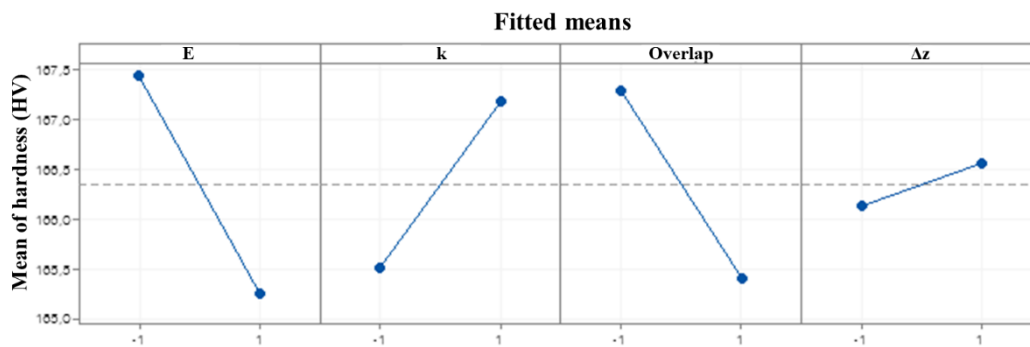


Figure 2.23 Effects of factors on the hardness response.

The analysis of the main effects factorial plots, as depicted in Fig. 2.23, reveals a significant trend. An increase in E_{pass} correlates with a notable decrease in microhardness (Fig. 2.23 (a)). This phenomenon can be attributed to heightened energy, which intensifies heat distribution, subsequently influencing cooling rates and grain growth coefficients. These modifications inevitably induce alterations in the microstructure of the specimens, a result in line with established theories such as the Hall-Petch law [185]. In the literature, a decrease in hardness with an increase in utilized energy is a generally accepted relationship [103].

On another front, an increase in the k value leads to a reduction in microhardness (Fig 2.23 (b)), likely due to mechanisms associated with thermal source attenuation. As more powder is spread, the energy is dispersed among a larger quantity of powder, including the portion not captured in the melt pool. Therefore, an increase in spread powder affects the total energy transferred in the melt pool, leading to lower energy density, similar to the effect of E_{pass} . This decrease in energy density results in higher hardness values [186].

A distinct decrease in microhardness becomes apparent when Ov is set to a value of 50 % (Fig. 2.23 (c)). The relationship between Ov and utilized volumetric energy density is direct. Volumetric energy density depends on h_d , which is a product of different Ov and W of the deposited track. Higher utilized volumetric energy density leads to lower hardness due to slower cooling rates and larger grain sizes [27], [103].

Furthermore, an increase in ΔZ fosters higher microhardness (Fig. 2.23 (d)). This is expected, given that the utilized volumetric energy density is also directly dependent on ΔZ . With higher ΔZ , the utilized volumetric energy density is decreased, resulting in increased microhardness [27], [103].

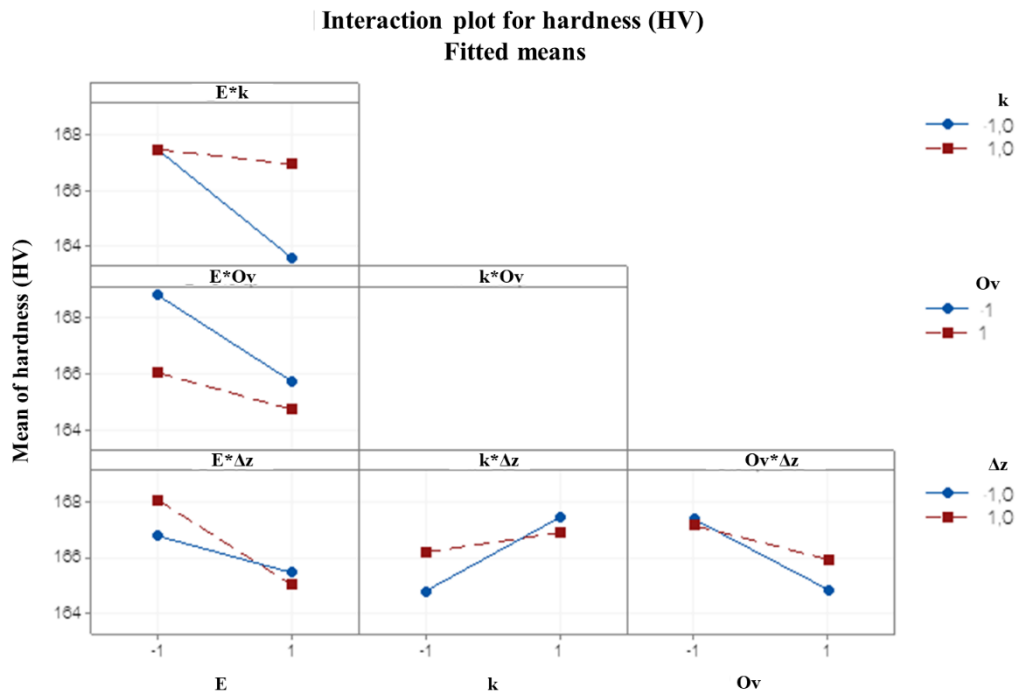


Figure 2.24 Two-way interaction plots for hardness response.

Regarding two-way interactions, as illustrated in Fig. 2.24, it is evident that only the interaction between E_{pass} and k is significant. This interaction results in heightened powder fusion. Specifically, under conditions of diminished k values accompanied by escalating E_{pass} , a notable drop in microhardness is observed. This influence becomes muted at elevated k values, suggesting that the excess powder expends some energy transitioning from a solid to the liquid phase.

The following equations have been derived from the simplified model, developed through the standard stepwise regression method:

$$(6) \text{ Hardness}/HV = 167.352 - 1.027 \times E + 0.715 \times k + 1.010 \times E \times k \quad (Ov = 0\%)$$

$$(7) \text{ Hardness}/HV = 165.345 - 1.027 \times E + 0.715 \times k + 1.010 \times E \times k \quad (Ov = 50\%)$$

The simplified model achieved an S value of 2.7, an $R^2(\text{adj})$ of 35.6 %, and an $R^2(\text{pred})$ of 19.8 %. No concerns regarding residuals or LOF were identified. Although its applicability is limited, the model offers valuable qualitative insights that will prove invaluable for future research endeavours. Lastly, Fig. 2.25 depicts the contour plots representing the response for the two qualitative levels of Ov.

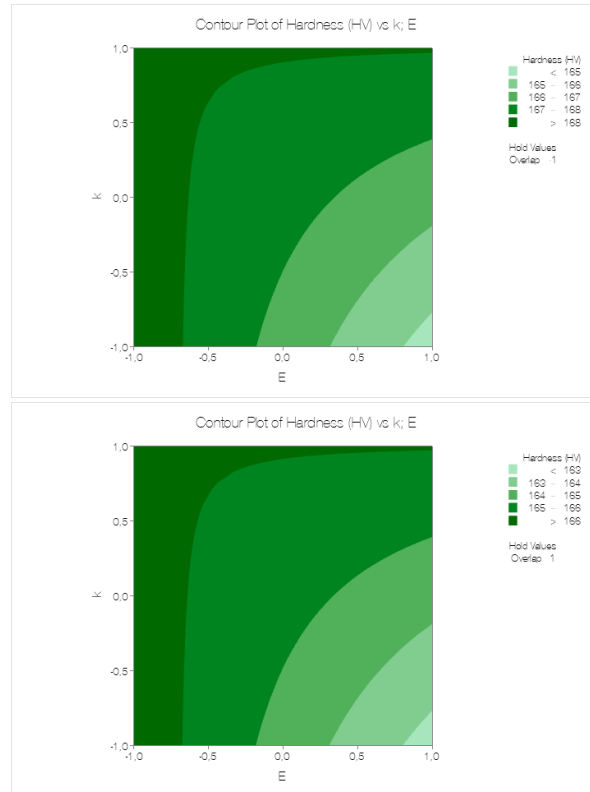


Figure 2.25 Contour plots of hardness: a) qualitative level Ov = 0 %, and b) qualitative level Ov = 50 %.

Expanding on the previous analysis, a comparison was made between the top five and bottom five points of each specimen. Subsequently, a two-sample t-test was performed, assuming equal variances. The results indicate that, except for three specimens, hardness at the top of the specimens is generally lower than at the bottom, aligning with the findings of Moheimani et al. [179].

2.5.5 Conclusions on factor screening

After thoroughly examining a range of mechanical and physical properties in the samples, the study has provided valuable insights into the complex interactions among the involved parameters. The key conclusions drawn from the research are summarized as follows:

- In the height analysis, significant factors included Z-step increment (ΔZ), which directly influenced height and layer thickness, and Ov, demonstrating a notable impact on height variations. Additionally, powder supply (k) and specific laser pass energy (E_{pass}) played crucial

roles, leading to thicker layers and enhanced melting capacity respectively. Interactions between E_{pass} and k , as well as E_{pass} and ΔZ , amplified responses, highlighting their combined influence. These findings were used to create a simplified model, showing strong reliability with consistent trends across different construction strategies.

- In the density analysis, the study revealed an average density of $7.927 \pm 0.006 \text{ g/cm}^3$ in the samples, suggesting a possible reduction in inherent porosity during fabrication. The consistent density dispersion highlights the method's reliability within specified parameters.
- In the evaluation of porosity, the data distribution was transformed to achieve normality standards. Despite this transformation, the ANCOVA model remained insignificant, and no correlations between density and porosity were observed. This emphasizes the necessity for future studies to utilize advanced tools for accurate porosity assessment.
- In the assessment of hardness, factors like E_{pass} , k , and O_v affect micro-hardness, but the established model accounts for only 30 % of the observed variability. This indicates the presence of unidentified variables or inherent variations shaping hardness properties. Notably, interactions between parameters, especially the synergy between E and k , have a substantial impact. The model provides qualitative accuracy in explaining the influences of various factors.

2.6 Effects of wire feeding direction and main process parameters in L-DED-W

This section contains the main experimental results due to the collaboration with the research group of Professor Michael Benoit, during 5 months visiting period at the University of British Columbia, to identify an optimal process window for multi-direction wire feeding in processing 316L.

In the domain of L-DED techniques, utilizing wire feedstocks have attracted considerable attention due to their unique advantages over powder feedstock methods. This approach offers distinct benefits, including reduced handling concerns (eliminating metal powder/dust and ensuring a clean environment), enhanced cost-effectiveness, a broader range of available feedstock materials, the capacity to produce larger components, nearly 100 % feedstock capture efficiency, lower porosity levels, and suitability for zero-gravity conditions [20], [36], [51], [187]. Despite these advantages, the use of wire feedstock does come with challenges, such as potential issues related to wire coil feeding and comparatively lower dimensional accuracy when compared to powder feedstock methods. Additionally, the direction of wire feed in L-DED-W processes can impact the optimal parameters within a single layer deposition, depending on the chosen toolpath. Typically, L-DED-W systems utilize wires with diameters ranging from 0.2 to 1.2 mm and can achieve deposition rates of up to approximately $300 \text{ cm}^3/\text{h}$ [20], [35].

In Laser-based Directed Energy Deposition using wire feedstocks (L-DED-W), selecting optimal process parameters is pivotal for successful material deposition, directly impacting the quality and characteristics of the manufactured parts. Key parameters influencing the process include laser power (P), scan speed (v), wire feed rate (f_w), wire diameter (d_w), and wire feed direction [41], [81], [188]. Laser P determines the thermal energy applied, affecting melt pool size, penetration depth, and the heat-affected zone (HAZ) [188]. The parameter v influences cooling rate and solidification behaviour [41]. Third main parameter f_w controls material deposition, ensuring desired part dimensions [41]. The d_w impacts melt pool size and bead geometry [51]. The direction of wire feed into the melt pool affects metal transfer and deposition characteristics (Fig. 1.9) [41].

Among wire feed directions, front feeding (F), opposite to deposition head travel, is generally preferable (Fig. 1.9 (a)). It ensures stable melting, smooth depositions, enhanced interactions between wire and melt pool, and superior metallurgical bonding, minimizing defects. In contrast, back feeding (B), aligned with deposition head travel (Fig. 1.9 (b)), leads to challenges like wire obstruction, lack of fusion, and poor bead formation, diminishing part quality. Side feeding (S), perpendicular to deposition head travel (Fig. 1.9 (c)), presents issues related to wire stability, positioning, and control, leading to irregular bead profiles and potential lack of fusion. Adjusting laser power, scan speed, and wire feed rate for each feed direction optimizes stability and deposition characteristics. Fine-tuning these parameters mitigates challenges, ensuring proper wire melting and material deposition [41], [81], [189].

The optimization of main process parameters guarantees deposition stability. However, there is limited research on how wire feed direction influences these parameters. This study explores the impact of multi-directional wire feeding on the optimal processing parameters for 316L stainless steel wire in L-DED-W, focusing on deposit geometric characteristics. Various combinations of P, v and f_w were tested for F, B, and S wire feeding, aiming to identify suitable parameter combinations for all feed directions.

In this study a commercially available 316L stainless steel wire (Executive Filler Metals 316Si/316LSi) with d_w of 0.762 mm (0.03”) and with nominal chemical composition reported in Table 2.15 was used. The wire was checked for internal porosity by analysing optical micrographs of 20 wire cross-sections (Fig. 2.26). Image analysis was performed using ImageJ software and the wire was found to contain less than 0.01 % porosity, indicating fully dense starting material. AISI 316L plates with dimensions of $20 \times 20 \times 1 \text{ cm}^3$ were used as a substrate. Substrates were cleaned with soap and water followed by ethanol prior to deposition trials. The L-DED system used in the current study was a Liburdi Automated Welding System (LAWS) 250 described in Appendix B.2.2.

Table 2.15 Nominal chemical composition of 316L wires employed.

Composition	C	Cr	Ni	Mo	Mn	Si	Fe
% wt.	0.02	18.26	11.24	2.53	1.57	0.89	Bal.

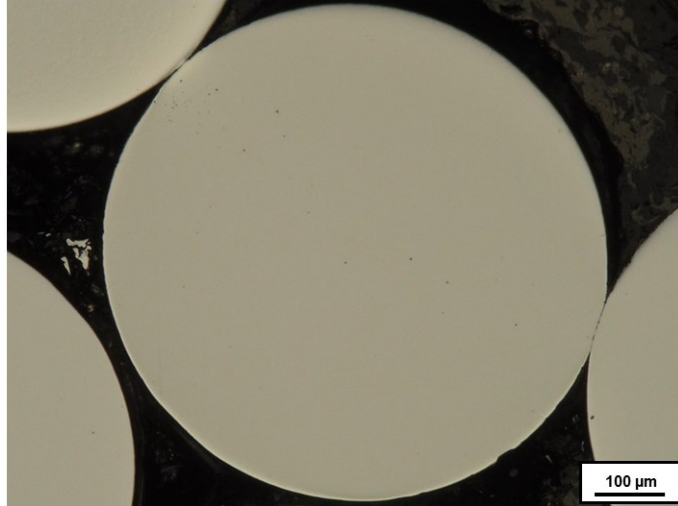


Figure 2.26 Optical micrograph of 316L wire cross-section.

2.6.1 Single track deposition

To identify the optimal processing parameters, 40 mm-long single tracks (STs) were deposited using various combinations of P , v , and f_w . This optimization process was conducted for three different feeding directions: F, B, and S, as illustrated in Fig. 1.9. The initial DoE aimed to assess a broad processing range for this system and the given starting material. In the first DoE (DoE #1), P varied from 300 to 700 W, while v was set at 600 and 900 mm/min, and f_w ranged between 660 and 840 mm/min, like summarized in Table 2.16. Additionally, STs characterized by $P = 700$ W, $v = 600$ mm/min, and $f_w = 660$ mm/min, was employed to pre-heat the substrate before depositing each set of STs. Following deposition, melt pool cross-sections were inspected, and melt pool dimensions were measured and analysed for dilution and aspect ratio (AR), as detailed in Appendix A.1.

Table 2.16 Process parameter ranges and steps used for deposition of STs for DoE #1 and DoE #2.

	<i>DoE #1</i>		<i>DoE #2</i>	
	Range	Step	Range	Step
<i>Power [W]</i>	300 – 700	100	450 – 600	40
<i>Scan speed [mm/min]</i>	600 – 900	300	900 – 1200	25
<i>Wire feed [mm/min]</i>	660 – 840	180	480 - 660	180

Analysis of melt pool cross-sections unveiled diverse geometries, as depicted in Fig. 2.27 for F feeding direction, alongside the corresponding dilution versus AR outcomes.

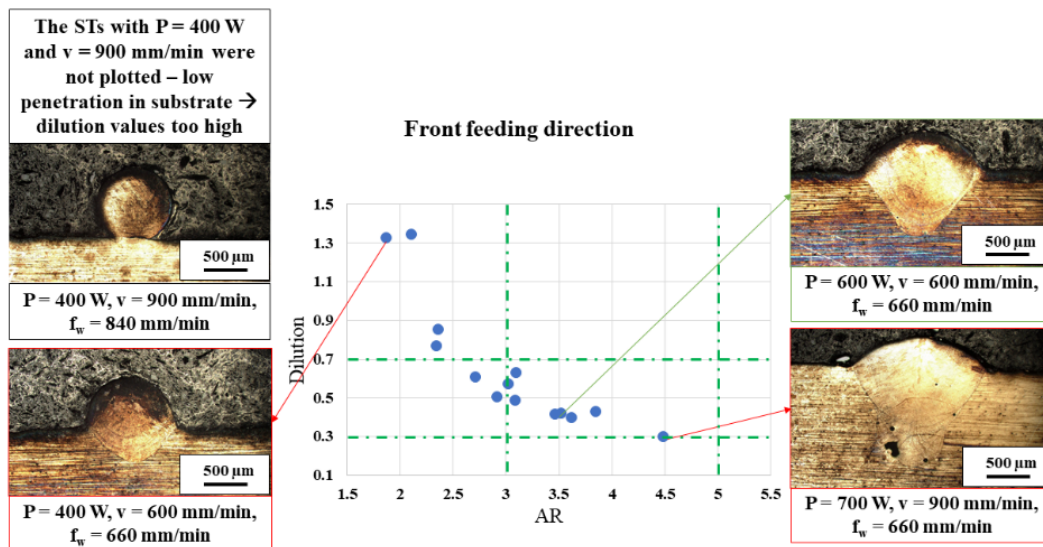


Figure 2.27 Diagram summarizing the dilution over AR with selection criteria lines for F feeding direction with selected OM micrographs of STs representing different extremes and acceptable melt pool geometry.

The dilution against AR results for the F feeding direction revealed a clear trend of decreasing the dilution values as P increased and v decreased. To be noted, STs at 300 W were not included in the analysis due to discontinuous deposition. Additionally, STs built with $P = 400$ W and $v = 900$ mm/min with both f_w of 660 mm/min and 840 mm/min were excluded from the diagram because of their exceptionally high dilution values (17.2 and 18.3, respectively), they both exhibited a balling geometry of cross-sections like shown in OM micrograph presented in the top-left corner of the Fig. 2.27. Despite the discontinuous construction of STs at 300 W, there were no operational issues during the deposition of any of the STs. Further analysis of the melt pool cross-sections revealed that all STs built with laser P of 700 W had a keyhole porosity, like the one presented in OM micrograph on bottom-right corner of the Fig. 2.27.

Following the F feeding direction, STs with the B feeding direction were deposited and analysed. The summarized results can be seen in Fig. 2.28.

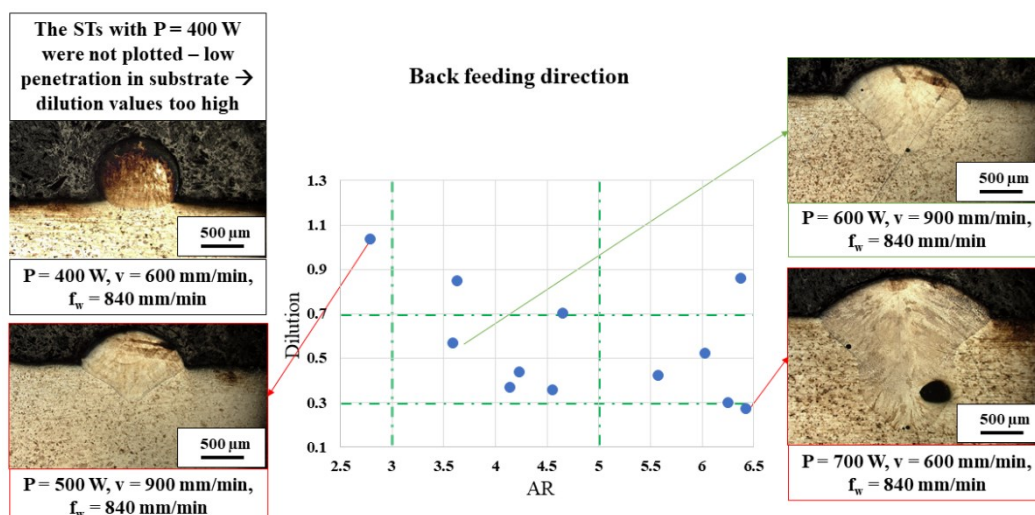


Figure 2.28 Diagram summarizing the dilution over AR with selection criteria lines for B feeding direction with selected OM micrographs of STs representing different extremes and acceptable melt pool geometry.

In contrast to the results from the F feeding direction, the B feeding exhibited more varied results in terms of dilution against AR. STs constructed with 400 W were excluded from the diagram due to their notably high dilution values, one example of the ST OM micrograph built with 400 W is given in the top left corner of the Fig. 2.28. Keyhole porosity was observed in ST built with $P = 700$ W, $v = 600$ mm/min, and $f_w = 840$ mm/min that is presented in the bottom-right corner of the Fig. 2.29. Similar observation was found in all the STs built with power of 700 W. The STs with a power setting of 300 W encountered deposition issues; insufficient energy at the start led to improper wire melting, causing the wire to become welded into the substrate initially and then bend away from the laser beam area, resulting in a deposition head collision. Consequently, STs with 300 W were not continued for the remaining DoE runs in both the B and S feeding directions.

Fig. 2.29 displays the outcomes of the STs constructed in the S feeding direction.

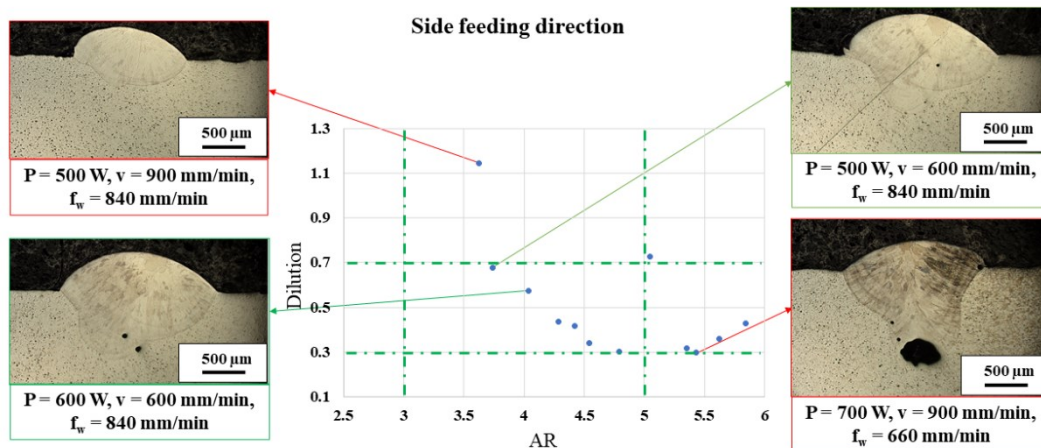


Figure 2.29 Diagram summarizing the dilution over AR with selection criteria lines for S feeding direction with selected OM micrographs of STs representing different extremes and acceptable melt pool geometry.

In the diagram in the Fig. 2.29 the STs dilution over AR results are shown only for the STs built with 500 W, 600 W and 700 W laser powder levels. Because during the deposition of STs with S feeding direction, issues arose with tracks deposited at 400 W laser power. The wire misalignment caused deposition failures due to scraping on the surface. In contrast to the symmetrical melt pool cross sections observed in F and B feeding directions, the S feeding direction resulted in asymmetrical melt pool shapes. Keyhole porosity was consistently found in all STs built with 700 W laser power level, the pores found were larger pores than those observed in other feeding directions, one example of ST built with 700 W with a large keyhole porosity is given in the bottom-right OM micrograph in Fig 2.29. Additionally, samples built with 600 W exhibited small keyhole porosities, like it

can be observed in the OM micrograph built with $P = 600 \text{ W}$, $v = 600 \text{ mm/min}$, and $f_w = 840 \text{ mm/min}$ shown in the bottom-left part of the Fig. 2.29.

Following the analysis of STs from DoE #1 and aiming to prevent the formation of keyhole porosity, DoE #2 was conducted. This experiment ranged between laser powers of 450 W and 600 W, with a scan speed set at 900 mm/min and increased to 1200 mm/min. The wire feed rate ranged between 480 and 660 mm/min, like summarized in the Table 2.16 under the column DoE #2. The same procedure was repeated as in DoE #1. Fig. 2.30 displays the dilution over the AR for all three feeding directions for each parameter set that met specific criteria ($0.3 \leq \text{dilution} \leq 0.7$ and $3 \leq \text{AR} \leq 5$) across both DoEs. The set marked with a red star, consisting of $P = 500 \text{ W}$, $v = 600 \text{ mm/min}$, and $f_w = 660 \text{ mm/min}$, showed the most promising parameters after the examination of OM micrographs. In Fig. 2.31, OM micrographs of the parameter sets presented in Fig. 2.30 are provided. Notably, only the selected set showed no signs of keyhole porosity, making it the most suitable choice for all feeding directions.

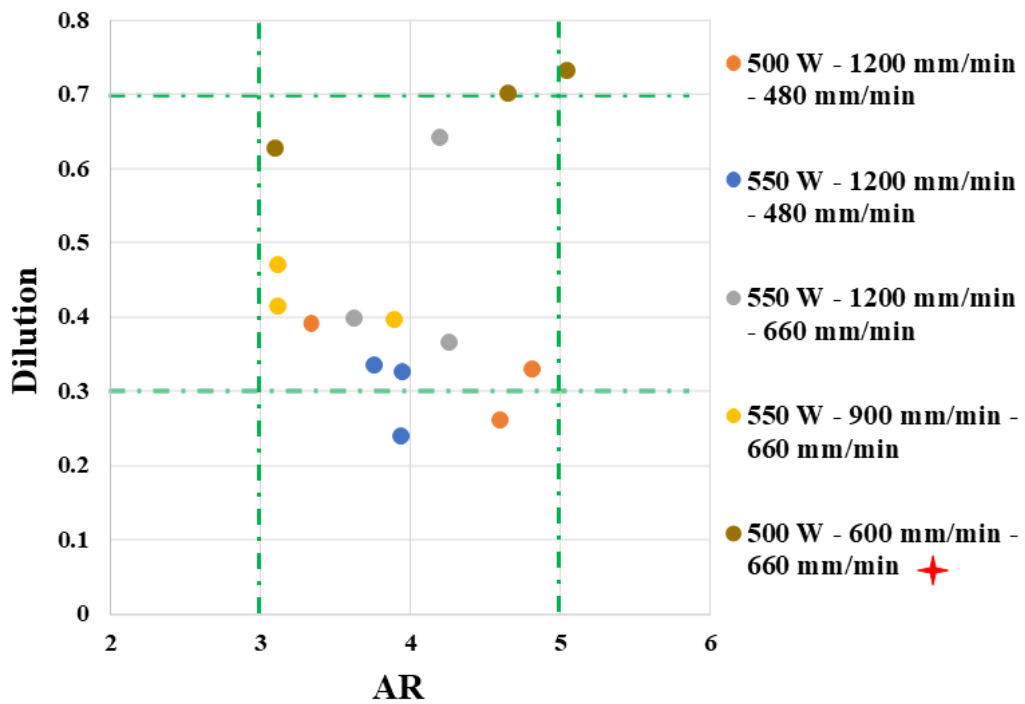


Figure 2.30 Diagram summarizing the dilution over AR with selection criteria lines for all three feeding directions for selected sets of parameters.

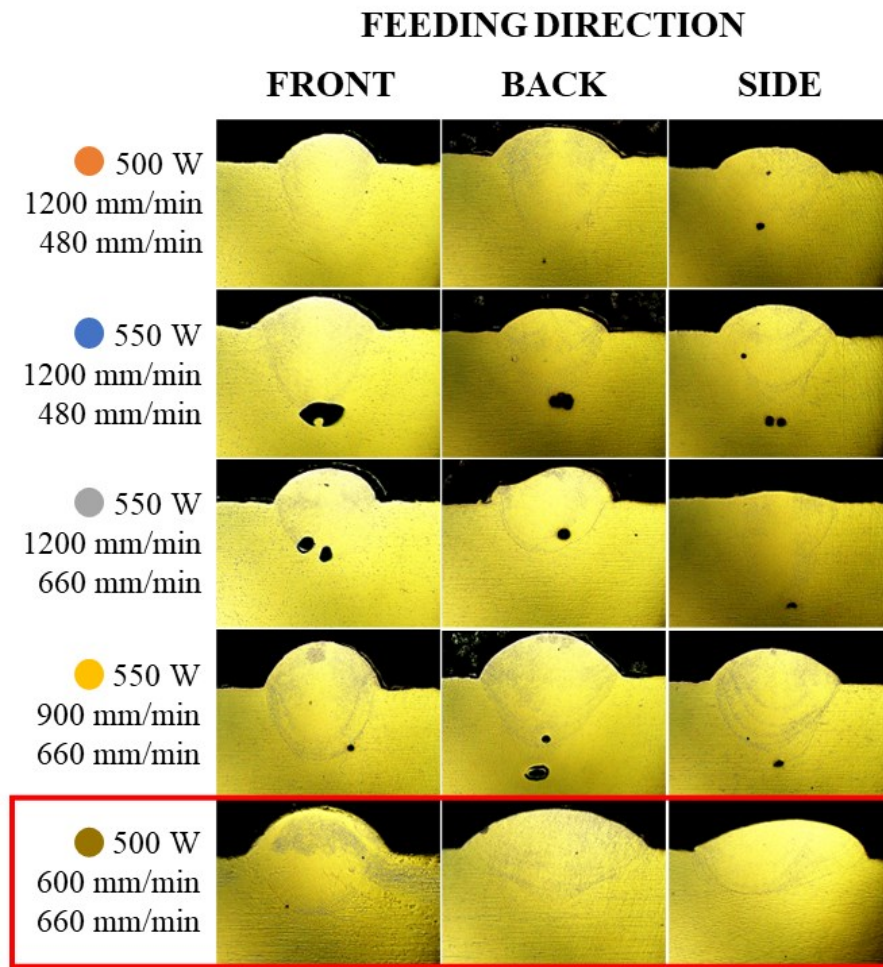


Figure 2.31 OM micrographs of STs cross-sections for sets of parameters plotted in Fig. 2.30.

2.6.2 Single layer deposition

After the STs were deposited, it was attempted to deposit single layers (SLs) constructed of 10 tracks with 30 % of overlap. For the F feeding direction it was deposited without any severe problems. But for the B and S feeding directions the control of deposition process was challenging. Due to all the problems regarding the wire deposition more detailed investigation on properties of 316L was not conducted. Nevertheless, after a time spent working with L-DED-W an overview of challenges regarding the control and configuration of the system can be given.

2.6.3 Control and configuration challenges on L-DED-W

The system employed features a laser spot diameter (d_l) of 0.3 mm, notably small for L-DED machines, especially in the context of L-DED-W. This small diameter concentrated the energy in the centre of the melt pool, which had a width

(W) of approximately 1.7 mm for the selected parameters. This melt pool was created from a wire with a diameter (d_w) of 0.762 mm. Examining the OM micrograph in Fig. 2.32 (a) revealed a "second" melt pool that led to deep penetration into the substrate, forming a keyhole geometry. Moving to the OM micrograph in Fig. 2.32 (b), a large keyhole porosity in this "second" melt pool was clearly visible. The keyhole shape indicated excessive energy input, but it also depended on the energy distribution within the melt pool, posing limitations when using a very small laser spot. Mazumder and Steen conducted a detailed analysis of heat transfer during laser welding, especially concerning the keyhole region and its effects [190]. While analytical methods and results from welding processes are somewhat applicable, they offer insights into heat transport in both L-DED processes and the HAZ. However, they serve as a starting point due to the challenge inherent in L-DED processes: the continuous addition of material through blown powder or wire feedstock. This continuous mass addition causes the part volume to expand over time, escalating the complexity of the problem and making the generation and application of analytical solutions highly challenging [23].

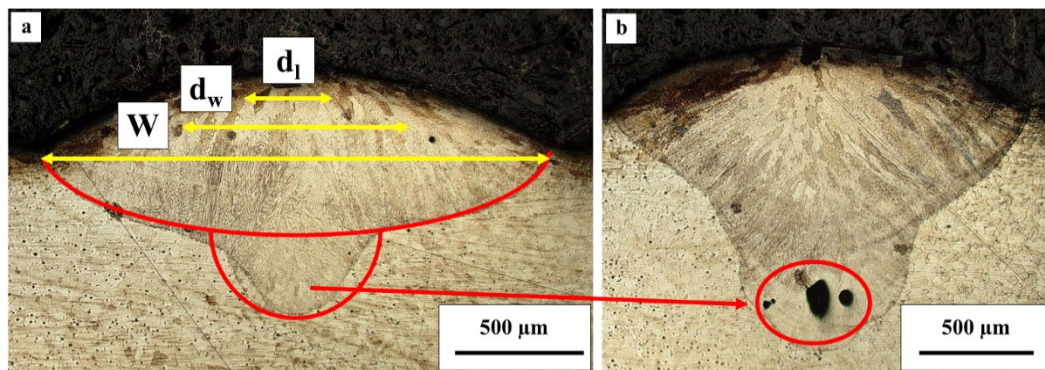


Figure 2.32 OM micrographs of STs cross section with indication of keyhole geometry and indicated relation in sizes of bead width, wire diameter and laser spot diameter.

The second problem discussed is the control of the deposition, that was poorly managed by the operating system, leading to several issues. These problems included deposition failures due to difficulties in separating the wire from the workpiece at the end of the track. Often, the wire remained welded to the substrate at the end of the track, necessitating manual intervention. The typical approach involved using a laser shot to release the wire while pulling the wire. However, this method had its drawbacks and sometimes failed, resulting in significant tension in the wire and, in some cases, leading to the abandonment of the deposition process for safety reasons. Even when the wire release was successful, it resulted in various wire tip shapes, as depicted in Fig. 2.33. At the start of deposition, the wire had a cut-off edge (Fig. 2.33 (a)), while a regular edge with no solidified metal droplet at the tip was observed in Fig. 2.33 (b). Fig. 2.33 (c) and (d) displayed different sizes of metal droplets solidified at the tip. These diverse wire tip shapes lead to the third problem observed on the machine. They posed challenges when identifying the starting position of the wire relative to the substrate. To clarify, the system

employed electricity to detect the contact between the wire and the substrate. Once identified, it initiated the deposition process. In the case of the regular tip shape, the wire feed occurred in the middle of the melt pool. However, when a droplet was formed, the wire feed was directed to the rear edge of the melt pool in the front feeding direction. In the case of a large droplet formation, it led to molten metal dropping on the surface instead of creating a continuous track. This happened because the distance between the wire and the substrate was too great. An example of melted metal dropping on the substrate is shown in Fig. 2.33 (e). This effect, caused by the shape of the wire tip, added complexity, especially when considering different feeding directions. Syed and Li [189] investigated the effects of wire feeding directions and wire positioning relative to the melt pool. Their study concluded that precise wire positioning within the melt pool played a crucial role in achieving well-formed tracks.

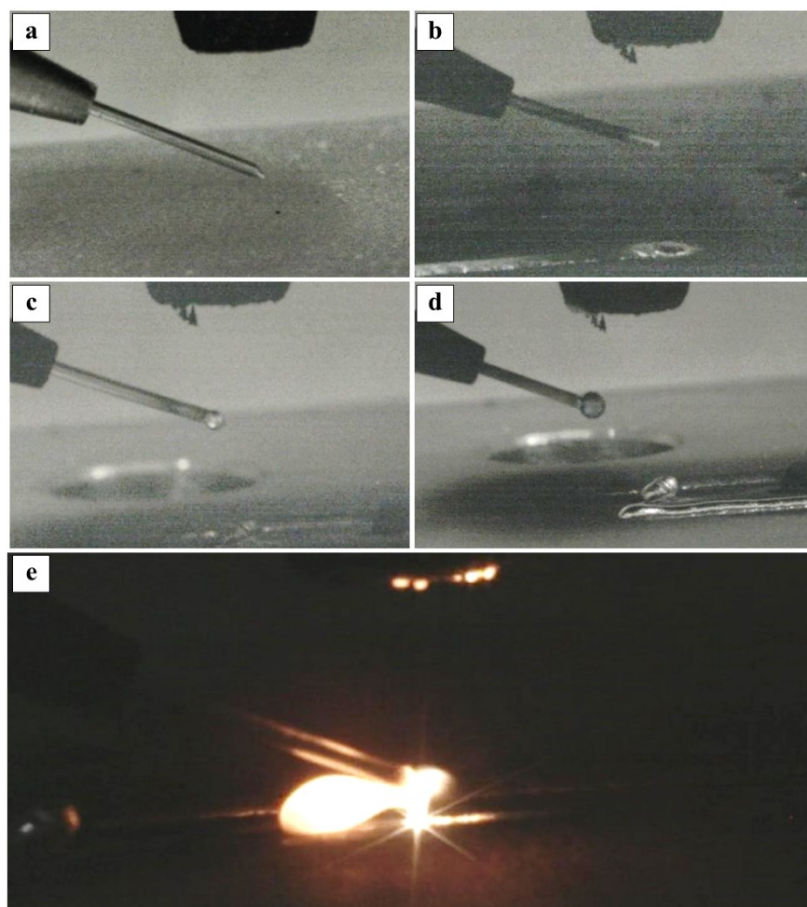


Figure 2.33 Frame captures of: a) cut off wire tip, b) regular shape wire tip, c) small droplet shape wire tip, d) large droplet shape wire tip, e) melted metal dropping during the deposition.

Furthermore, after the wire is released, the operating system requires the operator to manually position the wire tip at the centre of the crossbars, indicating the centre of the laser spot, before starting the next track deposition. This manual positioning not only poses challenges in terms of the relative positioning of the wire to the melt pool but is also physically demanding and prone to operational errors.

To illustrate the impact of this manual process, let's consider a cube with dimensions of 20 x 20 x 20 mm³, a typical object used for microstructural investigations. With a hatch distance of 1.2 mm and a 1 mm thick layer, completing the deposition would require 340 tracks. Assuming a skilled operator spends 15 seconds on each wire tip positioning, it would add up to 1 hour and 25 minutes of operating time for a single 8 cm³ cube. This manual step significantly extends the overall processing time and introduces room for human error.

Maintaining the correct stand-off distance is a common challenge in L-DED systems. In L-DED-P systems, if the Z-axis increment is greater than the actual deposited layer thickness, it can go out of focus and result in undergrown samples (Fig. 1.5 (b)). Overgrown samples can also be problematic, leading to non-uniform thermal histories between layers and the possibility of heated particles attaching to the nozzle, solidifying, and blocking the nozzle opening (Fig. 1.5 (c)). While L-DED-P systems face their challenges with stand-off distance, they are relatively less severe. For example, the Laserdyne 430, a laser-powder interaction system, has a tolerance of ± 1 mm from the ideal 8 mm stand-off distance. However, when it comes to front feeding direction, slightly increased stand-off distance can lead to the effect of melted metal dropping onto the workpiece surface, as shown in Fig. 2.33 (e). More significant problems arise in the case of back and side feeding directions. A decreased stand-off distance can result in the misalignment of the wire and may necessitate the abandonment of the deposition process for safety reasons. In L-DED-W systems, maintaining contact between the wire and the workpiece is crucial, but this can lead to questions about the perpendicular deposition of subsequent layer to the previous layer, as layers created with L-DED-W often exhibit a wavy surface due to overlapping tracks. This complicates the overall deposition process and quality.

The last criticism of the L-DED-W system pertains to the accessibility of the deposition head to the workpiece. The sequence in which multiple samples are deposited must be meticulously planned to prevent interference between the deposition head and previously deposited samples during the deposition process. This becomes particularly challenging in repair processes, where accessing hard-to-reach areas becomes crucial. Special attention and preparation are needed to navigate these limitations, especially in repair zone preparation, to ensure successful outcomes.

In conclusion, while L-DED-W systems offer significant advantages in terms of high-volume depositions, material efficiency, and safety, they do come with certain drawbacks in deposition control. Many of these challenges could be mitigated by implementing sensors and automated process control systems. A recent advancement in this field is the development of configurations utilizing wire feedstocks, such as coaxial laser wire additive manufacturing [191]. This technique stands out due to its central wire feed system, allowing versatile processing of various wire materials without directional constraints. It employs either multiple laser beams or a ring-shaped beam encircling the wire to melt both the wire and the base material. The creation of a ring-shaped beam involves laser sources and corresponding optics. Two approaches are used to generate multiple beams: one

involves a beam splitter dividing a focused beam into individual beams directed into the process zone via deflective mirrors, while the other utilizes a dedicated laser source for each beam, requiring specific optical units for collimation and focusing. These advancements hold promise for overcoming some of the limitations associated with basic L-DED-W systems with 3-axis deposition head control and fixed position of wire feeding nozzle.

Chapter 3

W360 by L-DED

This chapter is focused on the use of a new hot work tool steel patented by Böhler, to be processed for the first time by L-DED. It contains the process parameters optimization to obtain dense bulk samples crack-free, and the microstructural characterization of as built samples, and after heat treatments (quenching and hardening).

The main findings are divided into the following four sub-chapters:

- W360 powder for L-DED-P process
- Process parameters optimization for W360 by L-DED
- Heat treatment of the W360 as-built samples
- Microstructural evolution during heat treatment of W360

3.1 W360 powder for L-DED-P process

In the present study a commercially available gas atomized W360 tool steel powder sourced from voelstalpine Böhler Edelstahl GmbH & Co, a reputable steel producer based in Styria, Austria, was employed. This powder was chosen due to its high-quality and sustainable production process. The producer emphasized the use of renewable electrical energy and ensured that the powders were entirely recyclable, aligning with environmentally conscious practices.

The powder's chemical composition, detailed in Table 3.1, played a pivotal role in the AM sample production using the L-DED method. To assess its suitability, the powder was characterized in its as-received state first through laser granulometry. The findings, illustrated in Fig. 3.1, revealed a unimodal Gaussian particle size distribution. Specifically, the d10, d50, and d90 values were measured at 45.2 μm , 76.0 μm , and 131.3 μm , respectively. These values fell well within the typical range (50-150 μm) for L-DED processes, indicating the powder's appropriateness for the study.

Table 3.1 Nominal chemical composition of the W360 steel powder used in this study.

Composition	C	Si	Mn	Cr	Mo	V	Fe
Wt. %	0.50	0.20	0.25	4.5	3.0	0.55	Bal.

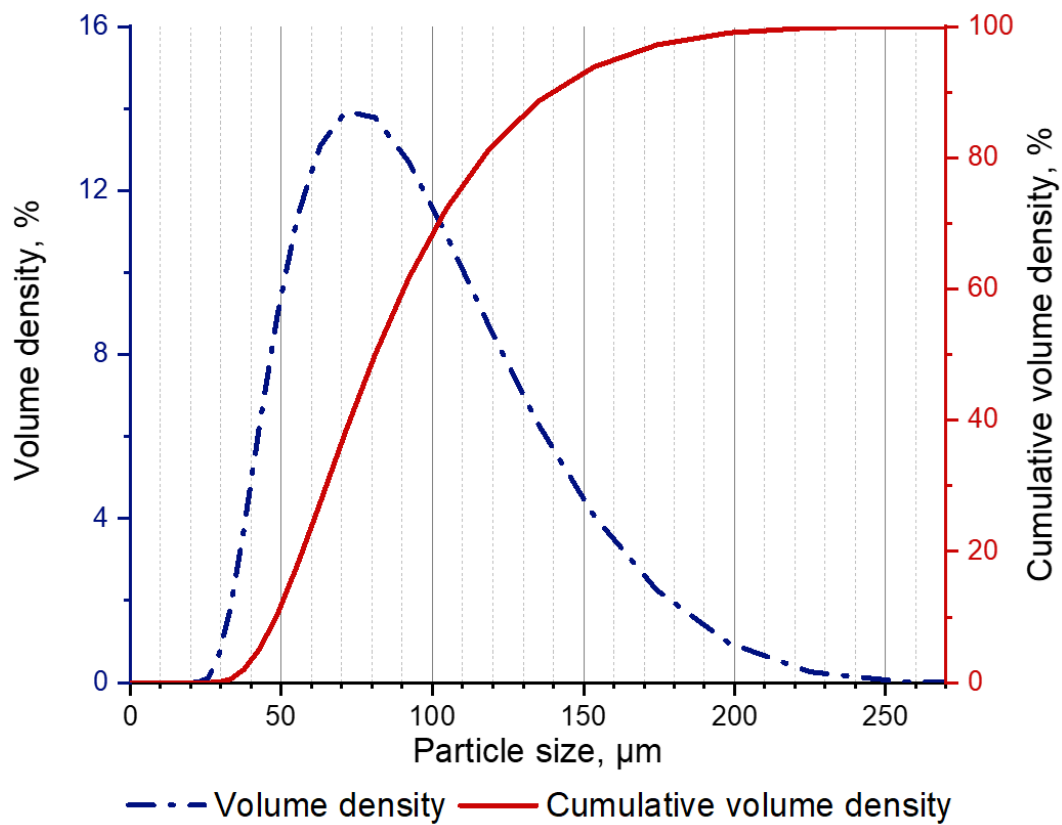


Figure 3.1 W360 powder particle size distributions in the as received condition: the dotted blue curve corresponds to the distribution in volume, while the red curve to the cumulative volume distribution [119].

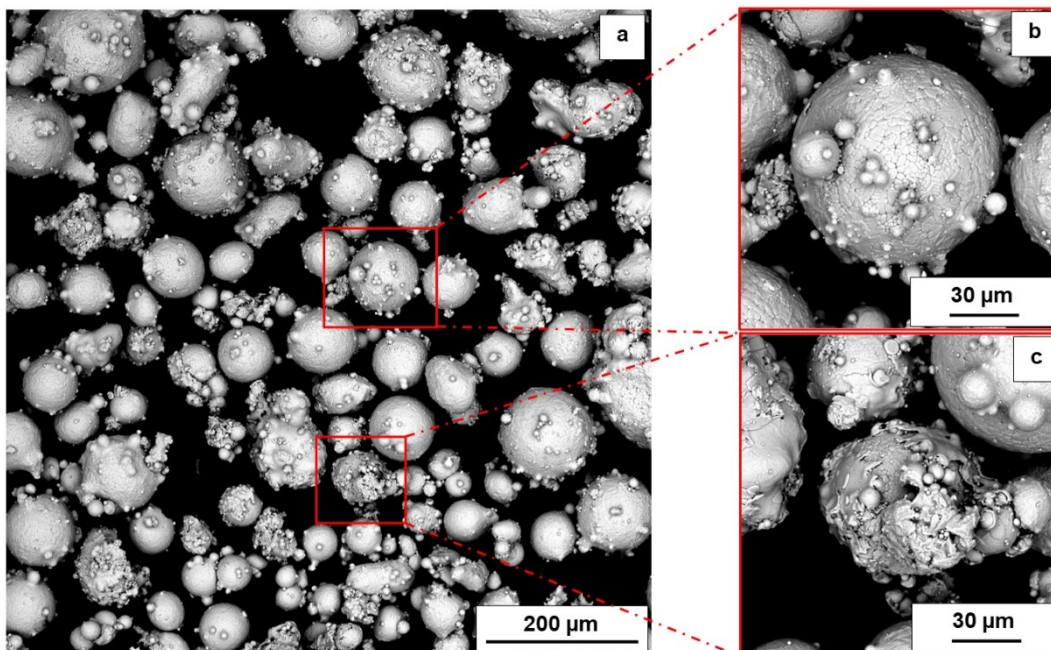


Figure 3.2 SEM micrographs of a) W360 powder in the as received condition, and magnifications showing b) a particle with smaller satellites, c) an agglomerated powder particle [119].

Following laser granulometry, the powder underwent SEM analysis. The SEM images shown in Fig. 3.2 reveal predominantly spherical-shaped particles, alongside numerous small satellite particles (Fig. 2(b)). Additionally, these images illustrate the presence of certain agglomerated small particles (Fig. 2(c)). This morphology is characteristic of gas-atomized powders, where smaller droplets, moving at higher velocities, may collide with larger droplets, leading to adhesion on the surface and the formation of satellite powder [155]. It is worth noting that this phenomenon is unlikely to have a significant impact on the material's processability during L-DED, as it is unrelated to the behaviour of the powder bed.

Nevertheless, the powder's bulk properties were assessed by measuring flowability, true density, as well as apparent and tap density. Using this data, CI and HR, indicators of flowability, were calculated. The results, detailed in Table 3.2, place the powder in the category with good flowability properties, bordering on excellent flowability properties.

Table 3.2 Bulk properties of W360 powder.

True density	7.79 g/cm ³
Apparent density	3.62 g/cm ³
Tap density	4.06 g/cm ³
Flowability	19 s/50 g
CI	10.8
HR	1.12

The starting material exhibited a significant number of irregular particles. However, after the analysis was conducted, it was determined to have acceptable properties, allowing the process to proceed to deposition and optimization of process parameters.

3.2 Process parameters optimization for W360 by L-DED

The study utilized the Laserdyne 430 L-DED system by Prima Additive, as detailed in Appendix B.2.1. To ensure the production of dense and crack-free L-DED-P samples, a meticulous multi-step approach outlined in Appendix A – Experimental Procedure was followed. Single tracks (STs) measuring 40 mm in length were deposited on a 316L substrate using the methodology described in Appendix A.1 Step 1: Single Tracks. The experimental design (DoE) encompassed a range of parameters, including laser power (P), scan speed (v), and powder feed rate (Q_p) for the initial process window, as summarized in Table 3.3. The reported values were chosen based on different literature utilized energy densities for similar steels by composition, like H13 tool steel and based on the machine properties. The Q_p was fixed at 8 g/min based on the previous experiences on using Laserdyne 430 with 2.0 mm laser spot diameter, providing an optimal layer growth of around 0.5 mm.

Table 3.3 Process parameter ranges and steps used for deposition of STs for DoE.

	Range	Step
Power [W]	500 – 900	100
Scan speed [mm/min]	300 – 600	150
Powder feed [g/min]	8	/

The produced STs were examined following the procedure outlined in Appendix A.1 Step 1: Single Tracks. The cross-sectional OM micrographs of the STs are displayed in Fig 3.3, and these results are summarized in Fig 3.4, where dilution is plotted over AR.

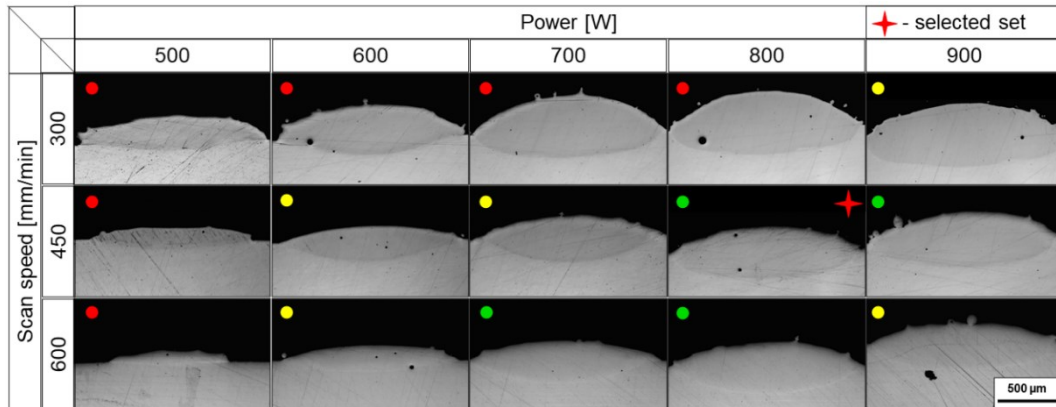


Figure 3.3 Optical micrographs of cross-sections of the W360 STs produced with coloured marks corresponding to criteria defined in legenda of the diagram of Fig. 3.4 [119].

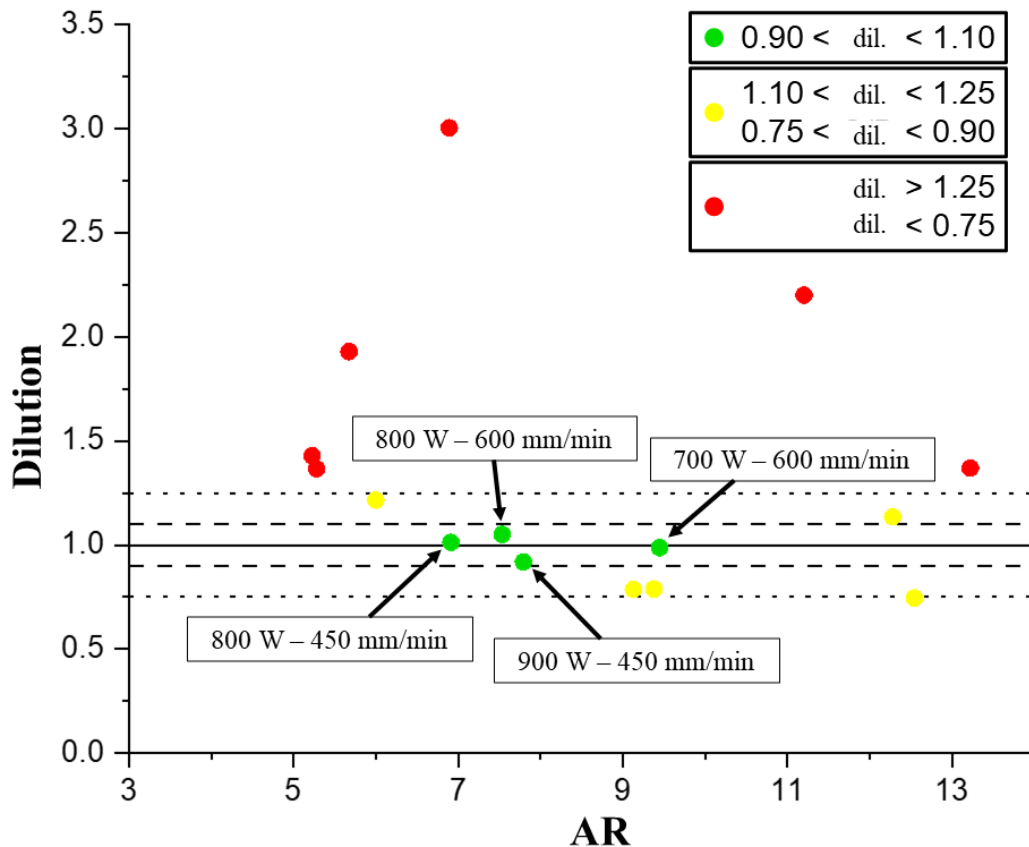


Figure 3.4 Diagram summarizing dilution over AR with selection criteria lines [119].

Examining the cross sections in Fig. 3.3, it becomes evident that STs with the lowest P exhibited a flat melt pool without penetration into the substrate. Conversely, STs with the lowest v showed higher growth than penetration, leading to dilution values exceeding 1.25, suggesting poor metallurgical bonding between consecutive layers. Further analysis revealed that STs with parameter pairs 600 W – 450 mm/min and 600 W – 600 mm/min had more acceptable dilution values based on the criteria defined in the legend of Fig. 3.4. However, their corresponding AR values were 12.54 and 12.28, indicating insufficient growth. Considering STs with P levels ranging from 700 to 900 W and v from 450 to 600 mm/min, it was observed that they fell within a favourable range. Particularly, the ST created with a combination of 800 W and 450 mm/min (highlighted with a red star in Fig. 3.3) displayed the dilution value closest to 1, indicating a regular melt pool geometry. Moreover, its corresponding AR value was the lowest among the STs with dilution values between 0.9 and 1.1. Consequently, this combination (800 W and 450 mm/min) was chosen for further single layers (SLs) and bulk sample depositions of W360 steel.

Additionally, based on the width of the ST obtained with this P , v and Q_p combination, and considering an overlap percentage (Ov) of 40%, the hatch distance (h_d) for SLs creation was determined to be 1.2 mm. Subsequently, the average growth of the five SLs produced was measured, resulting in a value of 0.65 mm. This measurement was adopted as the Z-axis increment (Δz) for manufacturing the bulk samples. The finalized process parameters for processing W360 steel using L-DED-P are summarized in Table 3.4.

Table 3.4 Main process parameters optimized to manufacture bulk samples made of W360 steel by L-DED.

P	800 W
v	450 mm/min
Q_p	8.0 g/min
V_{Ar}	5.0 L/min
d_t	2.0 mm
Ov	40 %
Δz	0.65 mm

All the produced samples exhibited a measured mean density above 99.80%, with a mean residual porosity value of 0.15%. The observed pores in the samples were spherical gas pores, a common characteristic of the L-DED-P process. This phenomenon arises because inert gases are employed for delivering powder to the melt pool and for shielding the melt pool to prevent oxidation. It's noteworthy that no cracks were found despite the high carbon equivalent content value of 2.15% calculated using eq. 1 from section 1.3.2. on Hot work tool steel by Directed Energy

Deposition. This absence of cracks can be attributed to the L-DED-P process lower cooling rates and distinct thermal history in comparison to the L-PBF process. The L-DED-P process utilizes a higher energy source, featuring a larger laser spot size with a nominal diameter one order of magnitude greater and lower scan speed [141], [192].

The nearly fully dense and crack-free samples demonstrate the successful optimization of the process parameters. The optimal process parameters result in E_V of 82.1 J/mm^3 calculated with the eq. 14 in Appendix A.3.

3.3 Heat treatment of the W360 as-built samples

In general, the samples built with L-DED exhibit specific characteristics. While they are dense and free of cracks, challenges remain, such as locally varying heat transfer rates during manufacturing, which directly impact cooling rates and subsequent changes in microstructure. Additionally, the layer-by-layer deposition process in L-DED generates IHT through repeated heating, austenitizing and tempering. The formation of martensite, re-austenitization, and tempering effects strongly depend on the process parameters and position within the parts along the building direction. At the tip of the part, corresponding to the last layer deposited, no further reheating occurs, and martensite forms without subsequent re-austenitization or tempering. As a result, the hardness within the as-built samples can vary along the building direction due to IHT, necessitating post-heat treatment for homogenization. Typically, this involves austenitizing followed by quenching and one or more tempering cycles [26], [34], [193].

In this context, the heat treatment process involves austenitizing followed by air quenching and three tempering cycles, as schematically described in Fig. 3.5.

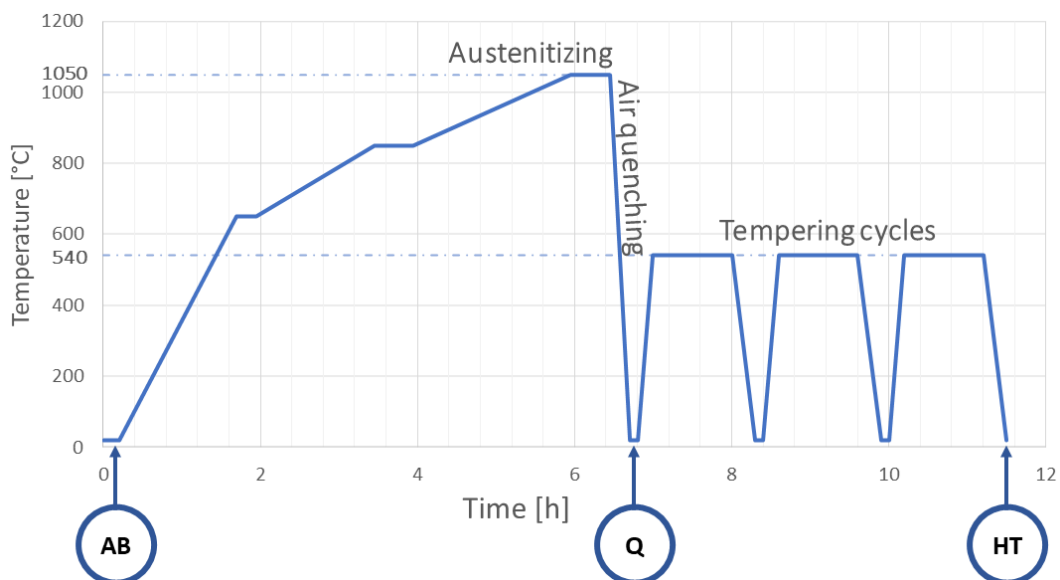


Figure 3.5 The complete heat treatment performed on W360 samples: diagram with indication of sample condition in each step considered for characterization [119].

Six parallelepiped samples were prepared for this investigation. Two samples labelled AB were analysed without post-processing in an as-built condition. The remaining samples underwent a heat treatment process in a tubular furnace (Appendix B.2.3) with an Ar-protected atmosphere, following a series of steps outlined in Fig. 3.5. The first heating to the austenitizing temperature was conducted in three stages: an initial step to 650 °C over 90 minutes, followed by an isothermal hold for 15 minutes. The temperature was then raised from 650 °C to 815 °C over 90 minutes, followed by another isothermal hold for 30 minutes. Finally, the temperature was increased from 815 °C to austenitizing temperature of 1050 °C over 120 minutes, followed by an isothermal hold for 30 minutes. In order to prevent grain coarsening, hardening must be carried out at the recommended austenitizing temperature. Subsequently, the samples were quenched using compressed air, and two of them, labelled Q, were chosen for microstructural analysis. Following the quenching process, the last two samples, labelled HT, underwent three consecutive tempering cycles. Each tempering cycle involved heating from room temperature to 540 °C, that is slightly above the maximum secondary hardening temperature [194] and in the range attributed to Mo carbide formation [195], in 10 minutes, holding at 540 °C for 60 minutes, and air cooling. The heat treatment was taken over from the heat treatment guidelines from Bohler [193].

3.4 Microstructural evolution during heat treatment of W360

The samples in different conditions, explained in the previous sections, were prepared for the microstructural analysis by following the standard metallurgical techniques.

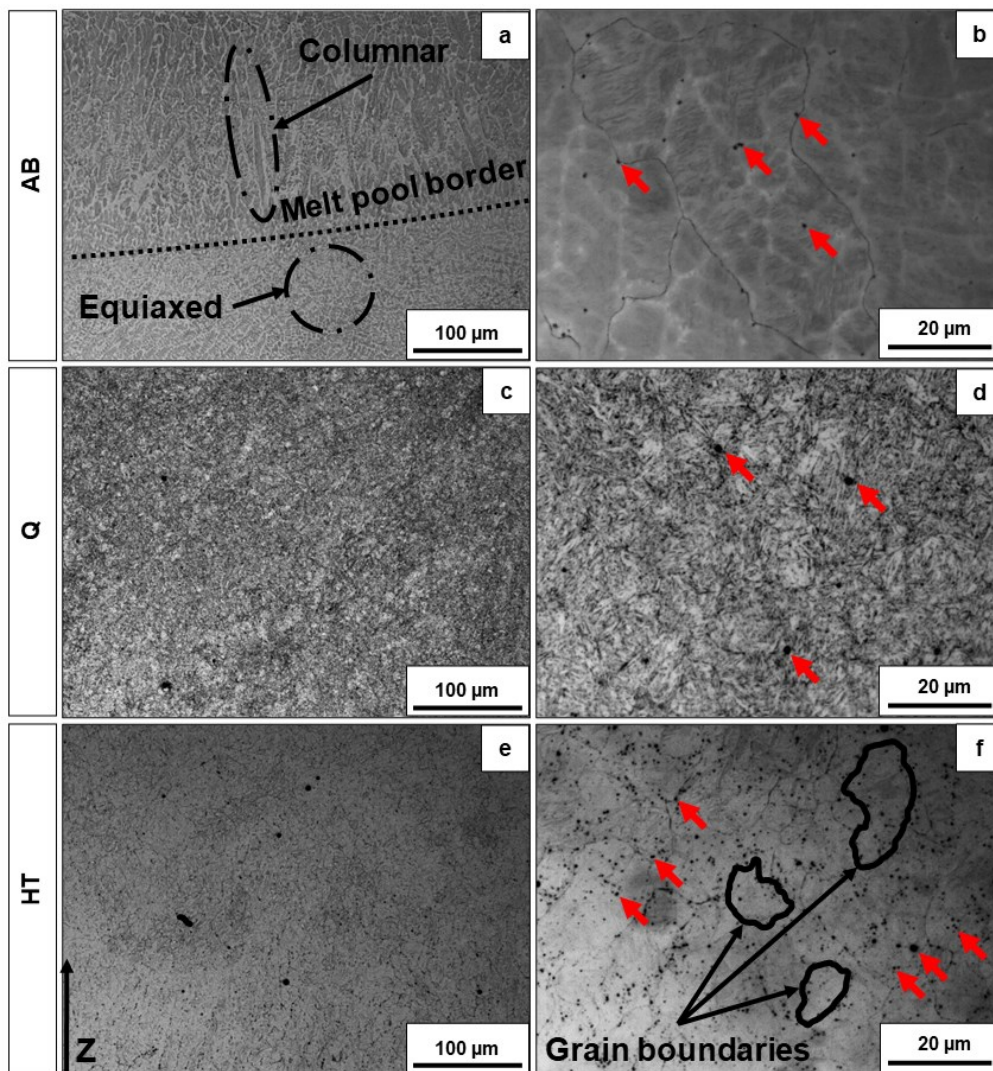


Figure 3.6 Optical micrographs of W360 AB (a, b), Q (c, d) and HT (e, f) samples at different magnifications [119].

The microstructure of the samples was examined using optical and SEM microscopes, and the observations are presented in Fig. 3.6. In Fig. 3.6 (a) depicting the AB sample, the characteristic L-DED microstructure is evident, showcasing interconnected melt pools and a dendritic-cellular pattern comprising equiaxed and columnar dendrites. Upon closer inspection (Fig. 3.6 (b)), cells, intercellular white phases, and very fine carbides in the form of black dots are discernible. Previous studies on similar as-built hot work tool steels like H13 have shown a comparable dendritic-cellular structure, accompanied by intercellular micro-segregation of alloying elements, suggesting the presence of retained austenite, a phenomenon discussed in previous research [26], [32], [196]. Notably, carbide particles (indicated by red arrows) were exclusively located within the intercellular regions. The microstructure of the Q sample is displayed in Fig. 3.6 (c) and (d), revealing the typical features of quenched hot work tool steels: numerous small martensite laths and carbides. Comparing this with the AB state, it is evident that after the austenitizing heat treatment, the melt pools and dendritic-cellular microstructure vanish. This transformation suggests that the heat treatment effectively modifies the

effects of the material's complex thermal history. The resulting microstructure is more homogenized, with the recovery of micro-segregated elements from the cell boundaries and partial dissolution of the carbides through a diffusional process facilitated by the austenitizing heat treatment. In the HT shown in Fig. 3.6 (e) and (f), the microstructure appears homogeneous, comprising tempered martensite and a significant quantity of carbides.

To gain deeper insights into the observed microstructural features (Fig. 3.6), a detailed investigation was conducted through FESEM, and the most representative micrographs of the three conditions are presented in Fig. 3.7.

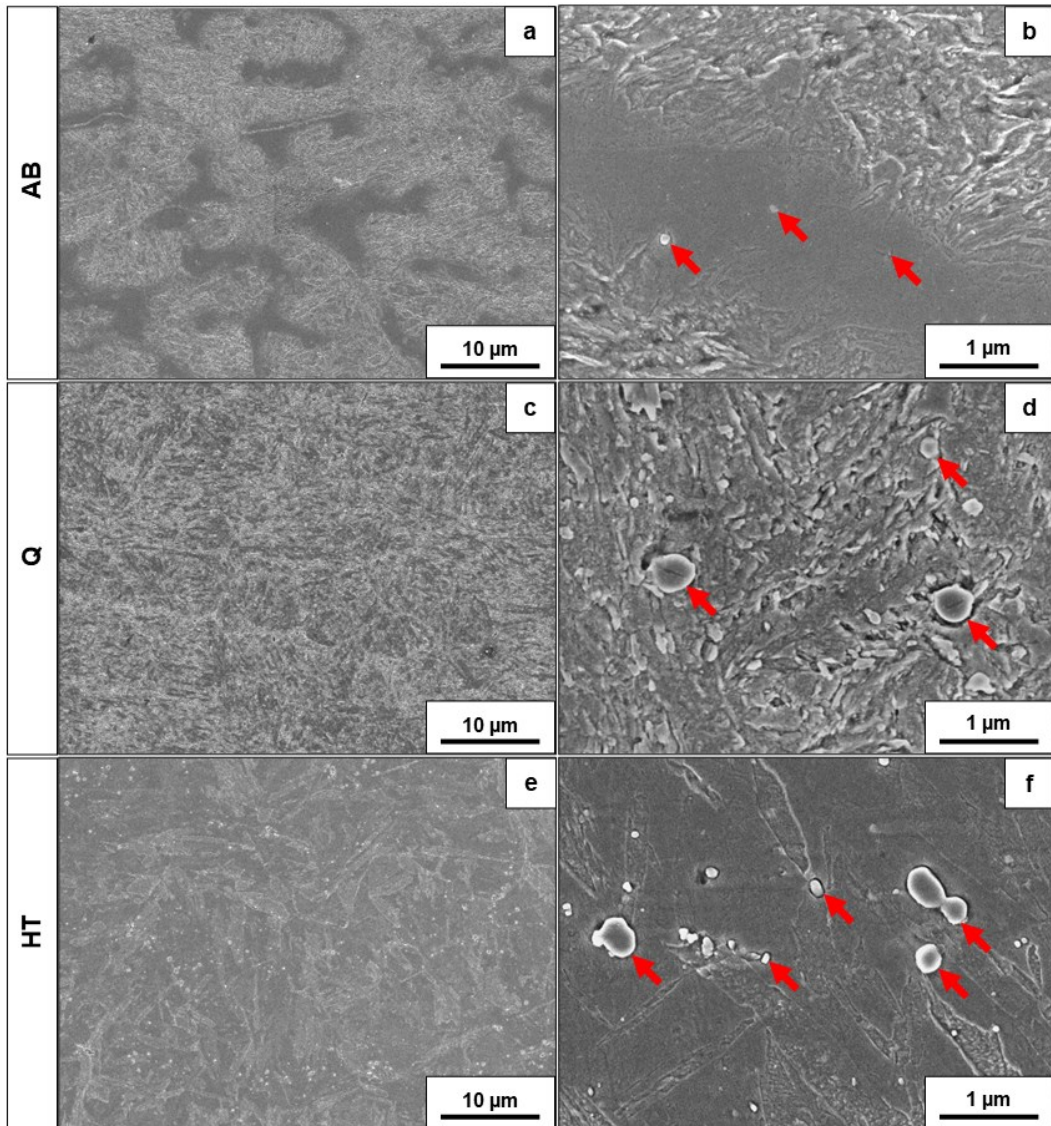


Figure 3.7 FESEM micrographs of revealed microstructure of AB (a, b), Q (c, d) and HT (e, f) samples at different magnifications [119].

In Fig. 3.7 (a), the dendritic-cellular microstructure of the AB sample is depicted, with the light grey phase representing tempered martensite within cells, and the darker grey phase indicating the intercellular region suspected to be retained austenite. At a higher magnification (Fig. 3.7 (b)), very fine carbides (highlighted with red arrows) can be seen in the intercellular area, displaying a distinct

microstructure compared to the cellular phase. The presence of these intercellular carbides aligns with findings from studies on H13, a similar hot work tool steel [26]. In the Q condition depicted in Fig. 3.7 (c) and (d), the austenite phase has transformed into a martensitic microstructure [197]. Moreover, in this sample, the dendritic-cellular microstructure typically observed in L-DED samples has vanished, likely due to the austenitizing temperature being reached. Upon closer inspection, larger carbides are visible (Fig. 3.7 (d)). In the HT condition shown in Fig. 3.7 (e) and (f), the characteristic microstructure of tempered hot work tool steels is apparent [198]. The growth of martensite laths and carbides can be observed, with the carbides appearing larger in size and number compared to the AB and Q samples.

To gain a deeper understanding of the matrix and carbide composition, EDS point analyses were conducted. The results, expressed as weight percentages of Fe, Mo, Cr, and V for the AB, Q, and HT samples, are presented in Table 3.5. The corresponding points are indicated in the SEM micrographs shown in Fig. 3.8. Note that the Si and Mn results are not included in the table, as they are not relevant for carbide analysis.

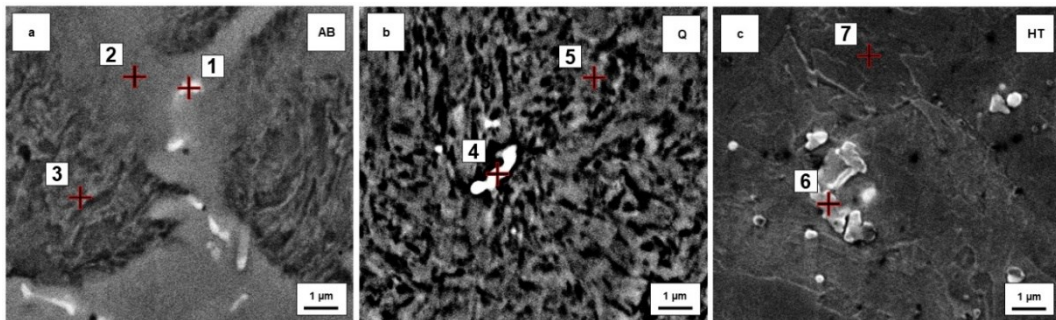


Figure 3.8 SEM micrographs used for EDS spot analysis a) of AB sample, b) of Q sample, c) of HT sample [119].

Table 3.5 EDS spot analysis with main alloying elements in % wt. of W360 by L-DED samples in AB, Q, and HT conditions. The spot number is related to Fig. 3.8.

Spot	Description	Fe	Mo	Cr	V
1	Carbide – AB	69.3	5.8	5.3	0.9
2	Cell boundary – AB	85.6	3.3	4.8	0.6
3	Cell – AB	87.9	2.5	4.2	0.5
4	Carbide – Q	51.0	21.1	6.7	3.8
5	Martensite – Q	87.1	2.6	4.2	0.4
6	Carbide – HT	74.9	8.9	4.2	0.7
7	Tempered martensite – HT	86.2	2.5	4.3	0.5

The provided EDS sensor was incapable of accurately measuring the C content, resulting in the absence of C results. In the micrograph of the AB sample (Fig. 3.8 (a)), a distinct microstructural difference is noticeable between the cell and the cell boundary, with carbides observed solely at the cell boundary. Comparison of EDS point analysis results for spots 1, 2, and 3 (Table 3.5) reveals slightly higher weight percentages of alloying elements Mo, Cr, and V in the cell boundary (spot 2) than in the cell (spot 3), confirming micro-segregation of alloying elements reported in previous studies [32], [196]. Moreover, the EDS spot analysis reveals an increase in the carbide-forming elements in the carbides. Notably, Mo exhibits a significant increase, rising from 2.5 % wt. in the cell (spot 4) to 3.3 % in the cell boundary (spot 3) and reaching 5.8 % in the carbide (spot 1).

Moving to the Q sample, EDS spot analysis (Fig. 3.8 (b)) indicates a homogenized martensitic matrix (spot 5), resulting from diffusion-based homogenization during the high-temperature austenitization phase, as observed by Amirabdollahian et al. on H13 by L-DED [26]. Additionally, some carbides in the Q sample exhibit increased content of all measured alloying elements (spot 4) compared to the carbide in the AB sample (spot 1). Specifically, Mo content increased from 5.8 % to 21.1 %, Cr content increased from 5.3 % to 6.7 %, and V content increased from 0.9 % to 3.8 %.

In the HT sample, the tempering process had no significant impact on the change in alloying element content in the matrix. The tempered martensite, in Fig. 3.8 (c) (spot 7), exhibited similar alloying element content as the as-quenched martensite (spot 5). Additionally, the carbide (spot 6) in the HT sample showed that the content of Cr remained at a similar level as in the matrix (spot 7), being 4.2 % in the carbide and 4.3 % in the matrix. Moreover, the amount of V slightly increased from 0.5 % in the matrix to 0.7 % in the carbide. Meanwhile, the content of Mo increased from 2.5 % to 8.9 %, indicating that there are mainly Mo-rich carbides, consistent with the findings of Amirarsalani et al. [199].

To sum up the EDX analysis, the carbides in the AB sample underwent intrinsic tempering, not controlled like the tempering process in the HT sample. This suggests that the carbides in the AB sample were tempered at different temperatures, ranging from high to low, as the deposition process progressed [30]. This intrinsic tempering phenomenon occurred at different stages, promoting the growth of different carbide types. It could be stated that at temperatures around 650 °C, the growth of V carbides was primarily encouraged, while at temperatures between 538 and 592 °C, the growth of Mo carbides was favored. Finally, at temperatures around 427 °C, the promotion of Cr carbides became significant [195]. This could explain the increase in the content of all carbide-forming elements in the spot analyses corresponding to the carbides of the AB sample. In contrast, it can be supposed that the HT sample underwent controlled tempering at 540 °C, which predominantly promoted the growth of Mo-rich carbides [195]. Furthermore, in the HT sample, the content of Cr did not increase in relation to the martensitic matrix, perhaps indicating that its role in W360 steel is mainly to stabilize martensite [198].

Subsequently, XRD measurements were conducted to validate the hypotheses presented in Fig. 3.6 and Fig. 3.7 regarding the detected phases (Fig. 3.9). The XRD

patterns of the AB, Q, and HT samples all exhibited peaks corresponding to the martensitic phase.

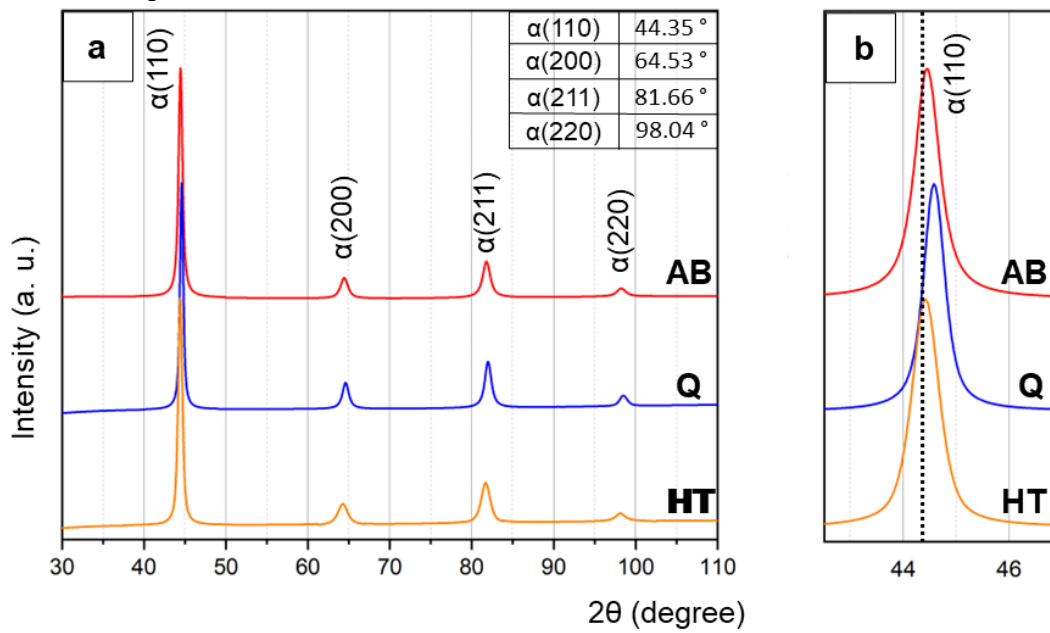


Figure 3.9 XRD patterns of a) AB, Q and HT samples with reported α values; b) a magnification of the first peak for the α (110) value in AB, Q and HT samples in comparison to the theoretical one (dotted line) [119].

The peak values reported in Fig. 3.9 (a) correspond to the body-centered cubic (bcc) system, representing a carbon-free steel structure. It is well-known that the lattice parameter of martensite changes with the increase of carbon content in the lattice [200]. In the magnified reflection shown in Fig. 3.9 (b), a noticeable shift of the first peak in all patterns compared to the α (110) value can be observed. This phenomenon can be explained by the rapid cooling from the austenitizing temperature, which traps carbon in the BCC lattice, leading to changes in lattice parameters. During tempering, carbon diffuses out of the lattice, restoring the peak related to the original lattice parameters. This carbon diffusion process promotes the formation and growth of carbides. However, it's essential to note that, although carbides are present, their content, as well as the content of retained austenite if present, is less than 4% of the volume content, making them undetectable by XRD instrument utilized. Nevertheless, the presence of different carbide contents can be assessed through DSC analyses.

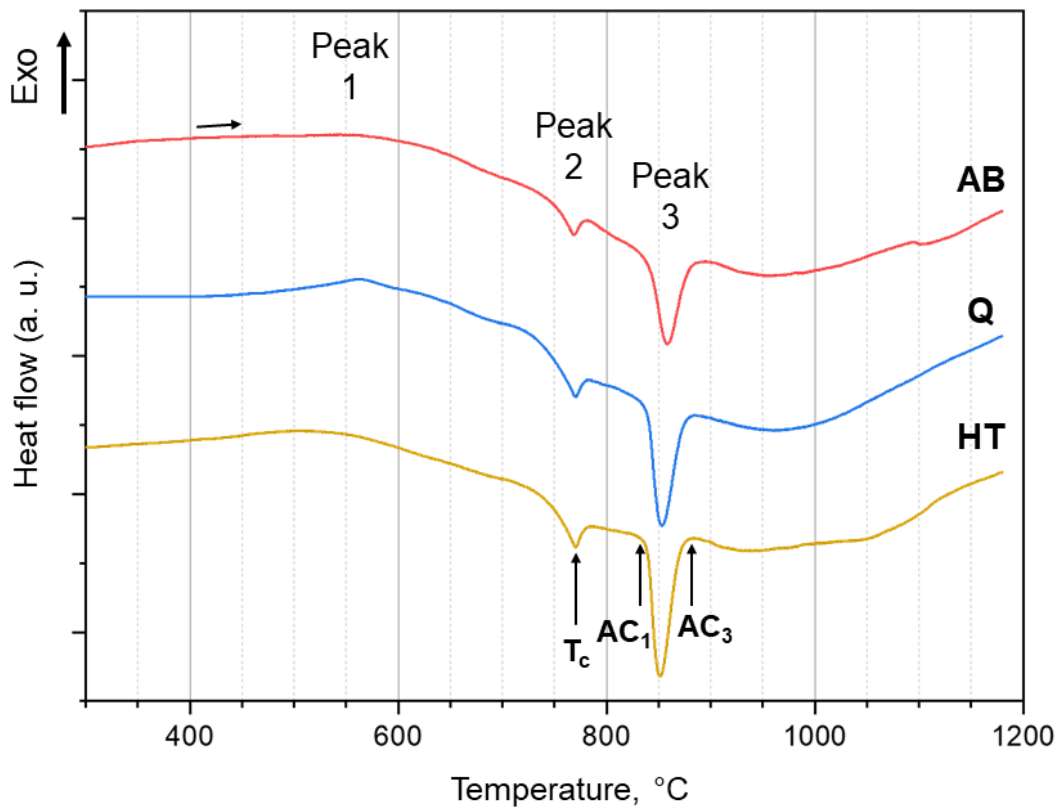


Figure 3.10 Heating DSC curves of the AB, Q and HT samples [119].

During the DSC measurements, two endothermic peaks, labelled as Peak 2 and Peak 3, were clearly observed in the thermograms of all bulk samples (Fig. 3.10). Additionally, an exothermic event was noted in the Q samples between 500 and 600 °C, likely attributed to Mo carbide formation, as reported in the literature, which occurs between 538 °C and 592 °C [195]. Peak 1 was absent in HT samples because the carbides had already formed. In the AB samples, as mentioned earlier, intrinsic tempering took place during the L-DED process, leading to carbide formation and growth. The first endothermic event, Peak 2, corresponds to the Curie temperature (T_c) related to the magnetic transformation. It appeared at 770 °C for Q and HT samples, while in the AB sample, the peak was slightly shifted to the right at 779 °C [201]. Peak 3 is associated with the transformation from α to γ phase. The austenite onset temperature (AC_1) was measured to be 839 °C for all three samples. However, the austenite finish temperature (AC_3) was observed at 874 °C for Q and HT samples, whereas for AB samples, it was found at 882 °C. The rightward shift of the T_c and AC_3 temperatures could be explained by differences in grain sizes. Optical micrographs of AB and HT samples (Fig. 3.6 (b) and (f)) clearly show variations in grain sizes. The transformation from martensite to austenite starts at the grain boundaries, and smaller grain sizes transform faster. In line with literature findings for H13 tool steel, under similar heating rates in DSC measurements, larger grain size conditions exhibited higher AC_3 temperatures, which aligns with our observations in AB samples [202], [203].

Finally, the effects of these microstructural features on material properties were evaluated through hardness tests. Fig. 3.11 displays the microhardness mean values

of AB, Q, and HT W360 steel samples, organized based on the positions where measurements were taken along the height of the cross-section, starting from the substrate and progressing along the build direction (as indicated in Fig. 3.11 (a)).

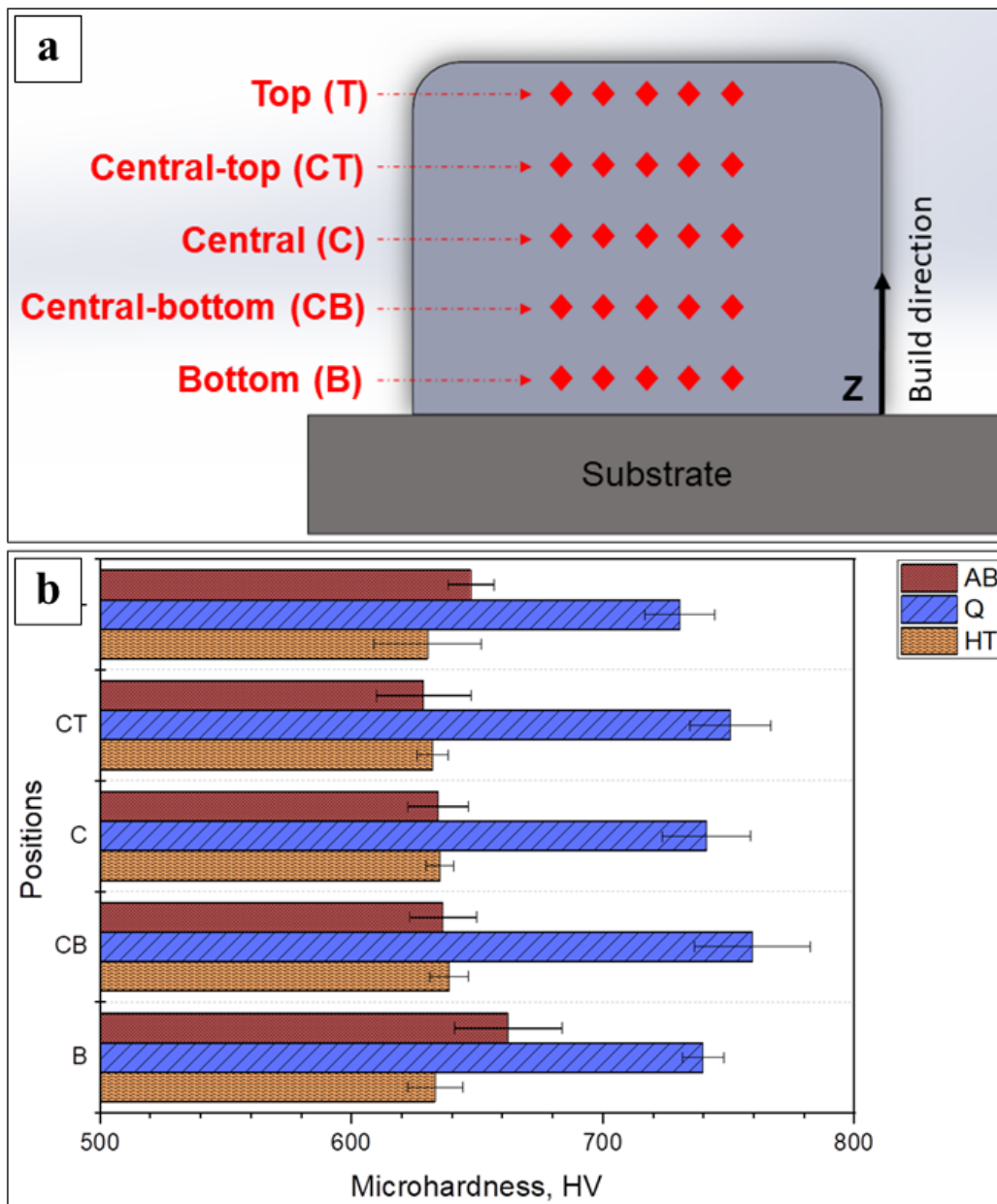


Figure 3.11 a) Schematic representation of microhardness measurements with reported zones of sampling along building direction; b) Microhardness mean values for AB, Q and HT W360 samples reported for different positions along building direction [119].

The hardness of the AB sample displayed a noticeable trend along the building direction. The bottom of the sample exhibited the highest values, with microhardness decreasing in the upper layers until an increase was observed at the top part of the sample. This pattern could be attributed to the increasing temperatures of the substrate as more layers were added, resulting in slower cooling rates and consequently lower microhardness values. The higher microhardness at

the top of the AB sample might be due to the absence of additional upper layers, allowing the top layer to cool more rapidly and preventing prolonged exposure to elevated temperatures, thus avoiding tempering effects. However, this trend observed in the AB condition was not evident in the Q and HT samples, indicating that the thermal history's influence can be erased through the performed heat treatment. The mean microhardness value for AB samples was 642, while the as-quenched (Q) sample exhibited the highest microhardness value of 744 HV, as expected due to the significant internal stress present due to the high amount of trapped alloying elements within martensitic cells, making it more brittle. With promotion of carbide growth and reduction of internal stresses and minimization of the risk of cracks through three tempering cycles, the microhardness of the HT samples dropped to 634 HV. This hardness level aligns with the expectations for the performed heat treatment and is suitable for applications in tool repair [193].

Chapter 4

18Ni-300 by L-DED

This chapter is dealing with L-DED process parameters optimization for the maraging steel 18Ni-300, followed by a microstructural analysis of as-built samples built. The work has been done in collaboration with the research group of Professor Michael Benoit, and in particular with Christopher Paul, during the period spent as visiting researcher at University of British Columbia.

The chapter is divided in three sections as follows:

- 18Ni-300 powder for L-DED-P process
- Process parameters optimization for 18Ni-300 by L-DED
- Microstructural analysis on as-built 18Ni-300

4.1 18Ni-300 powder for L-DED-P process

In this study a commercially available 18Ni-300 powder, gas atomized material sourced from Carpenter Additive, renowned for its quality in additive manufacturing applications, was used. The powder boasts a nominal particle size distribution ranging from 45 to 106 μm , as indicated in their specifications outlined in Table 4.1. To assess its appropriateness for the study, the powder's as-received state was meticulously examined using optical and SEM microscopes.

Table 4.1 Standard and nominal chemical composition of the 18Ni-300 powder.

wt.%	C	Fe	Ni	Co	Mo	Ti	P	S	Si	N
<i>Standard</i>	0.00-0.03	Bal.	17.0-19.0	8.5-10.0	4.50-5.20	0.80-1.20	Max 0.010	Max 0.010	Max 0.10	Max 0.10
<i>Nominal</i>	0.02	Bal.	18.0	9.1	4.81	0.93	0.005	0.003	0.04	<0.01

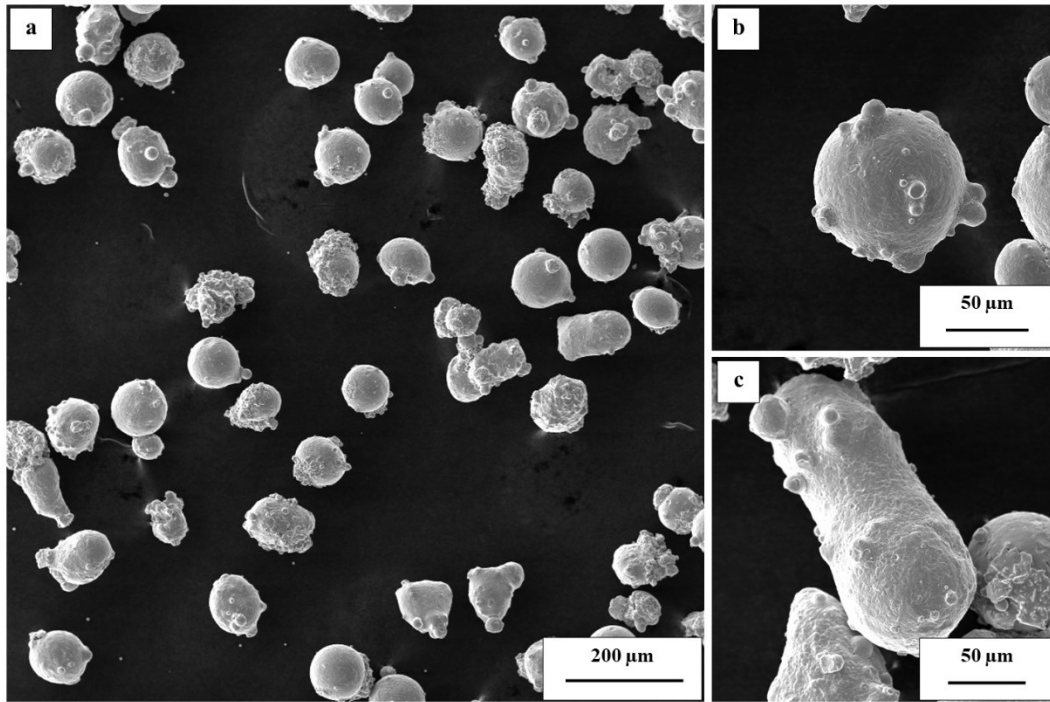


Figure 4.1 SEM micrographs of a) 18Ni-300 powder in as-received condition, b) spherical particle with some satellite powder, and c) elongated powder particle.

In Fig. 4.1, the as-received 18Ni-300 powder displays predominantly spherical particles, with occasional irregularities, notably satellite powders illustrated in Fig. 4.1 (b) and some elongated particles captured in Fig. 4.1 (c). While the overall morphology is satisfactory, the study further scrutinized the powder for internal porosity.

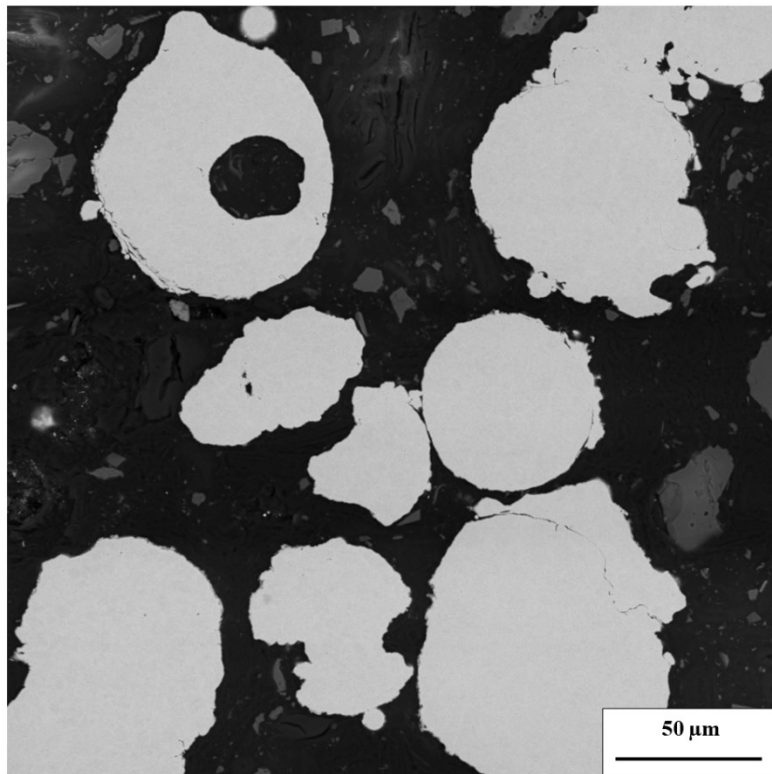


Figure 4.2 OM micrograph of 18Ni-300 powder cross-section.

Fig. 4.2 reveals that a few particles exhibited internal porosity, a common occurrence in gas atomized powders. It's worth noting that only a minor fraction of particles analysed displayed such porosity, highlighting the overall quality of the powder.

Additionally, key powder properties were measured, including an apparent density of 4.15 g/cm³ and a flowability of 18 s/50g. These properties underscore the material's suitability for the study, emphasizing its essential role in achieving reliable and consistent results in the subsequent AM process.

4.2 Process parameters optimization for 18Ni-300 by L-DED

In this study a LAWS 250 hybrid L-DED system, capable of using both powder and wire feedstock and manufactured by Liburdi Automation, as detailed in Appendix B.2.2, was employed. To ensure the production of dense and crack-free L-DED-P samples, a meticulous multi-step approach outlined in Appendix A – Experimental Procedure was followed. Single tracks (STs) measuring 30 mm in length were deposited on a 316L substrate following the methodology described in Appendix A.1 Step 1: Single Tracks. The experimental design (DoE) encompassed a range of parameters, including laser power (P), scan speed (v), and powder feed rate (Q_p) for the initial process window (DoE #1). The specific parameters are summarized in Table 4.2 under the DoE #1 column.

Table 4.2 Process parameters used for deposition of STs for DoE #1 and DoE #2.

	<i>DoE #1</i>	<i>DoE #2</i>
<i>P [W]</i>	200, 275, 350, 425, 500	300, 325, 350, 375, 400
<i>v [mm/min]</i>	600, 1000, 1400	700, 850, 1000
<i>Q_p [g/min]</i>	3, 5, 8	5

The resulting STs were examined using the procedure outlined in Appendix A.1 Step 1: Single tracks. The findings were summarized in Fig 4.3, where dilution was plotted over AR. Selected examples of OM micrographs illustrating extremes and acceptable cross-section geometries were included.

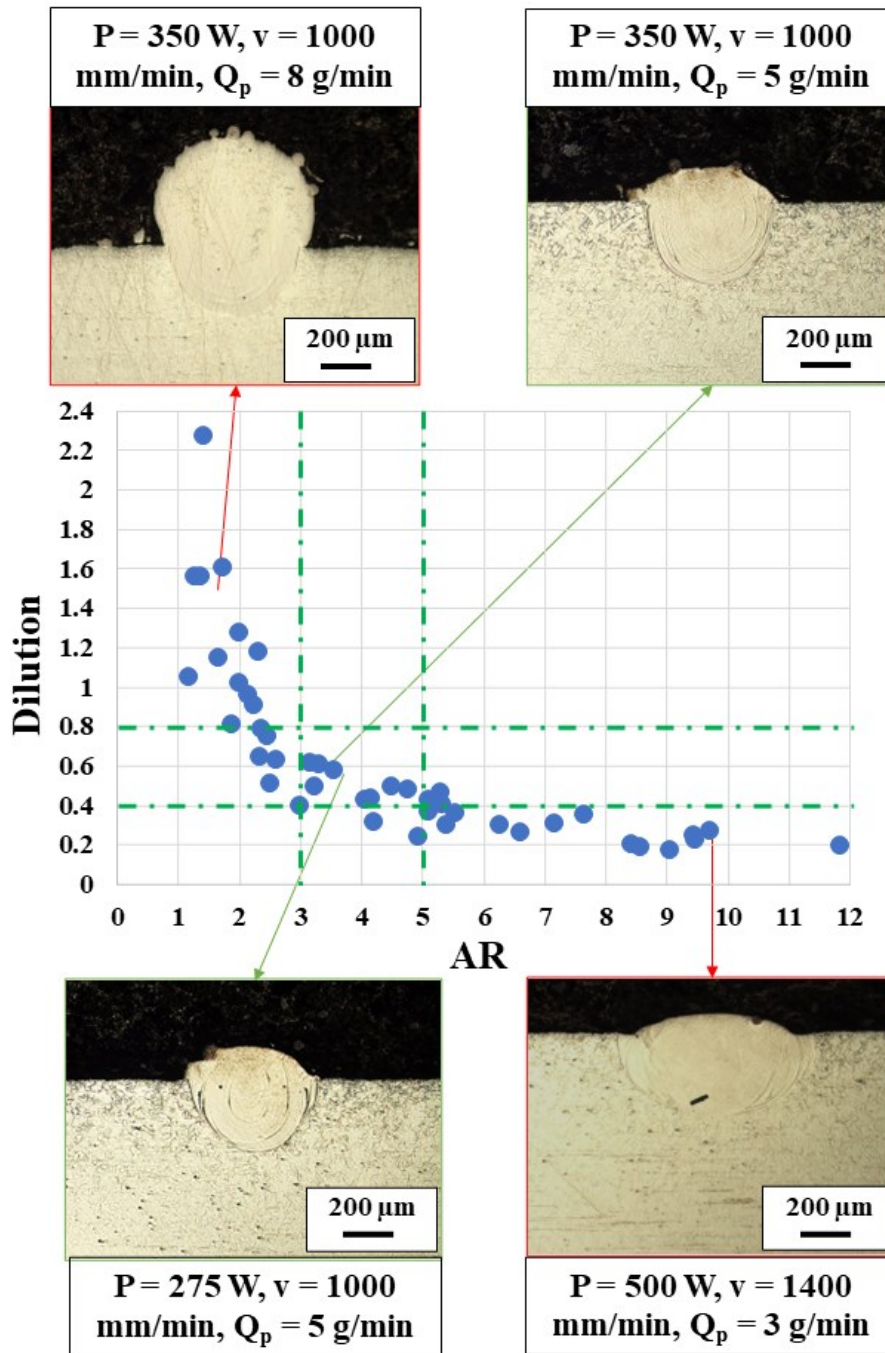


Figure 4.3 Diagram summarizing the dilution over AR with selection criteria lines with selected OM micrographs of STs representing different extremes and acceptable melt pool geometries for DoE #1 of 18Ni-300.

Fig. 4.3 depicted a clear trend in dilution over AR results. Criteria lines were established with dilution values between 0.4 and 0.8 and AR values between 3 and 5. These criteria were determined considering the machine's laser spot diameter of 0.3 mm, which led to narrower energy distribution and subsequently lower dilution values when compared to the values used for chapter 2 and chapter 3. After analysing the results and establishing clear trends, a second DoE (DoE #2) for ST deposition was formulated, with the parameters reported in Table 4.2 under the DoE #2 column.

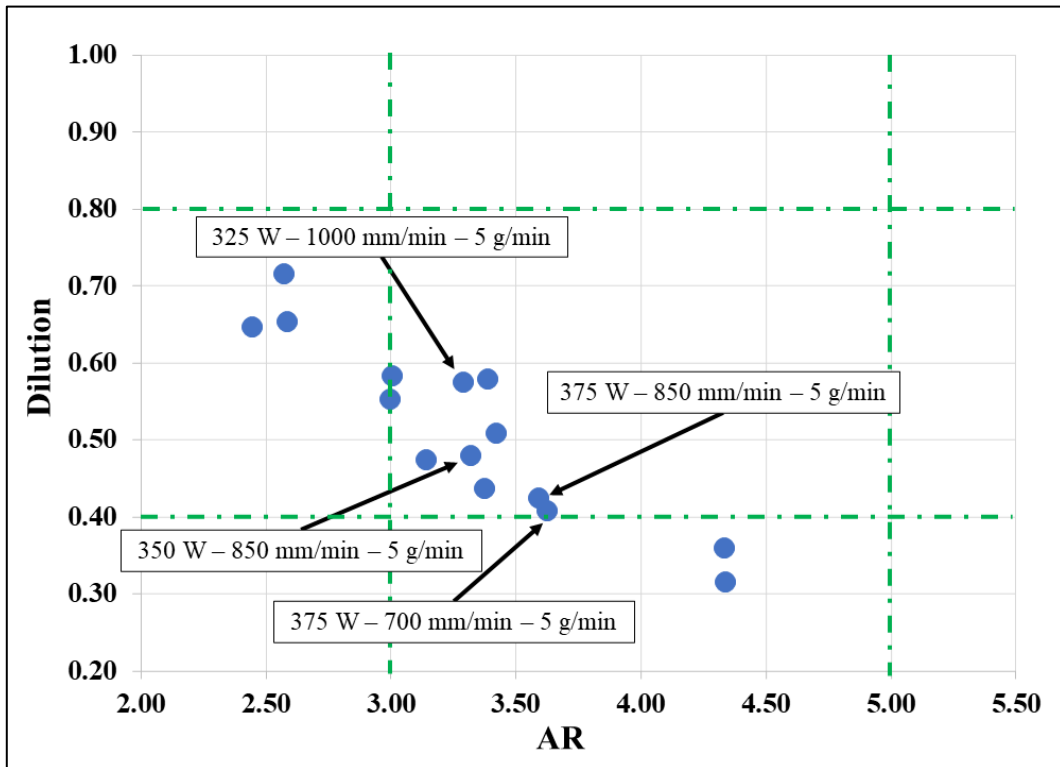


Figure 4.4 Diagram summarizing dilution over AR with selection criteria lines for DoE #2.

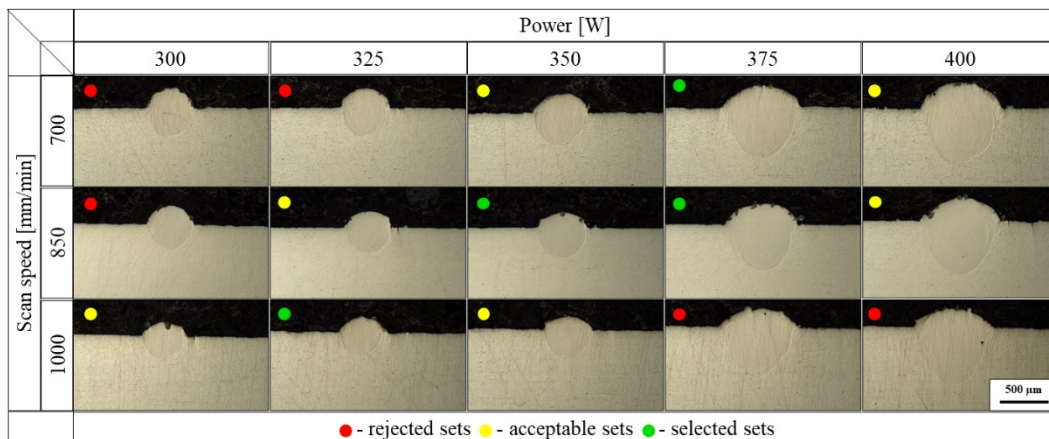


Figure 4.5 Optical micrographs of cross-sections of the 18Ni-300 STs from DoE #2 with coloured marks. Based on results in Fig. 4.4, if outside of the criteria line marked with red, if inside marked with yellow or green.

The DoE #2 results, shown in Fig. 4.4, indicated that most results fell within the criteria lines ($0.4 \leq \text{dilution} \leq 0.8$; $3 \leq \text{AR} \leq 5$). Only five sets, marked with red circles in Fig 4.5, did not meet the criteria. Four sets, marked with green circles, were selected for further deposition of SLs based on their position within the process window.

For the SLs, two different overlapping percentages were employed, 30 % and 40 % respectively. In Table 4.3, sets of parameters from 1 to 8 were labelled, reporting P, v, Q_p , bead width (W), Ov, h_d , specific surface energy density (E_s), the

measured layer thickness (Δz). The value Δz was subsequently used for cube with $20 \times 20 \times 15 \text{ mm}^3$ dimensions deposition.

Table 4.3 Labelled sets of parameters used for creation of SLs.

<i>Label</i>	<i>P</i> [W]	<i>v</i> [mm/min]	<i>Q_p</i> [g/min]	<i>W</i> [mm]	<i>O_v</i> [%]	<i>h_d</i> [mm]	<i>E_s</i> [J/mm ²]	<i>Δz</i> [mm]
1	375	700	5	0.78	30	0.55	58.9	0.48
2	375	700	5	0.78	40	0.47	68.7	0.53
3	375	850	5	0.73	30	0.51	51.8	0.38
4	375	850	5	0.73	40	0.44	60.4	0.43
5	350	850	5	0.50	30	0.35	70.6	0.49
6	350	850	5	0.50	40	0.30	82.4	0.63
7	325	1000	5	0.49	30	0.34	56.9	0.36
8	325	1000	5	0.49	40	0.29	66.3	0.40

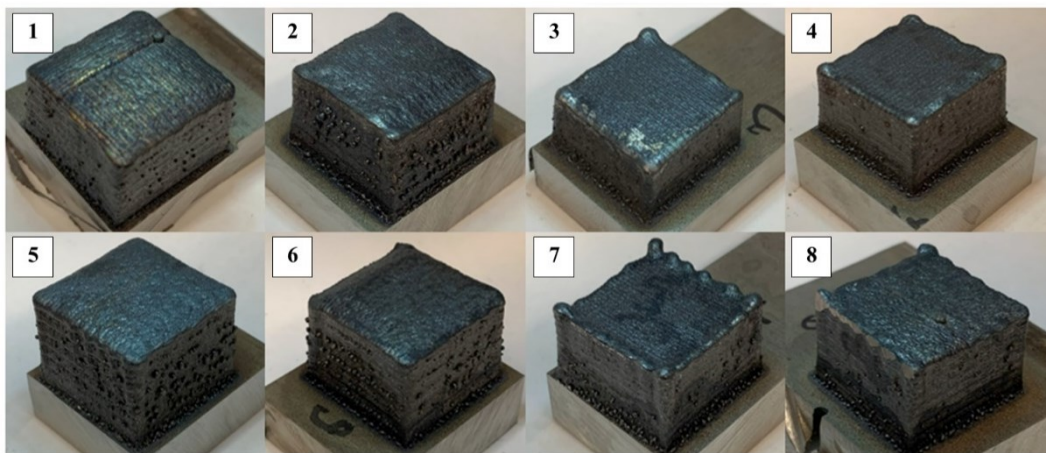


Figure 4.6 Pictures of cubes built with different sets of parameters, labelled as indicated in Table 4.3.

The deposited cubes, labelled as per Table 4.3, were illustrated in Fig. 4.6. While some cubes exhibited edge defects, potentially indicating unsuitable process parameters [24], all deposited cubes were evaluated for porosity using the method described in Appendix A.3.

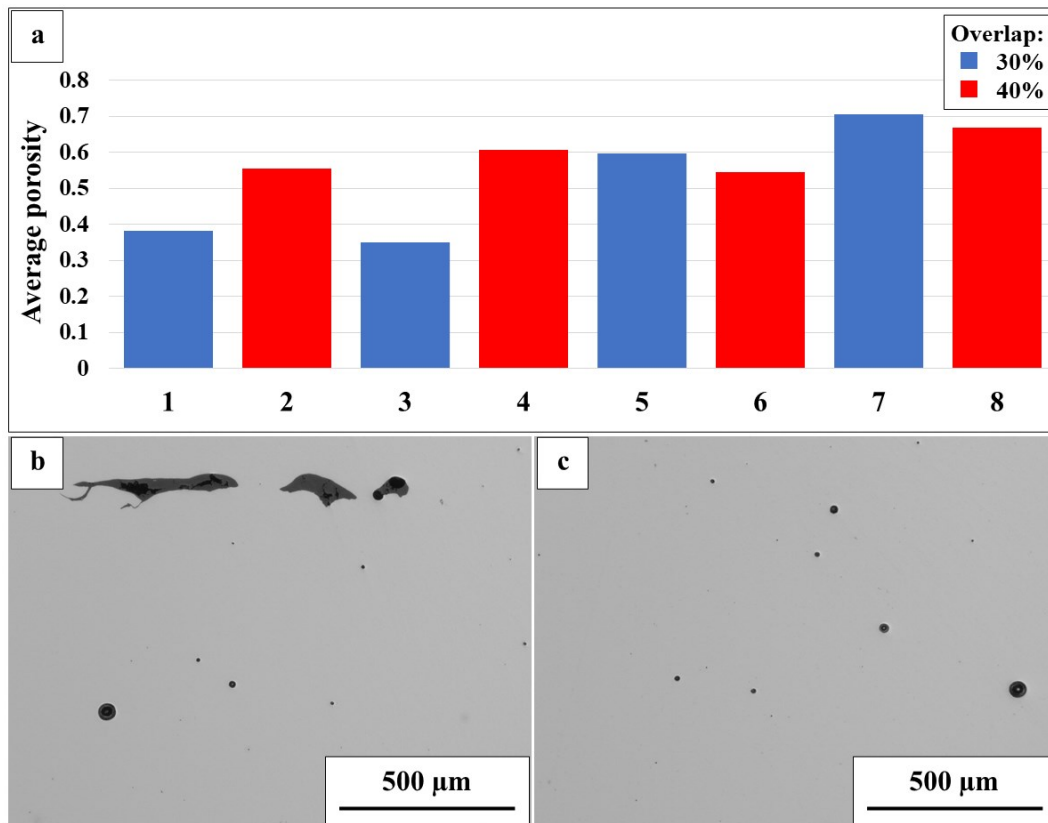


Figure 4.7 a) Average porosity per sample, b) example of void porosity, and c) example of different sizes of gas pores.

Average porosity results were plotted in Fig. 4.7 (a). The evaluation revealed that sample 3, despite having slightly poorer geometrical fitting (as seen in Fig. 4.6), exhibited the lowest porosity. Thus, sample 1, with slightly higher measured porosity (0.38 %), was selected as the optimal parameter set. Sample 7 showed the highest porosity of 0.71 %, correlating with its inferior geometrical fitting.

In all samples, two types of porosity were identified: void porosity (Fig. 4.7(b)) and various sizes of gas porosity (Fig. 4.7(c)). The void porosity likely resulted from the deposition strategy, which involved a 90° rotation after every two layers. This rotation method is suspected to have caused the observed voids due to the second layer, scanned in the same direction, being unable to fill the gaps between tracks in the previously deposited layer. Additionally, the first perpendicular layer may have been unable to adequately fill the V-shaped spaces between adjacent tracks in the previous layers, especially when the same scanning orientation was used two previously deposited layers causing the deeper V-shaped spaces as opposed to utilizing a 90° rotation after each layer. Gas porosity, on the other hand, could be reduced through optimization of gas flow rates.

Interestingly, the porosity results did not indicate that increasing the overlap percentage would result in lower porosity. For a comprehensive evaluation, cube pairs (1-2, 3-4, 5-6, and 7-8) were considered due to their same main process parameters (P , v , Q_p). For the first two pairs (cube pairs 1-2 and 3-4), an increase in Ov from 30 % to 40 % led to higher porosity levels. However, for the last two pairs (cube pairs 5-6 and 7-8), it resulted in a slight decrease in porosity.

In the final step, microhardness measurements were conducted on all samples, taken 5 mm above the substrate. The mean values are detailed in Table 4.4, along with the E_v used for the deposition, calculated using the eq. 14 from Appendix A.3, of each cube and the corresponding measured porosity.

Table 4.4 Measured microhardness, porosity and utilized energy density for each cube deposited.

<i>Cube</i>	<i>Energy density</i> [J/mm ³]	<i>Porosity</i> [%]	<i>Microhardness</i> [HV]
1	121.9	0.38	339.6 ± 5.7
2	130.1	0.55	341.3 ± 6.5
3	136.0	0.37	338.7 ± 6.0
4	141.5	0.60	329.4 ± 5.1
5	143.2	0.59	340.1 ± 4.3
6	130.7	0.53	340.3 ± 3.1
7	160.1	0.71	345.7 ± 5.2
8	164.2	0.67	334.6 ± 4.1

The absence of any noticeable trend in microhardness results, despite the varying energy densities during cube deposition, is intriguing. This phenomenon might be attributed to the unique characteristics of the 18Ni-300 material, which undergoes age hardening where the grain size, influenced by cooling rates, does not play a significant role [204]. However, it is worth noting that if the deposited sample had a larger volume and the deposition duration were extended, it is highly likely that Intrinsic Heat Treatment (IHT) would cause precipitate formation. Under these conditions, correlations between process parameters and hardness could potentially be identified.

Table 4.5 Summarized process parameters and calculated specific volumetric energy density for the selected set of parameters (cube 1).

<i>Parameters</i>	<i>Value</i>
<i>Powder</i>	375 W
<i>Scan speed</i>	700 mm/min
<i>Powder feed rate</i>	5 g/min
<i>Bead width</i>	0.78 mm
<i>Overlap</i>	30 %
<i>Z-axis increment</i>	0.48 mm
<i>Laser spot diameter</i>	0.30 mm
<i>Carrier gas (Ar)</i>	5 L/min
<i>Shielding gas (Ar)</i>	12 L/min
<i>Specific surface energy density</i>	58.9 J/mm ²
<i>Specific volumetric energy density</i>	121.9 J/mm ³

Following meticulous analysis, the parameter set used for cube 1, summarized in Table 4.5 yielding E_v of 121.9 J/mm³, was chosen for further detailed examination. This decision was primarily based on the geometric fit and the level of porosity observed in the sample. These factors, coupled with the absence of a

clear microhardness trend, highlighted the significance of geometric precision and porosity control in the overall material quality.

4.3 Microstructural analysis of 18Ni-300 samples built with optimized parameters

After selecting the set of parameters, cubic samples with dimension 15 x 15 x 15 mm³ were deposited on a 304L substrate. They were produced using a simple zigzag pattern, with a 90° rotation after every two layers. Subsequently, the samples underwent meticulous preparation for in-depth analysis, following the outlined procedure detailed in Appendix B.3, titled "Microstructural and Mechanical Analysis – Equipment and Procedure.

The first microstructural observations were made through a Optical Microscope.

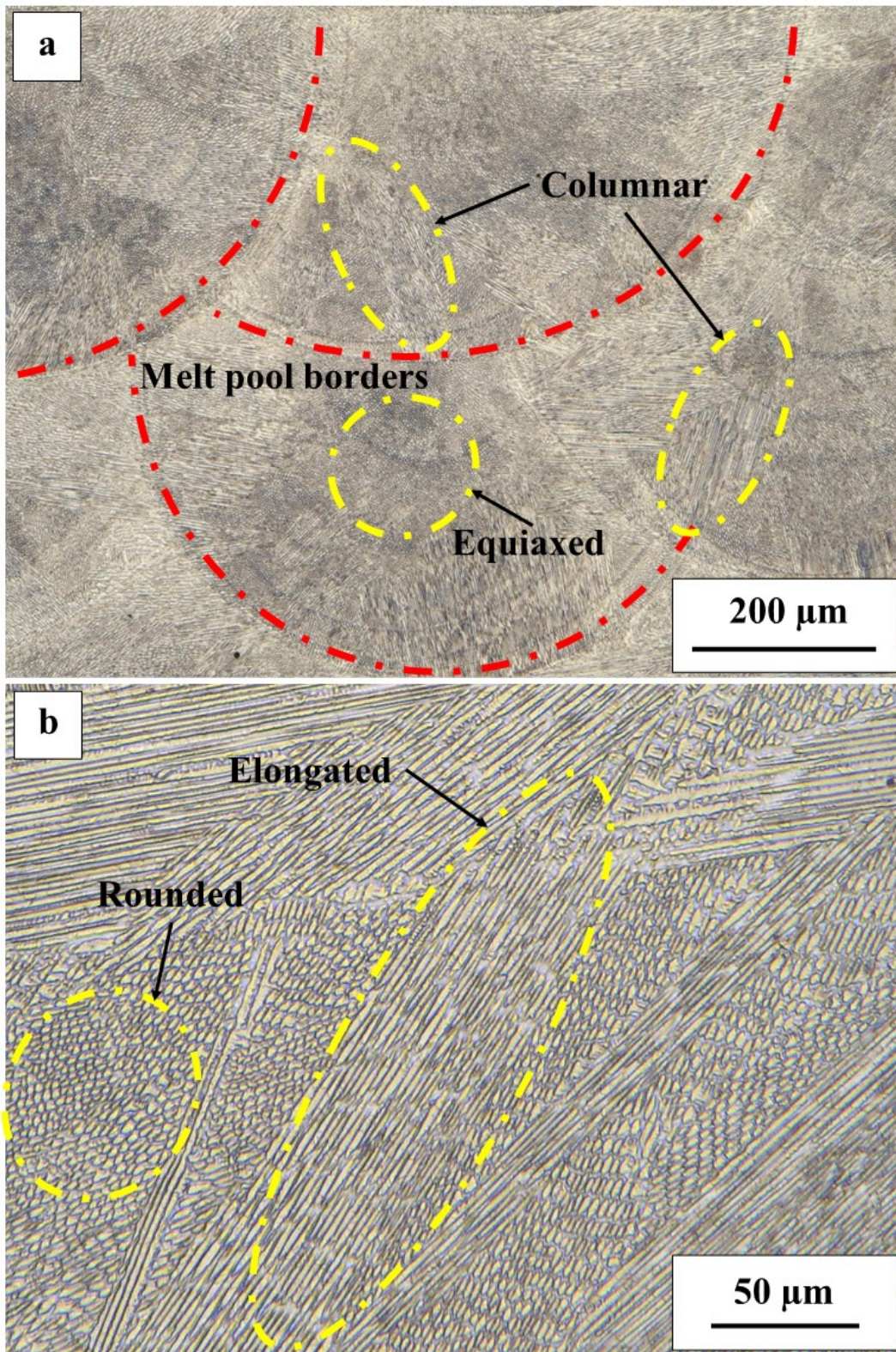


Figure 4.8 OM micrographs of etched as-built 18Ni-300 showing: a) interconnected melt pools, b) dendritic microstructure with both rounded and elongated cells.

The optical micrograph presented in Fig 4.8 (a) offers a glimpse into the typical AM microstructure of as-built 18Ni-300. This structure is characterized by interconnected melt pools and grains displaying a dendritic-cellular pattern. The

micrograph clearly highlights the borders of melt pools, some of which are delineated with red dashed lines. Within these melt pools, both columnar and equiaxed dendrites are visible. Columnar dendrites are oriented towards the melt pool border, while equiaxed dendrites are centrally located within melt pools, as indicated in Fig. 4.8 (a). Moving on to Fig. 4.8 (b), it reveals elongated dendrite arms and rounded cells, a microstructure commonly observed in L-DED built samples [152], [205].

Given that 18Ni-300 is a precipitation-hardening maraging steel, a closer analysis of the microstructure was conducted using SEM microscope.

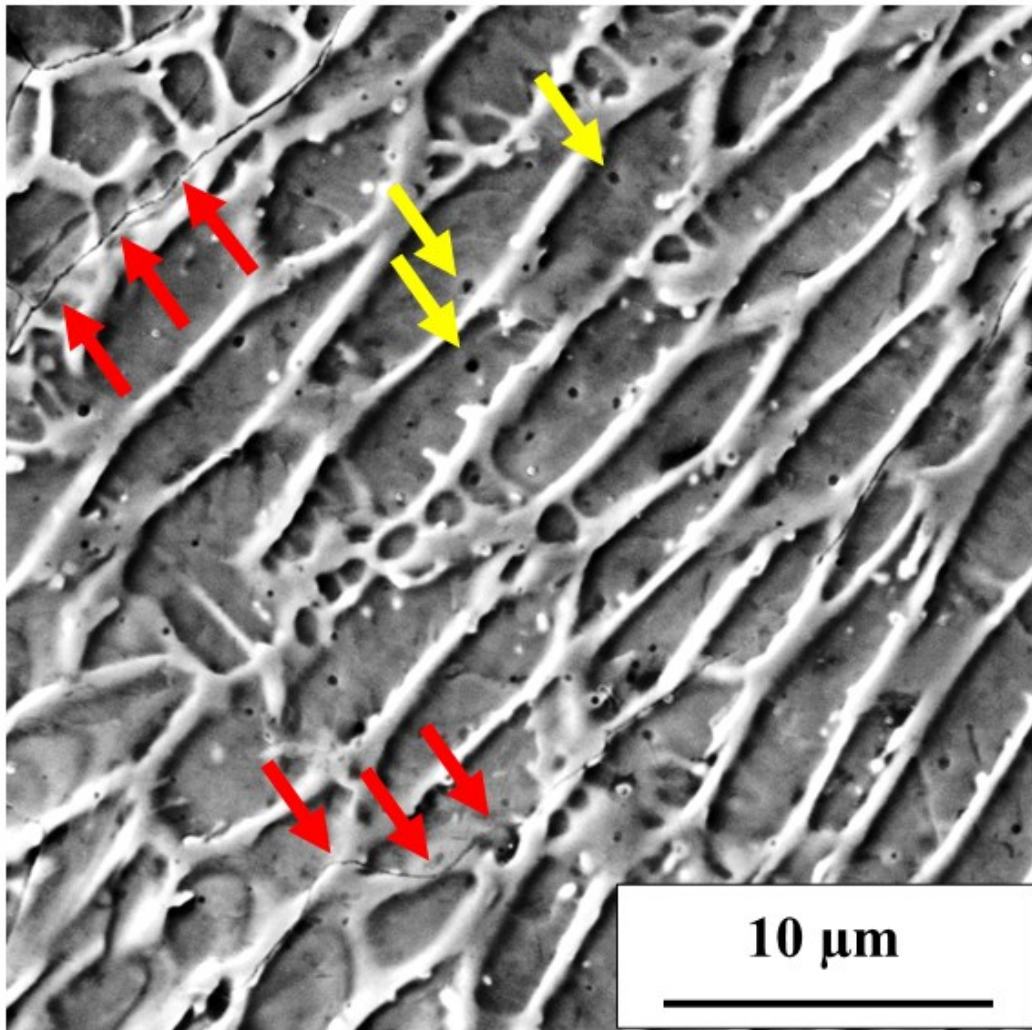


Figure 4.9 SEM micrograph of as-built 18Ni-300, red arrows highlighting grain boundaries and yellow arrows highlighting black precipitates.

The SEM micrograph of the as-built 18Ni-300 microstructure, presented in Fig. 4.9, reaffirms the previously observed elongated cellular-dendritic pattern. Apart from elongated cells, the microstructure exhibits distinctive intercellular regions, along with some black nanoparticles indicated by yellow arrows. Additionally, red arrows point out certain grain boundaries, likely related to sub-grain boundaries. In L-DED-built samples, martensite laths are expected within cells, while austenite is anticipated in the intercellular region due to micro-segregation of alloying elements.

The formation of nanoprecipitates in L-DED samples is influenced by in-process IHT, crucial for age-hardenable precipitation-hardening alloys like 18Ni-300 [205]. Studies by Jäggle et al. [206], [207] have identified the presence of Ti-Ti clustering in the middle section of L-DED-built samples, leading to Ni₃Ti precipitation.

To gain deeper insights into the phases and element distribution, an energy-dispersive X-ray spectroscopy (EDS) mapping was performed on the region depicted in Fig. 4.9.

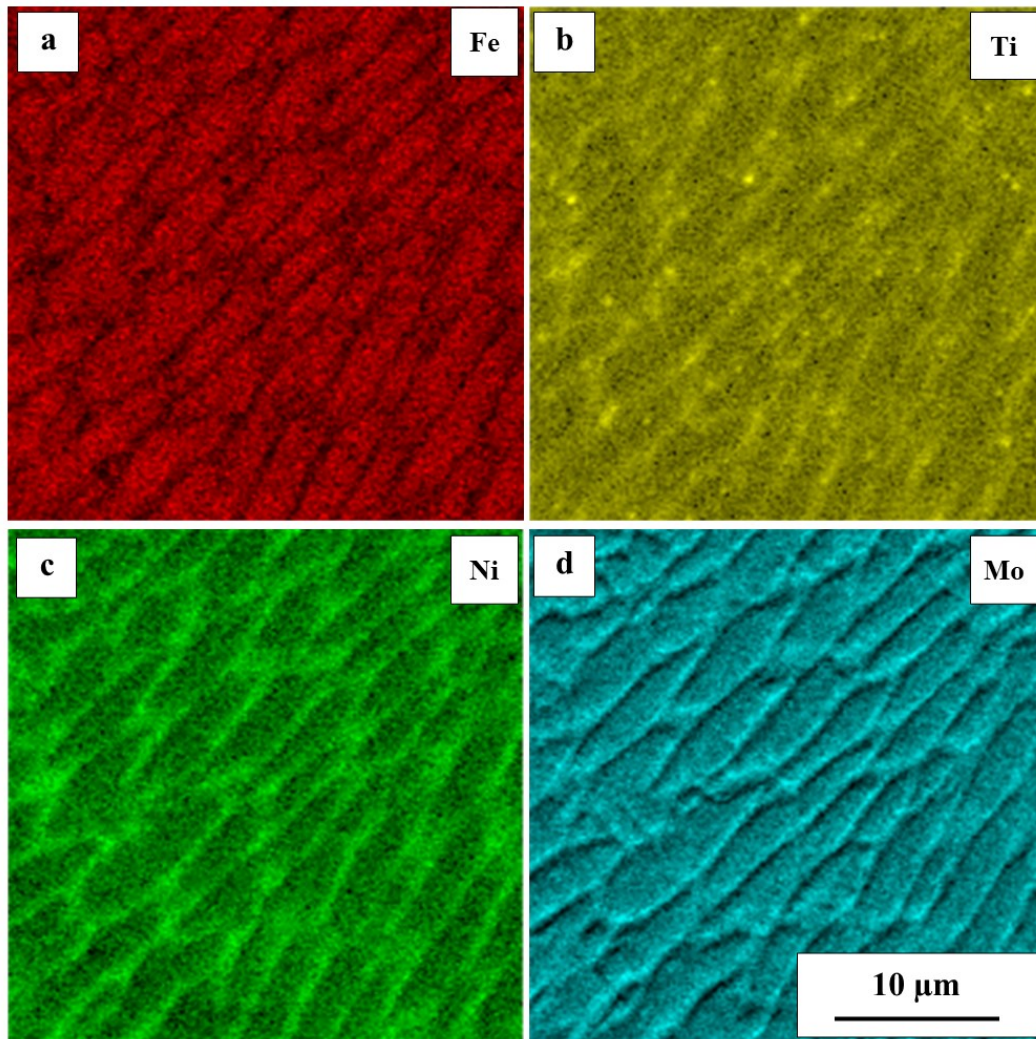


Figure 4.10 EDS element maps corresponding to the SEM micrograph from Fig. 4.9 of: a) Fe, b) Ti, c) Ni, and d) Mo.

The EDS maps in Fig. 4.10 vividly illustrate the typical micro-segregation of alloying elements during AM processes. The Fe map (Fig. 4.10 (a)) reveals higher Fe concentration within cells compared to cell boundaries. Conversely, elements Ti, Ni, and Mo (Fig. 4.10 (b), (c), and (d) respectively) exhibit higher concentrations in the intercellular region, likely associated with the retained austenite phase. Although Ti and Mo are known as ferrite-stabilizing elements, thermal calculation analysis indicates that their presence, along with high Ni content, reduces the martensite start temperature, stabilizing austenite at lower temperatures. Therefore, the elevated concentrations of Ti and Mo promote the formation of retained

austenite [205], [206], [208]. Fig. 4.10 (b) shows clusters of Ti corresponding to the black particles observed in the SEM micrograph (Fig. 4.9), making them highly likely to be Ni_3Ti precipitates [207].

To gain a comprehensive understanding of the present phases and confirm their identities, further analyses such as EBSD and XRD measurements would be necessary.

Regarding the mechanical response, microhardness measurements were conducted along the Z-axis, and the results are depicted in Fig. 4.11.

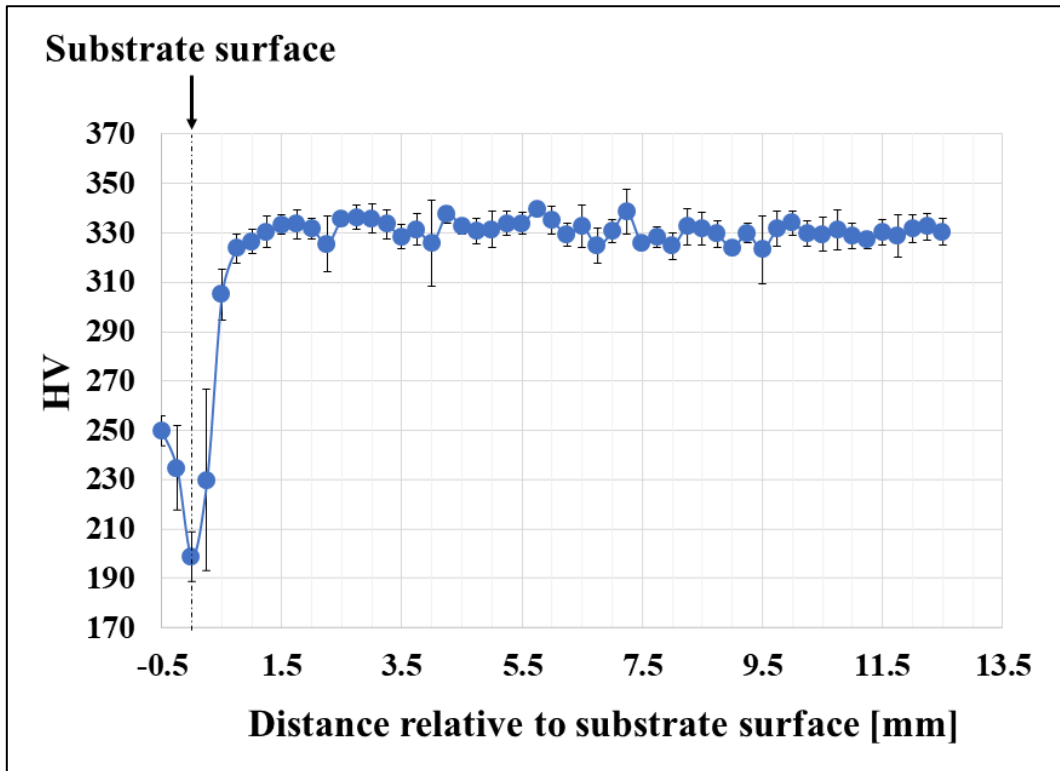


Figure 4.11 Results of microhardness measurements along building direction for 18Ni-300.

Interestingly, the microhardness measurements did not reveal any discernible trend along the building direction, except for the transition from the 304L substrate to the deposited 18Ni-300 maraging steel. The mean microhardness value, calculated using measurements taken from 2.5 mm above the substrate, was 331 ± 4 HV. When compared to the study conducted by Amirabdollahian et al. [204], a discrepancy of nearly 30 HV was noted. This variance could be attributed to the specific L-DED machine used and/or the size of the deposited samples. However, the uniform microhardness observed suggests a relatively consistent microstructure along the building direction. This uniformity indicates that L-DED-produced samples could be a promising choice for direct aging heat treatment applications.

Chapter 5

L-DED in repair of D2 steel components

In this chapter, the focus is on the use of L-DED as repair process especially for industrial tools from the perspective of substrate material. These investigations were conducted under the regional project 4ASSI “4 Assi Assieme per innovare”, funded by Regione Piemonte with Grant POR FESR Piemonte 2014-2020 Piattaforma tecnologica di “Bando PiTeF, which involved four partners, including Michelin as coordinator, and Politecnico di Torino.

The chapter is structured as follows:

- Characterization and preparation of an industrial tool for repair process
- Repair process of D2 steel using the W360 steel by L-DED

5.1 Characterization and preparation of an industrial tool for repair process

In the framework of 4ASSI project, a worn blade made of D2 cold work tool steel was received from the Michelin factory located in Cuneo, Italy. This blade had been utilized in the process of cutting natural and artificial rubber into smaller pieces for further production of tires. Upon reception, the blade was sliced into 8 mm thick pieces to create smaller substrates for subsequent analyses. Fig. 5.1 (a) displays the original blade, while Fig. 5.1 (b) showcases the sliced blade prepared for material analysis. Additionally, Fig. 5.1 (c) provides a technical drawing of the blade.

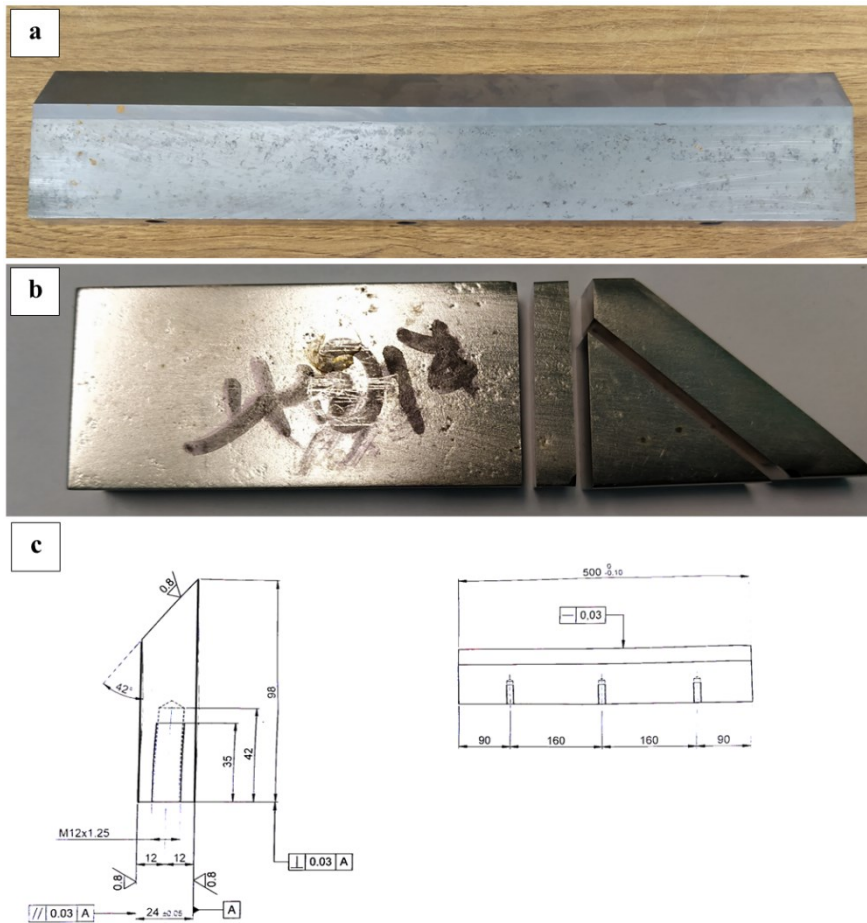


Figure 5.1 Received worn industrial blade: a) picture of received blade, b) sliced blade for material investigation, and c) technical drawing of as produced blade.

Table 5.1 Nominal chemical composition of D2 cold work tool steel.

%wt.	<i>C</i>	<i>Cr</i>	<i>Mo</i>	<i>Si</i>	<i>Mn</i>	<i>V</i>	<i>Fe</i>
<i>D2</i>	1.56	11.0	0.77	0.45	0.42	0.78	Bal.

The blade material was D2 tool steel, with its nominal chemical composition detailed in Table 5.1. The as-received blade exhibited a hardness of approximately 700 HV, indicating its hardened state achieved through processes involving austenitization, quenching, and tempering. This high level of microhardness represents also a fundamental requirement to be satisfied in repairing. Subsequently, the blade microstructure was examined using an OM microscope to gain insights into its composition.

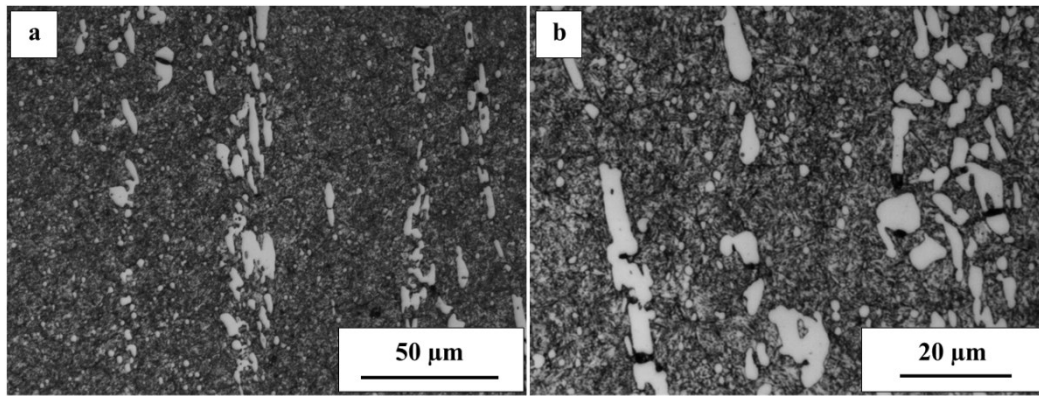


Figure 5.2 OM micrographs revealed microstructure of as-received D2 steel.

Fig. 5.2 illustrates the microstructure consisting of large carbides dispersed within a martensitic matrix. The carbides were primarily identified as M_7C_3 , with some presence of $M_{23}C_6$.

To gain a deeper understanding of D2 steel behaviour during the repair process, 20 mm long STs were created on substrates with dimensions of 24 x 20 x 8 mm³. These STs, involving various combinations of laser passes before and after deposition, were generated using AISI 316L powder for demonstration purposes. The STs were deposited using previously defined parameters, as reported in Chapter 2: 800 W – 600 mm/min – 8 g/min. Different combinations of laser-only passes and laser-powder passes were explored, leading to four distinct combinations labelled I to IV, as indicated in Table 5.2. These combinations were deposited with or without laser preheating and with or without laser remelting of the deposited STs.

Table 5.2 Combinations for 316L STs deposition on D2 substrate.

<i>ST label</i>	<i>Laser preheat</i>	<i>Deposition</i>	<i>Laser remelt</i>
<i>I</i>	On	On	On
<i>II</i>	Off	On	On
<i>III</i>	On	On	Off
<i>IV</i>	Off	On	Off

The resulting samples were prepared for cross-sectional analysis following the procedure outlined in Appendix A.1. The outcomes are summarized in Fig. 5.3.

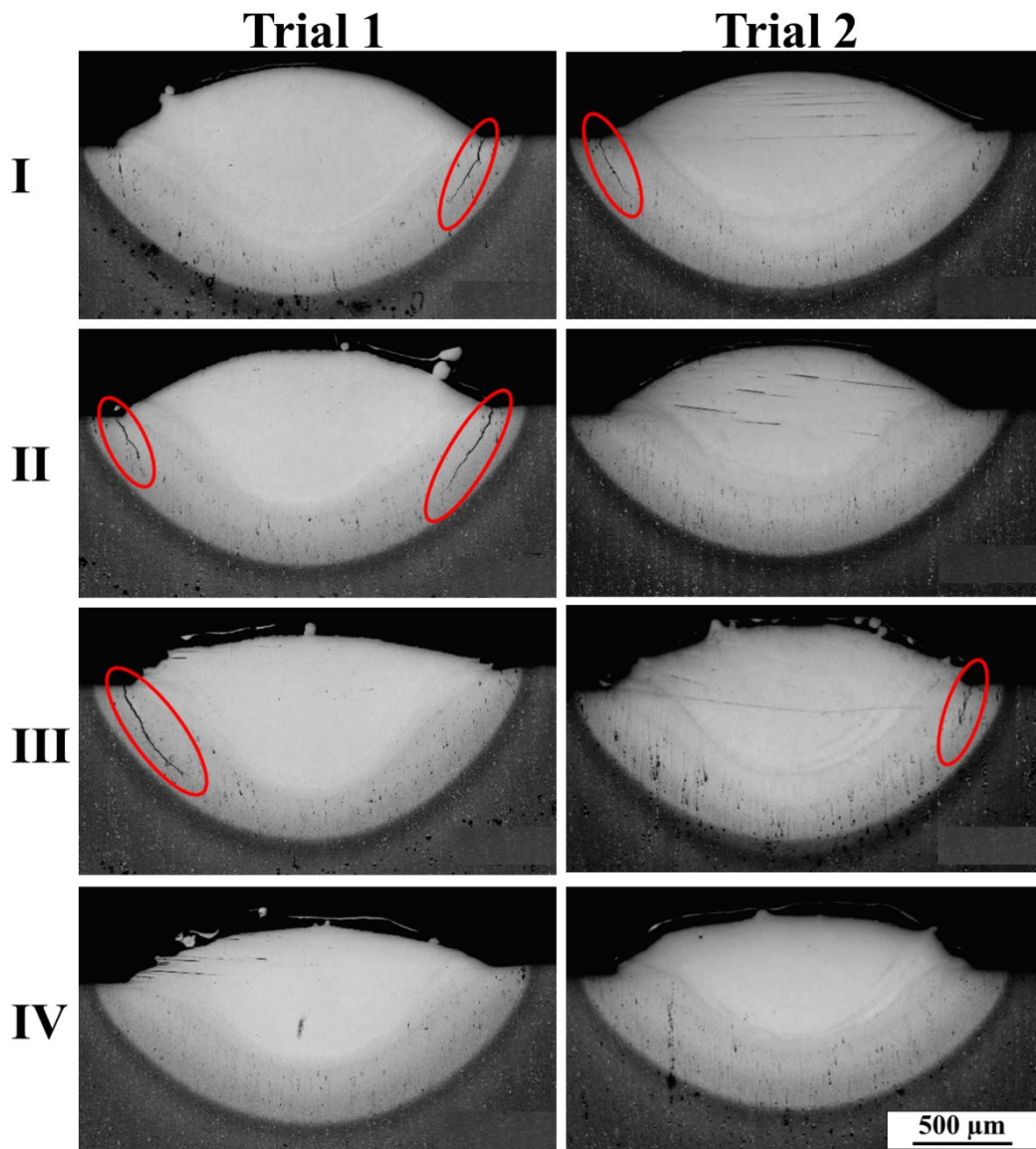


Figure 5.3 OM micrographs of 316L STs deposited on as-received D2 steel with different combinations of laser passes.

The OM micrographs in Fig. 5.3 revealed ductility dip cracks in the HAZ on the sides of the deposited STs, particularly near the deposited material where ductility drops along the solid metal [209]. Intriguingly, the only combination (IV) that did not display any cracks involved a single deposition pass, devoid of laser preheating or remelting. It's noteworthy that the D2 steel, due to its chemical composition, falls into the category of non-weldable steels susceptible to both cold and hot cracking according to welding literature. When utilized eq. 1 for equivalent carbon content, D2 steel exhibits a value of 4.14 %.

In an attempt to modify D2 steel properties and reduce its hardness and brittleness, annealing was carried out using a tubular furnace (Nabertherm RHTC 80-710/10), described in Appendix B.2.3. The heat treatment process involved heating the samples to 860 °C, the A_{c3} temperature and holding them at this temperature for 30 minutes. Subsequently, the samples were cooled down with two different rates: firstly to 780 °C with a cooling rate of 60 °C/h, and then to 700 °C

with a rate of 20 °C/h. To allow the austenite transform to ferrite crystal structure. Finally, the samples were air-cooled to room temperature. The annealed samples were polished to remove surface char formed during the heat treatment.

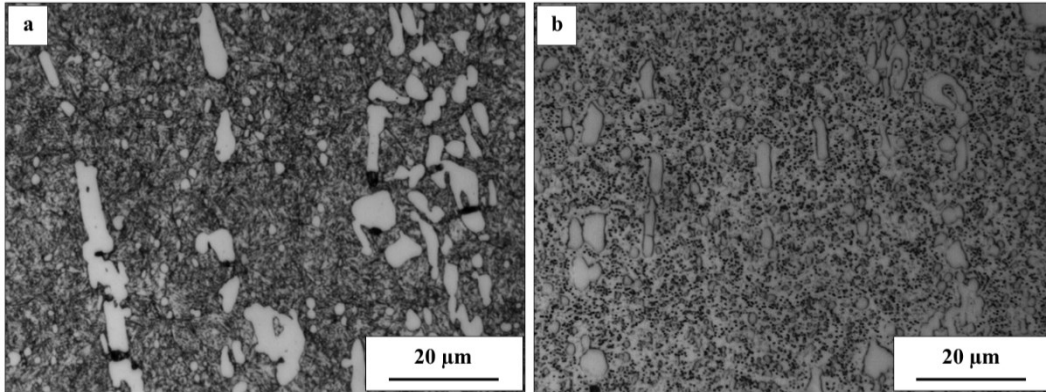


Figure 5.4 OM micrographs showing the microstructure of: a) as-received D2 steel, b) annealed D2 steel.

Observation of the annealed D2 microstructure through OM microscope (Fig. 5.4) revealed significantly different microstructures. In Fig. 5.4 (a), the carbides were larger and distinctly visible. After the annealing heat treatment, the carbides were mostly dissolved in the metal matrix, which was now suspected to be ferritic due to the slow cooling process during annealing.

X-ray Diffraction (XRD) analysis was performed to compare the phases present in the as-received and annealed conditions.

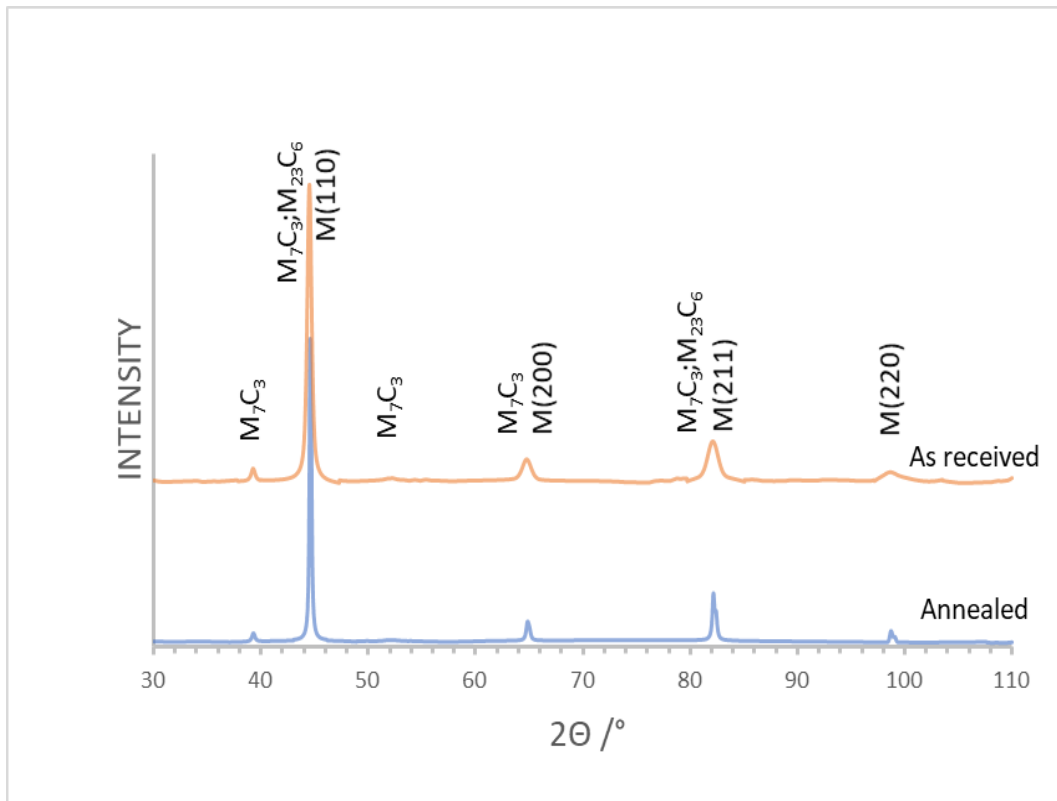


Figure 5.5 XRD patterns of as-received and annealed D2 steel.

The XRD patterns in Fig. 5.5 indicated the presence of M_7C_3 carbides and α -ferrite peaks in both samples. Although carbide peaks were still present in the annealed condition, they were significantly lower in intensity. The peaks at 44.6° , 64.9° , 82.2° , and 98.7° were possibly corresponding to martensite or ferrite. However, the as-received state was expected to be martensitic due to prior austenitization and quenching, and annealing allowed carbon diffusion, leading to the formation of soft ferrite.

The annealing process was primarily aimed at reducing D2 steel hardness. Consequently, microhardness measurements were performed, revealing a drop in hardness from around 700 HV to 232 HV.

After characterizing the annealed D2 steel, STs deposition was repeated on the as-received D2 substrate using the same deposition procedure as described in Table 5.2. The results presented in Fig. 5.6 demonstrated the absence of cracks in any of the trials for the various combinations performed. This finding suggested that utilizing annealed D2 steel as the substrate allowed successful deposition of new material, therefore allowing the repairing process by L-DED.

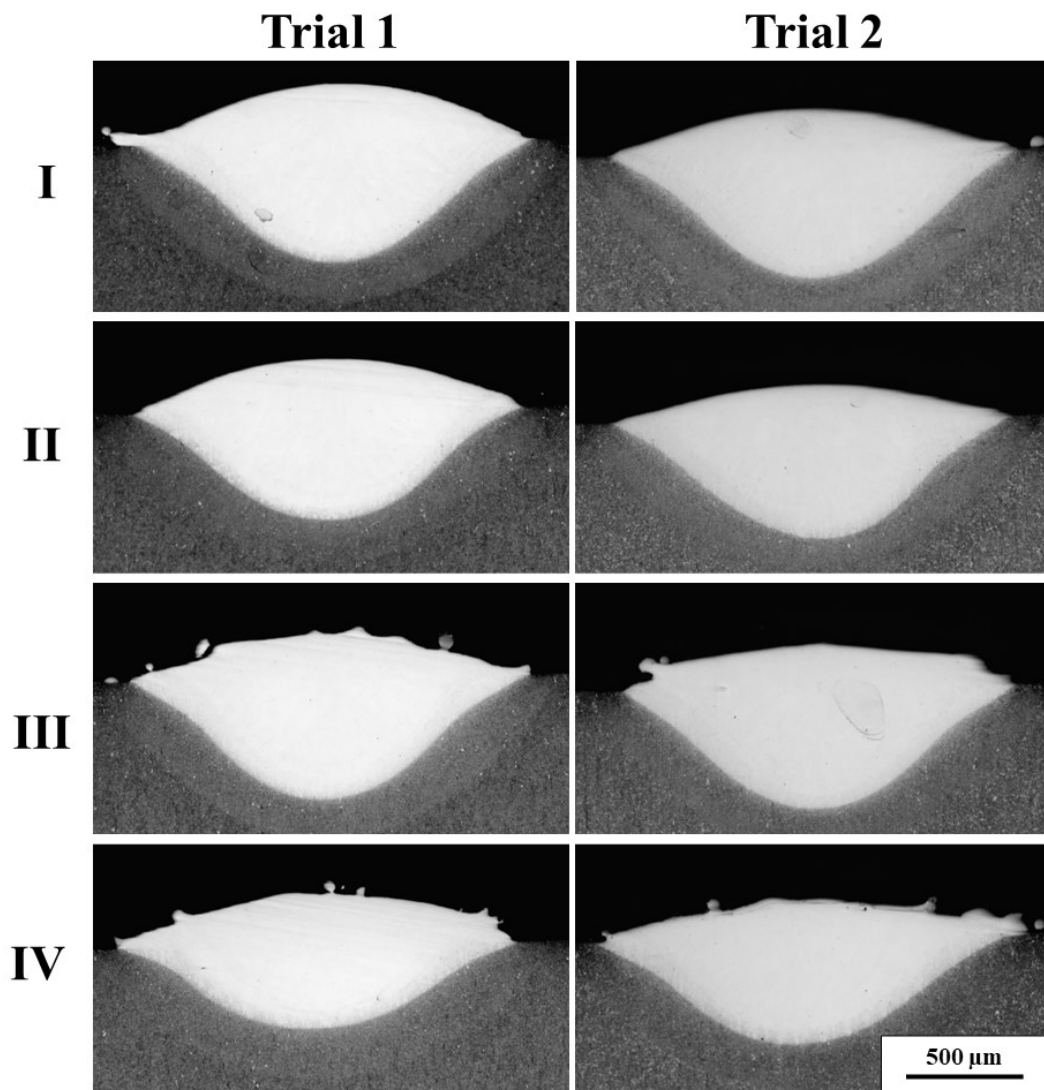


Figure 5.6 OM micrographs of 316L STs deposited on annealed D2 steel with different combinations of laser passes.

To explore the effects of heat transfer to the substrate, microstructural observations of the HAZ were conducted, along with microhardness measurements.

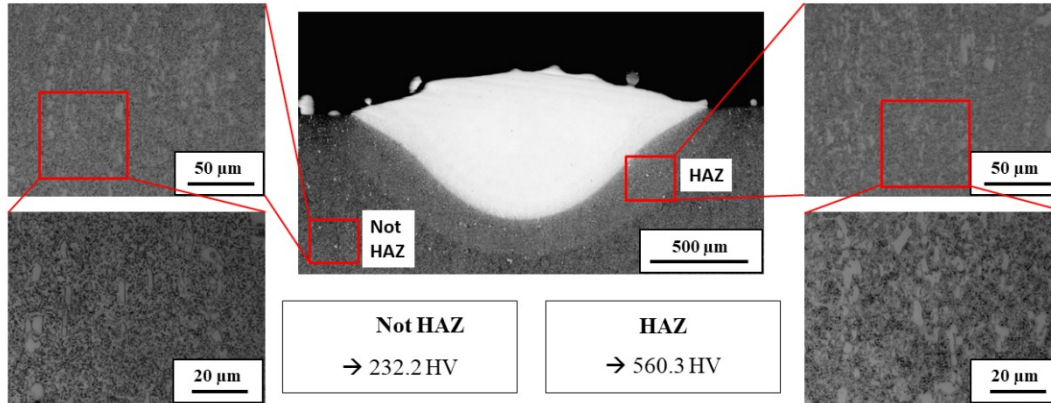


Figure 5.7 OM micrographs of the ST cross section with insert of micrographs showing the microstructure of not HAZ on the left and the microstructure of HAZ on the right, also microhardness measurements are reported for not HAZ and HAZ.

The OM micrographs in Fig. 5.7 revealed slightly coarser carbides in the HAZ due to the heat impact of the deposition. Additionally, there was a significant increase in microhardness compared to the non-HAZ area, rising from 232.2 HV to 560.3 HV. Despite the increased hardness, the absence of cracks in the depositions allowed the repair attempts to proceed.

5.2 Repair process of D2 steel using the W360 steel by L-DED

The W360 hot tool steel was selected for repairing the D2 cold work tool steel because both steels share the same alloying elements and can attain high hardness values of about 650 HV, offering good wear resistance. However, W360 has a lower equivalent carbon content, making it more suitable for L-DED deposition processes.

For the repair process, annealed D2 steel substrates measuring 24 x 20 x 8 mm³ were prepared. Four parallelepipeds of W360, each measuring 15 x 15 x 10 mm³, were deposited onto these substrates. After the deposition, two out of the four samples underwent heat treatment to recover the hardness of D2 steel, following the guidelines for hardening D2 steel. The heat treatment involved heating the samples to 750 °C for 90 minutes, holding them at this temperature for 30 minutes, further heating to 1050 °C for 120 minutes, holding for 15 minutes, and quenching in water. Tempering heat treatment was performed at 500 °C for 60 minutes, followed by air cooling, and the tempering cycle was repeated twice.

Microstructural analysis of both as-built and heat-treated samples was performed using OM, SEM, and EDS.

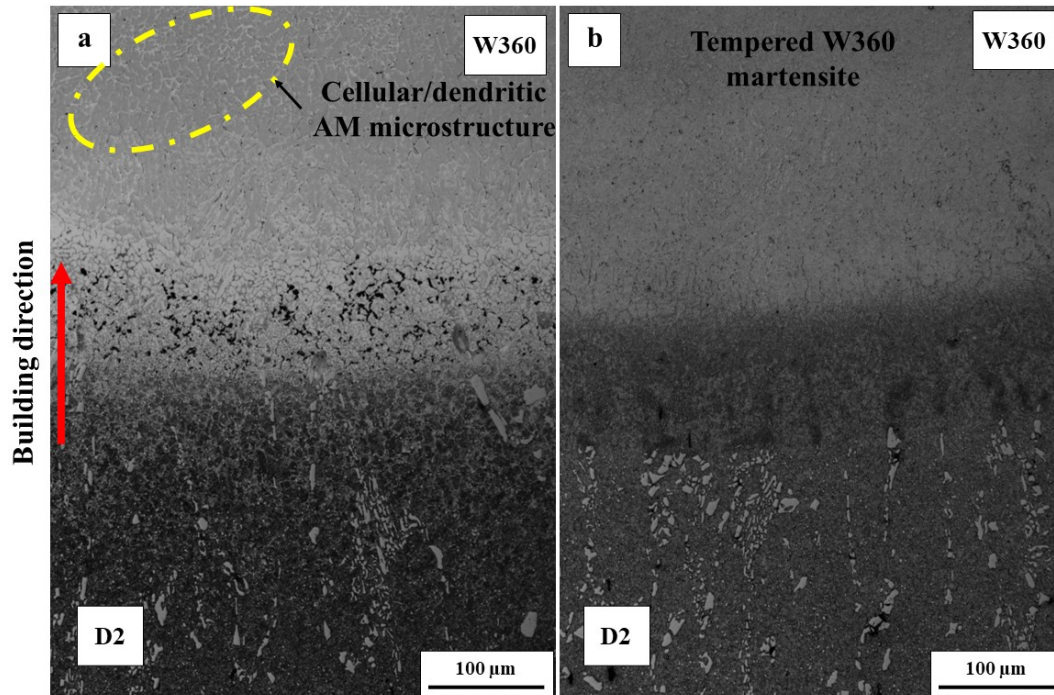


Figure 5.8 OM micrographs of transition zone between D2 substate and deposited W360 of: a) as-built sample, b) heat treated sample.

In the as-built sample (Fig. 5.8), the micrograph showed the typical AM microstructure constructed of a cellular-dendritic pattern of W360 in the top part, transitioning to the D2 substrate in the lower part. The carbides in the substrate were clearly visible within the dark metal matrix. In the heat-treated sample (Fig. 5.8b), the microstructure gradually changed as one moved from the W360 to the substrate. However, the carbides in the substrate showed no clear differences compared to the as-built sample, except in the color of the metal matrix, which was likely martensitic in the as-built sample and ferritic in the heat-treated sample. Notably, cracks were observed in the transition area between the materials in the heat-treated sample, as shown in Fig. 5.9.

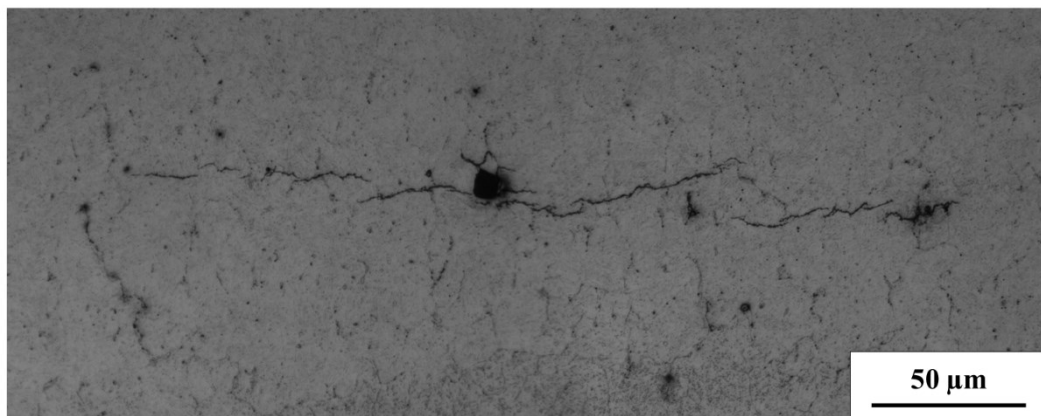


Figure 5.9 OM micrograph of a crack in the transition zone between deposited W360 and D2 substrate.

The observation of horizontal cracks following defects like gas porosity or carbides, particularly more pronounced towards the deposited material, suggested that the applied heat treatment, which included water quenching, was not suitable for the deposited material. This high cooling rate likely caused the cracks. To confirm this hypothesis, the same heat treatment was conducted on as-built W360 samples that were near to full dense and free of cracks when removed from the substrate. Similar horizontal cracks were found in the W360 samples after the heat treatment, confirming that the water quenching method led to cracks in the deposited material.

Therefore, the results indicated the need for an adjustment in the heat treatment process, specifically by changing the quenching media. Choosing a different quenching medium with a lower cooling rate could potentially prevent the formation of cracks in the deposited material. This adjustment is crucial to ensuring the integrity of the repaired components and preventing undesirable defects.

The microstructural analysis of samples consisting of W360 on D2 substrate was crucial to understanding the transition zone between the two materials.

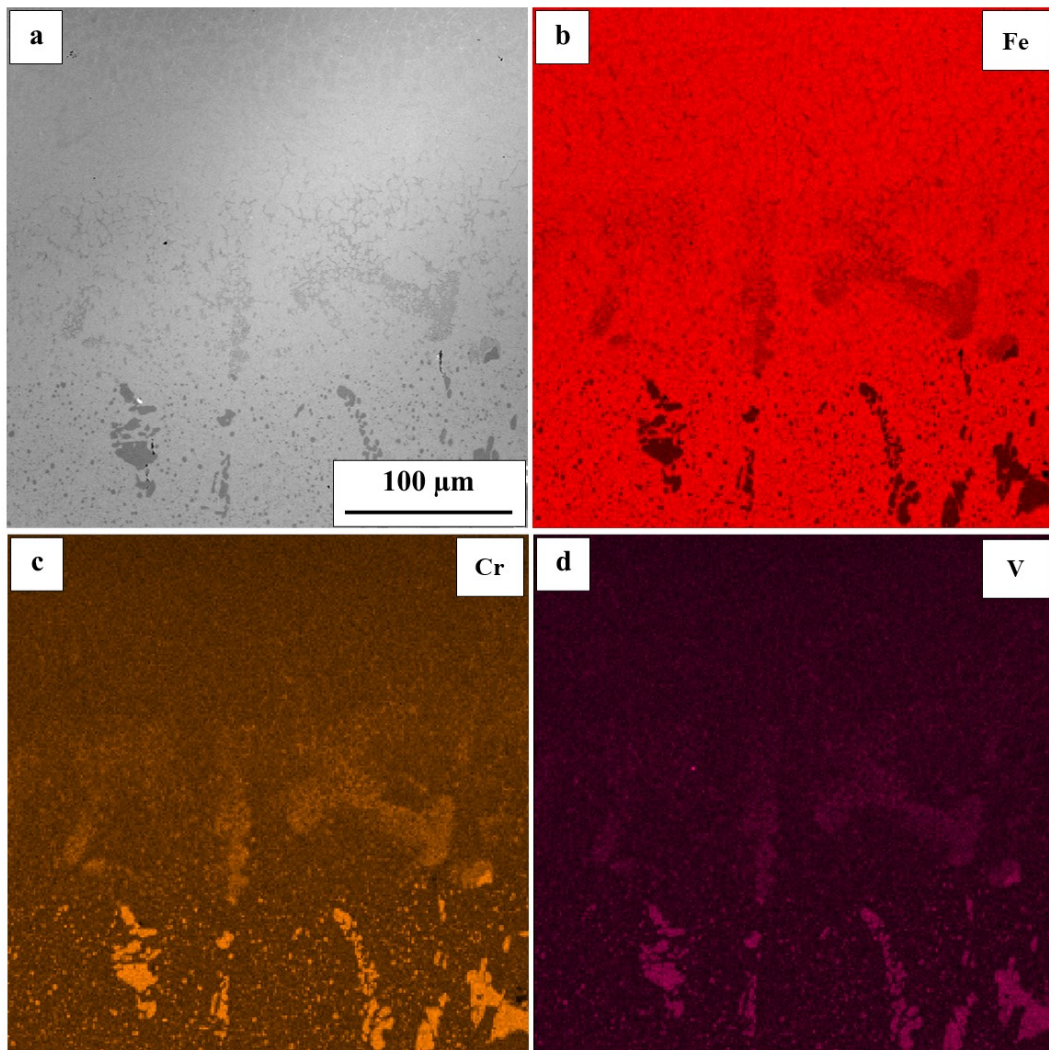


Figure 5.10 SEM micrograph of the transition zone between deposited W360 and D2 substrate in as-built sample with corresponding EDS maps for the most relevant elements.

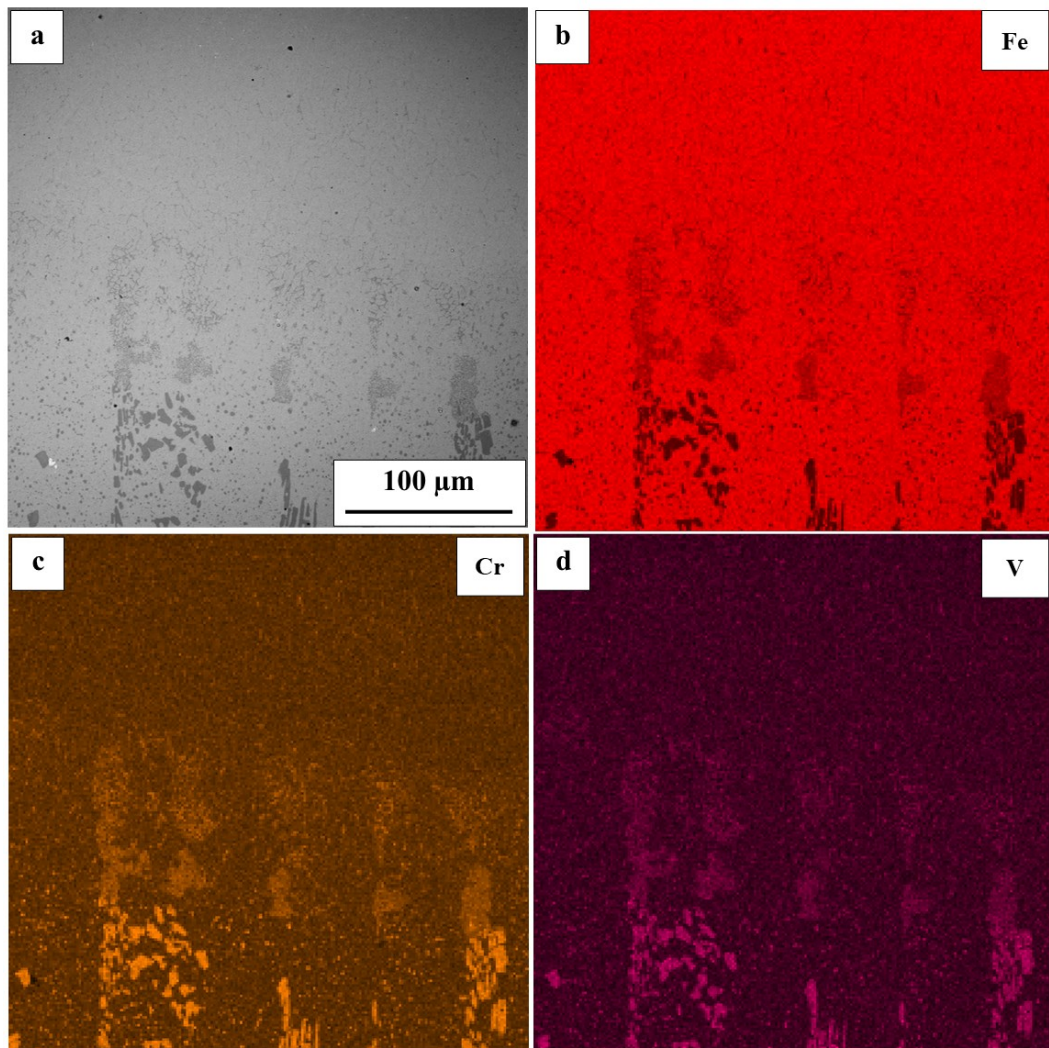


Figure 5.11 SEM micrograph of the transition zone between deposited W360 and D2 substrate in heat treated sample with corresponding EDS maps for the most relevant elements [210].

In the as-built condition (Fig. 5.10), distinct differences between the steels were observed. Moving from the bottom of the micrograph, the dark grey spots in the SEM micrograph indicated Cr and V-rich carbides (Fig. 5.10 (c) and (d)), with Fe appearing absent from these areas (Fig. 5.10 (b)). This observation suggested the presence of Cr and V-rich carbides in the transition zone. As the analysis moved towards the deposited W360, the carbides became less prominent, and carbide-forming elements Cr and V decreased while Fe became more prevalent, indicating a change in composition.

In the heat-treated sample (Fig. 5.11), a similar trend was observed. Carbides faded away from the D2 substrate towards the deposited W360. The similarity in microstructure between the substrate and the transition zone could be attributed to

the influence of the input heat during the deposition process. The examination of the D2 substrate indicated that it was within the heat-affected zone (HAZ), explaining the comparable microstructures between the substrate and the transition zone. This observation underscored the importance of understanding the effects of heat input during the deposition process on the microstructure of both the substrate and the deposited material.

This detailed microstructural analysis provided valuable insights into the composition and structure of the transition zone, showing the interactions between the two materials and the influence of the deposition process on their microstructures.

The microhardness evaluation was conducted on the samples according to the schematic depicted in Fig. 5.12 (a).

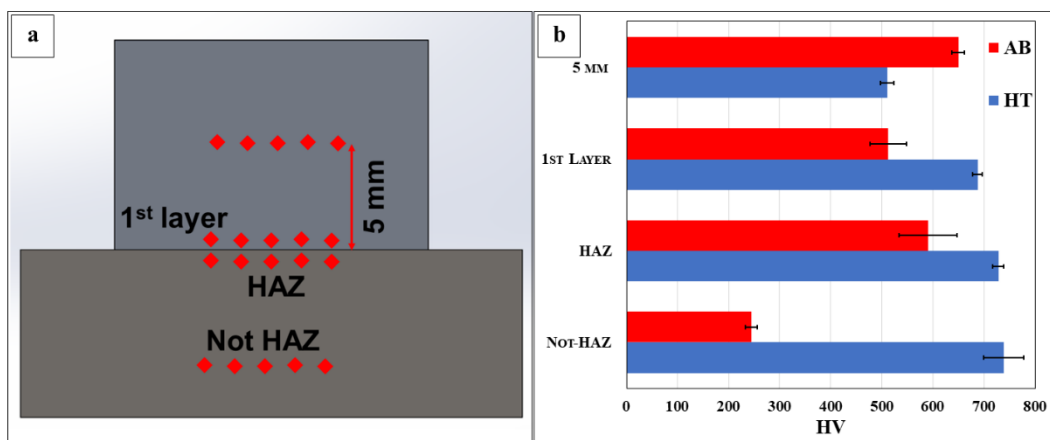


Figure 5.12 a) schematic representation of microhardness measurements performed and b) plotted microhardness results [210].

In the context of the microhardness test, it's important to note that the mean microhardness of the annealed D2 substrate sample was 247 HV. The anticipated hardness range for D2 steel, achieved through the hardening heat treatment with two tempering sessions, should ideally fall between 630-740 HV. The microhardness results are presented in Fig. 5.12, encompassing both the as-built and heat-treated samples, with distinctions made for each of the four considered regions.

Upon analysing the as-built condition of W360, it becomes evident that the L-DED process effectively imparts high hardness in the as-built W360 material (650 HV). Moving towards the substrate, the initial deposited layer exhibited slightly lower microhardness (513 HV), a discrepancy noted in comparison with the findings of the microhardness evaluation in Chapter 3. However, this disparity might be attributed to the use of different substrate materials in varied volumes and the careful removal of samples at a 1 mm height in the microstructural analysis of W360 from Chapter 3, eliminating the substrate material influence on deposited material. In the substrate region, the annealed D2 steel, starting at approximately 250 HV, displayed a substantial increase in microhardness, reaching a mean value of 591 HV. Notably, measurements conducted in the HAZ and the first deposited

layer exhibited more dispersed readings, likely due to the mixing of deposited and substrate materials, leading to variations in properties.

Upon subjecting the samples to heat treatment, the microhardness of D2 was successfully restored to values exceeding 700 HV. In the HAZ, the mean value measured 728 HV, and in the Not-HAZ region, it was 739 HV. It's worth mentioning that the Vickers instrument employed is slightly less precise for microhardness values at this high range, leading to a marginally higher error. Concerning the deposited W360, an increase in microhardness was observed in the first layer, to 688 HV. However, in the bulk of the deposited sample (5 mm above the substrate), a decline in microhardness was noted from 650 HV in as-built to 511 HV after heat treatment. This phenomenon could be attributed to the influence of the substrate material on the first deposited layer. Additionally, the performed heat treatment, while suitable for D2 steel, might not have been optimal for W360, as discussed earlier.

In summary, W360 demonstrates promising potential for repairing D2 cold work tool steel. However, adjustments in post-processing heat treatment steps are essential. Moreover, even after the deposition of a relatively large bulk sample (15 x 15 x 10 mm³) on a comparatively smaller substrate (24 x 20 x 8 mm³), the D2 material did not exhibit any heat-induced defects. These outcomes underscore the significant potential of using L-DED in repairing valuable tools, even those made from challenging to weld or “non-weldable” materials.

Chapter 6

Conclusions

In this study, the microstructural and mechanical properties of various steels produced using the Additive Manufacturing (AM) technique Laser Directed Energy Deposition (L-DED) using powders or wires as raw materials were thoroughly investigated and evaluated. The primary objectives were to demonstrate the capability of this technology both for creating 3D objects and for repairing industrial tools. The first part of the thesis delved into the technological landscape, explaining the processes involving both powder and wire feedstocks. It provided a comprehensive metallurgical background of steels in the AM field, with a comprehensive literature review on processability, microstructural details and mechanical main features of AM-produced samples. In particular the introduction section culminated with a summary of steels processed through L-DED, and an exploration of the steels used in this research.

The subsequent chapters were organized based on the steels studied experimentally. Beginning with stainless steel 316L (Chapter 2), the study progressed from characterizing the powder employed in the L-DED process to optimizing the main process parameters of the system employed to obtain bulk dense samples. Detailed analyses of the microstructure and mechanical properties of the bulk 316L samples fabricated by L-DED were conducted. Investigations into different deposition strategies were also undertaken, focusing on understanding the impact of heat accumulation. A factor screening approach was employed, measuring multiple responses concerning various factors and covariates. The chapter dedicated to stainless steel 316L concluded in determining also the optimal process window for another L-DED system with the starting material in wires.

The following experimental chapter (Chapter 3) delved into hot work tool steels, in particular the W360 steel (from Böhler). This segment commenced with characterizing the starting powder, followed by the optimization of the main process parameters. Heat treatments were then applied to the as-built L-DED samples of W360, leading to discussions on microstructural evolution of the as-built, as-quenched, and hardened W360 samples.

Chapter 4 was then focused on the 18Ni-300 maraging steel. The exploration commenced with characterizing the initial powder, proceeded to optimize the main process parameters, and culminated in a detailed analysis of the microstructural and mechanical properties of the samples fabricated by L-DED.

The final chapter, Chapter 5, focused on studies involving the application of L-DED in repair processes. A thorough investigation of D2 tool steel was conducted to comprehend its behaviour in the L-DED process used as a substrate. Once

understood, the deposition of W360 on the D2 steel substrate was executed to investigate the feasibility of the repairing process by L-DED.

316L by L-DED

In the investigation of 316L stainless steel by L-DED in both powder and wire forms, using therefore two different L-DED systems, several findings have been uncovered.

Considering powders, the as-received AISI 316L powder exhibited excellent flowability properties, with some irregular particles noted, including satellite powder, elongated, and agglomerated particles. Additionally, the powder displayed a true density of 7.896 g/cm^3 at 20°C , while in the literature the density value is taken as 7.98 g/cm^3 indicating a potential internal porosity. Optimization of process parameters, using a system Laserdyne 430 resulted in the fabrication of 316L samples with a power of 800 W, a scan speed of 600 mm/min, and a powder feed rate of 8 g/min, producing fully dense, crack-free specimens with a specific volumetric energy density of 133.3 J/mm^3 .

Microstructural analysis of the as-built 316L samples revealed a typical AM microstructure characterized by a columnar-dendritic pattern containing equiaxed and columnar dendrites. Micro-segregation of alloying elements was observed in the intercellular region, suspected to contain δ -ferrite.

Investigation into the influence of heat accumulation during deposition showed that simultaneous building of multiple 316L samples on the same substrate resulted in higher microhardness and more uniform properties compared to sequential deposition, highlighting the importance of the scanning strategy.

Factor screening research indicated predictive models for sample height and an increase in sample density during the process.

On the other hand, the study performed on processing 316L in wires by L-DED, using a LAWS 250 system with 0.3 mm laser spot diameter, revealing optimal main process parameters for all feeding directions. However, challenges were encountered with the wire feeding system, leading to porosity and misalignment issues during subsequent track depositions.

These findings collectively contribute to the understanding of 316L processing through L-DED, providing insights into starting material properties, process parameters, microstructure, and system configurations. Such insights hold potential for advancing the utilization of 316L by L-DED in various industrial applications.

W360 by L-DED

In the exploration of W360 hot work tool steel by L-DED using the Laserdyne 430 system (therefore starting from powders), critical insights were gained, shedding light on the material behaviour and properties, marking the first-time processing of this alloy by L-DED to the best of the author's knowledge.

The W360 powder obtained from Böhler showcased some irregularities, including satellite powder and agglomerated particles, yet demonstrated acceptable

flowability properties, making it suitable for L-DED processing. Optimization of process parameters unveiled a power setting of 800 W, a scan speed of 450 mm/min, and a powder feed rate of 8 g/min, resulting in a layer thickness of 0.65 mm and minimal porosity (0.15 %) with a specific volumetric energy density of 82.1 J/mm³.

Microstructural analysis of the as-built W360 sample revealed a typical AM microstructure characterized by a cellular-dendritic pattern with small carbides observed in the intercellular regions. Analysis further indicated micro-segregation of alloying elements and varied carbide growth attributed to the intrinsic heat treatment during L-DED processing. Post-quenching, the samples exhibited the typical microstructure of hot work tool steels, with a mean microhardness of 744 HV indicative of highly distorted martensite. Completing the heat treatment process with three consecutive tempering cycles at 540 °C resulted in a tempered martensite matrix with Mo-rich carbides, offering a mean microhardness of 634 HV, rendering it a promising candidate for tool repair through the L-DED process.

These findings significantly advance our understanding of W360 behaviour in L-DED processes, providing valuable insights for potential industrial tool repair applications.

18Ni-300 by L-DED

The investigation into 18Ni-300 maraging steel using L-DED technology, starting from powders using a LAWS 250 system has given a promising insights into the properties of material. The powder supplied by Carpenter Additive exhibited predominantly regular particles, with excellent flowability properties despite some observed irregularities. Through optimization of process parameters, the porosity level was significantly reduced, resulting in 0.38 % relative density. The optimized parameters for 18Ni-300 were determined to be a power setting of 375 W, scan speed of 700 mm/min, powder feed rate of 5 g/min, bead width of 0.78 mm, a 30% overlap resulting in a hatch distance of 0.55 mm, and a resultant layer thickness of 0.48 mm, achieving a specific volumetric energy density of 121.9 J/mm³.

Examination of the as-built 18Ni-300 samples revealed a typical microstructure commonly found in L-DED-manufactured samples, consisting of a cellular-dendritic pattern. From a mechanical properties point of view, the samples displayed a uniform microhardness along the building direction, indicating promise for direct aging heat treatment applications.

L-DED in repair of D2 steel components

In the context of using L-DED to repair industrial tools, the study main findings concentrate on the potential of W360 in repairing D2 cold work tool steel, providing valuable insights into the required adjustments in post-processing heat treatments. The initial worn industrial blade, made of D2 cold work tool steel in a hardened state, featured large carbides dispersed within the martensitic matrix, presenting challenges for repair attempts. Through an annealing process, the microhardness of

the D2 substrates decreased, facilitating successful welding on annealed D2 substrates. Subsequently, crack-free, nearly fully dense W360 samples were deposited onto annealed D2 steel substrates, indicating promising results for repair applications. Optical micrographs revealed a typical AM microstructure, and EDS analysis indicated Cr and V-rich carbides. However, microhardness measurements highlighted the need for adjustments in the heat treatment process for W360 steel to achieve the desired microhardness, emphasizing the importance of careful consideration and optimization of repair process parameters.

In summary, these findings underscore the significance of careful consideration and optimization of the repair process parameters to ensure successful and durable repairs of industrial components made in tool steels.

Appendix – A – Experimental procedure

In this chapter, a comprehensive description of the experimental procedure that was employed to optimize process parameters with the goal of achieving bulk samples that are near to full density is provided.

To fabricate dense and crack-free L-DED samples, a 3-step approach was employed, as schematically illustrated in Fig A.1, which includes the deposition of single tracks (ST), single layers (SL), and ultimately, the bulk samples. Each step played a crucial role in optimizing various process parameters. The deposition of STs was undertaken to determine the optimal combination of laser power (P), scan speed (v), and powder feed (Q_p). Once a suitable set of parameters was identified, the procedure advanced to the deposition of SLs. These were built with different the overlap percentages (Ov) between tracks and the layer growth (Δz) was measured. After establishing the optimal P, v, Q_p, Ov, Δz, the process proceeded to the deposition of bulk samples.

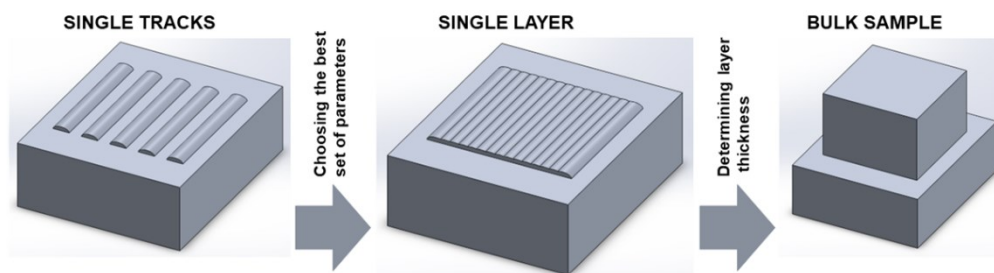


Figure A.1 Schematic explanation of the deposition procedure [210].

A.1 Step 1: Single tracks

The STs were deposited using different main process parameter combinations to evaluate the different sets of P, v, and Q_p. Using these combinations of process parameters, a linear energy density and a linear mass deposition density could be calculated by using the eq. 8 and eq. 9.

$$(8) \text{ Linear energy density [J/mm]} = P/v$$

$$(9) \text{ Linear mass deposition density [g/mm]} = Q_p/v$$

Then, STs were cut perpendicular to scanning direction for obtaining cross-sections, as schematically shown in Fig. A.2 (a). Cross-sections were then grinded and polished using a standard metallurgical procedure for obtaining mirror like surface. Then, OM micrographs of polished cross-sections were obtained and

characteristic geometrical features of cross-sections of STs such as width (W), growth (G), and depth (D) (Fig. A.2 (b)) were measured using the ImageJ software. Using the eq. 10 and eq. 11 dilution and aspect ratio (AR) were calculated. The dilution is indicating vertical metallurgical bonding. The regular, elliptical geometry of melt pool has the dilution value close to 1.0. On the other hand, high dilution values would result in insufficient bonding between deposited layers, eventually leading to the balling effect geometry. While low dilution values would lead to keyhole geometry melt pools, therefore causing the risk of keyhole porosity, examples of different dilution values are shown in Fig A.3. The other criteria considered was the AR where values are indicating the growth of the ST, with the lower value ST grows higher [44].

$$(10) \quad \text{dilution} = G/D$$

$$(11) \quad \text{AR} = W/G$$

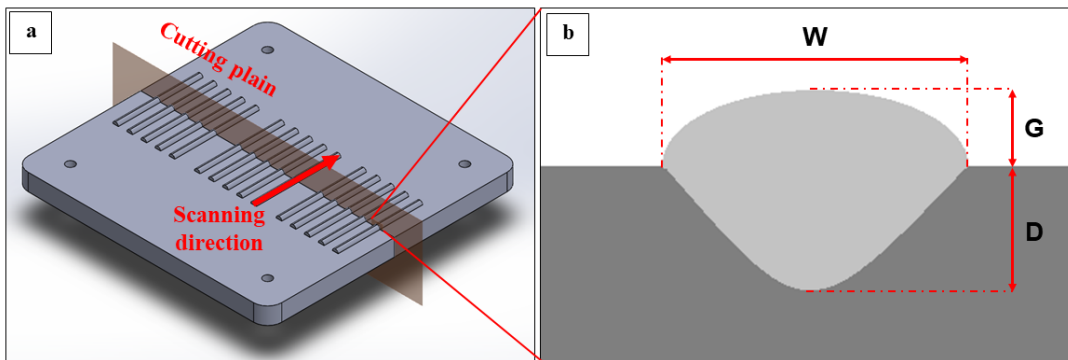


Figure A.2 Schematic explanation of: a) cut performed to analyse the single tracks deposited [119]; b) geometrical features of a ST cross-section considered as reference [119].

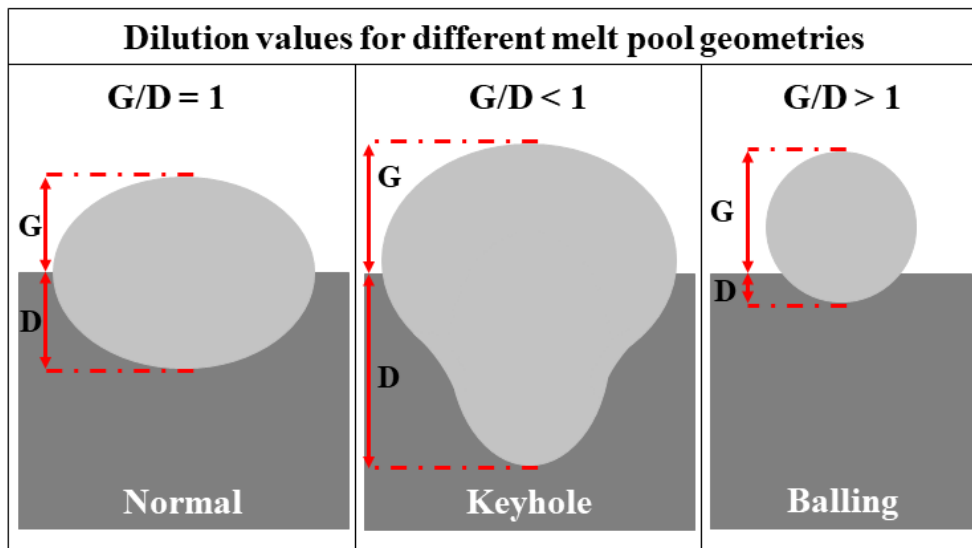


Figure A.3 Characteristic melt pool geometries with associated dilution values.

A.2 Step 2: Single layers

The second step is the deposition of SLs, initiated after the selection of one or more sets of primary process parameters: P , v , and Q_p , as determined from the STs evaluation outlined in step 1. In this phase, various hatch distances (h_d) are employed for deposition. The h_d is calculated using eq. 12, wherein W denotes the width of a single track and Ov represents the chosen overlap percentage (Fig A.4). The principal objective of this step is to achieve uniform layer growth, avoiding the development of pores that might occur between tracks. A higher Ov could lead to the formation of layers that elevate non-uniformly as the deposition continues. Conversely, a lower Ov could result in excessively deep V-shapes between tracks, causing porosity issues in the bulk samples. To address this, SLs were sectioned perpendicular to the scanning direction, and the obtained cross-sections were ground and polished using standard metallurgical procedures to attain mirror-like surfaces. Subsequently, OM micrographs of the polished cross-sections were acquired and inspected for potential porosity. Layer growth was measured at various positions using a TESA Micromaster digital calliper with a precision of ± 0.004 mm. The mean value was then employed as Δz for the subsequent step.

$$(12) \quad h_d = W \times (100 - ov\%) / 100$$

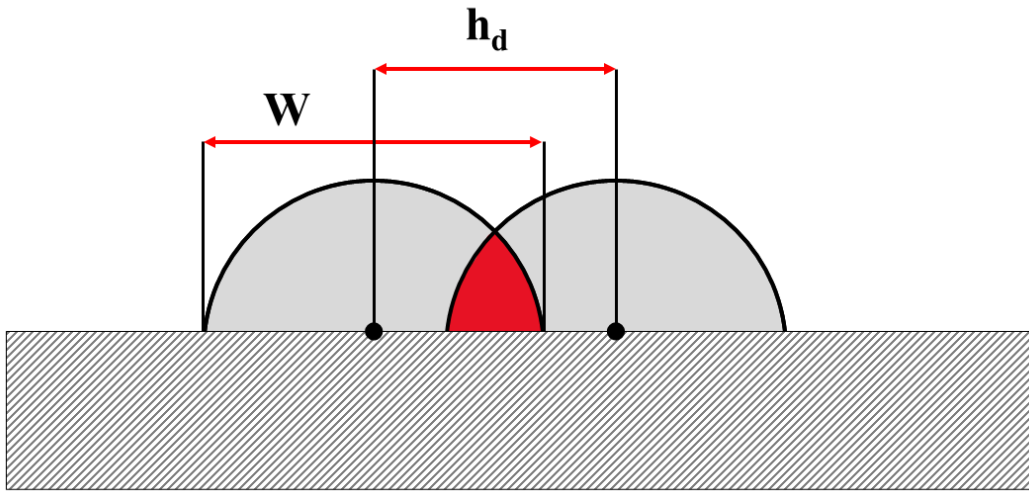


Figure A.4 Schematical representation of overlapping effect.

With the selected main process parameters and overlapping percentage, giving the hatch distance utilized the specific surface energy density (E_s) can be calculated with the following equation (eq. 13):

$$(13) \quad E_s = P / v \times h_d$$

A.3 Step 3: Bulk samples

In the final step, bulk samples are fabricated, utilizing the process parameters P , v , and Q_p determined from STs evaluation and the parameters h_d and Δz ascertained from SLs evaluation. With all the main process parameters defined, the specific volumetric energy density can be calculated as shown in eq. 12. Here, the bulk samples are produced employing a zig-zag toolpath pattern strategy (Fig A.5 (a)) and a rotation of 90° after the deposition of each layer (Fig A.5 (b)). Following this, cubic samples are excised along the X-Z or Y-Z plane to reveal the cross-section aligned with the building direction, Z. After subsequent grinding and polishing, OM micrographs are captured to assess the relative porosity utilizing ImageJ software. The cube manufactured with the set of parameters exhibiting the minimal relative porosity is then subjected to detailed analysis.

$$(14) \quad E_v = P/v \times h_d \times \Delta z$$

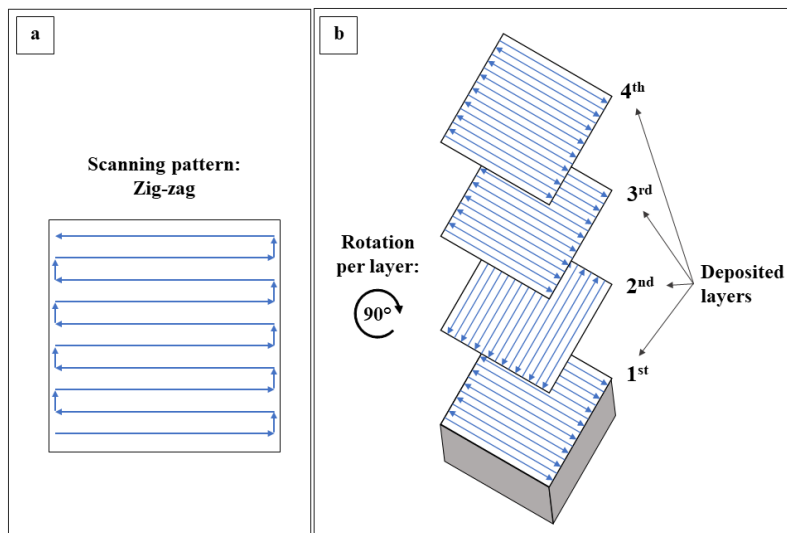


Figure A.5 Bulk sample deposition strategy: a) scanning pattern; b) rotation per layer.

Appendix – B – Experimental equipment and characterization methods

In this chapter, a detailed description of the experimental equipment and characterization techniques employed to analyse the samples discussed in this thesis will be provided.

The chapter is divided into three sections. The first section pertains to the characterization techniques used to analyse the powders discussed in this thesis. The second one is giving a detail of L-DED machines and furnace utilized in the thesis. The last one focuses on equipment used for analysis.

B.1 Powder characterization

B.1.1 Laser granulometry

The diameter distribution of the metal powders was assessed through laser granulometry, utilizing a Fritsch Analysette 22 Compact instrument, which has a measuring range between 0.3 μm and 300 μm . The computation of the mean size and frequency distribution were predicated on volumetric assumptions. Additionally, the d_{10} , d_{50} , and d_{90} values, representing the diameter values at 10%, 50%, and 90% of the cumulative size distribution respectively, were ascertained and documented.

B.1.2 Electron microscopy

The morphology of the metal powders was analysed through electron microscopy, utilizing a Scanning Electron Microscope (SEM) Phenom XL.

B.1.3 Apparent density measurement

The apparent density (ρ_{app}) was measured in accordance with the ASTM B212 standard [211]. To measure the apparent density of the sample, the empty density cup, 25 mL in volume (V_{dc}), was first weighed. Subsequently, the test portion was meticulously loaded into the flowmeter funnel and permitted to enter the density cup through the discharge orifice, ensuring the cup remained stationary during this process (Fig B.1). Once the cup was fully laden and the powder started overflowing its periphery, a nonmagnetic spatula, maintained perpendicular to the top edge of the cup, was employed to level the powder flush with the top of the density cup, exercising caution to avoid any jarring of the apparatus. After levelling, the density

cup was gently tapped on the side to settle the powder, preventing any spillage during transfer, and residual powder adhering to the external wall of the cup was removed. Subsequently, the filled density cup was transferred to the balance to ascertain the mass of the powder (m_p). The eq. 15 was used for calculating the ρ_{app} . This process was replicated thrice, each with a new test portion of powder, and the consequent apparent density values were averaged.

$$(15) \quad \rho_{app} = m_p/V_{dc}$$

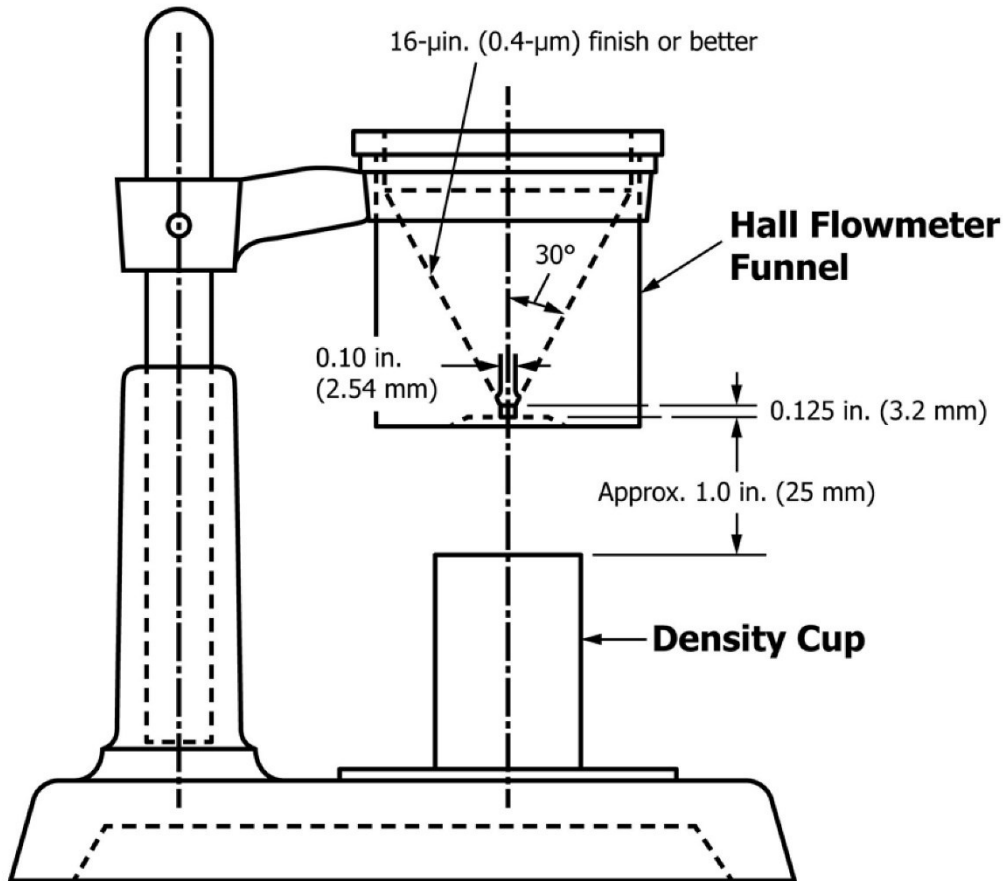


Figure B.1 Apparatus for measuring apparent density and flowability with density cup and Hall flowmeter funnel [212].

B.1.4 Tapped density measurement

The tapped density (ρ_{tap}) was ascertained in accordance with the ASTM B527 standard [212], utilizing a meticulous methodology. Initially, the internal wall of the graduated 25 mL cylinder was scrupulously cleaned with a suitable clean brush to ensure the absence of contaminants. Subsequently, the test portion of the powder (m_p) of around 100 g was precisely weighed to the nearest 0.1 g, emphasizing accuracy. This weighed powder was carefully dispensed into the graduated cylinder to maintain a level powder surface. Thereafter, the cylinder was securely placed within the tapping apparatus. The apparatus was operated until no observable

reduction in powder volume occurred, and the volume (V_{tap}) was meticulously recorded to the nearest 0.5 mL. Following this, the ρ_{tap} was computed employing eq. 16. To reinforce the reliability of the findings, this entire process was replicated thrice, each instance utilizing a new test portion of powder, and the computed tapped density values were subsequently averaged.

$$(16) \quad \rho_{tap} = m_p / V_{tap}$$

B.1.5 Flowability measurement

The flowability of the powder was assessed using a Hall flow meter (Fig B.1), coupled with calculations of the compressibility index (CI) and Hausner ratio (HR). The Hall flow rate was measured by adhering to the procedures outlined in Method I, Static Flow Method, of the ASTM B213 standard [213]. The funnel's bottom was sealed with a dry finger. A sample of 50 g of powder was gently poured into the centre of the flowmeter funnel, avoiding any tapping, vibration, or movement of the funnel. A weighing dish was positioned beneath the funnel orifice. Timing commenced simultaneously with the removal of the finger from the discharge orifice. The timing device was halted as the last of the powder exited the orifice, with the time recorded to the nearest 0.1 s. This procedure was replicated three times, each with a 50 g of fresh powder.

The CI and the HR serve as measures to quantify the proclivity of a powder to undergo consolidation. The CI is calculated utilizing eq. 17, while HR is determined through eq. 18. In these equations, ρ_{app} represents the apparent density and ρ_{tap} denotes the tapped density. A general scale of powder flow using the CI and HR is given in Table B.1 [214].

$$(17) \quad CI\% = 100 \times (1 - \rho_{app} / \rho_{tap})$$

$$(18) \quad HR = \rho_{tap} / \rho_{app}$$

Table B.1 Scale of Flowability for Compressibility Index and Hausner Ratio [214].

Flow character	Compressibility index, %	Hausner ratio
Excellent	≤10	1.00–1.11
Good	11–15	1.12–1.18
Fair	16–20	1.19–1.25
Passable	21–25	1.26–1.34
Poor	26–31	1.35–1.45
Very poor	32–37	1.46–1.59
Very, very poor	>38	>1.60

B.1.6 True density measurement

The true density of a powder ($\rho_{p,t^{\circ}C}$) is fundamentally characterized as the ratio of the average mass of the particles to the solid volume, excluding all the voids that are not inherent to the molecular packing arrangement. Three principal methodologies are established for determining true density: gas pycnometry or displacement, liquid displacement, and flotation in a liquid. For the purposes of this thesis, the method of gas pycnometry was employed.

To ascertain the average density of the powder, a meticulous two-step approach is implemented. Initially, the mass of the powder is precisely measured utilizing a high-precision ANJ-NM/ABS-N balance by KERN (Gottlieb, Germany), possessing a readability of 0.1 mg and a repeatability of 0.2 mg. Subsequently, the Ultrapyc 5000 pycnometer by Anton Paar (Graz, Austria) using helium gas is employed to determine the volume of the powder sample, with an accuracy of 0.03% and a repeatability of 0.015%. This instrument applies an iterative method, concluding the measurements once a variance of 0.01% is achieved.

B.1.7 Porosity evaluation

The assessment of internal porosity was conducted through two distinct methods. The first method involved the analysis of optical microscopy (OM) micrographs of the powder cross-section. Initially, the powder sample was mounted in resin using the hot mounting machine IPA 30 Remet. The mounted sample underwent grinding and polishing, adhering to standard metallurgical procedures to attain a mirror-like surface. Subsequently, an OM Leica DMI 5000 M was employed to capture micrographs of the powder cross-sections, which were analysed qualitatively.

The second method entailed a quantitative evaluation of internal porosity. The internal porosity (%por) was computed using eq. 19, necessitating data on the measured true density ($\rho_{p,t^{\circ}C}$) value and literature values of the fully dense material at the corresponding temperature ($\rho_{full\ dense,t^{\circ}C}$) of the measured true density.

$$(19) \quad \%por = 1 - \rho_{p,t^{\circ}C} / \rho_{full\ dense,t^{\circ}C}$$

B.1.8 LECO analysis

The content of oxygen, nitrogen, and hydrogen within the powders was quantitatively analysed utilizing the inert gas fusion method, executed with a LECO ONH836 Oxygen/Nitrogen/Hydrogen Elemental Analyzer.

B.1.9 Oxide evaluation

The presence of oxides on the surface of powder particles was confirmed through EDS spot analysis on suspected areas and surrounding regions, utilizing a SEM Phenom XL, equipped with an Energy-dispersive X-ray Spectroscopy (EDS) detector.

B.2 L-DED machines and heat treatment instrument

B.2.1 Laserdyne 430

The Laserdyne 430 L-DED-P system, depicted in Fig B.2, provided by Prima Additive (Torino, Italy), with a CNC system equipped with a roto-tilting table, enabling meticulous five-axis deposition, was utilized in this thesis. Detailed specifications of the machine are presented in Table B.2. The deposition head was engineered with four coaxial nozzles, designed to ensure stable powder flow with a powder spot focused to less than 4 mm in diameter at the focal point, and was operated at a standard distance of 7 to 9 mm from the top of the nozzle. A fibre laser, with a maximum power output of 1 kW, a laser beam diameter (d_l) of 2.00 mm, and a wavelength of 1075 ± 5 nm, was employed as the heat source. The Optomec CS 150 powder feeding system (Albuquerque, NM, USA) was paired with the L-DED-P machine. This system, featuring a rotating disk situated below a gravity hopper and pressurized gas, was meticulously calibrated to control the powder flow rate (Q_p) by modulating the rotational speed (w) of the perforated disk and the carrier gas flow rate (V_{cg}). The system was optimized to handle powders with particle sizes ranging between 45 and 200 μm .

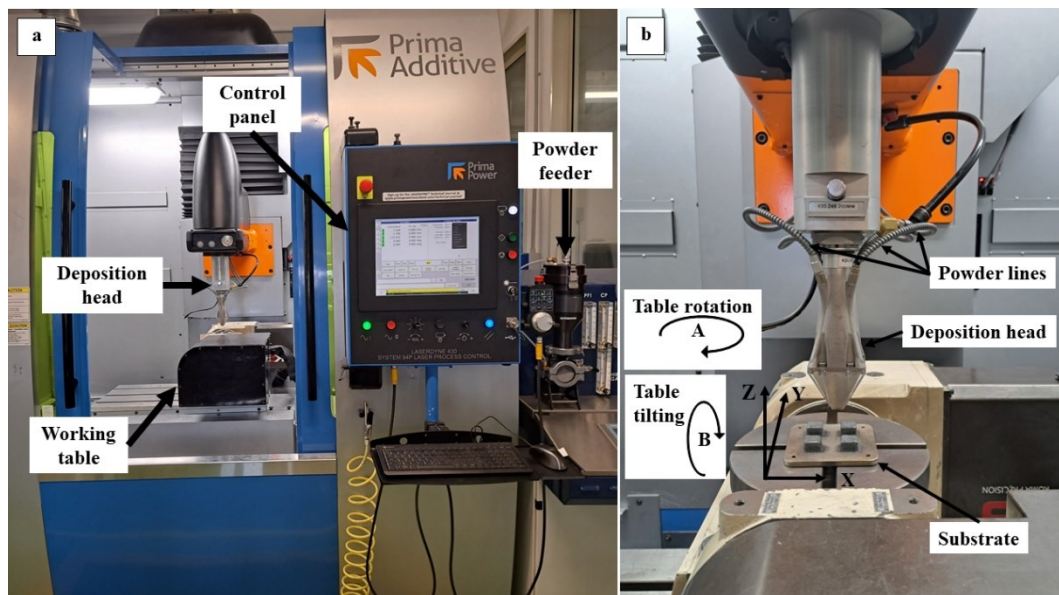


Figure B.2 Laserdyne 430 by Prima Additive: a) picture of building chamber, control panel and powder feeder; b) picture of deposition head and working table.

Table B.2 Specifications of Laserdyne 430 by Prima Additive.

Laser power	1 Kw
Type of laser	Fibre
Laser beam wavelength	1070 - 1080 nm
Working volume	585 x 400 x 500 mm ³
Axis configuration	5 axes: X-Y (deposition table movement) Z (deposition head movement) A (rotation of deposition table) B (tilting of deposition table)
Axis velocity X-Y-Z	0-15 m/min
Axis velocity A-B	0-90 rpm
Deposition rate	max 50 cm ³ /h; typical 20 cm ³ /h
Deposition accuracy	± 0.2 mm
Powder feeder capacity	2 hoppers of 1,5 dm ³

B.2.2 Laws 250

The hybrid L-DED system utilized in this thesis was the LAWS 250 by Liburdi Automation (Fig. B.3), a system capable of using both powder and wire feedstocks. The LAWS 250 is equipped with a 3-axis robotic system, allowing precise X-Y-Z movements of the deposition head. This system utilizes fibre laser, possessing the capability of delivering up to 1 kW of power, with a characteristic laser spot diameter (d_l) of 0.3 mm. The laser operates with a wavelength of 1075 ± 5 nm. The transfer of powder to the deposition head is managed by a commercial powder feeder developed by Oerlikon Metco. This feeder incorporates four coaxial multi-nozzles (4-way). The system maintains a standard operating distance of 7 mm from the deposition surface, ensuring optimal focal adherence and powder adhesion. To maintain powder integrity and prevent contamination, inert gas is used as the carrier gas for the powder stream maintaining a constant powder feed. The main machine specifications are summarized in Table B.3.

In the wire feedstock setup, the system features three-axis control for deposition head motion (X-Y-Z) and an additional two-axis control for wire positioning. These extra axes allow adjustment of the wire position both front to back, ensuring it aligns with the centre of the laser spot, and up and down, placing it precisely at the focal point of the laser beam. The wire feeder is positioned off-axis to the laser beam, fixed on the side of the deposition head, and maintains a constant feeding angle (α_w) of 30° (refer to Fig. B.3 (b)).

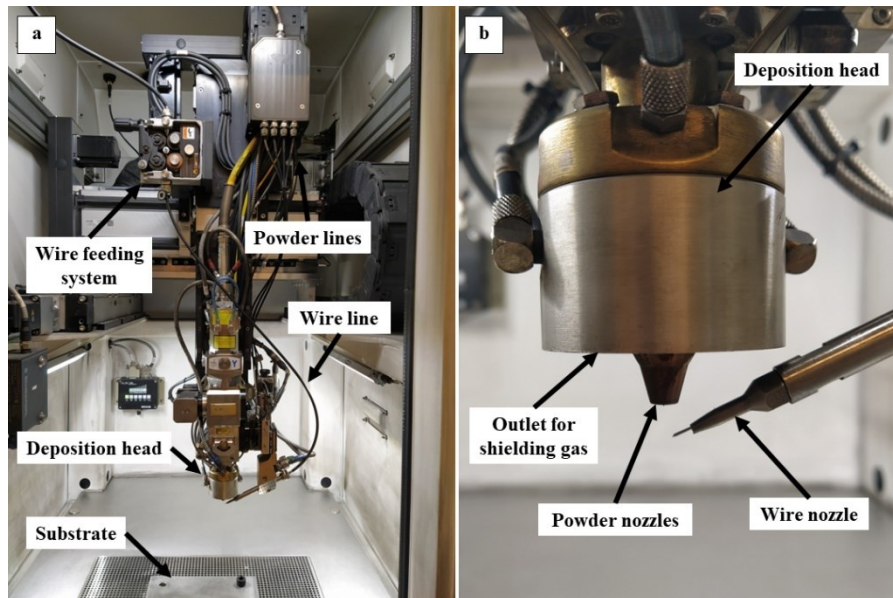


Figure B.3 LAWS 250 by Liburdi: a) picture of building chamber; b) picture of deposition head.

Table B.3 Specifications of LAWS 250 by Liburdi Automation.

Laser power	1 Kw
Type of laser	Fibre
Laser beam wavelength	1070 - 1080 nm
Laser spot diameter	0.30 mm
Axis configuration	3 axes: X-Y-Z (deposition head movement)
Feedstock	Powder or wire
Powder feeder capacity	2 hoppers of 1,5 dm ³

B.2.3 Nabertherm RHTC 80-710/15

In this research, a high-temperature horizontal tubular furnace was employed. This specific model boasts premium insulation materials composed of vacuum-formed fibre plates. Such a construction not only promotes energy-efficient operation but also facilitates rapid heating owing to the minimal heat storage and conductivity. The furnace operates over a temperature range extending from room temperature up to 1600°C. In the research argon gas was utilized to create an inert atmosphere. Apart from inert atmosphere, it is versatile in handling various atmospheres including air, oxidizing, and reducing environments. The system features a programmable set point regulator to control and stabilize the desired temperature. Structurally, the furnace tube possesses an internal diameter of 70 mm and an overall length of 1080 mm, with a heated segment spanning 710 mm. Within this segment, a length constant of 150 mm ensures a temperature uniformity of ± 5 K. The furnace supports a heating rate between 0.5 and 25°C/min, while its cooling rate ranges from 2.5 to 15°C/min. Notably, the furnace is also equipped to perform quenching operations when required.

B.3 Microstructural and mechanical analysis – equipment and procedure

B.3.1 Microstructural analysis

In the study, post L-DED sample microstructures were examined utilizing optical microscopy (OM), scanning electronic microscopy (SEM), energy-dispersive X-ray spectroscopy (EDS) and Electron Backscatter Diffraction (EBSD), as well as X-ray crystallography (XRD) analysis.

The preparation of vertical (XZ) cross-sections for these microstructural analyses involved hand grinding with SiC abrasive papers. This was followed by a sequential polishing using diamond suspension up to a granularity of 1 μm and concluding with a final polish employing a silica oxide suspension to achieve a fine finish of 0.06 μm .

B.3.1.1 Optical microscopy

For the 316L samples, OM analyses were conducted both pre and post chemical etching. The etching process employed an acid mixture comprising 15 mL HCl, 10 mL HNO₃, and 10 mL acetic acid for a duration of 10 seconds. The resultant samples were then inspected using a Leica DMI 5000 M optical microscope.

Similarly, W360 samples underwent OM analysis before and after a chemical etching process. In this case, nital 2 etchant was utilized for an etching duration of 60 seconds. The subsequent samples were also observed under a Leica DMI 5000 M optical microscope.

For the investigation on 18Ni-300, the nital 2 etchant was also used. The polished surface was swiped with the cotton sticks for 10 seconds. The samples were then observed under a Keyence VHX 7000 digital microscope

B.3.1.2 Electronic microscopy

The microstructural investigations of the chemically etched 316L samples were conducted using a SEM Phenom XL. In contrast, the W360 samples, post-etching, were examined utilizing the Zeiss Supra™ 40 Field Emission Scanning Electron Microscope (FESEM). For compositional analyses of the W360 samples, both the SEM EVO 15, equipped with an EDX detector, and the Focused Ion Beam-SEM (FIB-SEM) Tescan S9000G, furnished with an EBSD detector, were employed. The 316L samples' compositional investigations were facilitated by the SEM Phenom XL, which also featured an EDX detector. The 18Ni-300 samples were observed using the FESEM Tescan Mira 3 XMU equipped with Oxford Instruments X-Max EDS detector and a Oxford Instruments Nordlys EBSD detector.

B.3.1.3 X-ray crystallography

The phase composition within the cross-sectional samples was determined through X-ray diffraction (XRD) utilizing an Empyrean diffractometer equipped with Cu K α radiation. The measurements were conducted in a Bragg Brentano

configuration, spanning a 2θ range from 30 to 110°. The operational settings of the diffractometer were maintained at 40 kV and 40 mA, with a step size of 0.013 and a duration of 30 seconds per step.

B.3.2 Thermal analysis

The phase transformations in the W360 samples were investigated using Differential Scanning Calorimetry (DSC).

B.3.2.1 Differential Scanning Calorimetry

Differential Scanning Calorimetry (DSC) analyses of the W360 samples were conducted on a Setaram TGA-DSC 92 16.18 under an Argon atmosphere to prevent oxidation. Specimens, extracted from the cylinder, had an approximate mass of 200 mg. The heating protocol involved ramping from 200°C to 1120°C at a rate of 10°C/min, followed by a cool down to ambient temperature.

B.3.3. Mechanical properties

Among the evaluated mechanical properties, Vickers microhardness was distinctly assessed based on the material in question. Different methodologies were employed to cater to the specific characteristics and requirements of each material.

B.3.3.1 Microhardness evaluation

The microhardness of the 316L samples was assessed employing a micro-Vickers indenter under a load of 500 g with a dwell time of 15 s. Indentations were performed at both the bottom and top regions of the sample.

For the W360 bulk samples, microhardness measurements were conducted using a micro-Vickers indenter, applying a load of 500 g for 15 s. Five distinct indentations were carried out in separate zones on each sample at varying heights relative to the substrate. These zones were categorized as bottom (B), central-bottom (CB), central (C), central-top (CT), and top (T).

For the 18Ni-300 bulk samples, microhardness measurements were performed using a micro-Vickers indenter, applying a load of 500 g for 12 s. The measurements on eight cubes built with different parameters were done by performing 5 indentations in horizontal level at 5 mm distance from the substrate in Z direction. The measurements done on the sample built with optimized parameters were performed from 0.5 mm under the level of the substrate up to the 12.5 mm above the surface with 0.25 mm spacing between the indentations. The measurement was repeated 5 times per sample.

References

- [1] I. Gibson, D. Rosen, B. Stucker, and M. Khorasani, *Additive Manufacturing Technologies*. Cham: Springer International Publishing, 2021. doi: 10.1007/978-3-030-56127-7.
- [2] N. Guo and M. C. Leu, “Additive manufacturing: technology, applications and research needs,” *Frontiers of Mechanical Engineering*, vol. 8, no. 3, pp. 215–243, Sep. 2013, doi: 10.1007/s11465-013-0248-8.
- [3] S. A. M. Tofail, E. P. Koumoulos, A. Bandyopadhyay, S. Bose, L. O’Donoghue, and C. Charitidis, “Additive manufacturing: scientific and technological challenges, market uptake and opportunities,” *Materials Today*, vol. 21, no. 1, pp. 22–37, Jan. 2018, doi: 10.1016/j.mattod.2017.07.001.
- [4] D. L. Bourell, “Perspectives on Additive Manufacturing,” *Annu Rev Mater Res*, vol. 46, no. 1, pp. 1–18, Jul. 2016, doi: 10.1146/annurev-matsci-070115-031606.
- [5] A. Ambrosi and M. Pumera, “3D-printing technologies for electrochemical applications,” *Chem Soc Rev*, vol. 45, no. 10, pp. 2740–2755, 2016, doi: 10.1039/C5CS00714C.
- [6] A. Gisario, M. Kazarian, F. Martina, and M. Mehrpouya, “Metal additive manufacturing in the commercial aviation industry: A review,” *J Manuf Syst*, vol. 53, pp. 124–149, Oct. 2019, doi: 10.1016/j.jmsy.2019.08.005.
- [7] S. H. Huang, P. Liu, A. Mokasdar, and L. Hou, “Additive manufacturing and its societal impact: a literature review,” *The International Journal of Advanced Manufacturing Technology*, vol. 67, no. 5–8, pp. 1191–1203, Jul. 2013, doi: 10.1007/s00170-012-4558-5.
- [8] L. A. Verhoef, B. W. Budde, C. Chockalingam, B. García Nodar, and A. J. M. van Wijk, “The effect of additive manufacturing on global energy demand: An assessment using a bottom-up approach,” *Energy Policy*, vol. 112, pp. 349–360, Jan. 2018, doi: 10.1016/j.enpol.2017.10.034.
- [9] C. Sun, Y. Wang, M. D. McMurtrey, N. D. Jerred, F. Liou, and J. Li, “Additive manufacturing for energy: A review,” *Appl Energy*, vol. 282, p. 116041, Jan. 2021, doi: 10.1016/j.apenergy.2020.116041.
- [10] M. Armstrong, H. Mehrabi, and N. Naveed, “An overview of modern metal additive manufacturing technology,” *J Manuf Process*, vol. 84, pp. 1001–1029, Dec. 2022, doi: 10.1016/j.jmapro.2022.10.060.

- [11] D. Rejeski, F. Zhao, and Y. Huang, “Research needs and recommendations on environmental implications of additive manufacturing,” *Addit Manuf*, vol. 19, pp. 21–28, Jan. 2018, doi: 10.1016/j.addma.2017.10.019.
- [12] W. E. Frazier, “Metal Additive Manufacturing: A Review,” *J Mater Eng Perform*, vol. 23, no. 6, pp. 1917–1928, Jun. 2014, doi: 10.1007/s11665-014-0958-z.
- [13] M. Salmi, “Additive Manufacturing Processes in Medical Applications,” *Materials*, vol. 14, no. 1, p. 191, Jan. 2021, doi: 10.3390/ma14010191.
- [14] F. Calignano and V. Mercurio, “An overview of the impact of additive manufacturing on supply chain, reshoring, and sustainability,” *Cleaner Logistics and Supply Chain*, vol. 7, p. 100103, Jun. 2023, doi: 10.1016/j.clscn.2023.100103.
- [15] B. Ahuja, M. Karg, and M. Schmidt, “Additive manufacturing in production: challenges and opportunities,” H. Helvajian, A. Piqué, M. Wegener, and B. Gu, Eds., Mar. 2015, p. 935304. doi: 10.1117/12.2082521.
- [16] *ISO/ASTM 52900:2021 Additive manufacturing — General principles — Fundamentals and vocabulary*. 2021.
- [17] L. Yang *et al.*, *Additive Manufacturing of Metals: The Technology, Materials, Design and Production*. Cham: Springer International Publishing, 2017. doi: 10.1007/978-3-319-55128-9.
- [18] S. Sun, M. Brandt, and M. Easton, “Powder bed fusion processes,” in *Laser Additive Manufacturing*, Elsevier, 2017, pp. 55–77. doi: 10.1016/B978-0-08-100433-3.00002-6.
- [19] M. Khorasani, I. Gibson, A. H. Ghasemi, E. Hadavi, and B. Rolfe, “Laser subtractive and laser powder bed fusion of metals: review of process and production features,” *Rapid Prototyp J*, vol. 29, no. 5, pp. 935–958, May 2023, doi: 10.1108/RPJ-03-2021-0055.
- [20] D. G. Ahn, “Directed Energy Deposition (DED) Process: State of the Art,” *International Journal of Precision Engineering and Manufacturing - Green Technology*, vol. 8, no. 2. Korean Society for Precision Engineering, pp. 703–742, Mar. 01, 2021. doi: 10.1007/s40684-020-00302-7.
- [21] A. Saboori, A. Aversa, G. Marchese, S. Biamino, M. Lombardi, and P. Fino, “Application of Directed Energy Deposition-Based Additive Manufacturing in Repair,” *Applied Sciences*, vol. 9, no. 16, p. 3316, Aug. 2019, doi: 10.3390/app9163316.
- [22] X. Hu *et al.*, “Towards an integrated experimental and computational framework for large-scale metal additive manufacturing,” *Materials Science and Engineering: A*, vol. 761, p. 138057, Jul. 2019, doi: 10.1016/j.msea.2019.138057.
- [23] S. M. Thompson, L. Bian, N. Shamsaei, and A. Yadollahi, “An overview of Direct Laser Deposition for additive manufacturing; Part I: Transport phenomena, modeling and diagnostics,” *Addit Manuf*, vol. 8, pp. 36–62, Oct. 2015, doi: 10.1016/j.addma.2015.07.001.
- [24] M. Liu, A. Kumar, S. Bukkapatnam, and M. Kuttolamadom, “A Review of the Anomalies in Directed Energy Deposition (DED) Processes &

- Potential Solutions - Part Quality & Defects,” *Procedia Manuf*, vol. 53, pp. 507–518, 2021, doi: 10.1016/j.promfg.2021.06.093.
- [25] H. Mokhtarian *et al.*, “A Conceptual Design and Modeling Framework for Integrated Additive Manufacturing,” *Journal of Mechanical Design*, vol. 140, no. 8, Aug. 2018, doi: 10.1115/1.4040163.
- [26] S. Amirabdollahian, F. Deirmina, M. Pellizzari, P. Bosetti, and A. Molinari, “Tempering behavior of a direct laser deposited hot work tool steel: Influence of quenching on secondary hardening and microstructure,” *Materials Science and Engineering: A*, vol. 814, p. 141126, May 2021, doi: 10.1016/j.msea.2021.141126.
- [27] N. Shamsaei, A. Yadollahi, L. Bian, and S. M. Thompson, “An overview of Direct Laser Deposition for additive manufacturing; Part II: Mechanical behavior, process parameter optimization and control,” *Addit Manuf*, vol. 8, pp. 12–35, Oct. 2015, doi: 10.1016/j.addma.2015.07.002.
- [28] E. B. Fonseca, J. D. Escobar, A. H. G. Gabriel, G. G. Ribamar, T. Boll, and É. S. N. Lopes, “Tempering of an additively manufactured microsegregated hot-work tool steel: A high-temperature synchrotron X-ray diffraction study,” *Addit Manuf*, vol. 55, p. 102812, Jul. 2022, doi: 10.1016/j.addma.2022.102812.
- [29] E. S. Kim, F. Haftlang, S. Y. Ahn, G. H. Gu, and H. S. Kim, “Effects of processing parameters and heat treatment on the microstructure and magnetic properties of the in-situ synthesized Fe-Ni permalloy produced using direct energy deposition,” *J Alloys Compd*, vol. 907, p. 164415, Jun. 2022, doi: 10.1016/j.jallcom.2022.164415.
- [30] J. Epp, J. Dong, H. Meyer, and A. Bohlen, “Analysis of cyclic phase transformations during additive manufacturing of hardenable tool steel by in-situ X-ray diffraction experiments,” *Scr Mater*, vol. 177, pp. 27–31, Mar. 2020, doi: 10.1016/j.scriptamat.2019.09.021.
- [31] J. Mazumder, J. Choi, K. Nagarathnam, J. Koch, and D. Hetzner, “The direct metal deposition of H13 tool steel for 3-D components,” *JOM*, vol. 49, no. 5, pp. 55–60, May 1997, doi: 10.1007/BF02914687.
- [32] F. Deirmina, N. Peghini, B. AlMangour, D. Grzesiak, and M. Pellizzari, “Heat treatment and properties of a hot work tool steel fabricated by additive manufacturing,” *Materials Science and Engineering: A*, vol. 753, pp. 109–121, Apr. 2019, doi: 10.1016/j.msea.2019.03.027.
- [33] X. Peng, L. Kong, J. Y. H. Fuh, and H. Wang, “A Review of Post-Processing Technologies in Additive Manufacturing,” *Journal of Manufacturing and Materials Processing*, vol. 5, no. 2, p. 38, Apr. 2021, doi: 10.3390/jmmp5020038.
- [34] M. Laleh *et al.*, “Heat treatment for metal additive manufacturing,” *Prog Mater Sci*, vol. 133, p. 101051, Mar. 2023, doi: 10.1016/j.pmatsci.2022.101051.
- [35] Z. Li *et al.*, “High deposition rate powder- and wire-based laser directed energy deposition of metallic materials: A review,” *Int J Mach Tools Manuf*, vol. 181, p. 103942, Oct. 2022, doi: 10.1016/j.ijmachtools.2022.103942.

- [36] D. Svetlizky *et al.*, “Laser-based directed energy deposition (DED-LB) of advanced materials,” *Materials Science and Engineering: A*, vol. 840, p. 142967, Apr. 2022, doi: 10.1016/j.msea.2022.142967.
- [37] D. Dev Singh, S. Arjula, and A. Raji Reddy, “Functionally Graded Materials Manufactured by Direct Energy Deposition: A review,” *Mater Today Proc*, vol. 47, pp. 2450–2456, 2021, doi: 10.1016/j.matpr.2021.04.536.
- [38] M. Ostolaza, J. I. Arrizubieta, A. Lamikiz, S. Plaza, and N. Ortega, “Latest Developments to Manufacture Metal Matrix Composites and Functionally Graded Materials through AM: A State-of-the-Art Review,” *Materials*, vol. 16, no. 4, p. 1746, Feb. 2023, doi: 10.3390/ma16041746.
- [39] Y. Zhang, S. Shen, H. Li, and Y. Hu, “Review of in situ and real-time monitoring of metal additive manufacturing based on image processing,” *The International Journal of Advanced Manufacturing Technology*, vol. 123, no. 1–2, pp. 1–20, Nov. 2022, doi: 10.1007/s00170-022-10178-3.
- [40] J. M. Wilson, C. Piya, Y. C. Shin, F. Zhao, and K. Ramani, “Remanufacturing of turbine blades by laser direct deposition with its energy and environmental impact analysis,” *J Clean Prod*, vol. 80, pp. 170–178, Oct. 2014, doi: 10.1016/j.jclepro.2014.05.084.
- [41] D. Ding, Z. Pan, D. Cuiuri, and H. Li, “Wire-feed additive manufacturing of metal components: technologies, developments and future interests,” *The International Journal of Advanced Manufacturing Technology*, vol. 81, no. 1–4, pp. 465–481, Oct. 2015, doi: 10.1007/s00170-015-7077-3.
- [42] T. A. Rodrigues, V. Duarte, R. M. Miranda, T. G. Santos, and J. P. Oliveira, “Current Status and Perspectives on Wire and Arc Additive Manufacturing (WAAM),” *Materials*, vol. 12, no. 7, p. 1121, Apr. 2019, doi: 10.3390/ma12071121.
- [43] C. P. Paul, A. N. Jinoop, A. Kumar, and K. S. Bindra, “Laser-Based Metal Additive Manufacturing: Technology, Global Scenario and Our Experiences,” *Transactions of the Indian National Academy of Engineering*, vol. 6, no. 4, pp. 895–908, Dec. 2021, doi: 10.1007/s41403-021-00228-9.
- [44] E. Toyserkani, A. Khajepour, and S. F. Corbin, *Laser Cladding*. CRC Press, 2004. doi: 10.1201/9781420039177.
- [45] S. Negi *et al.*, “Review on electron beam based additive manufacturing,” *Rapid Prototyp J*, vol. 26, no. 3, pp. 485–498, Nov. 2019, doi: 10.1108/RPJ-07-2019-0182.
- [46] H.-E. Joe, E.-G. Kang, and M. B. G. Jun, “A Review of State of the Art of Electron Beam and Ion Beam Machining,” *Journal of the Korean Society for Precision Engineering*, vol. 35, no. 3, pp. 241–252, Mar. 2018, doi: 10.7736/KSPE.2018.35.3.241.
- [47] S. W. Williams, F. Martina, A. C. Addison, J. Ding, G. Pardal, and P. Colegrove, “Wire + Arc Additive Manufacturing,” *Materials Science and Technology*, vol. 32, no. 7, pp. 641–647, May 2016, doi: 10.1179/1743284715Y.0000000073.
- [48] A. M. Ralls, M. Daroonparvar, M. John, S. Sikdar, and P. L. Menezes, “Solid-State Cold Spray Additive Manufacturing of Ni-Based Superalloys:

- Processing–Microstructure–Property Relationships,” *Materials*, vol. 16, no. 7, p. 2765, Mar. 2023, doi: 10.3390/ma16072765.
- [49] S. Yin *et al.*, “Cold spray additive manufacturing and repair: Fundamentals and applications,” *Addit Manuf*, vol. 21, pp. 628–650, May 2018, doi: 10.1016/j.addma.2018.04.017.
- [50] A. Standard, “F3187-16 Standard Guide for Directed Energy Deposition of Metals,” *ASTM International: West Conshohocken, PA, USA*, 2016.
- [51] D. Svetlizky *et al.*, “Directed energy deposition (DED) additive manufacturing: Physical characteristics, defects, challenges and applications,” *Materials Today*, vol. 49, pp. 271–295, Oct. 2021, doi: 10.1016/j.mattod.2021.03.020.
- [52] J. M. Flynn, A. Shokrani, S. T. Newman, and V. Dhokia, “Hybrid additive and subtractive machine tools – Research and industrial developments,” *Int J Mach Tools Manuf*, vol. 101, pp. 79–101, Feb. 2016, doi: 10.1016/j.ijmachtools.2015.11.007.
- [53] T. Feldhausen *et al.*, “Review of Computer-Aided Manufacturing (CAM) strategies for hybrid directed energy deposition,” *Addit Manuf*, vol. 56, p. 102900, Aug. 2022, doi: 10.1016/j.addma.2022.102900.
- [54] Z. Y. Chua, I. H. Ahn, and S. K. Moon, “Process monitoring and inspection systems in metal additive manufacturing: Status and applications,” *International Journal of Precision Engineering and Manufacturing-Green Technology*, vol. 4, no. 2, pp. 235–245, Apr. 2017, doi: 10.1007/s40684-017-0029-7.
- [55] Y. Hu and W. Cong, “A review on laser deposition-additive manufacturing of ceramics and ceramic reinforced metal matrix composites,” *Ceram Int*, vol. 44, no. 17, pp. 20599–20612, Dec. 2018, doi: 10.1016/j.ceramint.2018.08.083.
- [56] M. Brandt, “Laser additive manufacturing: materials, design, technologies, and applications,” 2016.
- [57] M. Zavala-Arredondo *et al.*, “Laser diode area melting for high speed additive manufacturing of metallic components,” *Mater Des*, vol. 117, pp. 305–315, Mar. 2017, doi: 10.1016/j.matdes.2016.12.095.
- [58] R. Poprawe, K. Boucke, and D. Hoffman, *Tailored Light 1: High Power Lasers for Production*. Springer, 2018.
- [59] E. Kannatey-Asibu Jr, *Principles of Laser Materials Processing: Developments and Applications*. John Wiley & Sons, 2023.
- [60] “[https://www.akelalaser.com/markets/industrial/diode-laser-cutting/.](https://www.akelalaser.com/markets/industrial/diode-laser-cutting/)”
- [61] R. Koike, S. Takemura, Y. Kakinuma, and M. Kondo, “Enhancement of powder supply efficiency in directed energy deposition based on gas-solid multiphase-flow simulation,” *Procedia CIRP*, vol. 78, pp. 133–137, 2018, doi: 10.1016/j.procir.2018.09.061.
- [62] M. Lalegani Dezaki *et al.*, “A review on additive/subtractive hybrid manufacturing of directed energy deposition (DED) process,” *Advanced Powder Materials*, vol. 1, no. 4, p. 100054, Oct. 2022, doi: 10.1016/j.apmate.2022.100054.

- [63] M. L. Griffith *et al.*, “Understanding thermal behavior in the LENS process,” *Mater Des*, vol. 20, no. 2–3, pp. 107–113, Jun. 1999, doi: 10.1016/S0261-3069(99)00016-3.
- [64] M. Soshi, C. Yau, and R. Kusama, “Development and evaluation of a dynamic powder splitting system for the directed energy deposition (DED) process,” *CIRP Annals*, vol. 69, no. 1, pp. 341–344, 2020, doi: 10.1016/j.cirp.2020.04.048.
- [65] A. Simchi, “Direct laser sintering of metal powders: Mechanism, kinetics and microstructural features,” *Materials Science and Engineering: A*, vol. 428, no. 1–2, pp. 148–158, Jul. 2006, doi: 10.1016/j.msea.2006.04.117.
- [66] S. Wen and Y. C. Shin, “Modeling of transport phenomena during the coaxial laser direct deposition process,” *J Appl Phys*, vol. 108, no. 4, Aug. 2010, doi: 10.1063/1.3474655.
- [67] X. He and J. Mazumder, “Transport phenomena during direct metal deposition,” *J Appl Phys*, vol. 101, no. 5, Mar. 2007, doi: 10.1063/1.2710780.
- [68] P. Peyre, P. Aubry, R. Fabbro, R. Neveu, and A. Longuet, “Analytical and numerical modelling of the direct metal deposition laser process,” *J Phys D Appl Phys*, vol. 41, no. 2, p. 025403, 2008.
- [69] Y.-L. Huang, J. Liu, N.-H. Ma, and J.-G. Li, “Three-dimensional analytical model on laser-powder interaction during laser cladding,” *J Laser Appl*, vol. 18, no. 1, pp. 42–46, Feb. 2006, doi: 10.2351/1.2164476.
- [70] M. L. Griffith, D. M. Keicher, and C. L. Atwood, “Free form fabrication of metallic components using laser engineered net shaping (LENS {trademark}),” Sandia National Lab.(SNL-NM), Albuquerque, NM (United States), 1996.
- [71] A. J. Pinkerton and L. Li, “Modelling the geometry of a moving laser melt pool and deposition track via energy and mass balances,” *J Phys D Appl Phys*, vol. 37, no. 14, pp. 1885–1895, Jul. 2004, doi: 10.1088/0022-3727/37/14/003.
- [72] R. R. Unocic and J. N. DuPont, “Process efficiency measurements in the laser engineered net shaping process,” *Metallurgical and Materials Transactions B*, vol. 35, no. 1, pp. 143–152, Feb. 2004, doi: 10.1007/s11663-004-0104-7.
- [73] J. I. Arrizubieta, S. Martínez, A. Lamikiz, E. Ukar, K. Arntz, and F. Klocke, “Instantaneous powder flux regulation system for Laser Metal Deposition,” *J Manuf Process*, vol. 29, pp. 242–251, Oct. 2017, doi: 10.1016/j.jmapro.2017.07.018.
- [74] A. J. Pinkerton, “Laser direct metal deposition: theory and applications in manufacturing and maintenance,” in *Advances in Laser Materials Processing*, Elsevier, 2010, pp. 461–491. doi: 10.1533/9781845699819.6.461.
- [75] J. L. Koch and J. Mazumder, “Rapid prototyping by laser cladding,” in *International Congress on Applications of Lasers & Electro-Optics*, AIP Publishing, 1993, pp. 556–565.

- [76] A. Singh, S. Kapil, and M. Das, “A comprehensive review of the methods and mechanisms for powder feedstock handling in directed energy deposition,” *Addit Manuf*, vol. 35, p. 101388, Oct. 2020, doi: 10.1016/j.addma.2020.101388.
- [77] S. Carty, I. Owen, W. M. Steen, B. Bastow, and J. T. Spencer, “Catchment efficiency for novel nozzle designs used in laser cladding and alloying,” *Laser processing: surface treatment and film deposition*, pp. 395–410, 1996.
- [78] W. M. Steen, “Laser Surface Cladding in Laser Surface Treatment of Metals,” eds. *CW Draper and P. Mazzoldi, NATO ASI Series E*, no. 155, 1985.
- [79] Y. Hu, C. Chen, and K. Mukherjee, “Innovative Laser-Aided Manufacturing of Patterned Stamping and Cutting Dies: Processing Parameters,” *Materials and Manufacturing Processes*, vol. 13, no. 3, pp. 369–387, May 1998, doi: 10.1080/10426919808935255.
- [80] J.-D. Kim and Y. Peng, “Plunging method for Nd:YAG laser cladding with wire feeding,” *Opt Lasers Eng*, vol. 33, no. 4, pp. 299–309, Apr. 2000, doi: 10.1016/S0143-8166(00)00046-4.
- [81] S. H. Mok, G. Bi, J. Folkes, and I. Pashby, “Deposition of Ti–6Al–4V using a high power diode laser and wire, Part I: Investigation on the process characteristics,” *Surf Coat Technol*, vol. 202, no. 16, pp. 3933–3939, May 2008, doi: 10.1016/j.surfcoat.2008.02.008.
- [82] A. Heralić, A.-K. Christiansson, and B. Lennartson, “Height control of laser metal-wire deposition based on iterative learning control and 3D scanning,” *Opt Lasers Eng*, vol. 50, no. 9, pp. 1230–1241, Sep. 2012, doi: 10.1016/j.optlaseng.2012.03.016.
- [83] H. Bhadeshia and R. Honeycombe, “Iron and Its Interstitial Solutions,” in *Steels: Microstructure and Properties*, Elsevier, 2017, pp. 1–22. doi: 10.1016/B978-0-08-100270-4.00001-9.
- [84] F. P. Bundy, “Pressure—Temperature Phase Diagram of Iron to 200 kbar, 900°C,” *J Appl Phys*, vol. 36, no. 2, pp. 616–620, Feb. 1965, doi: 10.1063/1.1714038.
- [85] R. Singh, “Physical Metallurgy,” in *Applied Welding Engineering*, Elsevier, 2016, pp. 13–26. doi: 10.1016/B978-0-12-804176-5.00003-7.
- [86] W. Hume-Rothery, “The Crystal Structures of Iron: Ideal Structures,” in *The Structures of Alloys of Iron*, Elsevier, 1966, pp. 18–27. doi: 10.1016/B978-0-08-011249-7.50005-9.
- [87] H. Bhadeshia and S. R. Honeycombe, “Iron and its Interstitial solid solutions,” *Steels. 3rd ed. Oxford: Butterworth-Heinemann*, pp. 1–16, 2006.
- [88] E. Jäggle, Z. Sheng, P. Kürsteiner, S. Ocylok, A. Weisheit, and D. Raabe, “Comparison of Maraging Steel Micro- and Nanostructure Produced Conventionally and by Laser Additive Manufacturing,” *Materials*, vol. 10, no. 1, p. 8, Dec. 2016, doi: 10.3390/ma10010008.
- [89] H. Bhadeshia and R. Honeycombe, “Stainless Steel,” in *Steels: Microstructure and Properties*, Elsevier, 2017, pp. 343–376. doi: 10.1016/B978-0-08-100270-4.00012-3.

- [90] A. J. Sedriks, "Corrosion of Stainless Steels," in *Encyclopedia of Materials: Science and Technology*, Elsevier, 2001, pp. 1707–1708. doi: 10.1016/B0-08-043152-6/00304-1.
- [91] J. R. Davis, *Stainless steels*. ASM international, 1994.
- [92] G. A. Roberts, R. Kennedy, and G. Krauss, *Tool steels*. ASM international, 1998.
- [93] P. M. Novotny and M. K. Banerjee, "Tool and Die Steels," in *Reference Module in Materials Science and Materials Engineering*, Elsevier, 2016. doi: 10.1016/B978-0-12-803581-8.02534-0.
- [94] J. R. Davis and A. S. M. I. H. Committee, *ASM Specialty Handbook: Tool Materials*. in ASM Specialty Handbook. ASM International, 1995. [Online]. Available: <https://books.google.it/books?id=JwntzgEACAAJ>
- [95] "Steels for aircraft structures," in *Introduction to Aerospace Materials*, Elsevier, 2012, pp. 232–250. doi: 10.1533/9780857095152.232.
- [96] G. I. Silman, "Compilative Fe – Ni phase diagram with author's correction," *Metal Science and Heat Treatment*, vol. 54, no. 3–4, pp. 105–112, Jul. 2012, doi: 10.1007/s11041-012-9463-x.
- [97] N. Haghdadi, M. Laleh, M. Moyle, and S. Primig, "Additive manufacturing of steels: a review of achievements and challenges," *J Mater Sci*, vol. 56, no. 1, pp. 64–107, 2021, doi: 10.1007/s10853-020-05109-0.
- [98] W. Xu, E. W. Lui, A. Pateras, M. Qian, and M. Brandt, "In situ tailoring microstructure in additively manufactured Ti-6Al-4V for superior mechanical performance," *Acta Mater*, vol. 125, pp. 390–400, Feb. 2017, doi: 10.1016/j.actamat.2016.12.027.
- [99] R. Shi, S. A. Khairallah, T. T. Roehling, T. W. Heo, J. T. McKeown, and M. J. Matthews, "Microstructural control in metal laser powder bed fusion additive manufacturing using laser beam shaping strategy," *Acta Mater*, vol. 184, pp. 284–305, Feb. 2020, doi: 10.1016/j.actamat.2019.11.053.
- [100] S.-H. Sun, T. Ishimoto, K. Hagihara, Y. Tsutsumi, T. Hanawa, and T. Nakano, "Excellent mechanical and corrosion properties of austenitic stainless steel with a unique crystallographic lamellar microstructure via selective laser melting," *Scr Mater*, vol. 159, pp. 89–93, Jan. 2019, doi: 10.1016/j.scriptamat.2018.09.017.
- [101] F. Bartolomeu *et al.*, "316L stainless steel mechanical and tribological behavior—A comparison between selective laser melting, hot pressing and conventional casting," *Addit Manuf*, vol. 16, pp. 81–89, Aug. 2017, doi: 10.1016/j.addma.2017.05.007.
- [102] P. A. Hooper, "Melt pool temperature and cooling rates in laser powder bed fusion," *Addit Manuf*, vol. 22, pp. 548–559, Aug. 2018, doi: 10.1016/j.addma.2018.05.032.
- [103] M. Ma, Z. Wang, and X. Zeng, "A comparison on metallurgical behaviors of 316L stainless steel by selective laser melting and laser cladding deposition," *Materials Science and Engineering: A*, vol. 685, pp. 265–273, Feb. 2017, doi: 10.1016/j.msea.2016.12.112.

- [104] P. Bajaj, A. Hariharan, A. Kini, P. Kürnsteiner, D. Raabe, and E. A. Jäggle, “Steels in additive manufacturing: A review of their microstructure and properties,” *Materials Science and Engineering: A*, vol. 772, p. 138633, Jan. 2020, doi: 10.1016/j.msea.2019.138633.
- [105] T. Guan, S. Chen, X. Chen, J. Liang, C. Liu, and M. Wang, “Effect of laser incident energy on microstructures and mechanical properties of 12CrNi2Y alloy steel by direct laser deposition,” *J Mater Sci Technol*, vol. 35, no. 2, pp. 395–402, 2019, doi: <https://doi.org/10.1016/j.jmst.2018.10.024>.
- [106] Y. Yao, Y. Huang, B. Chen, C. Tan, Y. Su, and J. Feng, “Influence of processing parameters and heat treatment on the mechanical properties of 18Ni300 manufactured by laser based directed energy deposition,” *Opt Laser Technol*, vol. 105, pp. 171–179, 2018, doi: <https://doi.org/10.1016/j.optlastec.2018.03.011>.
- [107] R. S. Amano and P. K. Rohatgi, “Laser engineered net shaping process for SAE 4140 low alloy steel,” *Materials Science and Engineering: A*, vol. 528, no. 22–23, pp. 6680–6693, Aug. 2011, doi: 10.1016/j.msea.2011.05.036.
- [108] H. Kim, Z. Liu, W. Cong, and H.-C. Zhang, “Tensile Fracture Behavior and Failure Mechanism of Additively-Manufactured AISI 4140 Low Alloy Steel by Laser Engineered Net Shaping,” *Materials*, vol. 10, no. 11, p. 1283, Nov. 2017, doi: 10.3390/ma10111283.
- [109] J. Liu, J. Li, X. Cheng, and H. Wang, “Microstructures and tensile properties of laser clad AerMet100 steel coating on 300 M steel,” *J Mater Sci Technol*, vol. 34, no. 4, pp. 643–652, Apr. 2018, doi: 10.1016/j.jmst.2017.11.037.
- [110] G. Sun, R. Zhou, J. Lu, and J. Mazumder, “Evaluation of defect density, microstructure, residual stress, elastic modulus, hardness and strength of laser-deposited AISI 4340 steel,” *Acta Mater*, vol. 84, pp. 172–189, Feb. 2015, doi: 10.1016/j.actamat.2014.09.028.
- [111] C. Huang, X. Lin, H. Yang, F. Liu, and W. Huang, “Microstructure and Tribological Properties of Laser Forming Repaired 34CrNiMo6 Steel,” *Materials*, vol. 11, no. 9, p. 1722, Sep. 2018, doi: 10.3390/ma11091722.
- [112] L. Cao *et al.*, “Effect of laser energy density on defects behavior of direct laser depositing 24CrNiMo alloy steel,” *Opt Laser Technol*, vol. 111, pp. 541–553, Apr. 2019, doi: 10.1016/j.optlastec.2018.10.025.
- [113] X. Zhao *et al.*, “The martensitic strengthening of 12CrNi2 low-alloy steel using a novel scanning strategy during direct laser deposition,” *Opt Laser Technol*, vol. 132, p. 106487, Dec. 2020, doi: 10.1016/j.optlastec.2020.106487.
- [114] X. Chen, S. Chen, T. Cui, J. Liang, C. Liu, and M. Wang, “A new 50Cr6Ni2Y alloy steel prepared by Direct laser Deposition: Its design, microstructure and properties,” *Opt Laser Technol*, vol. 126, p. 106080, Jun. 2020, doi: 10.1016/j.optlastec.2020.106080.
- [115] Y. Shi, Z. Lu, H. Xu, R. Xie, Y. Ren, and G. Yang, “Microstructure characterization and mechanical properties of laser additive manufactured

- oxide dispersion strengthened Fe-9Cr alloy,” *J Alloys Compd*, vol. 791, pp. 121–133, Jun. 2019, doi: 10.1016/j.jallcom.2019.03.284.
- [116] S. M. T. Omar and K. P. Plucknett, “The influence of DED process parameters and heat-treatment cycle on the microstructure and hardness of AISI D2 tool steel,” *J Manuf Process*, vol. 81, pp. 655–671, Sep. 2022, doi: 10.1016/j.jmapro.2022.06.069.
- [117] D.-S. Shim, G.-Y. Baek, S.-B. Lee, J.-H. Yu, Y.-S. Choi, and S.-H. Park, “Influence of heat treatment on wear behavior and impact toughness of AISI M4 coated by laser melting deposition,” *Surf Coat Technol*, vol. 328, pp. 219–230, Nov. 2017, doi: 10.1016/j.surfcoat.2017.08.059.
- [118] Y. K. Park *et al.*, “Wear resistance of direct-energy–deposited AISI M2 tool steel with and without post-heat treatment,” *The International Journal of Advanced Manufacturing Technology*, vol. 116, no. 11–12, pp. 3917–3931, Oct. 2021, doi: 10.1007/s00170-021-07741-9.
- [119] J. Vinčić, A. Aversa, M. Lombardi, and D. Manfredi, “Processability and Microstructural Evolution of W360 Hot Work Tool Steel by Directed Energy Deposition,” *Metals and Materials International*, Sep. 2023, doi: 10.1007/s12540-023-01508-5.
- [120] A. Saboori, A. Aversa, G. Marchese, S. Biamino, M. Lombardi, and P. Fino, “Microstructure and Mechanical Properties of AISI 316L Produced by Directed Energy Deposition-Based Additive Manufacturing: A Review,” *Applied Sciences*, vol. 10, no. 9, p. 3310, May 2020, doi: 10.3390/app10093310.
- [121] M. A. Melia, H.-D. A. Nguyen, J. M. Rodelas, and E. J. Schindelholz, “Corrosion properties of 304L stainless steel made by directed energy deposition additive manufacturing,” *Corros Sci*, vol. 152, pp. 20–30, May 2019, doi: 10.1016/j.corsci.2019.02.029.
- [122] M. K. Alam, M. Mehdi, R. J. Urbanic, and A. Edrisy, “Mechanical behavior of additive manufactured AISI 420 martensitic stainless steel,” *Materials Science and Engineering: A*, vol. 773, p. 138815, Jan. 2020, doi: 10.1016/j.msea.2019.138815.
- [123] I. Mathoho, E. T. Akinlabi, N. Arthur, and M. Tlotleng, “Impact of DED process parameters on the metallurgical characteristics of 17-4 PH SS deposited using DED,” *CIRP J Manuf Sci Technol*, vol. 31, pp. 450–458, Nov. 2020, doi: 10.1016/j.cirpj.2020.07.007.
- [124] M. Brázda, P. Salvetr, S. Rzepa, D. Melzer, and J. Vavřík, “Effect of heat treatment on mechanical properties of duplex steel SAF 2507 manufactured by DED,” *IOP Conf Ser Mater Sci Eng*, vol. 1178, no. 1, p. 012008, Aug. 2021, doi: 10.1088/1757-899X/1178/1/012008.
- [125] H. J. Im *et al.*, “Thermally driven changes in the microstructure and mechanical properties of martensitic 15–5 precipitation-hardened stainless steel during directed energy deposition,” *Addit Manuf*, vol. 74, p. 103729, Jul. 2023, doi: 10.1016/j.addma.2023.103729.
- [126] A. Maier *et al.*, “Influence of process parameters on microstructural and mechanical properties of duplex stainless steel 2205 (1.4462) processed by

- DED-LB\M,” *Procedia CIRP*, vol. 111, pp. 241–246, 2022, doi: 10.1016/j.procir.2022.08.058.
- [127] A. Zadi-Maad, R. Rohib, and A. Irawan, “Additive manufacturing for steels: a review,” *IOP Conf Ser Mater Sci Eng*, vol. 285, p. 012028, Jan. 2018, doi: 10.1088/1757-899X/285/1/012028.
- [128] A. Saboori *et al.*, “Production of Single Tracks of Ti-6Al-4V by Directed Energy Deposition to Determine the Layer Thickness for Multilayer Deposition,” *Journal of Visualized Experiments*, no. 133, Mar. 2018, doi: 10.3791/56966.
- [129] F. Bosio *et al.*, “Directed energy deposition of 316L steel: Effect of type of powders and gas related parameters,” in *Proceedings of the Euro PM2018 Congress & Exhibition, Bilbao, Spain, 2018*, pp. 14–18.
- [130] M. Ziętała *et al.*, “The microstructure, mechanical properties and corrosion resistance of 316L stainless steel fabricated using laser engineered net shaping,” *Materials Science and Engineering: A*, vol. 677, pp. 1–10, Nov. 2016, doi: 10.1016/j.msea.2016.09.028.
- [131] A. Yadollahi, N. Shamsaei, S. M. Thompson, and D. W. Seely, “Effects of process time interval and heat treatment on the mechanical and microstructural properties of direct laser deposited 316L stainless steel,” *Materials Science and Engineering: A*, vol. 644, pp. 171–183, Sep. 2015, doi: 10.1016/j.msea.2015.07.056.
- [132] Z. Wang, T. A. Palmer, and A. M. Beese, “Effect of processing parameters on microstructure and tensile properties of austenitic stainless steel 304L made by directed energy deposition additive manufacturing,” *Acta Mater*, vol. 110, pp. 226–235, May 2016, doi: 10.1016/j.actamat.2016.03.019.
- [133] J. S. Park, J. H. Park, M.-G. Lee, J. H. Sung, K. J. Cha, and D. H. Kim, “Effect of Energy Input on the Characteristic of AISI H13 and D2 Tool Steels Deposited by a Directed Energy Deposition Process,” *Metallurgical and Materials Transactions A*, vol. 47, no. 5, pp. 2529–2535, 2016, doi: 10.1007/s11661-016-3427-5.
- [134] K. Saeidi, X. Gao, F. Lofaj, L. Kvetková, and Z. J. Shen, “Transformation of austenite to duplex austenite-ferrite assembly in annealed stainless steel 316L consolidated by laser melting,” *J Alloys Compd*, vol. 633, pp. 463–469, Jun. 2015, doi: 10.1016/j.jallcom.2015.01.249.
- [135] K. Zhang, S. Wang, W. Liu, and X. Shang, “Characterization of stainless steel parts by Laser Metal Deposition Shaping,” *Mater Des*, vol. 55, pp. 104–119, Mar. 2014, doi: 10.1016/j.matdes.2013.09.006.
- [136] P. Guo, B. Zou, C. Huang, and H. Gao, “Study on microstructure, mechanical properties and machinability of efficiently additive manufactured AISI 316L stainless steel by high-power direct laser deposition,” *J Mater Process Technol*, vol. 240, pp. 12–22, Feb. 2017, doi: 10.1016/j.jmatprotec.2016.09.005.
- [137] R. W. Hinton and R. K. Wiswesser, “Estimating welding preheat requirements for unknown grades of carbon and low-alloy steels,” *Weld J*, vol. 87, no. 11, pp. 273–276, 2008.

- [138] M. Bruneau, U. Chia-Ming, and R. Sabelli, *Ductile Design of Steel Structures*, 2nd edition. McGraw-Hill Education, 2011.
- [139] J. Krell, A. Röttger, K. Geenen, and W. Theisen, “General investigations on processing tool steel X40CrMoV5-1 with selective laser melting,” *J Mater Process Technol*, vol. 255, pp. 679–688, May 2018, doi: 10.1016/j.jmatprotec.2018.01.012.
- [140] O. S. Odebiyi, S. M. Adedayo, L. A. Tunji, and M. O. Onuorah, “A review of weldability of carbon steel in arc-based welding processes,” *Cogent Eng*, vol. 6, no. 1, Jan. 2019, doi: 10.1080/23311916.2019.1609180.
- [141] J. Boes, A. Röttger, C. Mutke, C. Escher, and S. Weber, “Microstructure and Properties of a Novel Carbon-Martensitic Hot Work Tool Steel Processed by Laser Additive Manufacturing without Preheating,” *Steel Res Int*, vol. 94, no. 4, Apr. 2023, doi: 10.1002/srin.202200439.
- [142] J. Mazumder, A. Schifferer, and J. Choi, “Direct materials deposition: designed macro and microstructure,” *Materials Research Innovations*, vol. 3, no. 3, pp. 118–131, Oct. 1999, doi: 10.1007/s100190050137.
- [143] M. J. Holzweissig, A. Taube, F. Brenne, M. Schaper, and T. Niendorf, “Microstructural Characterization and Mechanical Performance of Hot Work Tool Steel Processed by Selective Laser Melting,” *Metallurgical and Materials Transactions B*, vol. 46, no. 2, pp. 545–549, Apr. 2015, doi: 10.1007/s11663-014-0267-9.
- [144] L. Xue, J. Chen, and S.-H. Wang, “Freeform Laser Consolidated H13 and CPM 9V Tool Steels,” *Metallography, Microstructure, and Analysis*, vol. 2, no. 2, pp. 67–78, Apr. 2013, doi: 10.1007/s13632-013-0061-0.
- [145] R. Cottam, J. Wang, and V. Luzin, “Characterization of microstructure and residual stress in a 3D H13 tool steel component produced by additive manufacturing,” *J Mater Res*, vol. 29, no. 17, pp. 1978–1986, Sep. 2014, doi: 10.1557/jmr.2014.190.
- [146] M. Åsberg, G. Fredriksson, S. Hatami, W. Fredriksson, and P. Krakhmalev, “Influence of post treatment on microstructure, porosity and mechanical properties of additive manufactured H13 tool steel,” *Materials Science and Engineering: A*, vol. 742, pp. 584–589, Jan. 2019, doi: 10.1016/j.msea.2018.08.046.
- [147] M. Zanni, A. Morri, S. Messieri, and L. Ceschini, “Tensile behaviour of a hot work tool steel manufactured via Laser Powder Bed Fusion: effect of an innovative high pressure heat treatment,” *Procedia Structural Integrity*, vol. 47, pp. 370–382, 2023, doi: 10.1016/j.prostr.2023.07.087.
- [148] A. J. Pinkerton and L. Li, “Direct additive laser manufacturing using gas- and water-atomised H13 tool steel powders,” *The International Journal of Advanced Manufacturing Technology*, vol. 25, no. 5–6, pp. 471–479, Mar. 2005, doi: 10.1007/s00170-003-1844-2.
- [149] C. Félix-Martínez, J. Ibarra-Medina, D. A. Fernández-Benavides, L. A. Cáceres-Díaz, and J. M. Alvarado-Orozco, “Effect of the parametric optimization and heat-treatment on the 18Ni-300 maraging steel microstructural properties manufactured by directed energy deposition,” *The*

- International Journal of Advanced Manufacturing Technology*, vol. 115, no. 11–12, pp. 3999–4020, Aug. 2021, doi: 10.1007/s00170-021-07320-y.
- [150] N. Rońda, K. Grzelak, M. Polański, and J. Dworecka-Wójcik, “The Influence of Layer Thickness on the Microstructure and Mechanical Properties of M300 Maraging Steel Additively Manufactured by LENS® Technology,” *Materials*, vol. 15, no. 2, p. 603, Jan. 2022, doi: 10.3390/ma15020603.
- [151] S. L. Campanelli, A. Angelastro, C. G. Signorile, and G. Casalino, “Investigation on direct laser powder deposition of 18 Ni (300) marage steel using mathematical model and experimental characterisation,” *The International Journal of Advanced Manufacturing Technology*, vol. 89, no. 1–4, pp. 885–895, Mar. 2017, doi: 10.1007/s00170-016-9135-x.
- [152] P. Kürsteiner, M. B. Wilms, A. Weisheit, P. Barriobero-Vila, E. A. Jäggle, and D. Raabe, “Massive nanoprecipitation in an Fe-19Ni-xAl maraging steel triggered by the intrinsic heat treatment during laser metal deposition,” *Acta Mater*, vol. 129, pp. 52–60, May 2017, doi: 10.1016/j.actamat.2017.02.069.
- [153] B. Mooney, K. I. Kourousis, and R. Raghavendra, “Plastic anisotropy of additively manufactured maraging steel: Influence of the build orientation and heat treatments,” *Addit Manuf*, vol. 25, pp. 19–31, Jan. 2019, doi: 10.1016/j.addma.2018.10.032.
- [154] R. Casati, J. Lemke, A. Tuissi, and M. Vedani, “Aging Behaviour and Mechanical Performance of 18-Ni 300 Steel Processed by Selective Laser Melting,” *Metals (Basel)*, vol. 6, no. 9, p. 218, Sep. 2016, doi: 10.3390/met6090218.
- [155] S. Luo, H. Wang, Z. Gao, Y. Wu, and H. Wang, “Interaction between high-velocity gas and liquid in gas atomization revealed by a new coupled simulation model,” *Mater Des*, vol. 212, p. 110264, Dec. 2021, doi: 10.1016/j.matdes.2021.110264.
- [156] D. Beckers, N. Ellendt, U. Fritsching, and V. Uhlenwinkel, “Impact of process flow conditions on particle morphology in metal powder production via gas atomization,” *Advanced Powder Technology*, vol. 31, no. 1, pp. 300–311, Jan. 2020, doi: 10.1016/j.apt.2019.10.022.
- [157] K. Danjo, K. Kinoshita, K. Kitagawa, K. Iida, H. Sunada, and A. Otsuka, “Effect of particle shape on the compaction and flow properties of powders,” *Chem Pharm Bull (Tokyo)*, vol. 37, no. 11, pp. 3070–3073, 1989, doi: 10.1248/cpb.37.3070.
- [158] P. Zhu, X. He, H. Guan, Z. Zhang, T. Zhang, and X. Qu, “Investigation on the Attainment of High-Density 316L Stainless Steel with Selective Laser Sintering,” *Materials*, vol. 17, no. 1, p. 110, Dec. 2023, doi: 10.3390/ma17010110.
- [159] C. Kamath, B. El-dasher, G. F. Gallegos, W. E. King, and A. Sisto, “Density of additively-manufactured, 316L SS parts using laser powder-bed fusion at powers up to 400 W,” *The International Journal of Advanced Manufacturing Technology*, vol. 74, no. 1–4, pp. 65–78, Sep. 2014, doi: 10.1007/s00170-014-5954-9.

- [160] A. Saboori *et al.*, “An investigation on the effect of powder recycling on the microstructure and mechanical properties of AISI 316L produced by Directed Energy Deposition,” *Materials Science and Engineering: A*, vol. 766, p. 138360, Oct. 2019, doi: 10.1016/j.msea.2019.138360.
- [161] B. Kocabekir, R. Kaçar, S. Gündüz, and F. Hayat, “An effect of heat input, weld atmosphere and weld cooling conditions on the resistance spot weldability of 316L austenitic stainless steel,” *J Mater Process Technol*, vol. 195, no. 1–3, pp. 327–335, Jan. 2008, doi: 10.1016/j.jmatprotec.2007.05.026.
- [162] P. L. Ferrandini, C. T. Rios, A. T. Dutra, M. A. Jaime, P. R. Mei, and R. Caram, “Solute segregation and microstructure of directionally solidified austenitic stainless steel,” *Materials Science and Engineering: A*, vol. 435–436, pp. 139–144, Nov. 2006, doi: 10.1016/j.msea.2006.07.024.
- [163] S. Atamert and J. E. King, “Elemental partitioning and microstructural development in duplex stainless steel weld metal,” *Acta Metallurgica et Materialia*, vol. 39, no. 3, pp. 273–285, Mar. 1991, doi: 10.1016/0956-7151(91)90306-L.
- [164] F. Yan, W. Xiong, E. Faierson, and G. B. Olson, “Characterization of nano-scale oxides in austenitic stainless steel processed by powder bed fusion,” *Scr Mater*, vol. 155, pp. 104–108, Oct. 2018, doi: 10.1016/j.scriptamat.2018.06.011.
- [165] J. T. Pacheco *et al.*, “Laser directed energy deposition of AISI 316L stainless steel: The effect of build direction on mechanical properties in as-built and heat-treated conditions,” *Advances in Industrial and Manufacturing Engineering*, vol. 4, p. 100079, May 2022, doi: 10.1016/j.aime.2022.100079.
- [166] D. Zhang *et al.*, “Grain Refinement of Alloys in Fusion-Based Additive Manufacturing Processes,” *Metallurgical and Materials Transactions A*, vol. 51, no. 9, pp. 4341–4359, Sep. 2020, doi: 10.1007/s11661-020-05880-4.
- [167] J. W. Fu, Y. S. Yang, J. J. Guo, and W. H. Tong, “Effect of cooling rate on solidification microstructures in AISI 304 stainless steel,” *Materials Science and Technology*, vol. 24, no. 8, pp. 941–944, Aug. 2008, doi: 10.1179/174328408X295962.
- [168] H. Yin and S. D. Felicelli, “Dendrite growth simulation during solidification in the LENS process,” *Acta Mater*, vol. 58, no. 4, pp. 1455–1465, Feb. 2010, doi: 10.1016/j.actamat.2009.10.053.
- [169] X. Zhao, L. Liu, Z. Yu, W. Zhang, J. Zhang, and H. Fu, “Influence of directional solidification variables on the microstructure and crystal orientation of AM3 under high thermal gradient,” *J Mater Sci*, vol. 45, no. 22, pp. 6101–6107, Nov. 2010, doi: 10.1007/s10853-010-4696-9.
- [170] B. Zheng, Y. Zhou, J. E. Smugeresky, J. M. Schoenung, and E. J. Lavernia, “Thermal Behavior and Microstructural Evolution during Laser Deposition with Laser-Engineered Net Shaping: Part I. Numerical Calculations,” *Metallurgical and Materials Transactions A*, vol. 39, no. 9, pp. 2228–2236, Sep. 2008, doi: 10.1007/s11661-008-9557-7.

- [171] H. El Kadiri *et al.*, “Phase transformations in low-alloy steel laser deposits,” *Materials Science and Engineering: A*, vol. 494, no. 1–2, pp. 10–20, Oct. 2008, doi: 10.1016/j.msea.2007.12.011.
- [172] R. A. Fisher, “The design of experiments,” 1949.
- [173] S.-W. Cheng and C. F. J. Wu, “Factor screening and response surface exploration,” *Stat Sin*, pp. 553–580, 2001.
- [174] A. Aversa, G. Marchese, and E. Bassini, “Directed Energy Deposition of AISI 316L Stainless Steel Powder: Effect of Process Parameters,” *Metals (Basel)*, vol. 11, no. 6, p. 932, Jun. 2021, doi: 10.3390/met11060932.
- [175] A. Aversa *et al.*, “The role of Directed Energy Deposition atmosphere mode on the microstructure and mechanical properties of 316L samples,” *Addit Manuf*, vol. 34, p. 101274, Aug. 2020, doi: 10.1016/j.addma.2020.101274.
- [176] Y.-Y. Chang, J.-R. Qiu, and S.-J. Hwang, “Multi-objective optimization of directed energy deposition process by using Taguchi-Grey relational analysis,” *The International Journal of Advanced Manufacturing Technology*, vol. 120, no. 11–12, pp. 7547–7563, Jun. 2022, doi: 10.1007/s00170-022-09210-3.
- [177] Z. E. Tan, J. H. L. Pang, J. Kaminski, and H. Pepin, “Characterisation of porosity, density, and microstructure of directed energy deposited stainless steel AISI 316L,” *Addit Manuf*, vol. 25, pp. 286–296, Jan. 2019, doi: 10.1016/j.addma.2018.11.014.
- [178] I. Z. Era, M. Grandhi, and Z. Liu, “Prediction of mechanical behaviors of L-DED fabricated SS 316L parts via machine learning,” *The International Journal of Advanced Manufacturing Technology*, vol. 121, no. 3–4, pp. 2445–2459, Jul. 2022, doi: 10.1007/s00170-022-09509-1.
- [179] S. K. Moheimani, L. Iuliano, and A. Saboori, “The role of substrate preheating on the microstructure, roughness, and mechanical performance of AISI 316L produced by directed energy deposition additive manufacturing,” *The International Journal of Advanced Manufacturing Technology*, vol. 119, no. 11–12, pp. 7159–7174, Apr. 2022, doi: 10.1007/s00170-021-08564-4.
- [180] G. Piscopo, E. Atzeni, and A. Salmi, “A Hybrid Modeling of the Physics-Driven Evolution of Material Addition and Track Generation in Laser Powder Directed Energy Deposition,” *Materials*, vol. 12, no. 17, p. 2819, Sep. 2019, doi: 10.3390/ma12172819.
- [181] A. J. Pinkerton, “Advances in the modeling of laser direct metal deposition,” *J Laser Appl*, vol. 27, no. S1, Feb. 2015, doi: 10.2351/1.4815992.
- [182] I. Garmendia, J. Pujana, A. Lamikiz, M. Madarieta, and J. Leunda, “Structured light-based height control for laser metal deposition,” *J Manuf Process*, vol. 42, pp. 20–27, Jun. 2019, doi: 10.1016/j.jmapro.2019.04.018.
- [183] W.-S. Woo, E.-J. Kim, H.-I. Jeong, and C.-M. Lee, “Laser-Assisted Machining of Ti-6Al-4V Fabricated by DED Additive Manufacturing,” *International Journal of Precision Engineering and Manufacturing-Green Technology*, vol. 7, no. 3, pp. 559–572, May 2020, doi: 10.1007/s40684-020-00221-7.

- [184] A. B. Spierings, N. Herres, and G. Levy, "Influence of the particle size distribution on surface quality and mechanical properties in AM steel parts," *Rapid Prototyp J*, vol. 17, no. 3, pp. 195–202, Apr. 2011, doi: 10.1108/13552541111124770.
- [185] Y. Li, A. J. Bushby, and D. J. Dunstan, "The Hall–Petch effect as a manifestation of the general size effect," *Proceedings of the Royal Society A: Mathematical, Physical and Engineering Sciences*, vol. 472, no. 2190, p. 20150890, Jun. 2016, doi: 10.1098/rspa.2015.0890.
- [186] Y.-L. Huang, G.-Y. Liang, J.-Y. Su, and J.-G. Li, "Interaction between laser beam and powder stream in the process of laser cladding with powder feeding," *Model Simul Mat Sci Eng*, vol. 13, no. 1, pp. 47–56, Jan. 2005, doi: 10.1088/0965-0393/13/1/004.
- [187] X. Xu, G. Mi, Y. Luo, P. Jiang, X. Shao, and C. Wang, "Morphologies, microstructures, and mechanical properties of samples produced using laser metal deposition with 316 L stainless steel wire," *Opt Lasers Eng*, vol. 94, pp. 1–11, Jul. 2017, doi: 10.1016/j.optlaseng.2017.02.008.
- [188] E. Brandl, V. Michailov, B. Viehweger, and C. Leyens, "Deposition of Ti–6Al–4V using laser and wire, part II: Hardness and dimensions of single beads," *Surf Coat Technol*, vol. 206, no. 6, pp. 1130–1141, Dec. 2011, doi: 10.1016/j.surfcoat.2011.07.094.
- [189] W. U. H. Syed and L. Li, "Effects of wire feeding direction and location in multiple layer diode laser direct metal deposition," *Appl Surf Sci*, vol. 248, no. 1–4, pp. 518–524, Jul. 2005, doi: 10.1016/j.apsusc.2005.03.039.
- [190] J. Mazumder and W. M. Steen, "Heat transfer model for cw laser material processing," *J Appl Phys*, vol. 51, no. 2, pp. 941–947, Feb. 1980, doi: 10.1063/1.327672.
- [191] N. Schwarz *et al.*, "Development of a Coaxial Laser Wire System for the Additive Manufacturing of Functional Graded Materials using Direct Energy Deposition," in *Innovative Product Development by Additive Manufacturing 2021*, Cham: Springer International Publishing, 2023, pp. 49–62. doi: 10.1007/978-3-031-05918-6_4.
- [192] Roberts G., Krauss G., and Kennedy R., *Tool Steels*, Fifth edition. ASM International, 1998.
- [193] "Heat Treatment Guidelines - Bohler W360 Isobloc," 2017. Accessed: Sep. 16, 2022. [Online]. Available: <http://www.sayah.com/pdf/BOHLER-W360-ISOBLOC-htr.pdf>
- [194] voestalpine BÖHLER Edelstahl GmbH & Co KG, "W360 heat treatment diagrams." [Online]. Available: <https://www.voestalpine.com/bohler-edelstahl/de/>
- [195] R. A. Grange, C. R. Hribal, and L. F. Porter, "Hardness of tempered martensite in carbon and low-alloy steels," *Metallurgical Transactions A*, vol. 8, no. 11, pp. 1775–1785, Nov. 1977, doi: 10.1007/BF02646882.
- [196] F. Deirmina, B. AlMangour, D. Grzesiak, and M. Pellizzari, "H13–partially stabilized zirconia nanocomposites fabricated by high-energy mechanical

- milling and selective laser melting,” *Mater Des*, vol. 146, pp. 286–297, May 2018, doi: 10.1016/j.matdes.2018.03.017.
- [197] T. Ungár, S. Harjo, T. Kawasaki, Y. Tomota, G. Ribárik, and Z. Shi, “Composite Behavior of Lath Martensite Steels Induced by Plastic Strain, a New Paradigm for the Elastic-Plastic Response of Martensitic Steels,” *Metallurgical and Materials Transactions A*, vol. 48, no. 1, pp. 159–167, Jan. 2017, doi: 10.1007/s11661-016-3845-4.
- [198] P. W. R. J. F. C. Lins, S. R. P., P. S. N. Mendes, and R. E. Pereira, “Microstructural evolution under tempering heat treatment in AISI H13 hot-work tool steel,” *Int J Eng Res Appl*, vol. 07, no. 04, pp. 67–71, Apr. 2017, doi: 10.9790/9622-0704046771.
- [199] R. Amirarsalani, M. Morakabati, and R. Mahdavi, “EVALUATING HOT DEFORMATION BEHAVIOR OF W360 TOOL STEEL BY HOT COMPRESSION TEST,” *Journal of Advanced Materials in Engineering*, vol. 40, no. 1, May 2021, doi: 10.47176/jame.40.1.22122.
- [200] Y. Lu, H. Yu, X. Cai, Y. Rong, and R. D. Sisson, “Martensite Lattice Parameter Measured by Modern X-ray Diffraction in Fe-C alloy,” 2016. [Online]. Available: <https://www.researchgate.net/publication/303364253>
- [201] V. Chaudhary, S. A. Mantri, R. V. Ramanujan, and R. Banerjee, “Additive manufacturing of magnetic materials,” *Prog Mater Sci*, vol. 114, p. 100688, Oct. 2020, doi: 10.1016/j.pmatsci.2020.100688.
- [202] S. Raju, B. J. Ganesh, A. Banerjee, and E. Mohandas, “Characterisation of thermal stability and phase transformation energetics in tempered 9Cr–1Mo steel using drop and differential scanning calorimetry,” *Materials Science and Engineering: A*, vol. 465, no. 1–2, pp. 29–37, Sep. 2007, doi: 10.1016/j.msea.2007.01.127.
- [203] R. Casati, M. Coduri, N. Lecis, C. Andrianopoli, and M. Vedani, “Microstructure and mechanical behavior of hot-work tool steels processed by Selective Laser Melting,” *Mater Charact*, vol. 137, pp. 50–57, Mar. 2018, doi: 10.1016/j.matchar.2018.01.015.
- [204] S. Amirabdollahian *et al.*, “Towards controlling intrinsic heat treatment of maraging steel during laser directed energy deposition,” *Scr Mater*, vol. 201, p. 113973, Aug. 2021, doi: 10.1016/j.scriptamat.2021.113973.
- [205] L. Guo, L. Zhang, J. Andersson, and O. Ojo, “Additive manufacturing of 18% nickel maraging steels: Defect, structure and mechanical properties: A review,” *J Mater Sci Technol*, vol. 120, pp. 227–252, Sep. 2022, doi: 10.1016/j.jmst.2021.10.056.
- [206] E. Jäggle, Z. Sheng, P. Kürsteiner, S. Ocylok, A. Weisheit, and D. Raabe, “Comparison of Maraging Steel Micro- and Nanostructure Produced Conventionally and by Laser Additive Manufacturing,” *Materials*, vol. 10, no. 1, p. 8, Dec. 2016, doi: 10.3390/ma10010008.
- [207] E. A. Jäggle *et al.*, “Precipitation Reactions in Age-Hardenable Alloys During Laser Additive Manufacturing,” *JOM*, vol. 68, no. 3, pp. 943–949, Mar. 2016, doi: 10.1007/s11837-015-1764-2.

- [208] C. Liu, Z. Zhao, D. O. Northwood, and Y. Liu, "A new empirical formula for the calculation of MS temperatures in pure iron and super-low carbon alloy steels," *J Mater Process Technol*, vol. 113, no. 1–3, pp. 556–562, Jun. 2001, doi: 10.1016/S0924-0136(01)00625-2.
- [209] A. Wall and M. J. Benoit, "A review of existing solidification crack tests and analysis of their transferability to additive manufacturing," *J Mater Process Technol*, vol. 320, p. 118090, Nov. 2023, doi: 10.1016/j.jmatprotec.2023.118090.
- [210] J. Vinčić, A. Aversa, M. Lombardi, and D. Manfredi, "Repairing D2 Tool Steel Parts By Directed Energy Deposition Using A Hot Work Tool Steel Or A Metal Matrix Composite," in *World PM 2022 Congress Proceedings*, 2022.
- [211] "ASTM Standard B212: Test Method for Apparent Density of Free-Flowing Metal Powders Using the Hall Flowmeter Funnel", doi: 10.1520/B0212-17.
- [212] "ASTM B527 Standard: Test Method for Tap Density of Metal Powders and Compounds", doi: 10.1520/B0527-15.
- [213] "ASTM B213 Standard: Test Methods for Flow Rate of Metal Powders Using the Hall Flowmeter Funnel", doi: 10.1520/B0213-17.
- [214] G. E. Amidon, P. J. Meyer, and D. M. Mudie, "Particle, Powder, and Compact Characterization," in *Developing Solid Oral Dosage Forms*, Elsevier, 2017, pp. 271–293. doi: 10.1016/B978-0-12-802447-8.00010-8.